From the Agulhas to the South Atlantic: Measuring Inter-ocean Fluxes

Deirdre Ann Byrne

Submitted in partial fulfillment of the
requirements for the degree
of Doctor of Philosophy
in the Graduate School of Arts and Sciences

COLUMBIA UNIVERSITY

2000

ABSTRACT

From the Agulhas to the South Atlantic: Measuring Inter-ocean Fluxes

Deirdre Ann Byrne

The Agulhas Retroflection transfers heat, salt and vorticity from the Indian Ocean to the South Atlantic. The transfer is accomplished by discrete meso-scale features and by the advection of a water column of mixed Atlantic and Indian Ocean origins. The objectives of this thesis are to measure the strength of the Agulhas-South Atlantic (ASA) exchange and to develop a generalized method for the measurement of mass and thermohaline fluxes.

First, ASA mass and energy fluxes are estimated by using sea surface height (SSH) anomalies from satellite altimetry to monitor Agulhas eddies, a significant component of ASA transport. ~20 eddies are tracked from SSH during 1986 - 1989. Six eddies/year are observed entering the South Atlantic; when combined with information from hydrography this suggests minimum annual ASA mass and energy fluxes of $O(5\times10^6)$ m^3s^{-1} and $O(10^{17})$ J. Next, the accuracy of altimetric tide models, critical to measurements of ASA fluxes using altimetry, is evaluated in the Agulhas region by a comparison with *in situ* bottom pressure (BP). The CSR 3.0 model accounts for 98.5% - 99.4% of the variance in bottom pressure at four locations, with maximum discrepancies between model and *in situ* tides reaching 6.5 cm.

In Enhanced Thermohaline Transport Analysis (ETTA), developed herein, vertically averaged thermohaline transport coefficients are parameterized as functions of SSH and acoustic travel time (τ). These quantities, which can be directly measured, are then used as proxies to determine mass and thermohaline fluxes from time-series of altimetric SSH and τ from inverted echo sounder moorings. Using ETTA, the 1992 - 1993 baroclinic-barotropic ASA fluxes through a moored array at 30°S (2°E - 17°E) are estimated at $O(14.5 \times 10^6)$ m^3s^{-1}, $O(15 \times 10^{20})$ J and $O(83 \times 10^{12})$ kg salt per annum. Meso-scale eddies accomplish at least 18% of the transport. Lastly, ETTA is combined with the Gravest Empirical Mode (GEM) technique to create continuous parameterizations of temperature and salinity fields with pressure, τ and SSH. Thus τ and SSH become proxies for vertically resolved thermohaline profiles. With data from the Caribbean region, GEM-ETTA is shown to have the potential to resolve inter-ocean mass and thermohaline fluxes with time and depth.

Contents

Table of Contents **ii**

List of Tables **iii**

List of Figures **iv**

1 Introduction **1**

2 Agulhas Eddies: A Synoptic View Using Geosat ERM Data **10**

2.1 Introduction: The Importance of Agulhas Eddies 11
2.2 Geosat ERM (Exact Repeat Mission) data 12
2.3 Eddy Paths 15
2.4 Eddy amplitudes: Dissipation Rates 18
2.5 Hydrographic data 21
2.6 Eddy Translation 25
2.7 Comparison of Geosat and Hydrographic data 26
2.8 Conclusions 28

3 A Comparison between global tidal model CSR 3.0 and *in situ* bottom pressure in the southeastern South Atlantic **51**

3.1 Introduction 51
3.2 Bottom Pressure 52
3.3 The CSR 3.0 Tide Model 53
3.4 Discussion 53
3.5 Tables 55

4 Eddies in the South Atlantic: Remote Monitoring of Inter-ocean Thermohaline Transport **66**

4.1 Introduction 67
4.2 Data and Data Processing 68
    4.2.1 The BEST project: mooring and hydrographic data 69
    4.2.2 Inverted Echo Sounders 69
    4.2.3 Bottom Pressure 72
    4.2.4 TOPEX/POSEIDON data 72

4.3 Thermohaline variability of the southeastern South Atlantic 74
  4.3.1 Agulhas eddies 77
  4.3.2 13 °C stad eddies 78
  4.3.3 The effect of thermohaline variability on observed quantities . 79
  4.3.4 Water column types 80
  4.3.5 The modified Atlantic water column 82
4.4 Methodology 82
  4.4.1 Baroclinic Transport 83
  4.4.2 Barotropic Transport 84
  4.4.3 Thermohaline anomaly transports 84
4.5 Feasibility Test: SSH$_{T/P}$ and $\delta\tau$ from hydrography 87
4.6 Mooring signals vs. SSH$_{T/P}$ 89
4.7 Application of the ETTA Method 95
  4.7.1 Baroclinic Transports 95
  4.7.2 Barotropic Transports 100
  4.7.3 Mass, Heat and Salt Fluxes at 30°S 101
4.8 Discussion 103
4.9 Conclusions 107

5 Future Work: GEM-ETTA in the Caribbean 165
5.1 Introduction 165
5.2 The Data 166
5.3 Thermohaline variability in the Caribbean region 167
5.4 The GEM-ETTA Method 167
5.5 Results 169
5.6 Using GEM-ETTA 170
5.7 Conclusions 171

List of Tables

3-1a 55
3-1b 56
3-2 56
4-1 91
4-2 98
4-3 103
4-1A 111

List of Figures

2-1 . . . 39
2-2 . . . 40
2-3 . . . 41
2-4 . . . 42
2-5 . . . 43
2-6 . . . 44
2-7 . . . 45
2-8 . . . 46
2-9 . . . 47
2-10 . . . 48
2-11 . . . 49
2-12 . . . 50

3-1 . . . 60
3-2 . . . 61
3-3 . . . 62
3-4 . . . 63
3-5 . . . 64
3-6 . . . 65

4-1 . . . 129
4-2 . . . 130
4-3 . . . 131
4-4 . . . 132
4-5 . . . 133
4-6 . . . 134
4-7 . . . 135
4-8 . . . 136
4-9 . . . 137
4-10 . . . 138
4-11 . . . 139
4-12 . . . 140
4-13 . . . 141
4-14 . . . 142
4-15 . . . 143
4-16 . . . 144

4-17 . . . 145
4-18 . . . 146
4-19 . . . 147
4-20 . . . 148
4-21 . . . 149
4-22 . . . 150
4-23 . . . 151
4-24 . . . 152
4-25 . . . 153
4-26 . . . 154
4-27 . . . 155
4-28 . . . 156
4-29 . . . 157
4-30 . . . 158
4-31 . . . 159
4-32 . . . 160
4-33 . . . 161
4-34 . . . 162
4-35 . . . 163
4-36 . . . 164

5-1 . . . 176
5-2 . . . 177
5-3 . . . 178
5-4 . . . 179
5-5 . . . 180
5-6 . . . 181

Chapter 1

Introduction

While much has been written about the inter-ocean transport of water masses, (see Schmitz [1995] for a review) mass and thermohaline fluxes and their connection to global climate are still the subject of controversy. Inter-ocean transport controls the equalization of properties between ocean basins. The slower or more constricted the transport the more the water masses on either side may potentially differ. At a number of locations, inter-ocean transport variability and the contrast in water mass properties can be large, with a potentially significant effect on the global climate. The Agulhas Retroflection region is a location of strong and variable inter-ocean transport, where warm, salt-enriched waters from the South Indian ocean enter the South Atlantic (e.g., [Gordon, 1986]). As demonstrated by Gordon [1985] the Agulhas Retroflection region as part of the warm water route is the only possible source for waters warm and saline enough to maintain the observed balance in the Atlantic thermocline, a balance which preconditions it for the formation of North Atlantic Deep water (NADW).

Conceptually, much of the circulation in the subtropical South Atlantic ocean (Fig. 2-4) forms a typical ocean gyre: the Brazil Current is the western boundary current [Stramma and Peterson, 1989], the South Atlantic Current serves as the poleward limb of the gyre [Stramma and Peterson, 1990], while the Benguela [Garzoli and Gordon, 1996, Stramma and Peterson, 1989] and the South Equatorial Currents [Stramma, 1991] close the loop as the returning eastern boundary current. This straightforward schematic breaks down, however, when one considers the influence of the Agulhas Current on this system, for the Agulhas is the western boundary current of the South Indian subtropical gyre. As noted by [Gordon, 1985] this makes the South Atlantic subtropical gyre unique in that it receives heat at its poleward extremity. Leakage from the Agulhas current, in the form of incomplete retroflection [Gordon, 1985], eddies (also referred to as rings in the literature) and filaments [Lutjeharms and Gordon, 1987, Lutjeharms and Stockton, 1987, Luteharms and van Ballegooyen, 1988, Shannon et al., 1990, Duncombe Rae, 1991, Valentine et al., 1993, Byrne et al., 1995] serve as a source of heat and salt to the South Atlantic subtropical gyre [Gordon, 1986, Gordon et al., 1992, van Ballegooyen et al., 1994, Duncombe Rae et al., 1996], changing its thermohaline balance from what might otherwise be a colder, fresher Atlantic [Gordon, 1985, 1986, Gordon et al., 1987, 1992]. The Agulhas Retroflection region is also acknowledged to be the most energetically variable of all inter-ocean connections [Zlotnicki et al., 1989]. The Retroflection is found to meander over more than fifteen degrees of longitude [Luteharms and van Ballegooyen, 1988] with two common positions, 13°E and 19°E [Harris el al., 1978] and with current speeds of up to 119 cm s^{-1} [Gründlingh, 1978].

From time to time, the Retroflection is occluded, pinching off an eddy (e.g, Olson and Evans [1986], Lutjeharms and Gordon [1987], Luteharms and van Ballegooyen [1988]). Each eddy traps at it center a remnant of modified Indian Ocean water [Gordon, 1985, Olson et al., 1992]. Feron et al. [1992] determined from a harmonic and principal component analysis of Geosat altimeter data that eddies form in this manner at quasi-periodic intervals of approximately 56 days (a frequency of 6.5 per year). Luteharms and van Ballegooyen [1988] estimated eddy-shedding events to occur on average 39 days apart. Byrne et al. [1995] and Witter and Gordon [1999] have shown that Agulhas eddies are capable of drifting far into the interior of the South Atlantic subtropical gyre. Individual eddy paths are highly idiosyncratic [van Ballegooyen et al., 1994, Byrne et al., 1995, Witter and Gordon, 1999] and not all Agulhas eddies move northwestward; some drift southward toward the subtropical convergence zone [Lutjeharms and Valentine, 1988] meaning that the number of eddies formed is not necessarily a good estimate of the number contributing to inter-ocean transport from the Indian to the South Atlantic.

The observed characteristics of Agulhas eddies vary widely. Duncombe Rae's, [1991] survey of hydrographic data indicated eddy sizes from 180 km - 300 km in diameter, while van Ballegooyen et al. [1994] recorded diameters from 190 km - 320 km in a single year. Lutjeharm's and Gordon's, [1987] *in situ* survey of one very recently formed Agulhas eddy indicated it to be about 375 km in diameter. Eddy drift (translation) speeds can be anywhere from nearly stationary Byrne et al. [1995] to 9.5 cm s^{-1} [Olson and Evans, 1986, Shannon et al., 1990, van Ballegooyen et al., 1994, Byrne et al., 1995]. Agulhas eddies are subject to intense evaporation and cooling at the surface, increasing their salt content relative to their surroundings [Gordon et al., 1987, Olson et al., 1992].

These losses, estimated at up to 485 W m^{-2} and 1.2 cm day^{-1} by van Ballegooyen et al. [1994] and 610 W m^{-2} and 15 kg s^{-1} by Olson et al. [1992], both enrich the salt content and mask the sea surface temperature signal of an Agulhas eddy before it is very far from the source (e.g., Luteharms and van Ballegooyen [1988], McDonagh and Heywood [1999]). Individual eddies have been estimated to provide as much as $13.10\text{x}10^{12}$ kg salt and $2.6\text{x}10^{20}$ J to the South Atlantic [van Ballegooyen et al., 1994]. With estimates of 4-9 of them being formed and/or entering the South Atlantic each year [Luteharms and van Ballegooyen, 1988, Feron et al., 1992, Byrne et al., 1995, Witter and Gordon, 1999], Agulhas eddies have the potential to significantly influence the thermohaline balance of the central and intermediate waters of the subtropical South Atlantic. The inter-ocean thermohaline exchange is not the only one of significance carried out by Agulhas eddies. Olson and Evans [1986] estimate that one Agulhas eddy brought into the South Atlantic the equivalent of 7% of the total annual wind energy input. Their large available potential energy (APE) may also affect the energy balance of the gyre.

Less well documented but also significant are the other Agulhas transports – leakage inshore of the Retroflection, estimated at $20\text{x}10^6$ m^3 s^{-1} [Gordon, 1985] and other intrusions (e.g., filaments) of warm water spun off the Retroflection (see Lutjeharms and Gordon [1987], Lutjeharms and Stockton [1987], Shannon et al. [1990]). Recent work by Lutjeharms and Cooper [1996] indicates that Agulhas filaments are a frequent occurrence and may contribute O(5% - 10%) of the interbasin salt flux estimated to be achieved by Agulhas eddies.

More recently, the transport of another anomalous water mass through the Agulhas region has been observed. This transport comes in the form of anticyclonic rings. Smaller than typical Agulhas eddies, these rings were at first posited to be of Brazil Current origin [Smythe-Wright et al., 1996, Duncombe Rae et al., 1996] and more recently have been thought to be Subantarctic Mode Water (SAMW) formed in the Indian Ocean near 60°E which has become entrained into the Agulhas Current [McDonagh and Heywood, 1999]. These rings contain an intense winter or southern mode water of between 12 °C and 13 °C, ~35.35 psu found in extensive (> 400 m) layers, here referred to as "13 °C stad" water.

It is evident from the many studies referred to above that no ship-based program will adequately sample the region and no satellite will resolve the thermohaline transports. Yet the energy and intensity of the Agulhas-South Atlantic (ASA) exchange make obtaining a measure of the Agulhas input into the South Atlantic a critical task; this transport lies at the center of some of the most significant and difficult questions pertaining to variability and control in the global thermohaline circulation. For while eddies are transient phenomena, their cumulative effect on the ocean is not. The large area over which Agulhas exports might occur, the absence of a sea surface temperature signal, the variability in heat and salt content of intruding Agulhas waters, and the irregularity of the phenomena in time and space make such a task problematic.

In the following chapters, two methods of monitoring inter-ocean transport are examined, both of which use combinations of altimetry and hydrography. In Chapter 2 historic hydrography and GEOSAT altimetry are used to obtain a measure of the ASA mass and energy fluxes that are carried by Agulhas eddies. This is done by tracking Agulhas eddies using maps of anomaly sea surface height (SSH) from the GEOSAT altimeter and modeling their volumetric decay over time.

Chapter 3 contains a comparison of *in situ* measurements of ocean tides in the Agulhas region with the CSR 3.0 global tide model used to correct TOPEX/POSEIDON (T/P) sea surface height ($\mathrm{SSH}_{T/P}$). As barotropic tides in this area have a peak-to-trough amplitude of ∼2 m while meso-scale features like Agulhas eddies might reach 80 cm, the ability to correct accurately for the tides is essential.

In Chapter 4, a new method of monitoring inter-ocean transport called Enhanced Thermohaline Transport Analysis (ETTA) is developed which uses hydrographic information in conjunction with anomaly acoustic travel time ($\delta\tau$) and SSH. First water column type (a combination of associated water masses) is parameterized as a function of $\delta\tau$ and the baroclinic component of SSH from hydrography. Water column type is also used to determine vertically averaged mass, heat and salt transport coefficients. Mass and thermohaline transports are then estimated from time-series of altimetric SSH and τ (from inverted echo sounder moorings). Regional hydrography and IES data from the Benguela Sources and Transports (BEST) project and T/P altimetry are used to test the ETTA method. An examination of the water mass properties in the BEST hydrography reveals that much of the water which is clearly of subtropical South Atlantic origin has been modified by a significant amount of mixing with water from the Agulhas current, with approximately 38%±4% of the Atlantic subtropical water having been replaced. The transport of three water column types (Agulhas, 13 °C stad, and modified Atlantic) through the BEST mooring array is estimated using ETTA.

In Chapter 5, the initial implementation of ETTA is improved by combining it with the "Gravest Empirical Mode" (GEM) technique developed by Watts el al. [1998] and Meinen and Watts [1999]. In GEM-ETTA, pressure, $\delta\tau$ and SSH from historic hydrography are used to parameterize temperature and salinity fields, creating three-dimensional look-up tables where $\delta\tau$ and SSH become proxies for vertically resolved thermohaline profiles. Thus time-series of $\delta\tau$ from (IES moorings) and SSH (from altimetry) can provide estimates of mass and thermohaline fluxes resolved with time, depth and distance. With hydrographic data from the Caribbean region and simulated time-series of $\delta\tau$ and $\mathrm{SSH}_{T/P}$, it is shown that GEM-ETTA has the potential to resolve time-varying inter-ocean mass and thermohaline transports with accuracy and detail.

Bibliography

van Ballegooyen, R.C., M.L. Gründlingh and J.R.E. Lutjeharms, Eddy fluxes of heat and salt from the southwest Indian Ocean into the southeast Atlantic Ocean: a case study, *J. Geophys. Res., 99*, 14,053-14,070, 1994.

Byrne, D.A., A.L Gordon and W.F. Haxby. Agulhas eddies: A Synoptic view using Geosat ERM Data, *J. Phys. Oc, 25*, 902-917, 1995.

Duncombe Rae, C. M., Agulhas Retroflection Rings in the South Atlantic Ocean: An Overview. *S. Afr. J. mar. Sci.*, **11**, 327-344, 1991.

Duncombe Rae, C.M., S.L. Garzoli and A.L. Gordon, The eddy field of the southeast Atlantic ocean: a statistical census from the Benguela Sources and Transports Project, *J. Geophys. Res., 101*, 11,949-11,964, 1996.

Feron, R.C., W.P.M. de Ruijter and D. Oskam, Ring shedding in the Agulhas Current system, *J. Geophys. Res., 97*, 9467-9477, 1992.

Garzoli, S.L. and A.L. Gordon, Origins and variability of the Benguela Current, *J. Geophys. Res., 101*, 897-906, 1996.

Gordon, A.L., Interocean exchange of thermocline water, *J. Geophys. Res.*, 91, 5037-5046, 1986.

Gordon, A.L., Indian-Atlantic transfer of thermocline water at the Agulhas Retroflection, *Science, 227*, 1030-1033, 1985.

Gordon, A.L., J.R.E. Lutjeharms and M.L. Gründlingh, Stratification and circulation at the Agulhas Retroflection, *Deep-Sea Res., 34*, 565-599, 1987.

Gordon, A.L., R.F. Weiss, W.M. Smethie and M.J. Warner, Thermocline and intermediate water communication between the South Atlantic and Indian Oceans, *J. Geophys. Res., 97*, 7223-7240, 1992.

Gründlingh, M.L., Drift of a satellite-tracked buoy in the southern Agulhas Current and Agulhas Return Current, *Deep-Sea Res., 25*, 1209-1224, 1978.

Harris, T.F.W, R. Legeckis and D. van Foreest, The Agulhas Current in March 1969, *Deep-Sea Res., 25*, 549-561, 1978.

Lutjeharms, J.R.E and R.C. van Ballegooyen, The Retroflection of the Agulhas Current, *J. Phys. Oc., 18*, 1570-1583, 1988.

Lutjeharms, J.R.E. and J. Cooper, Interbasin leakage through Agulhas Current filaments, . *Deep-Sea Res, 43*, Part I, 213-238, 1996.

Lutjeharms, J.R.E. and A.L. Gordon, Shedding of an Agulhas ring observed at sea, . *Nature, 325*, 138-140, 1987.

Lutjeharms, J.R.E., and P.L. Stockton, Kinematics of the upwelling front off southern Africa, *S. Afr. J. Mar. Sci., 5*, 35-49, 1987.

Lutjeharms, J.R.E. and H.R. Valentine, Eddies at the subtropical convergence south of Africa. *J. Phys. Oc., 18*, 761-774, 1988.

McDonagh, E.L. and K.J. Heywood, The origin of an Anomalous Ring in the Southeast Atlantic. *J. Phys. Oc., 29*, 2050-2064, 1999.

Meinen, C. S. and D. R. Watts, Vertical structure and transport on a transect across the North Atlantic Current near 42° N, *J. Geophys. Res.*, submitted, 2000.

Olson, D.B. and R.H. Evans. Rings of the Agulhas Current. *Deep-Sea Res., 33*, 27-42, 1986.

Olson, D.B. R. Fine and A.L. Gordon, Convective modification of water masses in the Agulhas, *Deep-Sea Res., 39*, suppl. 1, S163-S181, 1992.

Shannon, L.V., J.J. Agenbag, N.D. Walker and J.R.E. Lutjeharms, A major perturbation in the Agulhas retroflection area in 1986. *Deep-Sea Res., 37*, 493-512, 1990.

Schmitz, W. J., On the interbasin-scale thermohaline circulation, *Rev. Geophys., 33*, 151-173, 1995.

Smythe-Wright, D., A.L. Gordon, P. Chapman and M.S. Jones, CFC-113 shows a Brazil eddy cross the South Atlantic to the Agulhas Retroflection area, *J. Geophys. Res., 101*, 885-895, 1996.

Stramma, L., Geostrophic transport of the South Equatorial Current in the Atlantic, *J. Mar. Res., 49*, 281-294, 1991.

Stramma, L. and R.G. Peterson, The South Atlantic Current, *J. Phys. Oc., 20*, 846-859, 1990.

Stramma, L. and R.G. Peterson, Geostrophic transport in the Benguela Current region, *J. Phys. Oc., 19*, 1440-1448, 1989.

Valentine, H.R., J.R.E. Lutjeharms and G.B. Brundrit, The water masses and volumetry of the southern Agulhas Current region, *Deep-Sea Res., 40*, 1285-1305, 1993.

Witter, D.L and A.L. Gordon, Interannual variability of South Atlantic circulation from four years of TOPEX/POSEIDON satellite altimeter observations, *J. Geophys. Res., 104*, 20,927-20,948, 1999.

Watts, D.R., C. Sun, and S. Rintoul, Combining IES and hydrography to observe the time-varying baroclinic structure of the Subantarctic front, (http://calvin.gso.uri.edu/SAF/woce/GEMposter.html), presented at the World Ocean Circulation Experiment Conference, Halifax, N.S., May 1998.

Zlotnicki, V. L.-L. Fu and W. Patzert, Seasonal Variability in Global Sea Level Observed With Geosat Altimetry, *J. Geophys. Res., 94*, 17,959-17,969, 1989.

Chapter 2

Agulhas Eddies: A Synoptic View Using Geosat ERM Data

Deirdre A. Byrne, Arnold L. Gordon and William F. Haxby

J. Phys. Oc., 25:902-917, 1995

Abstract

Warm core rings formed in the Agulhas Retroflection transfer water from the Indian Ocean to the South Atlantic. In an attempt to measure the strength of this exchange, a combination of satellite altimeter and hydrographic data are used to examine Agulhas eddy paths and decay rates in the South Atlantic. Because the surface dynamic height of a warm-core eddy is higher than surrounding waters, the rings are visible in satellite altimeter measurements. Over 20 Agulhas eddies have been tracked from maps of anomaly sea surface height (SSH) derived from the Geosat Exact Repeat Mission (ERM) dataset. The correlation (r^2) of dynamic height referenced to 2000 dbar and anomaly SSH for one coincidentally sampled area is 97% within an Agulhas eddy, dropping to a fraction of that outside of it, indicating that the SSH anomaly signal is a reliable measure for strong features like Agulhas eddies.

The sizes and distribution of the Agulhas eddies in the ERM record compare favorably with those in recent hydrographic records from the area. Individual eddy tracks from the ERM show the influence of topography, with slowed translation over areas of steep relief. The eddies tracked take a generally WNW course across the South Atlantic, propelled by the mean flow and internal dynamics. While propagating westward, Agulhas eddies decay in amplitude with an e-folding distance of O(1700 km - 3000 km) along-track. As they approach the western boundary of the South Atlantic, at 40°W, the eddies have O(10%) of their initial amplitude remaining.

This study finds the residence time of an Agulhas eddy in the South Atlantic to be 3-4 years. On average, we see six eddies per year formed by the Retroflection which enter the South Atlantic. The 20 eddies tracked therefore represent 50% to 60% of the population that would have been extant during the ERM. We find Agulhas eddies to contribute a minimum of $5 \times 10^6 \mathrm{m}^3\mathrm{s}^{-1}$ to the Indian - South Atlantic water mass transfer, with a corresponding energy flux on the order of 10^{17} Joules.

2.1 Introduction: The Importance of Agulhas Eddies

There has been much discussion in the current literature of the possible sources for South Atlantic thermocline waters and their ramifications. Gordon [1986, 1985] suggests the likelihood of an strong contribution from the Indian ocean, a conclusion supported by recent model studies (e.g. Matano and Philander [1993], Semtner and Chervin [1992, 1988]). The source waters have varying properties, but are referred to collectively as South Indian Ocean Central Water (SICW). Their overall effect is to make the South Atlantic relatively warmer and saltier than do other sources [Gordon et al., 1992, Olson et al., 1992] such as water from the South Atlantic current. Global heat and salinity budgets require an Indian-South Atlantic volume transport of 15 Sv. [Gordon, 1985] where 1 Sv. $\equiv 1 \times 10^6 \mathrm{m}^3\mathrm{s}^{-1}$.

The Agulhas Retroflection produces warm rings which drift into the South Atlantic [van Ballegooyen et al., 1994, Gordon and Haxby, 1990, Lutjeharms and van Ballegooyen, 1988]. These large eddies transfer heat, salt and energy from the Indian ocean into the South Atlantic subtropical gyre [Olson, 1991, Olson and Evans, 1986, van Ballegooyen et al., 1994]. The core of Agulhas eddies carries SICW, which has been modified through evaporation and convection until it is anomalously salty with respect to its origin. A distinct component of this water is a layer originally between 17°C and 18°C, the South Indian Subtropical Mode Water (SIMW). Olson et al. [1992] find the SIMW modified by -0.8°C and $+0.02$ psu within an Agulhas eddy core; dispersed in the subtropical gyre, this water will create a warmer, saltier South Atlantic thermocline. van Ballegooyen et al. [1994] measure heat and salt anomalies of 0.73×10^{20}J-2.36×10^{20}J and 4.35×10^{12}kg-13.10×10^{12}kg for four Agulhas eddies found within 600km from their source in the Retroflection.

Measurements of the Indian Ocean-South Atlantic flux are difficult because of the similarity between the water mass properties of South Atlantic water and those of water leaving the Retroflection [Gordon, 1985, Valentine et al., 1993]. The flux must be calculated before the water is mixed into the South Atlantic thermocline.

We use Geosat altimeter data to examine the volume and energy content of the flux contained within Agulhas eddies. Hydrographic data are used as supporting evidence (see Appendix A). The eddies are detectable in altimetry because the thick layer of SIMW at the eddy center causes an elevation in sea level. As noted by van Ballegooyen et al. [1994], the nature and magnitude of the eddy flux will depend upon the rate at which Agulhas eddies enter the South Atlantic, the extent of their thermohaline anomaly, their subsequent motion and rate of decay, and the processes by which their properties are transferred to surrounding waters. We look at the magnitude of the flux, the number of eddies, their motion in the South Atlantic, and their rate of decay by addressing the following questions:

1. How many Agulhas eddies enter the South Atlantic each year?
2. What path do they take and how long do they survive?
3. How do the energy level and altimeter signal of the eddies change over time?
4. How much mass and energy do they contribute to the Indian Ocean/South Atlantic flux?

2.2 Geosat ERM (Exact Repeat Mission) data

The Geosat ERM lasted from November 1986 to 9 August 1989, $\sim$ 1037 days (2.8 yr). The cycle time for the satellite was 17.05 days, during which it covered 488 ground tracks, 244 descending and 244 ascending. Sixty-one cycles were completed during the mission, but the last two are virtually useless for our purposes, due to extensive data dropout and excessive noise. The initial measurements are every 0.1s, or 0.67 km along-track. Geosat Geophysical Data Records ("GDR", [Cheney et al., 1987]) provide 1s sea surface height (SSH) estimates, 6.7km apart along the satellite track. Each datum is the mean of ten 0.1s measurements by the altimeter. The rms difference between these 10 measurements and a linear least squares fit to them is provided as an error estimate Cheney et al. [1987]. We reject measurements with an associated error $>$ 10cm.

Our data processing scheme follows that of Gordon and Haxby [1990] with the addition of a bandpass filter. In brief, each of the 61 ERM cycles is treated as independent. The data are interpolated to regular points along the groundtrack using an along-track cubic spline. Data gaps are left unfilled. The average slope at every point for which there are 20 or more estimates is calculated. The slopes are integrated to heights, adjusted to minimize the difference between the individual measurements and the time-average profile. This produces a mean SSH field for the dataset. This profile is subtracted from the data of each cycle, resulting in a complete record of residual or anomaly SSH, η, for the world ocean every 17 days.

Orbit error, the difference between an average of each 3 consecutive orbits and the mean over the entire ERM, is modeled and removed from the central orbit of the 3, using a long-wavelength sinusoidal model with a wavelength of 20,000km. We smooth these data with a 5-point running average, leaving us with 512 measurements along each of 488 tracks. Finally, the data along each track are processed using a bandpass filter in the spatial domain with an unattenuated wavelength between 5000 km and 200 km and cutoffs at 100 km and 20,000 km. These filter wavelengths were found by experiment to be the most satisfactory ones for the purposes of identifying Agulhas eddies, which have a characteristic length scale (1/2 wavelength) of O(200 km - 300 km) [Duncombe Rae, 1991, van Ballegooyen et al., 1994].

Binned into $1^\circ \times 1^\circ$ boxes, and averaged over time, the South Atlantic variability in η in the processed data is 3.7cm (Fig. 2-1) for the quiet, mid-gyre area 35°W - 10°E, 35°S - 20°S, which is just above the expected post-processing instrument noise level of 2.2cm (based on Sailor and LeShack [1987]). This variability is comparable to the 3.8cm level reported by Zlotnicki et al. [1989] for the equatorial north Atlantic obtained with a 2500 km second order polynomial orbit correction. However, the bandpass filter, found necessary for efficient eddy tracking, significantly reduces the variability of the Agulhas Retroflection region in our dataset. The maximum variability there is 24.5cm for a 2° square, in contrast with Zlotnicki et al.'s [1989] value of 44cm. The possible effects this reduction will have on our energy calculations will be dealt with in later sections.

The appearance of an Agulhas eddy in the processed data is shown in Figure 2-2. For tracking purposes the processed data from one ERM are interpolated onto a grid and contoured; a least squares planar fit is further removed (Fig. 2-3). From such an interpolation, the position and amplitude of an eddy can be estimated, even if the satellite did not cross the eddy center. Eddy size cannot be determined to within acceptable limits using this method.

For some ocean features, the removal of the 2.8-year mean SSH field can remove a significant portion of its signature on the ocean surface if the feature is not sufficiently variable over the mission time scale [Horton et al., 1992, Kelly, 1991, Kelly and Gille, 1990]. Since Agulhas eddies are transient features that typically translate several km/day, the removal of mean SSH from the data record is not likely to erase the eddy signal. It may however be attenuated, especially if the eddies take a common path in the South Atlantic. We will discuss the effects of this attenuation in Section 2.4.

Horton et al. [1992] show that strong eddies can be reliably identified by satellite altimetry, even in a region of dynamic activity where the SSH variance is high, and van Ballegooyen et al. [1994] have proven the case for the Agulhas Retroflection in particular. In areas of the South Atlantic that are dynamically quiet, Agulhas eddies are even more prominent. As a result, Agulhas eddies can be tracked relatively consistently across the South Atlantic subtropical gyre as long as the data loss remains small.

Instrument and geophysical noise can occur at the wavelengths and amplitudes expected of an eddy. The short-wavelength variability of the atmospheric water vapor signal is inadequately modeled by the corrections applied to the data (FNOC model). An anomalously high water vapor signal produces a low in η which can be of the same horizontal and vertical scales as an Agulhas eddy Monaldo [1990]. It is conceivable that a low water vapor signal might in turn appear identical to the signal of an Agulhas eddy in the data record. The long lifespan of an Agulhas eddy, however, should greatly reduce the likelihood of a misidentification occurring, as water vapor events ought to be much more ephemeral. In practice, the extremely long temporal persistence of Agulhas eddies combined with spatial transience make them ideal candidates for tracking with SSH anomaly data.

2.3 Eddy Paths

More than 20 Agulhas eddies have been tracked from maps like Figure 2-3. The approximate center of the eddy is determined from the map; a succession of such locations determines our estimate of the eddy's path. The eddy-tracking reveals both the rate of Agulhas eddies entering the South Atlantic as their eventual dispersion across the subtropical gyre, moving towards the higher steric heights of the central gyre (see 2-4 4). Some Agulhas eddies have been followed in the ERM record to further than 5000 km from the Retroflection. At the observed translation speeds, (averaging 4.3 cm s^{-1}, $\sigma = 1.8$), and assuming a relatively straight path, this distance indicates the eddy has reached an age of 3-4 years.

Agulhas eddies in the central South Atlantic move westward (Fig. 2-5). The majority of the eddies tracked were first identified around 1°E, outside of the high variability zone of the Retroflection. Tracking proceeded both backwards (east) and forwards (west) in time to obtain the longest record possible of their evolution. A few eddies were followed from a point midway across the South Atlantic ($\sim$ 15°W). For most of the tracks in Figures 2-4 and 2-5, the termination point lies near the end of the satellite lifetime, where data dropout made further tracking difficult.

We have counted 16-18 eddies shed into the South Atlantic during the ERM period; the last two identifications are less certain because of problems with the satellite near the end of its lifetime and the fact that these eddies could not be tracked over a long enough time period to make the identification definitive. The frequency of Agulhas eddies entering the South Atlantic, then, by our estimate averages 6 per year. Feron et al. [1992] using a statistical method with the ERM data to identify eddy shedding variability patterns, found 18 ±2 Agulhas eddies shed during the ERM period. The possible discrepancy, 16-18 vs. 18±2, may be the result of some Agulhas eddies returning eastward and not entering into the region of our study.

Several of the Agulhas eddies that appear in this study have been tracked and sampled in the near-Retroflection area by van Ballegooyen et al. [1994]. The tracking methods of this study is similar to ours and the correspondence is good between features identified in the areas where the studies overlap. This provides a measure of reliability for the tracking method, although we did not have the difficulty in tracking the eddies outside of the immediate area of the Retroflection which they report.

Eddy motion is a combination of self-generated velocity and advection by the surrounding mean flow. Quite visible in Figure 2-4 is the confinement of the eddy tracks to the 28°S-40°S latitudinal band, between the extension of the Benguela current to the north and the South Atlantic Subtropical Front to the south. It is possible this distribution results from limitations in the resolution of the data rather than the influence of large-scale dynamics. However, it is clear from their tracks that the eddies do not simply follow the mean flow, contoured at 500 dbar from Reid [1989] (Fig. 2-4).

Not all Agulhas eddies necessarily take this northwestward route into the South Atlantic; Lutjeharms and Valentine [1988] describe a probable Agulhas eddy south of the Retroflection at 41.5°S and 15°E (perhaps being swept eastward by the Agulhas Return Current). In terms of inter-ocean transport, however, only Agulhas eddies that travel westward from the Retroflection are of interest. Our observations indicate that once westward of 10°E, the eddies' entry into the South Atlantic is assured.

A few of the features that pass our criteria for eddies have been found in the mid-South Atlantic(15°W-30°W, $\sim$ 35°S), outside of where Agulhas eddies have been identified in other studies and somewhat apart from the other eddies tracked in this study (Fig. 2-5). These features are long-lived ($>$ 1 year), of an amplitude 3-4cm above the local noise level, even with the smoothed data, and are observed to translate in a westerly direction at speeds (4-6 cm s^{-1}) like those of other Agulhas eddies (this study, van Ballegooyen et al. [1994], Duncombe Rae [1991], Olson and Evans [1986]).

These features are located in an area where the hydrographic data record is very sparse [Lutjeharms et al., 1992]; so that the fact no Agulhas eddy has been previously observed in the region is not a sufficient criterion to reject the tentative identification. While there is a possibility that these features may be recirculated Brazil Eddies, at this point we include them into our Agulhas Eddy census until further investigation is completed with the more precise TOPEX/Poseidon altimeter data.

Arguably, individual tracks (Fig. 2-5) deviate from the general WNW course in the vicinity of the topographic features like the Rio Grande rise (at 30°S, 35°W) and the Walvis Ridge (stretching from 20°S, 10°E to 40°S, 15°W). Smith and O'Brien [1983] have shown that for an anticyclonic, baroclinic eddy in an ocean otherwise at rest, an eastward component of translation velocity is expected to develop on encountering a meridional ridge. The net velocity is a combination of this self-induced translation and advection by large-scale currents. Eddies tracked with Geosat exhibit a noticeable decrease in their total velocity when crossing the Walvis ridge, even at the 17-day sampling resolution (Fig. 2-6). Drifter data [Olson and Evans, 1986] provide corroborative evidence of topographic steering and slowed translation over steep topography. Eddies moving over steep/shallow ($D < 4000$ m) bathymetry averaged 2.9 km/day (N = 179, $\sigma = 1.4$), while those crossing smooth/deep ($D > 4000$ m) terrain averaged 4.1 km/day (N = 652, $\sigma = 1.2$). It is possible that the eddies' immediate response to topography is much more complex than a simple deceleration, but the categorization is appropriately detailed for the temporal and spatial resolution of our data.

Agulhas eddies appear more likely to cross the Walvis ridge at gaps in the topographic profile. A plot of the distribution of eddy tracks projected against the ridge topography illuminates this behavior (Fig. 2-7). The eddy center locations have been binned by 0.5° latitude. The distribution of eddies crossing the ridge shows a negative correlation (r = -0.57) with topographic height. However, it cannot be concluded from these data if the uneven distribution is a result of the eddies' own interaction with topography, or because of the steering effect of a deep current passing through the ridge gap.

Due to the geography of the Retroflection, Agulhas eddies once formed are free to propagate across the entire South Atlantic basin. This circumstance allows them a lifetime and path length substantially longer than most other warm core rings, e.g. Gulf Stream rings, which have been documented to last a year or two Richardson

[1993], Olson et al. [1985]. Several Agulhas eddies have been tracked to the edge of the Brazil/Malvinas western boundary current area, or 40°W (see Fig. 2-5). In this region, detecting the eddies is especially difficult as they are entering a region of increasingly strong background circulation. In addition, their signal is weaker this far from the source region. While some of them are clearly approaching the western boundary of the South Atlantic, their fate here remains unknown.

2.4 Eddy amplitudes: Dissipation Rates

The amplitudes of eddies in the Geosat GDR show a decrease over time and with distance from the Retroflection. The energetic decay can be expected to depend on the strength of the circulation within the eddy, the time elapsed since its formation, its translation speed, and on the topography over which it passes as well. We use the elapsed distance along the eddy path, from the place it was first identified, as a simple measure of the age and speed.

Elapsed distance from first sighting was found to have a more robust correlation with amplitude than did elapsed time or straight-line distance from an assumed point of origin in the Retroflection. It also performed better than an elapsed distance corrected to the position of the Retroflection core (see Lutjeharms and van Ballegooyen [1988]). However, it should be noted that the eddies' decay, in particular their response to topography is much more complex than this simple estimate; van Ballegooyen et al. [1994] report a noticeable decrease in the decay rate of an Agulhas eddy ('A8') as it comes into contact with the Walvis Ridge.

The height signature of Agulhas eddies in our dataset will have been attenuated by three factors. The maximum amplitude for each eddy recorded by the satellite during one ERM cycle depends on the position of the eddy relative to the satellite groundtracks. Unless the satellite crosses the near the center of the eddy, it will record a height less than the maximum. Therefore we apply a running median filter to each time series of eddy amplitudes. The filter is biased towards higher SSH values [median - 0.6σ, median+ 2σ] to counteract the underrepresentation of maximum eddy height inherent in these data.

The subtraction of a mean field from the SSH record, necessary to remove signals introduced by the inaccuracy of the known geoid and by the less variable component of ocean circulation, will also attenuate the eddy signal; the presence of eddies, particularly near the source region, will be a component of the mean removed. This effect will decrease with distance from the source, as the eddies fan out across the interior of the South Atlantic subtropical gyre. We have measured the strength of this attenuation factor in the SSH fields from the free surface refinement of the Semtner and Chervin 1/4 degree eddy-resolving model [Semtner and Chervin, 1988, 1992]. As these data are uncontaminated by any geoid signal or noise, the instantaneous eddy SSH, relative to its surroundings, can be easily measured and directly compared with its residual SSH (annual mean removed). In the model, attenuation may decrease the eddy signal up to 50% between the longitude of the Retroflection and 10°E, but is much less, around 10%, from the Greenwich meridian westward.

Since the modeled eddies follow a more regular path than the observed ones, the attenuation present in η will be stronger in the modeled than in the real eddies, perhaps by a factor of several times. Because of the variability in the paths taken by real Agulhas eddies, we believe the attenuation will be but slight away from the Retroflection. This is one reason we have concentrated our study on eddies at some distance from the Retroflection. van Ballegooyen et al. [1994] report an attenuation of 15cm out of 70cm (21%) for Agulhas eddy 'A4' in the Geosat record. The location of this eddy at the time was relatively close to the Retroflection at 38°S, 15°E. In comparison, the discrepancy in modeled eddies at the same location is 60cm out of 140cm (42%).

Construction of a synthetic profile [Kelly, 1991, Kelly and Gille, 1990] is another method that has been developed to avoid the attenuation inherent in residual SSH data. We prefer to rely on hydrographic data for more accurate initial eddy amplitudes, and to relate this to the altimeter data, rather than trying to correct the altimeter dataset.

The smoothing of the residual SSH data used to produce a field appropriate for mesoscale eddy-tracking has lowered the variability of the dataset and reduced the recorded amplitudes. The smoothed Geosat anomaly SSH has a standard deviation of 25cm (see Fig. 2-1), compared to 44cm in a similarly processed, unsmoothed version [Zlotnicki et al., 1989]). In our data, the initial eddy amplitudes hover around 1 - 1.5 times the value of the standard deviation of anomaly SSH found in the Retroflection area (Fig. 2-8b). Therefore we take 40cm-60cm as a good measure of the initial amplitude of Agulhas eddies as expressed in residual SSH. This agrees well with hydrographic data and other studies [van Ballegooyen et al., 1994].

To estimate the decay rate, we use 10 eddies that have the most stable height signature which were tracked for an average of 26 ERM cycles (442 days, minimum 100, maximum 940 days). The poor signal-to-noise ratio of the data does not allow the functional form of the decay relationship to be determined with certainty; some researchers have proposed an exponential decay relationship as appropriate [Chassignet et al., 1990], Duncombe Rae, [pers. comm.]. For this relationship, the least squares e-folding distance for the filtered data falls between 1600 km and 1800 km, which translates to a 93%-96% reduction in amplitude between 15°E to 40°W for a the typical Agulhas eddy. An preliminary estimate of the e-folding decay scale in the Semtner and Chervin model eddies compares very favorably at 1700 km.

It can be argued, however, that the true amplitudes of the eddies are better represented by the upper edge of the amplitude envelope, rather than a least squares fit. An initial height of 44cm and an e-folding scale of 3000 km produces a good fit by eye to that edge (Fig. 2-8b). This scale distance represents an 81% reduction in amplitude over the above span. While the amplitude difference between an eddy that has been reduced by 81% and one that has been reduced by 93% (about 6-7cm) may seem small, the difference in the energy content and the possible impact of these eddies on the Brazil Current system is vast.

McWilliams and Flierl's [1979] numerical model produced a roughly linear decay in amplitude with time for a two-layer eddy. We therefore also estimate the linear decay rate. The ensemble mean decay rate of a linear least squares fit to each of the 10 eddies is $\frac{dh}{dx} = 0.077$mm/km. This fit, used with the observed amplitudes, would have the eddies disappearing about 3200 km from the Retroflection, which contradicts our observations. With a more realistic initial amplitude of 55cm, this decay rate represents a decrease of about 70% – the linear relationship being much more sensitive to initial height than the exponential. In both of the calculated decay relationships (linear and exponential) the standard deviation of the least squares decay rate is of the same order as the rate itself. However, we feel that the exponential decay is the more realistic one and will use it in further calculations.

2.5 Hydrographic data

Station data from 10 cruises conducted in the 1980's were scanned for possible Agulhas eddies (see Appendix A). The eddies show in these data as a depression of the 10°C isotherm, h. Most also show a 15°C-17°C thermostad (a layer in which temperature varies little with depth). Approximately 500 stations were included in the search (Fig. 2-9a). Forty-four (9%) were found to have been taken within an eddy, with a total of 15 eddies being sampled. Not surprisingly, most of the eddies that have been encountered were found near the Retroflection region.

The distribution of stations at which eddies were detected agrees rather well with the distribution of eddies found in the Geosat data record (Fig. 2-9b), although a couple of possible eddies have been crossed on cruises a few hundred kilometers north of where we have seen any eddies in the Geosat record. The South Indian Subtropical Mode Water, with its characteristic 17°C layer, is well developed in the stations near to the Retroflection (Fig. 2-10, Appendix B). The stad is capped by a warm summer mixed layer in some of the stations. With increasing distance from the Retroflection, the SIMW stad is eroded from above and below, but is still recognizable.

The core of water trapped within an Agulhas eddy is a measure of the amount it might contribute to the Indian ocean/South Atlantic exchange. Estimates of this amount range from 0.4-1.1 Sv. [McCartney and Woodgate-Jones, 1991], 1.05-1.25 Sv. [van Ballegooyen et al., 1994], to 1-3 Sv. [Gordon and Haxby, 1990]. McCartney and Woodgate-Jones' [1991] transport values have been calculated using Flierl's [1981] theory. Flierl defines a parameter, ϵ, which is the ratio of maximum azimuthal velocity to translation speed at a particular depth. For $\epsilon > 1$, water will be trapped within the eddy. McCartney and Woodgate-Jones [1991] find a trapping depth of 1100 m in the eddy found at stations 098 and 099 of the 1983 R/V *Oceanus* 23°S cruise. Using two different translation velocities, the result is the range given above; the volume of water trapped depends strongly on the translation velocity.

Eddy 'A' (crossed by the RRS *Discovery* during the Benguela program and described in Gordon and Haxby [1990], is closer to the source region and hence more representative of the young eddies facilitating the Indian-South Atlantic inter-ocean transport. For this eddy, the maximum geostrophic velocity in combination with the mean eddy translation speed found from Geosat data, gives a trapping depth of $>$ 2000 m with a radius of maximum azimuthal velocity, L, at 130km from the eddy center. We use a translation speed of 5 cm s^{-1}, close to the average estimated with Geosat data.

With Flierl's [1981] method, which models the azimuthal velocity field found by Olson [1980], we find eddy A accounts for an Indian-South Atlantic flux of 1.8 Sv. above 1000 dbar. Using the entire volume of trapped water, the volume of eddy A divided into a year period represents a flux of 2.1 Sv into the South Atlantic. Other young eddies, namely the Cape Town and Retroflection eddies (CTE and RE) analyzed by Olson and Evans [1986], have trapped volumes which, averaged over the year, contribute 1.4 and 1.8 Sv. respectively to the Indian/South Atlantic flux. For the sum total of eddies found in the search, the volume of trapped water represents an average flux of 0.8Sv. per eddy, assuming that they translate at 5cm s^{-1}. Since most of the eddies found were encountered by chance, undersampled, and at an average of 1400 km from the Retroflection, 0.8 Sv. is a minimum bound. Using this value and a generation rate of 6 eddies per year, Agulhas eddies account for a 5 Sv. flow from the Indian Ocean into the South Atlantic above 1000 dbar. The average trapped volume in 3 well-sampled young eddies, the CTE, the RE, and Eddy A, is 1.7 Sv, which at 6 eddies/year results in a flux of 10 Sv. Taking this as an upper bound, we conclude the flux due to Agulhas eddies is on the order of 7 Sv., or half the 15 Sv. proposed by Gordon [1985] for the total interbasin transport. This agrees with the conclusions of van Ballegooyen et al. [1994], who calculate a volume flux of between 6.3 Sv. and 7.3 Sv. of water warmer than 10°C in Agulhas eddies reaching the South Atlantic.

If the eddy hydrographically surveyed in detail, eddy 'A4', in van Ballegooyen et al. [1994] can be taken as typical, each Agulhas eddy the enters the South Atlantic is responsible for a corresponding inter-ocean salt flux on the order of 0.42×10^6kg s^{-1} – a source of 2.5×10^6kg s^{-1} with six eddies a year of this size and composition, and a total heat input of 0.045 PW for the same. As the authors mention, the exact amount of the flux will depend on the depth to which the eddy anomaly is considered when making the calculation.

Assuming the ratio between barotropic and baroclinic modes within an Agulhas eddy is approximately constant, the vertical displacement of an isotherm at depth can be expected to decline in the same manner as the surface signature of the dynamic height anomaly. There is a strong linear relationship in general between the dynamic height anomaly and h, the depth of the 10°C isotherm, which can be written

$$D_{100/2000dbar} = \frac{g'}{9.8}h + C \tag{2.1}$$

where C is a constant and $g' = g\Delta\rho/\overline{\rho}$. We find $D_{100/2000dbar} = 0.9935 + 0.00159h$ or $g' = 0.016\text{m s}^{-2}$ (see Figure 2-11a), for 30 stations within the eddies surveyed. This is comparable with Olson et al.'s [1985] result $g' = 0.018\text{m s}^{-2}$ for the CTE and RE, which used the Levitus [1982] dataset as a reference for the area. van Ballegooyen et al. [1994] find $g' = 0.0126$ for the southwest Atlantic but as mentioned in that study, the authors feel the result of their regression, which used data from only one cruise, is anomalously low. The correlation between the 16° isotherm and surface dynamic height, while proposed by Horton et al. [1992] for use in this manner (and further for correlation to the SSH anomaly), is found to be unacceptably weak in our data.

Olson and Evans [1986] also examine $dh = h - h^{\infty}$, the displacement of the 10° isotherm within the eddy relative to the ambient water.The perturbed isotherms within an eddy can be expected to relax as the eddy decays ($dh \rightarrow 0$). We find an average depression of 193m, decreasing in general with distance from the Retroflection (see Figure 2-11b). This is smaller than has been reported by other researchers; for example, Duncombe Rae [1991] in an overview of related work, reports an average displacement of 350m. Our average includes some eddies that are further westward and therefore older and weaker than those of other studies; at locations similar to those reported by other researchers, our results compare favorably to theirs. For the eddy stations used in this investigation, the exponential relaxation scale for dh with distance from the Retroflection is O(3000) km similar to one such estimate of the scale for anomaly SSH (see Section 2.4).

We use Olson and Evans [1986] method to calculate the kinetic and (gravitational) available potential energies (KE and APE) of the eddies above the 10° isotherm of a Gaussian-shaped eddy:

$$APE = \frac{\rho g'}{2}\Sigma dh^2 \qquad KE = \frac{\rho}{2}\Sigma hv^2 \tag{2.2}$$

where Σ is summation over the eddy. The APE of twelve of the eddies for which sufficient data were available to calculate it averages 18×10^{15}J (Fig. 2-8a). The APE's of the Cape Town and Retroflection eddies are included in the twelve. In a more detailed calculation, Olson and Evans [1986] find the APE and KE to be 30.5×10^{15}J and 6.2×10^{15}J for the Cape Town eddy, and 51.4×10^{15}J and 8.7×10^{15}J for the Retroflection eddy. The eddy APE in the hydrographic data appears to dissipate exponentially with distance from the source region, which is consistent with the exponential decay of amplitude and Eq. (2) and leads us to expect an initial APE at the Retroflection of 70×10^{15}J. While Olson and Evans [1986] used the gradient balance velocity, our energy estimates are based on geostrophic velocities which are about 10% lower than those obtaining from the gradient balance. The calculation of kinetic energy is also sensitive to the radial distribution of velocity, which is cannot be ascertained from our data; again using Flierl's [1981] model of azimuthal velocity distribution mentioned above, we find the KE of the twelve eddies to average 4.5×10^{15}J. This does not include kinetic energy from the barotropic velocity field.

2.6 Eddy Translation

Agulhas eddy dynamics are only weakly non-linear. From hydrographic and altimeter data, we estimate the Rossby number, $R_o = V/fL$. Here V is the maximum geostrophic velocity found within the eddy (the velocity at L), and f is the Coriolis parameter. We find $R_o = 0.077$, comparable to the value of 0.055 estimated by Chassignet et al. [1990]. While weak, the non-linearity is not unimportant. Chassignet et al. [1990] define an eddy Burger number, $B' = g'dh/f^2L^2$, (or $B \equiv {R_D}^2/L^2$ where $R_D = \sqrt{g'dh}/f$), which gives a measure of the eddy strength. The Rossby and Burger numbers have been found in theory to be controlling parameters describing eddy motions. Nof's [1981] results for a two-layer, isolated anticyclonic eddy on a β-plane lead us to expect a motion that is self-induced and slightly north of west, at a translation speed, V_T that is a fraction of the baroclinic Rossby wave phase speed, $\beta {R_D}^2$. Nof [1981] finds the fraction to be 1/3 to 2/3, increasing with greater non-linearity; Agulhas eddy speeds would fall near the lower end of that solution. Eddies with stronger tangential velocities are expected to propagate faster. The theory is limited to nearly circular eddies with constant translation velocities.

Cushman-Roisin et al. [1990] in a more general treatment, place limits on self-induced eddy motion of

$$\frac{-\beta g' H}{{f_0}^2} < \frac{dX}{dt} < \frac{-\beta g'(H + h_{max})}{2{f_0}^2} \tag{2.3}$$

Cushman-Roisin et al.'s [1990] results seem to indicate the eddy speed should be about half the baroclinic Rossby wave speed. Here, H is the depth of an undisturbed layer about the eddy and h_{max} is the maximum interfacial displacement at the eddy center. Using the Nof's [1981] formula as a lower bound and Cushman-Roisin et al.'s [1990] upper limit, with typical values of $H \sim 300 - 400$m, 475m $< h_{max} <$ 700m and $g' = 0.016$ (Section 2.5), the limits on self-induced translation become roughly 2km/day $< V_T <$ 8km/day to the west for a young (more energetic) eddy and 1.5km/day $< V_T <$ 5km/day for an old (less energetic) one. For the eddies we have tracked, V_T averages 3.8 +/- 1.5 km/day, implying that about half to most of the observed eddy velocity is due to self-induced translation and the remaining to advection by the mean flow.

2.7 Comparison of Geosat and Hydrographic data

Blaha and Lunde [1992] have developed a relationship between the Geosat SSH anomaly and the geopotential (dynamic) height anomaly for the Western North Atlantic, which they measured with airborne XBT's during simultaneous underflights of the Geosat satellite while it was operational. The processing methods for the satellite data in their study are unfortunately quite different from ours, but we use an analogous method, based on the hydrographic data for eddy A. These data were collected in the spring of 1987, while Geosat was operating in ERM cycles 10 and 11.

We define D' as the difference between $D_{100/2000dbar}$ at the eddy center and its value in the surrounding region. For eddy A, D' has a range of -7mm to 276mm . Dynamic height compares favorably with η within eddy A (Fig. 2-12a). A radial average of η, using 3 ascending and 3 descending tracks has a range of -5mm to 175mm. The radial average is used to compensate for the fact the cruise track and nearby Geosat groundtracks are not colinear or even parallel. Smoothing and averaging have expectedly decreased the amplitude range. The correlation between D' and η is very strong: $r^2 = 0.97$ (with D' also radially averaged about the eddy center and both datasets interpolated to 10km) for 23 hydrographic stations and 4 Geosat tracks (Fig. 2-12b).

One eddy diameter away, the correlation has dropped to a fraction of this value, indicating a much higher proportion of the variance outside the eddy is uncorrelated noise. With D' in dynamic meters and η in mm, we find

$$D' = \alpha\eta, \quad \alpha = 1.5372 \times 10^{-3}. \tag{2.4}$$

Using the regression performed in Section 2.5,

$$dh = \frac{9.8\alpha\eta}{g'}, \tag{2.5}$$

giving $dh = 0.95\eta$ (again with dh expressed in m and η in mm). This is an intuitively satisfying result, confirming the utility of satellite-measured sea surface height as a proxy for surface dynamic height.

While the volume transport will be based on L, the radius of maximum azimuthal velocity, this value cannot be derived from the altimeter record. We choose another length scale from the altimeter observations, a radius R_η where η becomes negligible. We also define R_h, the distance from the eddy center at which dh goes to zero. The strong correlation between h and D makes R_h characteristic of D' as well. For eddy A, R_η and R_h are both 240km (±20km). Note that R_η was obtained directly from along-track altimeter data rather than the gridded version. Model results from Chassignet et al. [1990] lead us to expect a ratio of $L/R_h = 0.63$. For Eddy A we find $L/R_h = 0.52$. The data processing is likely to have decreased this ratio, as the filtering will increase the apparent eddy radius in the Geosat data.

Care must be taken, however, not to over-generalize from our single eddy. With caution, we will use Geosat SSH anomaly as a measure of isotherm depth within Agulhas eddies. The simple relation $D' = \frac{275}{175} \times \eta = 1.6\eta$ is defined by the relative amplitudes of anomaly dynamic height and anomaly SSH within eddy A. We use $g' = 0.016\text{m s}^{-2}$ from the regression above, an e-folding distance of 3000 km (Fig. 2-8b) and a constant radius of $L = 200$ km; with extrapolation to a nominal point of entry into the South Atlantic at 40°S, 15°E, Olson & Evans' [1986] equation for APE (see Section 2.5) provides an estimate of the APE of the Agulhas eddies in the Geosat altimeter record as they enter the South Atlantic.

Of 28 estimates, several were an order of magnitude larger or an order smaller than the expected range; these are probably the result of noise contamination in the altimeter record and are discarded. The 20 remaining measurements of initial Agulhas eddy APE range from 10×10^{15} J to 86×10^{15}J, averaging $40(\pm 26) \times 10^{15}$J.

This is comparable to the APE reported for the (young) Cape Town and Retroflection Eddies reported by Olson and Evans [1986], but smaller by almost a factor of 2 than the initial APE that the hydrographic data suggest. This is quite possibly an artifact of the smoothing in our dataset more than anything else.

Using an e-folding scale distance of 1700 km and the same 20 eddies, the mean initial energy is 165×10^{15}J, with an uncertainty of the same order – in other words, our method of determining an initial maximum amplitude becomes unstable at some e-folding scale less than 3000 km. However, the results do suggest that the true scale distance lies somewhere between these two values; a scale distance of 2300 km reproduces the initial APE's in a range very close to those of Olson & Evans' [1986] measurement. Since we are interested in gauging the effect Agulhas eddies might have on the South Atlantic, we will use the energy estimate based on an e-folding scale of 3000 km as a lower bound for the actual value.

The kinetic energy of each eddy, proportional to the square of geostrophic velocity, is harder to evaluate accurately from these data, but in Olson & Evans' [1986] study it is on the order of one-fifth as much as the APE. Using this ratio, the energy flux (APE + KE, neglecting heat) into the South Atlantic from Agulhas eddies, based on Geosat measurements, is then at least $O(9 \times 10^9)$W assuming six eddies/year, and possibly as much as twice that. If the decay scale length is chosen as 3000 km, the amount of energy reaching the western South Atlantic via Agulhas eddies would be 5 to 10 times more than the amount available with a decay scale of 1700 km – on the order of 6×10^{15}J to 10×10^{15} J as opposed to $O(1 \times 10^{15})$ J.

2.8 Conclusions

Agulhas eddies are the dominant component of South Atlantic mesoscale variability [Olson and Evans, 1986]. Our record of Agulhas eddy tracks indicates 6 eddies per year enter the South Atlantic. The Retroflection geometry allows the eddies a long lifetime (3 to 4 years). Steep topography has a noticeable effect on eddy trajectories and translation speeds. Our tracking method does not reveal what percentage (if any) of eddies produced at the Agulhas Retroflection do not enter the South Atlantic. However, since we observe 16-18 eddies generated during the ERM period, while Feron et al. [1992] estimate 18 ± 2 using a method independent of the eddy's subsequent path, it appears the majority reach the South Atlantic and are able to be tracked at least part way across the subtropical gyre. This stands in contrast to the estimate of a 50% tracking success rate deduced by van Ballegooyen et al. [1994]. While 6 eddies per year is the average, it should be noted that the number of eddies in any particular 12-month period is extremely variable, ranging from 4 to 8 [van Ballegooyen et al., 1994].

Agulhas eddies are observed to travel the width of the South Atlantic basin, having been tracked as far west as 40°W. Their amplitudes at this point are a small fraction of the initial values; we estimate the e-folding scale distance at 2300 km. Even at much reduced strength, the Agulhas eddy in the western South Atlantic represents a significant source of energy. While having been observed near the Brazil current, it is not clear whether the eddies interact directly with it. One probable effect of such an interaction would be to add energy and vorticity to the Brazil current. Collectively, the eddies may have $O(6 \times 10^{15} J)$ available the spin up the Brazil current system, and perhaps influence the eddy generating behavior of the Brazil-Malvinas Confluence. A closer study of Agulhas eddies in the western South Atlantic is needed to address the question of how this energy is utilized.

Analyses of eddy dynamics suggest that half or more of the observed translation speed may be able to be attributed to self-induced motion. The mean trajectory is towards the northwest at 293° True, and most excursions from it are in the vicinity of steep topography. The interaction between baroclinic and barotropic modes within an eddy is likely to be extremely important in determining its response to topography [Smith and O'Brien, 1983]. Topography also appears to influence the rate of decay [van Ballegooyen et al., 1994] but the extent of this effect has not been thoroughly investigated.

Fifteen probable Agulhas eddies are found in data from 10 cruises (four of these are identified as such by McCartney and Woodgate-Jones [1991], Gordon and Haxby

[1990], and Olson and Evans [1986]), accounting for 44 stations out of a total of over 500. The distribution of stations falls generally within the envelope of Geosat-observed eddy locations but most stations lie east of the Greenwich meridian, where the eddies are relatively young. These fifteen eddies are transporting an average of 0.8 Sv. of trapped Indian Ocean water each, visible in part as the SIMW stad at 17°C. Each eddy is also transporting kinetic and available potential energy. The mean APE and KE, from the hydrographic measurements, are 18×10^{15}J and 4.5×10^{15}J per eddy. This average, composed of eddies at differing distances from the Retroflection, is not representative of the amount of energy entering the South Atlantic via an Agulhas eddy, which is considerably higher, on the order of 40×10^{15}J to 70×10^{15}J.

Anomaly SSH and anomaly dynamic height within one Agulhas eddy surveyed at a time coincident to the ERM mission show a very strong correlation, ($r^2 = 97\%$) once they have been interpolated to the same scale and radially averaged within the eddy. The correlation drops off extremely rapidly with distance away from the eddy. A relationship between anomaly SSH and the depth of the 10°C isotherm is obtained for this eddy; by extrapolation the transport of the six or so Agulhas eddies produced a year is at least 7 Sv. of Indian Ocean water into the South Atlantic. Gordon et al. [1987] estimated the net transfer at 5-14 Sv, while Gordon [1985] suggests a total flux of 15 Sv.; van Ballegooyen et al. [1994] estimate the eddy component of this transfer at 6.3 Sv - 7.3 Sv. The energy input of this flow, estimated from the altimeter data, is at least $O(9 \times 10^9)$W assuming six eddies per year.

Each Agulhas eddy the enters the South Atlantic will contribute not only energy but heat and salt to the South Atlantic thermocline waters; van Ballegooyen et al. [1994] conclude an eddy-contained salinity anomaly for one well-sampled eddy of 13×10^{12} kg, leading to an eddy-based salt flux of perhaps $O(2.5 \times 10^6 \text{kg s s}^{-1})$ (for 6 eddies/year) with a corresponding heat influx of 0.045 PW.

Agulhas eddies are a significant component of the Indian/South Atlantic inter-basin exchange and of the South Atlantic meridional thermohaline flux. The Geosat data have shown their utility in monitoring the production and distribution of this mesoscale feature. Further satellite monitoring will be able to help resolve the interannual variability in eddy generation rates and paths, and better altimeter data will allow the dissipation rate of the eddies to be quantified in a more robust manner. While we are able to estimate the apparent potential and kinetic energies of an eddy by remote sensing, the evolution of water mass properties is far more subtle. The initially strong SIMW stad, which can be 400m or more thick, decays with distance from the Retroflection at what is arguably the same rate as that measured by anomaly SSH. The diffusion of heat and salt from the eddy as it progresses afield may be far more complex than this simple decay, and requires *in situ* measurement. A number of cruises have surveyed Agulhas eddies near the Retroflection, but there is a need for direct measurements further from the source – particularly at locations west of the Walvis ridge. With such information, and the use of an improved satellite altimeter such as the TOPEX and POSEIDON instruments now in operation, a more precise evaluation of the role of Agulhas eddies in the Indian-South Atlantic balance may be at hand.

Acknowledgments. The authors would like to thank Douglas Martinson, Donald Olson, Hsien Wang Ou and Victor Zlotnicki for their helpful comments on the manuscript. This work was supported by Office of Naval Research grant N00014-90-J-1233 and NASA grants NAGW 1925 and NGT 30217. This is Lamont-Doherty contribution no. 0000.

Appendix A: Hydrographic Cruises Used in Survey

Ajax Leg 1 (R/V *Knorr*)

Agulhas Retroflection Cruise (using only data collected on the R/V *Knorr*)

Benguela (RRS *Discovery* 165-B)

U.S. Naval Oceanographic Office, data collected on the *Wilkes*, 1983-1984

Oceanus 23°S (R/V *Oceanus* Cruise 133)

South Atlantic Ventilation Experiment 3 (SAVE3) (R/V *Knorr*)

SAVE 4 (R/V *Melville*)

SAVE 5 (R/V *Melville*)

SAVE 6 (R/V *Melville*)

SAVE 7 (F/S *Meteor*)

Appendix B: Stations Appearing in Figure 2-11

ARC 028	38.9598°S	18.5073°E
ARC 070	38.3945°S	17.279°E
ARC 011	36.0017°S	15.4617°E
ARC 077	35.5095°S	14.0708°E
ARC 079	34.6195°S	13.7235°E
NAVO 300	33.972°S	9.935°E
SAVE4 224	29.9667°S	6.9333°E
NAVO 296	31.985°S	6.113°E
SAVE4 220	29.9833°S	2°E
Ajax 038	30.005°S	1.8333°E
Ajax 042	33.985°S	1.2483°E
Ajax 041	33.0183°S	0.995°E
SAVE3 140	26°S	0.2333°W
OCEANUS 099	24.0083°S	5.6°W
NAVO 028	22.553°S	29.968°W

Bibliography

Ajax Expedition, 1988: Ajax Data Report, Physical, Chemical and in-situ CTD Data from the Ajax Expedition in the South Atlantic Ocean aboard the R/V *Knorr*, Leg I, 7 October - 6 November 1983, Leg II, 11 January - 19 February 1984, *SIO Ref. 84-24*, Scripps Inst. of Oceanogr., U. of CA, San Diego, La Jolla.

Blaha, J. and B. Lunde, Calibrating altimetry to Geopotential Anomaly and Isotherm Depths in the Western North Atlantic, *J. Geophys. Res., 97*, 7465-7477, 1992.

van Ballegooyen, R.C., M. L. Gründlingh and J. E. Lutjeharms, Eddy Fluxes of Heat and Salt from the Southwest Indian Ocean into the Southeast Atlantic Ocean: A Case Study, *J. Geophys. Res., 99*, 14053-14070, 1994.

Camp, D. B., W. E. Haines, B.A. Huber, S. E. Rennie and A. L. Gordon, *Agulhas Retroflection Cruise*, Lamont-Doherty Geological Observatory Technical Report L-DGO-86-1, 1986.

Chassignet, E. P., D. B. Olson and D. B. Boudra, Motion and Evolution of Oceanic Rings in a Numerical Model and in Observations. *J. Geophys. Res., 95*, 22121-22140, 1990.

Cheney, R. E., B. C. Douglas, R. W. Agreen, L. L. Miller, and D. L. Porter, Geosat Altimeter geophysical data record (GDR) user handbook, *NOAA Tech. Memo. NOS-NGS-46.*, 1987.

Cushman-Roisin, B., E. P. Chassignet and B. Tang, Westward Motion of Mesoscale Eddies, *J. Phys. Oc., 20*, 758-768, 1990.

Duncombe Rae, C. M., Agulhas Retroflection Rings in the South Atlantic Ocean: An Overview, *S. Afr. J. mar. Sci., 11*, 327-344, 1991.

Feron, R.C.V., W.P.M. de Ruijter and D. Oskam, Ring Shedding in the Agulhas Current System, *J. Geophys. Res., 97*, 9467-9477, 1992.

Flierl, G. R., Particle Motions in large-amplitude wave fields, *Geophys. and Astrophys. Fluid Dyn., 18*, 39-74, 1981.

Gordon, A. L., Interocean Exchange of Thermocline Water, *J. Geophys. Res., 91*, 5037-5046, 1986.

Gordon, A. L., Indian-Atlantic Transfer of Thermocline Water at the Agulhas Retroflection. *Science, 227*, 1030-1033, 1985.

Gordon, A. L. and W. F. Haxby, Agulhas eddies invade the South Atlantic: evidence from Geosat altimeter and shipboard conductivity-temperature-depth survey, *J. Geophys. Res., 95*, 3117-3125, 1990.

Gordon, A. L., J. R. E. Lutjeharms and M. L. Gründlingh, Stratification and Circulation at the Agulhas Retroflection, *Deep-Sea Res., 34*, 565-599, 1987.

Gordon, A. L., R. F. Weiss, W. M. Smethie Jr. and M. J. Warner, Thermocline and Intermediate Water Communication Between the South Atlantic and Indian Oceans. *J. Geophys. Res., 97*, 7223-7240, 1992.

Horton, C. W., D. L. Porter, P. W. deWitt and W.E. Rankin, Airborne Expendable Bathythermograph Survey of the Kuroshio Extension and Comparison with Simultaneous Altimeter Measurements During the Geosat Exact Repeat Mission, J. Geophys. Res., 97, 7447-7463, 1992.

Kelly, K., The Meandering Gulf Stream as Seen by the Geosat Altimeter: Surface Transport, Position, and Velocity Variance from 73° to 46°W, *J. Geophys. Res., 96*, 16271-16738, 1991.

Kelly, K. and S. T. Gille, Gulf Stream Surface Transport and Statistics at 69°W from the Geosat Altimeter, *J. Geophys. Res., 95*, 3149-3161, 1990.

Levitus, S., Climatological Atlas of the World Ocean, *NOAA Prof. Pap.*, 13, 173 pp., U.S. Govt. Printing Office, Washington, D.C., 1982.

Lutjeharms, J. R. E. and R. C. van Ballegooyen, The Retroflection of the Agulhas Current, *J. Phys. Oc., 18*, 1570-1583, 1988.

Lutjeharms, J. R. E. and H. R. Valentine, Eddies at the Subtropical Convergence South of Africa, *J. Phys. Oc, 18*, 761-774, 1988.

Lutjeharms, J. R. E., H. R. Valentine, and R. C. van Ballegooyen, The Subtropical Convergence in the South Atlantic Ocean, *S. Afr. J. Sci., 89*, 552-559, 1992.

Matano, R. P. and S. G. H. Philander, Heat and Mass Balances in the South Atlantic Ocean Calculated from a Numerical Model. *J. Geophys. Res., 98*, 977-984, 1993.

McCartney, M. S. and M. E. Woodgate-Jones, A deep-reaching anticyclonic eddy in the subtropical gyre of the eastern South Atlantic, *Deep-Sea Research, 38*, S411-S443, 1991.

McWilliams, J.C. and G.R. Flierl, On the evolution of isolated, nonlinear vortices, *J. Phys. Oceanogr., 9*, 1155-1182, 1979.

Mele, P. A., W. E. Haines, B. A. Huber and A. L. Gordon, CTD and Hydrographic Data from Cruise 165B of RRS *Discovery* - Benguela, Lamont- Doherty Geological Observatory Technical Report, L-DGO-90-2, 1990.

Monaldo, F., Pathlength Variations Caused by Atmospheric Water Vapor and Their Effects on the Measurement of Mesoscale Ocean Circulation Features by a Radar Altimeter, *Jour. Geophys. Res., 95*, 2923-2932, 1990.

Nof, D., On the beta-induced motion of baroclinic eddies, *J. Phys. Oceanogr., 11*, 1662-1672, 1981.

Olson, D. B., The physical Oceanography of two rings observed by the cyclonic ring experiment. Part II: dynamics, *J. Phys. Oceanogr., 10*, 514-528, 1980.

Olson, D. B., Rings in the ocean, *Annu. Rev. Earth Planet. Sci., 19*, 283-311, 1991.

Olson, D. B., R. W. Schmitt, M. Kennelly and T. M. Joyce, A Two-Layer Diagnostic Model of the Long-Term Physical Evolution of Warm-Core Ring 82B, *J. Geophys. Res., 90*, 8813-8822, 1985.

Olson, D. B., and R. H. Evans, Rings of the Agulhas current, *Deep-Sea Res., 33*, 27-42, 1986.

Olson, D. B., R. A. Fine and A. L. Gordon, Convective modifications of water masses in the Agulhas, *Deep-Sea Research*, **39**, S163-S181, 1992.

Reid, Joseph L., On the total geostrophic circulation of the South Atlantic Ocean: Flow patterns, tracers, and transports, *Prog. Oc., 23*, 149-244, 1989.

Richardson, P. L., A census of eddies observed in North Atlantic SOFAR Float Data, *Prog. Oc., 31*, 1-50, 1993.

Sailor, R. V. and A. R. LeShack, Preliminary Determination of the GEOSAT Radar Altimeter Noise Spectrum, *Johns Hopkins APL Technical Digest, 8*, 182-182, 1987.

Semtner, A. J., and R.M. Chervin, Ocean general circulation from a global eddy resolving model, *J. Geophys. Res., 97*, 5493-5550, 1992.

Semtner, A. J. and R. M. Chervin, A Simulation of the Global Ocean Circulation With Resolved Eddies, *J. Geophys. Res., 93*, 15502-15522, 1988.

Smith IV, D. C. and J. J. O'Brien, The interaction of a two-layer isolated mesoscale eddy with bottom topography. *J. Phys. Oceanogr., 13*, 1681-1697, 1983.

Valentine, H. R., J. R. E. Lutjeharms and G. B. Brundit, The water masses and volumetry of the southern Agulhas Current region. *Deep-Sea Res., 40*, 1285-1305, 1993.

Zlotnicki, V. L.-L. Fu and W. Patzert, Seasonal Variability in Global Sea Level Observed With Geosat Altimetry, *J. Geophys. Res., 94*, 17,959-17,969, 1989.

Figure 2-1. SSH variability in the processed data for the South Atlantic, contoured in cm. The Agulhas Retroflection region is the area of highest variability. Within the Retroflection region, unnumbered contours are at intervals of 1cm.

Figure 2-2. A Geosat track over time. The x-axis is along-track distance. The y-axis is time, expressed in 17-day cycles. The data are contoured separately at each cycle. An Agulhas eddy is crossed in the first cycle, and can be seen moving out from underneath the track as time progresses. The diagonal line connects the positions of the eddy maxima at succeeding points in time.

Figure 2-3. The Geosat data after it has been processed and interpolated onto a regular grid using a natural cubic spline. A planar surface has further been removed from the mapped area. These data are from one 17-day repeat ERM period. Values of $\eta > 0$ are contoured in solid lines. Some distortion (order L) will occur because of the movement of the eddies, and because of the data processing. Several eddies are visible in the figure, at this point about 1000km from their source.

Figure 2-4. The distribution of Agulhas eddies in the South Atlantic ocean. Triangles show the positions of eddy centers located with Geosat ERM data. Steric anomaly at 500 dbar from Reid, [1989] is contoured.

Figure 2-5. Paths of some of the individual eddies that have been tracked with Geosat data. Underlying bathymetry is contoured in 1000m intervals. The tracks are smoothed from estimates of the eddy center, with shapes at evenly spaced time intervals of 34 days (2 ERM cycles).

Figure 2-6. The standardized distributions of eddy translation velocities. The solid line shows the distribution of velocities for eddies moving over smooth/deep topography, averaging 4.1 km/day (N = 652, $\sigma = 1.2$). The dotted line is the velocity distribution for eddies moving over shallow/steep terrain, averaging 2.9 km/day (N

= 179, $\sigma = 1.4$).

Figure 2-7. The distribution of Agulhas eddies with latitude as they cross the Walvis ridge. A transect of the Walvis ridge is plotted below for comparison. The bathymetry has been contoured along a line following the crest of the ridge, which is approximately meridional.

Figure 2-8a,b. (a) The available potential energy (APE) of twelve Agulhas eddies surveyed hydrographically, plotted versus distance from the Retroflection. The e-folding distance for the energetic decay is 650km. (b) The decay of eddy amplitude with distance from the Retroflection. The least-squares e-folding distance is 1700km (thick line). The thin line shows an e-folding scale of 3000km, here with an initial amplitude of 44cm.

Figure 2-9a,b. (a) Stations used in the hydrographic survey. Non-eddy stations are open squares, eddy stations are black circles. (b) Eddy stations (circles) plotted over the distribution of eddies found in the Geosat data (squares).

Figure 2-10. θ/Z plots for 15 of the eddy stations. 17°C has been marked with a dashed line. The horizontal axis is marked in 1°C increments from 6°C to 24°C. The stations are arranged in increasing distance from the Agulhas Retroflection, left to right, top to bottom. A list of the station ID's appears in Appendix B. The first two stations fall within the so-called Retroflection Eddy (RE), while the next three are in the Capetown Eddy (CTE) (see Olson et al., [1992] and Gordon et al., [1987] for details).

Figure 2-11a,b. (a) Dynamic height vs. depth of the 10°C isotherm within Agulhas eddies. (b) The perturbation of the 10°C isotherm within the eddies plotted versus distance from the Retroflection.

Figure 2-12a,b. (a) The solid line denotes anomaly dynamic height D' (in dyn m) measured from the RRS *Discovery* in March 1987. The dotted line is η, anomaly SSH, measured by the Geosat altimeter. Both data types have been interpolated to 10km using a cubic spline, and then radially averaged around the eddy center. The secondary 'bump' at the top of the eddy is the result of an irregularity in the eddy on the SW side having been smeared all the way around the radial average profile. (b) The regression of D' on η. $D' \propto 1.5372\eta$. The correlation (r^2) is 97%.

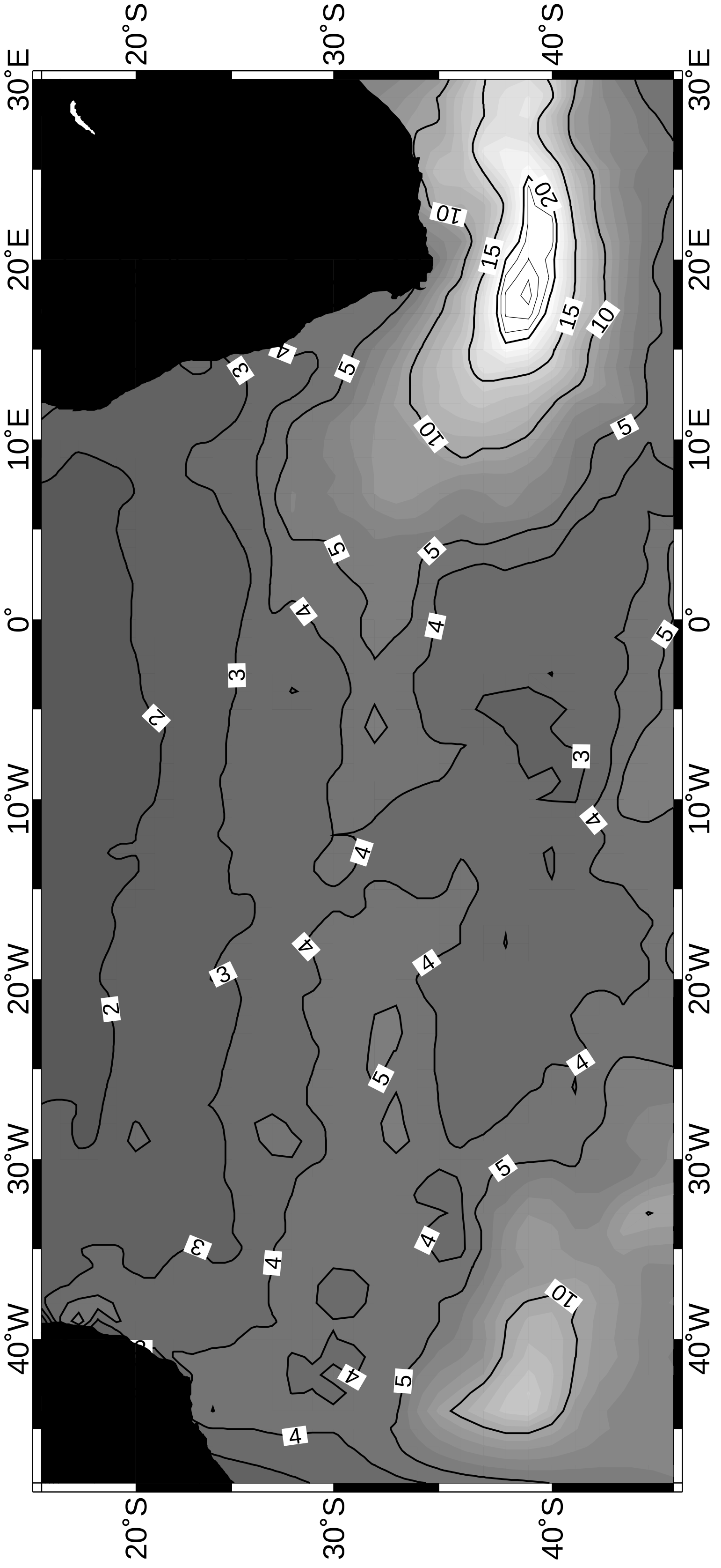

SSH Variability of the South Atlantic

Figure 2-1.

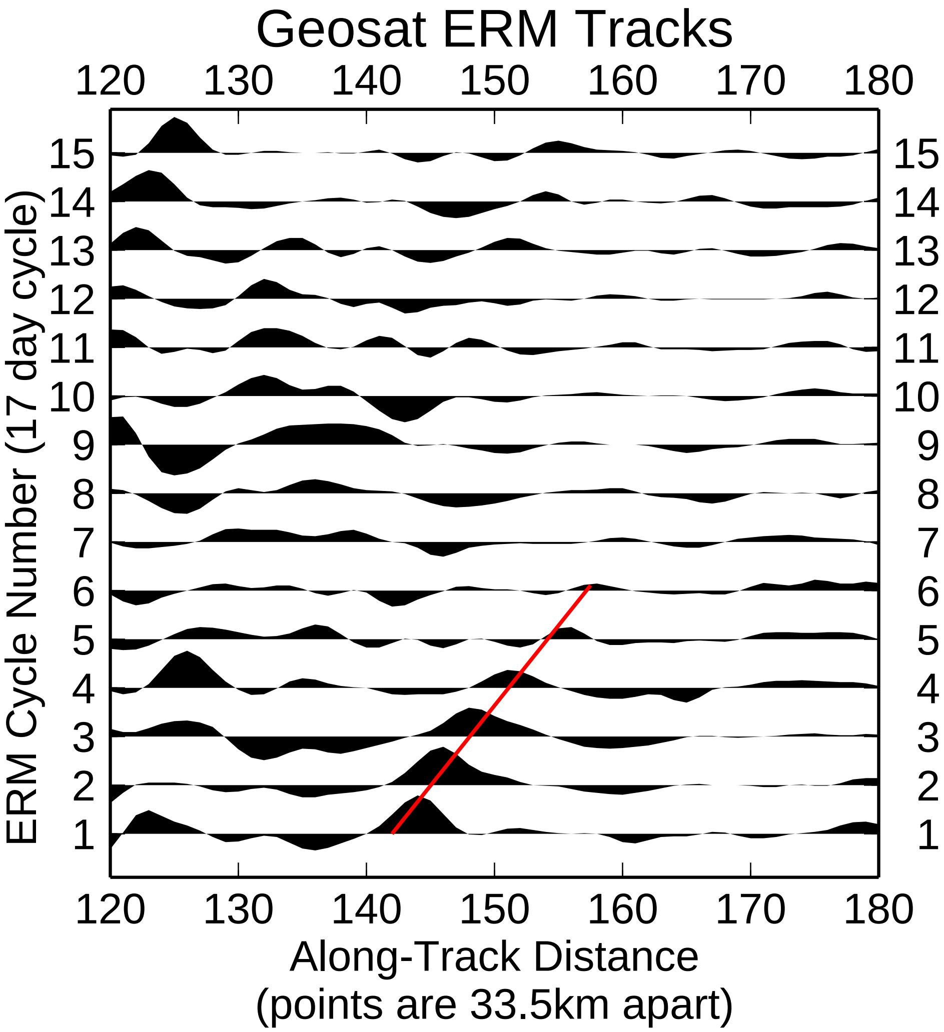
Geosat ERM Tracks
120
130
140
150
160
170
180
ERM Cycle Number (17 day cycle)
1
2
3
4
5
6
7
8
9
10
11
12
13
14
15
Along-Track Distance
(points are 33.5km apart)

Figure 2-2.

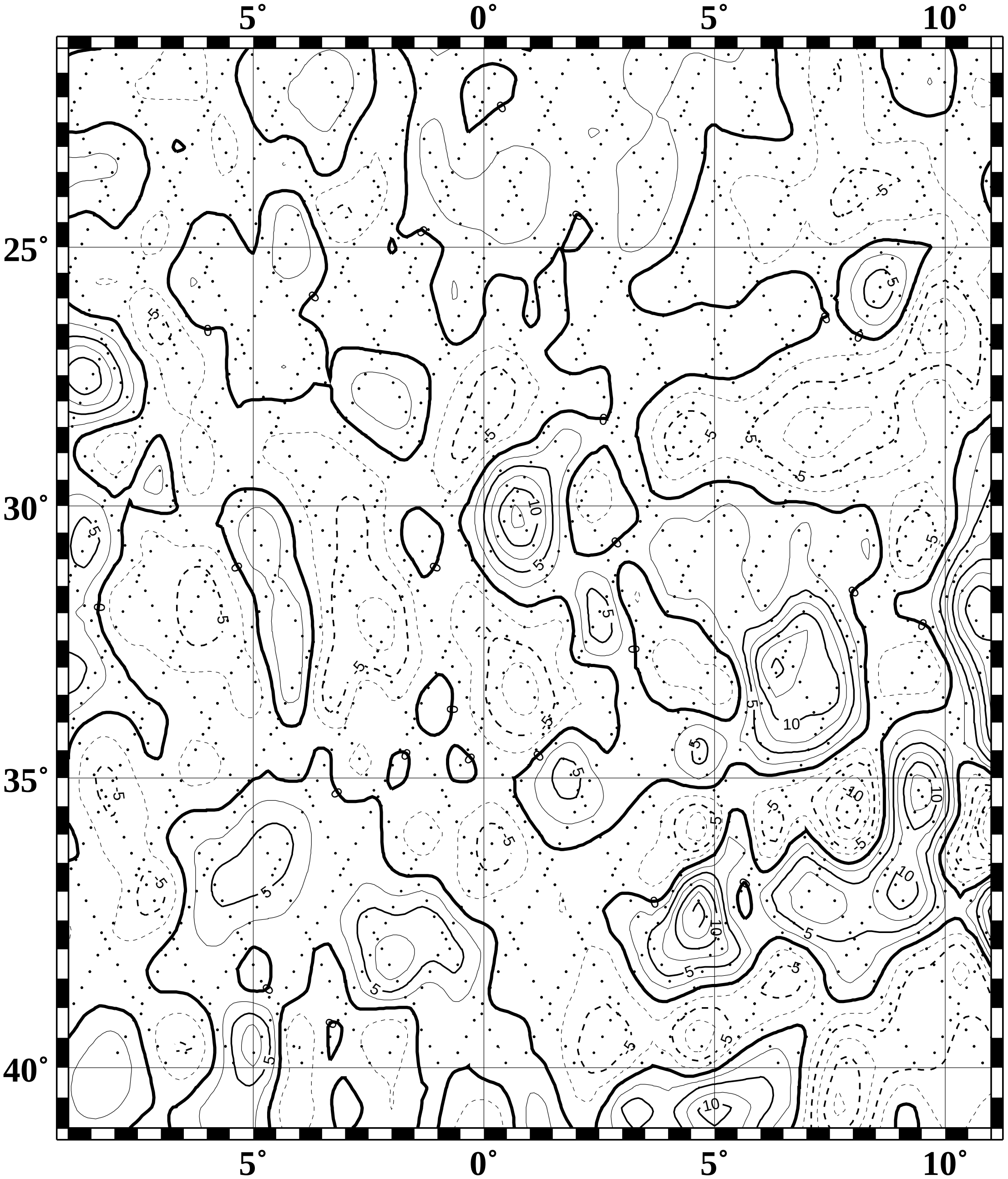

Figure 2-3.

Dispersion of Agulhas Eddies Across the South Atlantic

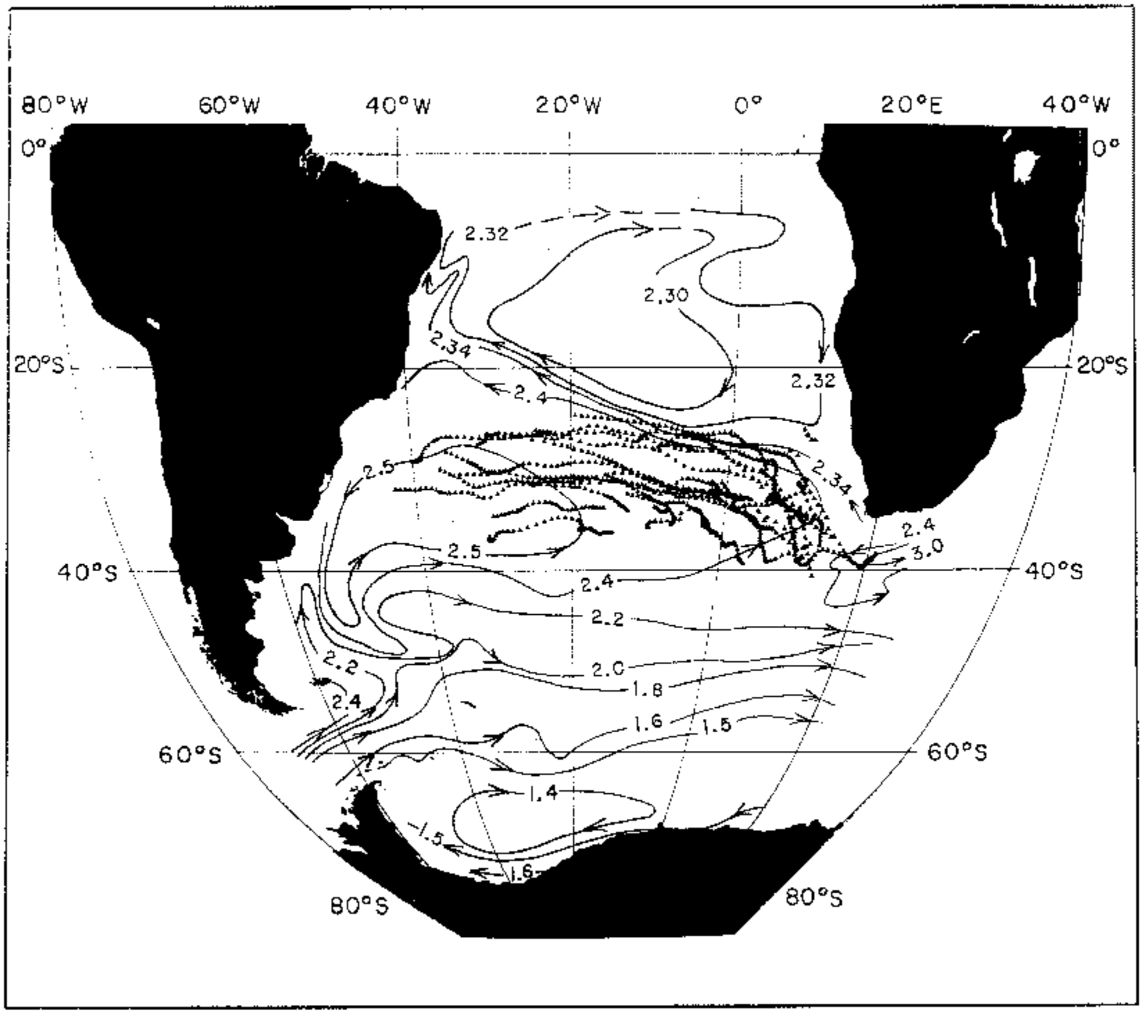

Figure 2-4.

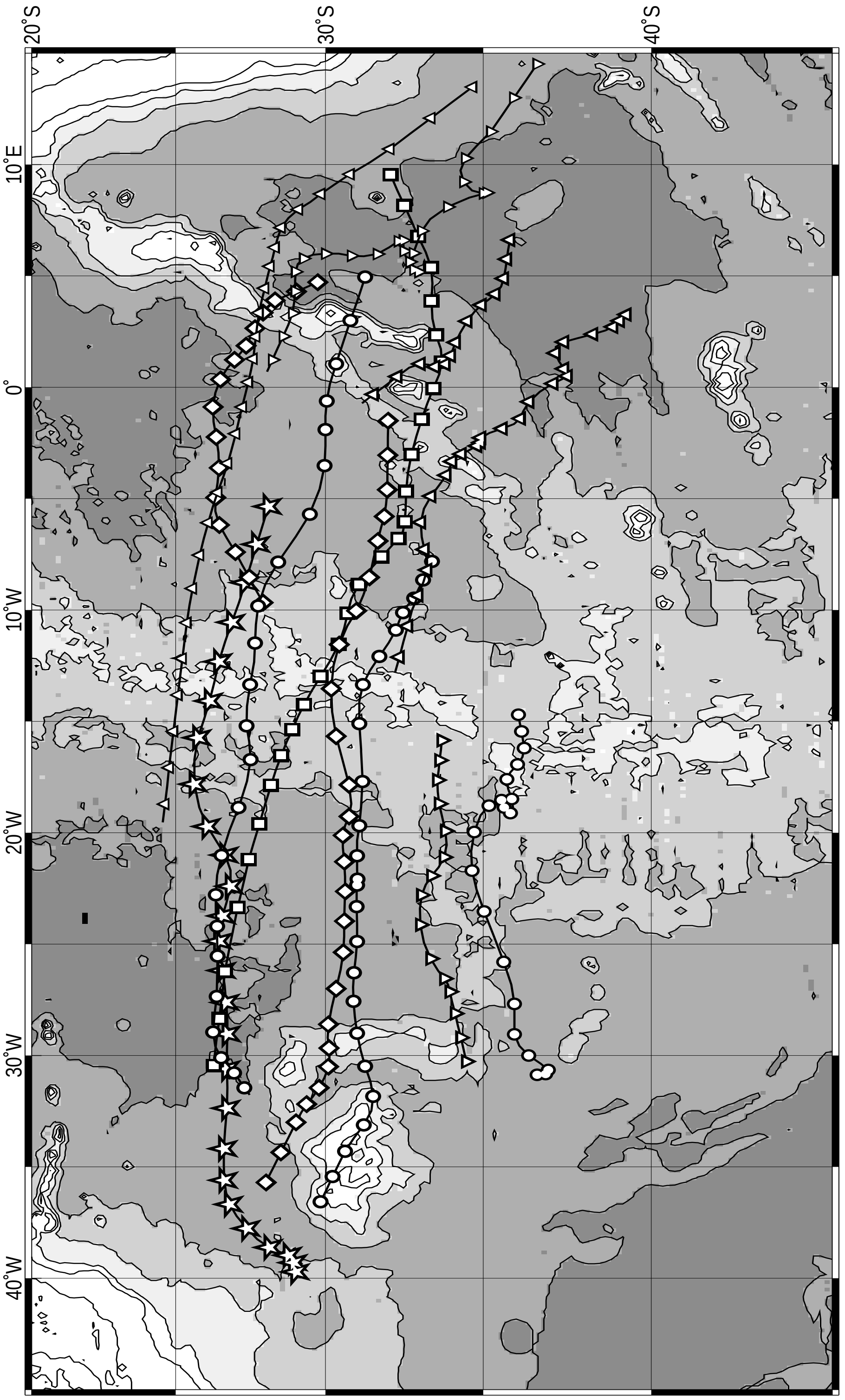

Figure 2-5.

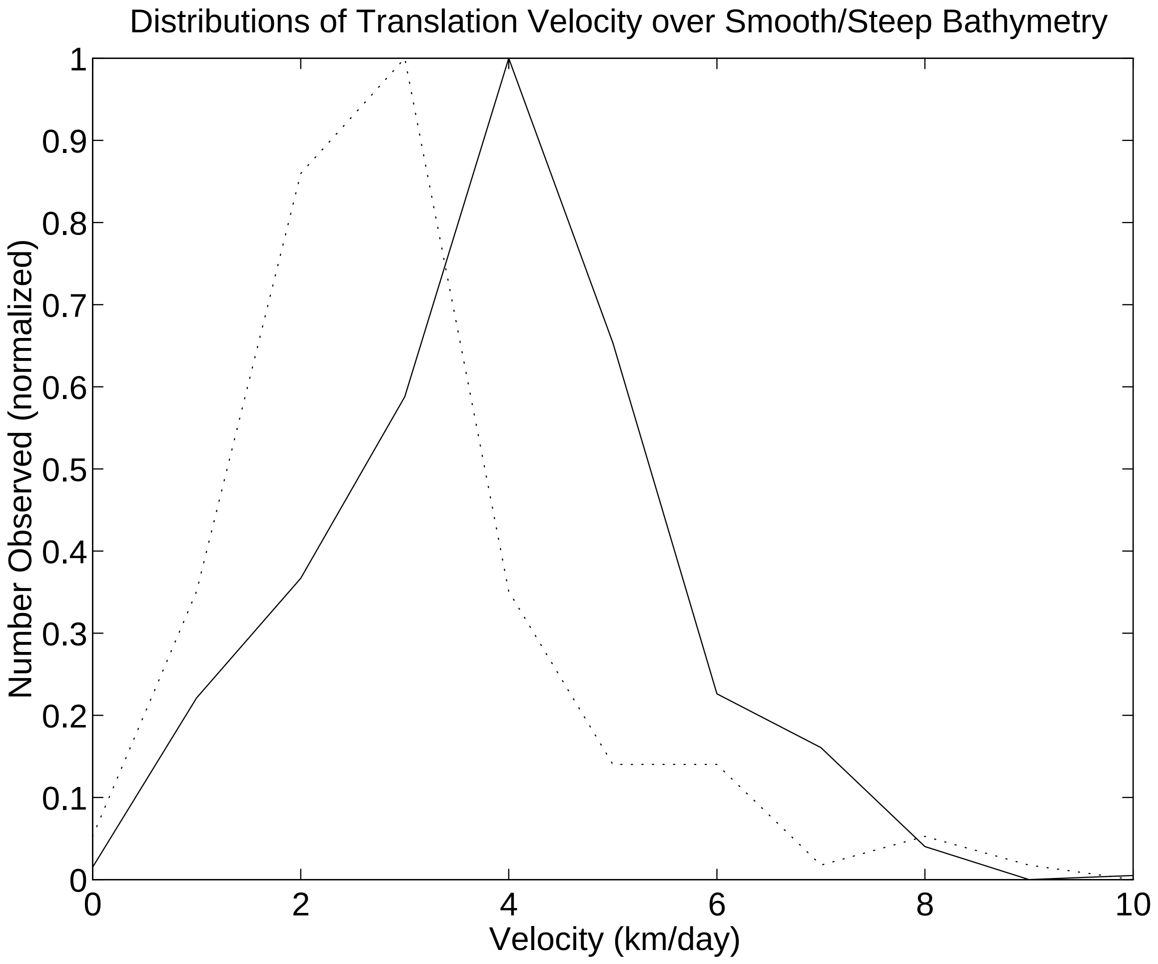
Distributions of Translation Velocity over Smooth/Steep Bathymetry
Number Observed (normalized)
Velocity (km/day)
0
0.1
0.2
0.3
0.4
0.5
0.6
0.7
0.8
0.9
1
0
2
4
6
8
10

Figure 2-6.

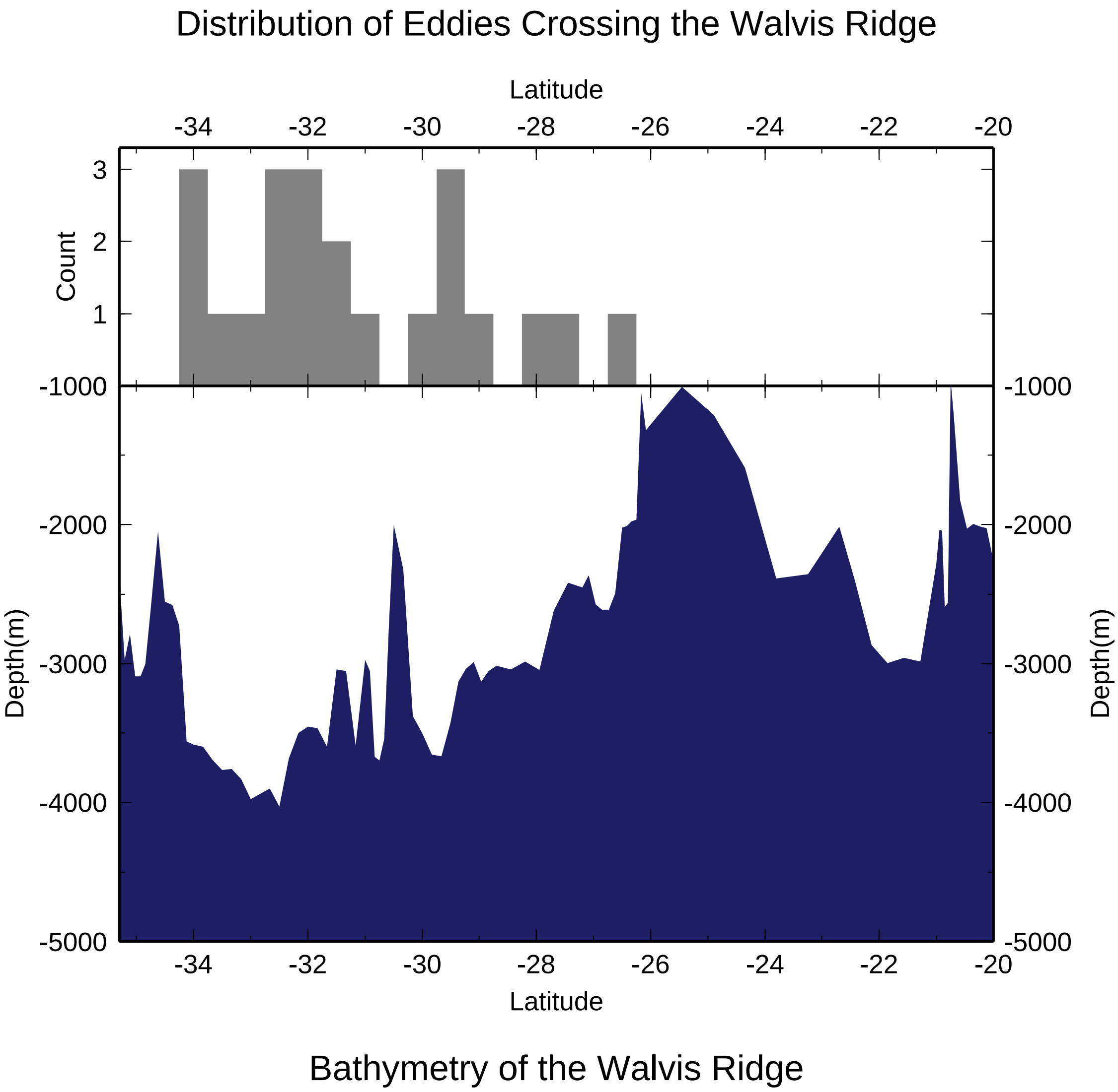
Distribution of Eddies Crossing the Walvis Ridge
Latitude
-34
-32
-30
-28
-26
-24
-22
-20
Count
3
2
1
-1000
-2000
-3000
-4000
-5000
Depth(m)
Latitude
Bathymetry of the Walvis Ridge

Figure 2-7.

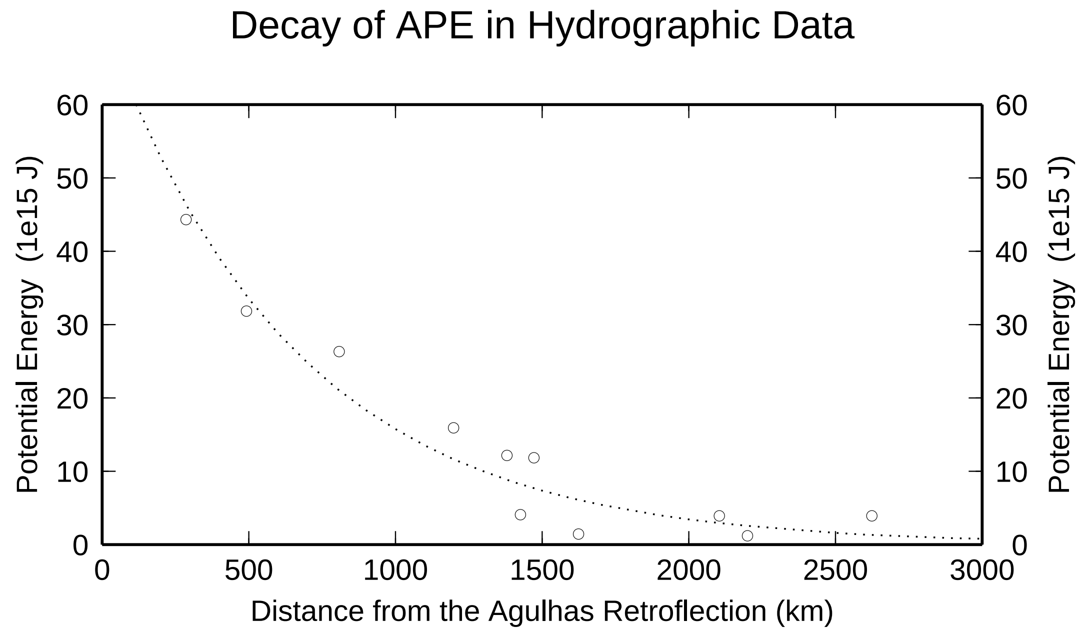
Decay of APE in Hydrographic Data

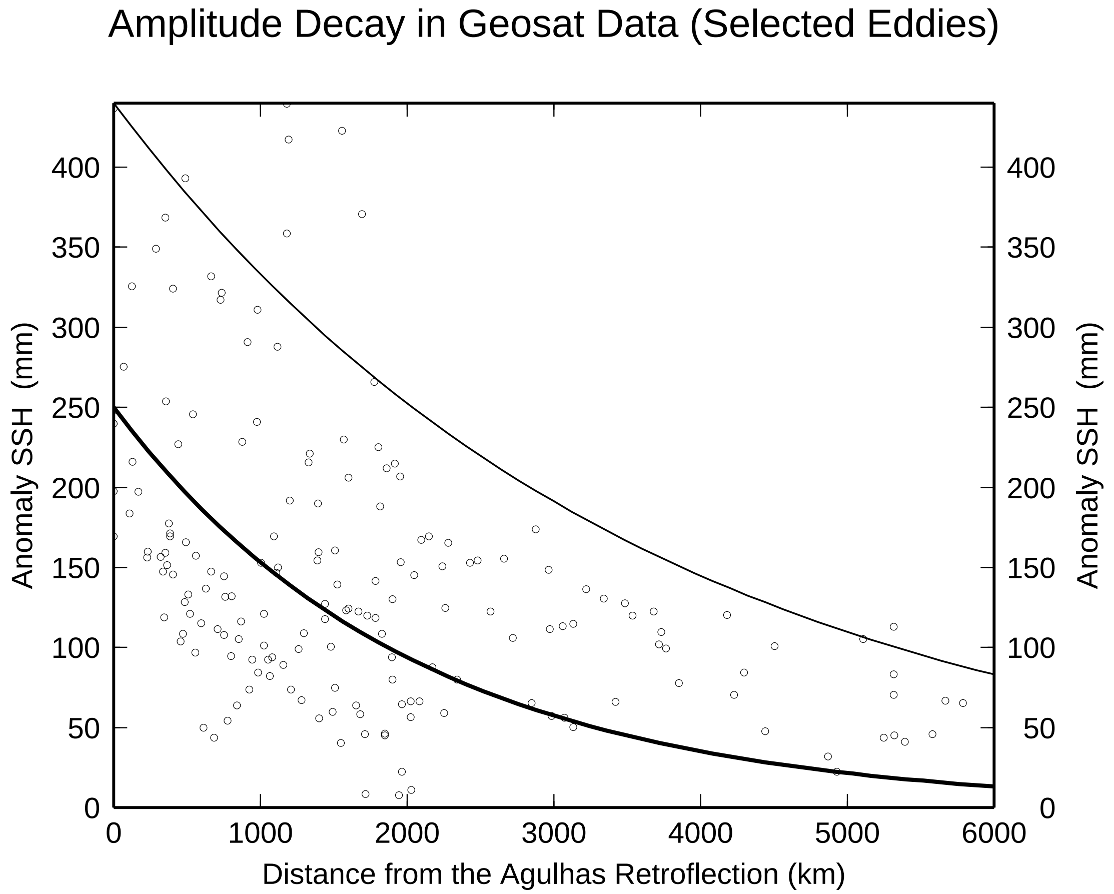
Amplitude Decay in Geosat Data (Selected Eddies)

Figure 2-8.

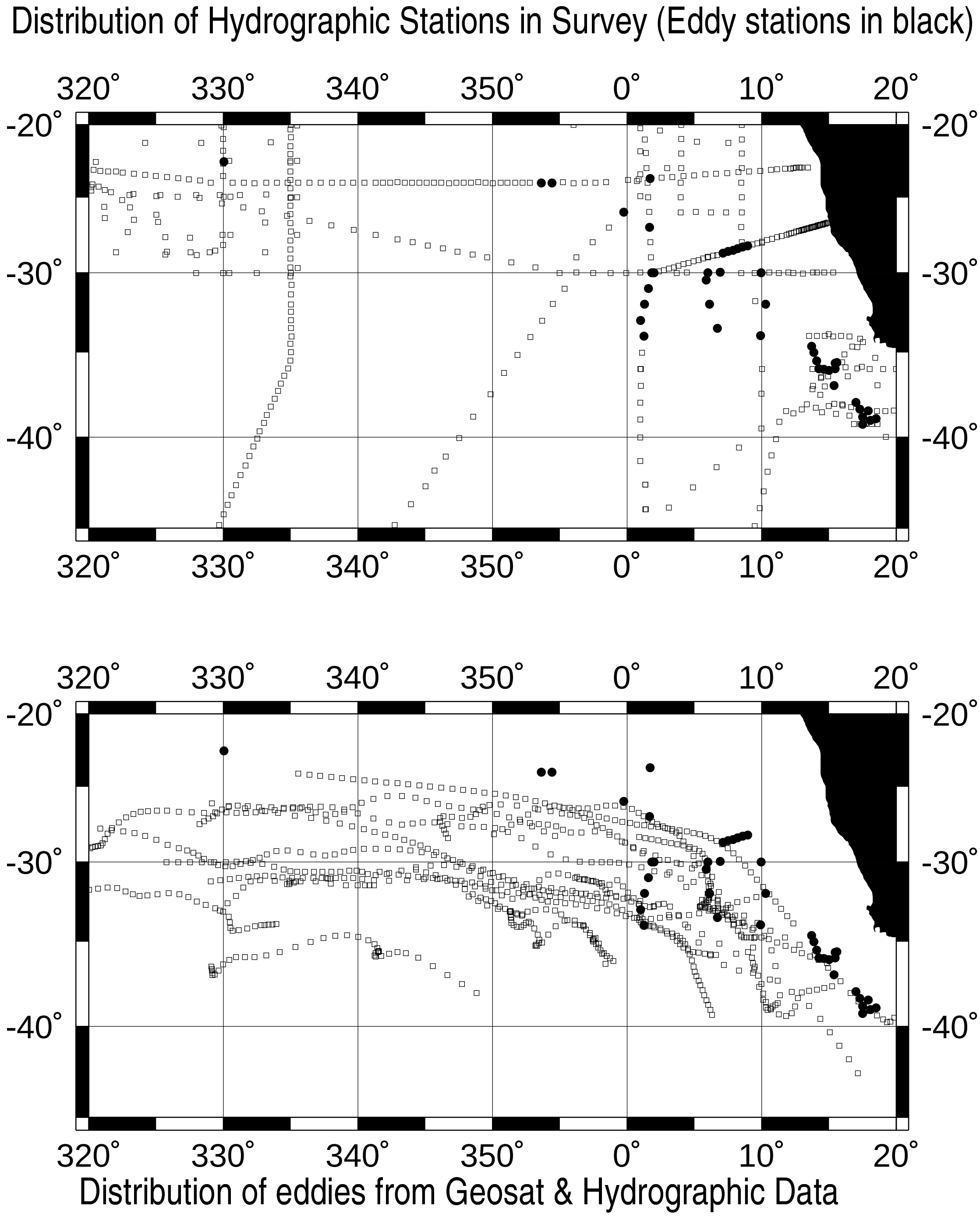

Distribution of Hydrographic Stations in Survey (Eddy stations in black)

Distribution of eddies from Geosat & Hydrographic Data

Figure 2-9.

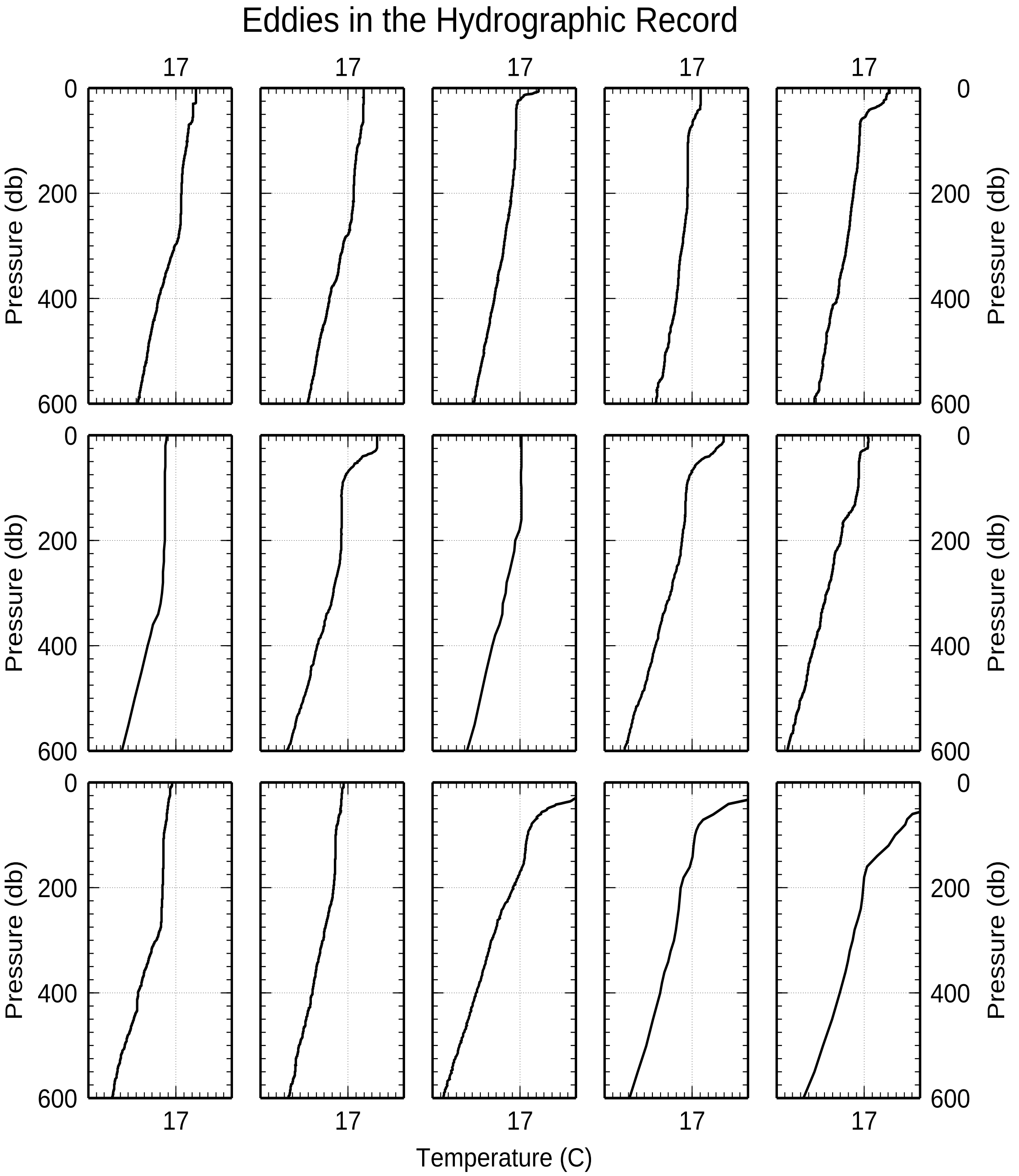
Eddies in the Hydrographic Record
17
17
17
17
17
0
200
400
600
0
200
400
600
0
200
400
600
Pressure (db)
Pressure (db)
Pressure (db)
Pressure (db)
Pressure (db)
Pressure (db)
17
17
17
17
17
Temperature (C)

Figure 2-10.

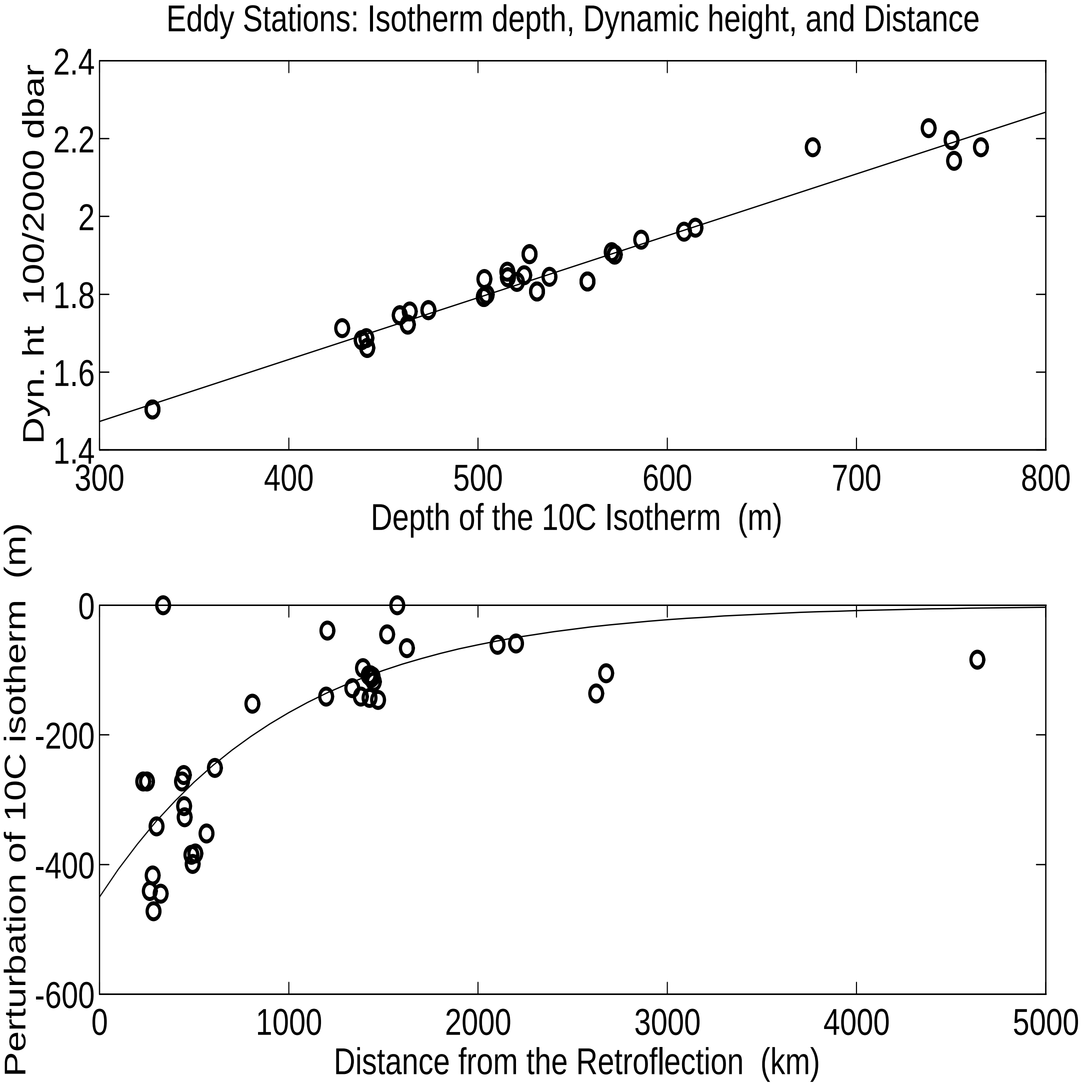
Eddy Stations: Isotherm depth, Dynamic height, and Distance
Dyn. ht 100/2000 dbar
2.4
2.2
2
1.8
1.6
1.4
300
400
500
600
700
800
Depth of the 10C Isotherm (m)
Perturbation of 10C isotherm (m)
0
-200
-400
-600
0
1000
2000
3000
4000
5000
Distance from the Retroflection (km)

Figure 2-11.

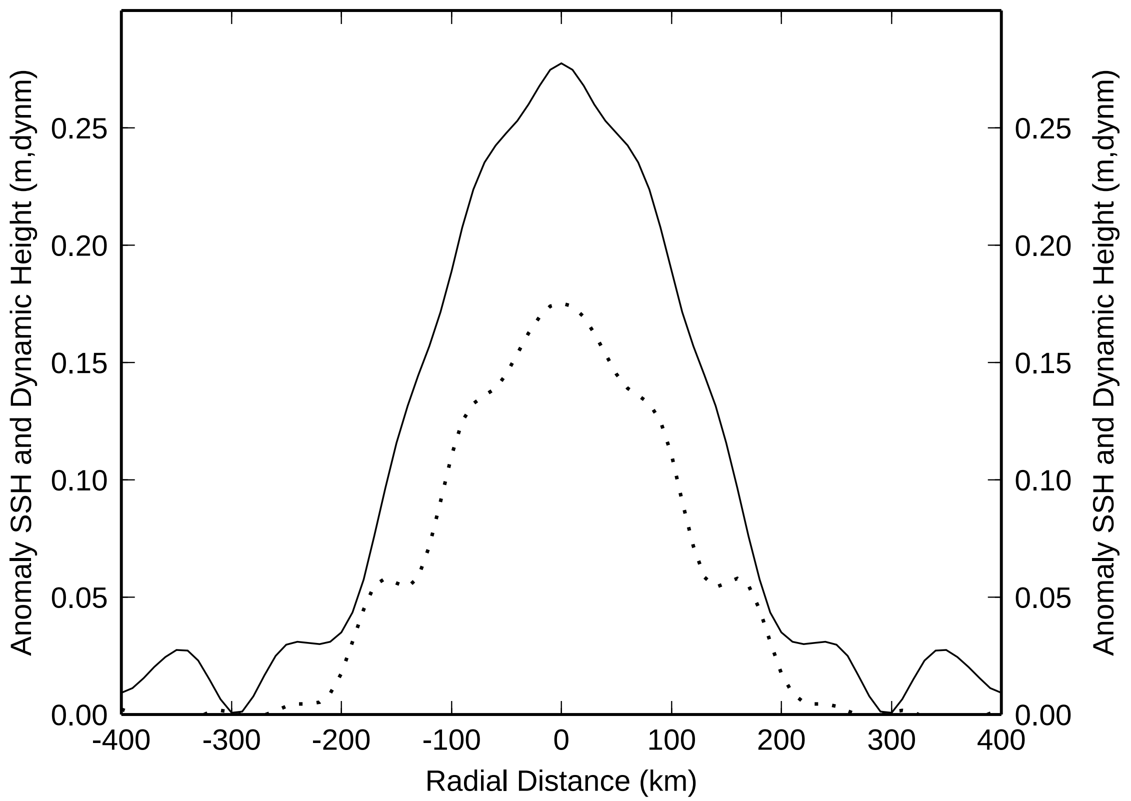

Eddy A Anomaly SSH and Anomaly Dynamic Height

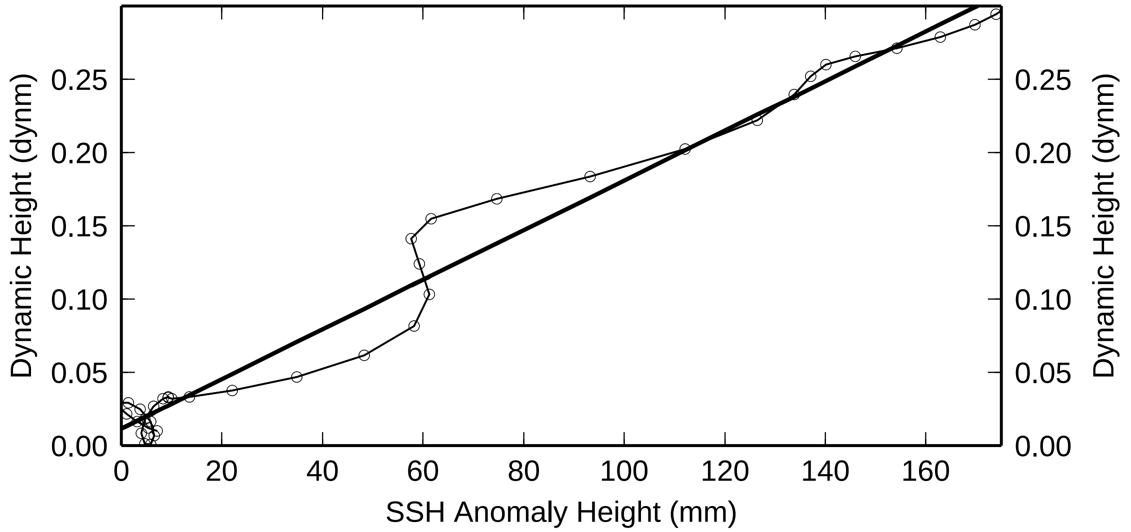

Linear Regression of Dynamic Height on SSH

Figure 2-12.

Chapter 3

A Comparison between global tidal model CSR 3.0 and *in situ* bottom pressure in the southeastern South Atlantic

Abstract

Bottom pressure records from the Cape Basin in the southeastern South Atlantic are compared with TOPEX/POSEIDON tide model CSR 3.0 to assess the regional accuracy of the model. Tides in the Cape Basin have a peak-to-trough amplitude in the raw records of ~2 dbar (approximately 2 m) even in deep areas, with about half the energy at the M2 frequency. The tidal components of significance in the study region are, in order of importance, M2, S2, N2, K2, and K1. The CSR 3.0 tide explains 98.5%-99.4% of the variance in the *in situ* tidal records, compared with a global estimate of 97.9%.

3.1 Introduction

Four inverted echo sounder (IES) moorings equipped with bottom pressure (BP) sensors were deployed in mid-1992 as part of the Benguela Sources and Transports (BEST) program. These sensors recorded pressure at one hour intervals for over a year [Garzoli et al., 1994], providing a measure of the meso-scale barotropic variability in the region. The BP records are additionally interesting because they contain a high-resolution *in situ* record of the barotropic component of ocean tides in the area. The energetic spectrum of sea surface height (SSH) variability in the southeastern South Atlantic is dominated by the barotropic ocean tides, which have a peak-to-trough amplitude of ~2 m. This region is often the subject of altimetry-based studies using meso-scale and regional SSH variability, (e.g., van Ballegooyen et al. [1994], Byrne et al. [1995], Gründlingh [1995], Goni et al. [1997], Witter and Gordon [1999]) the amplitude of which is two to ten times smaller than the tidal signal. Thus an accurate correction of the tidal component of SSH is critical to the viability of such work. Yet few direct comparisons of an altimetric tide model and *in situ* data (for example see Shum et al. [1997] and Desai et al. [1997]) have included the southeastern South Atlantic, and to the author's knowledge, none that have, (e.g., Anderson et al. [1996]), have had a temporal resolution comparable to the BEST mooring data. In this chapter, the tidal record from each of BEST project BP sensors is analyzed and compared to the output of (University of Texas) CSR 3.0 tide model [Eanes and Bettadpur, 1996] at the mooring locations.

3.2 Bottom Pressure

Four of the BEST moorings were equipped with BP sensors. The moorings, deployed in the Cape Basin of the southeastern South Atlantic along 30°S (Fig. 3-1), were in place for approximately 18 months [Garzoli et al., 1994]. Two mooring records (SN61 and SN62) contained small data gaps; the gappy parts of the sequences were not used in this analysis. A problem with SN62 late in its deployment leads us to discard the data collected after June 27, 1993. Bottom pressure variability is converted to SSH using information from conductivity-temperature-depth (CTD) stations taken at and near the mooring locations and the hydrostatic equation. Relative sensor accuracy is estimated at 0.02 dbar [Garzoli et al., 1996]. The relative and not absolute accuracy is of importance since the tidal signal is contained in change in pressure with time ($\frac{dp}{dt}$). Bottom pressure was referenced to variability in the water column above 1000 dbar, i.e., the mean *in situ* density between 0 dbar - 1000 dbar at the reference hydrographic stations was used in the conversion of pressure to SSH:

$$\mathrm{SSH} = dp/\overline{\rho}g \tag{3.1}$$

The energetic spectrum of unfiltered BP records is dominated by the tidal cycle (Fig. 3-2); tides in the Cape Basin have a peak-to-trough amplitude in the raw records of $\sim$ 2dbar (approximately 2 m, Fig. 3-3), even in deep ($D > 4000$ m) areas, with about half the energy at the M2 frequency. The BEST mooring records indicate that the tidal components of significance in the study region are, in order of importance, M2, S2, N2, K2, and K1 (Fig. 3-4). In addition to having recorded tidal and mesoscale activity, the BP sensors were apparently prey to a small amplitude, long-term drift [Garzoli et al., 1996] which we model and remove with a sixth-degree polynomial (Fig. 3-5). Because of the polynomial drift correction applied above, calculation of the mooring tides is limited to the diurnal and semi-diurnal frequencies.

3.3 The CSR 3.0 Tide Model

The (University of Texas) CSR 3.0 tide model [Eanes and Bettadpur, 1996] is used in the comparison. This model performed the best over all in a recent comparison of ocean tide models, with the lowest (globally computed) residual SSH variance compared with TOPEX/POSEIDON (T/P) data, the lowest crossover residual SSH, and the best fit to a set of 102 globally distributed tide and pressure gauges, explaining 97.9% of the observed tidal variance [Shum et al., 1997]. The CSR 3.0 ocean tide model includes 30 tidal components 11 semi-diurnal, 11 diurnal, and 8 long-period (Table 3-1a,b). The CSR 3.0 tide is generated at the BP mooring locations and measurement times for comparison the tidal records computed from the mooring data.

3.4 Discussion

The CSR 3.0 tide accounts for 98.5%-99.4% of the tidal variance in the BP records (Table 3-2), which compares very favorably with the global figure of 97.9% derived from the 102 gauges mentioned above. The least squares tidal solution, calculated from the BP records for only the diurnal and semi-diurnal tidal frequencies, accounts for 98.7%-99.6% of the variance. The additional unexplained variance left when using CSR 3.0 as a tidal correction adds O(5) mm rms to the residual (non-tidal) component of SSH.

Instantaneous differences between tides computed from the mooring records and the CSR 3.0 tide average between 1.0 cm and 1.75 cm, reaching a maximum of 6.5 cm at the four moorings considered. The tidal solution computed from the mooring data contains no correction for atmospheric tides, which is anticipated to contribute an O(1) cm error in the S2 component [Shum et al., 1997]. Obviously the long-period tidal components included in CSR 3.0 will not enhance its agreement with the mooring records, which have had much of the longwave signal removed in the drift correction above; the spatial smoothing inherent in the CSR 3.0 solution, however, probably accounts for the bulk of the disagreement between it and the tide record from the mooring data. The de-tided records seem reasonably similar (Fig. 3-6a,c,e,g) but should be noted that the difference often reaches 4 cm - 5 cm (Fig. 3-6b,d,f,h).

The results of this analysis show that strong O(20) cm SSH events such as the passage of meso-scale eddies can be unambiguously identified directly from the corrected T/P altimetric record. For SSH events which have lower amplitudes, for example regional variability, averaging of SSH estimates will be necessary to improve the signal-to-noise ratio.

Acknowledgments. The author is indebted to Richard Eanes for his help in discovering the problem with bottom pressure gauge SN62 and in locating the discontinuities in gauges SN61 and SN62.

3.5 Tables

Table 3-1(a): Tidal Components included in CSR 3.0

Name	Frq. (cycle/d)	Period
Diurnal		
2Q1	0.856952384	-6.904
Q1	0.893244048	-9.213
O1	0.929535695	-13.841
M1	0.966446233	-28.297
P1	0.997262079	-221.060
S1	1.000000000	-559.897
K1	1.002737898	1050.246
PHI1	1.008213699	155.580
J1	1.039029527	26.850
OO1	1.075940083	13.485
NU1	1.112231730	9.054
Semi-diurnal		
227	1.828255527	-5.704
2N2	1.859690264	-6.950
MU2	1.864547173	-7.193
N2	1.895981946	-9.295
NU2	1.900838820	-9.734
M2	1.932273593	-14.026
L2	1.968565204	-28.566
T2	1.997262163	-158.475
S2	2.000000000	-279.994
K2	2.005475795	525.123
285	2.041767407	26.181

Table 3-1(b): Tidal Components included in CSR 3.0

Name	Frq. (cycle/d)	Period
Long Period		
LP	0.000147094	6798.382
Sa	0.002737779	365.260
Ssa	0.005475819	182.621
TERa	0.008213597	121.749
Mm	0.036291647	27.555
Mf	0.073202203	13.661
TERm	0.109493850	9.133
93a	0.140928587	7.096

Table 3-2: Comparison of CSR 3.0 with locally modeled tide

SN	SSH (rms)	SSH-local (rms)	SSH-CSR (rms)	EV (local)	EV (CSR)	Max. Diff.
50	41.0	2.7	3.3	99.57	99.13	6.5
58	40.8	4.6	4.9	98.74	98.54	6.0
61	37.5	2.6	2.8	99.53	99.43	4.1
62	41.2	3.1	3.7	99.44	99.21	6.2

Bibliography

Anderson, O.B., P.L. Woodworth and R.A. Flather, Intercomparison of recent ocean tide models. *J. Geophys. Res., 100*, 25,261-25,282, 1996.

van Ballegooyen, R.C., M.L. Gründlingh and J.R.E. Lutjeharms, Eddy fluxes of heat and salt from the southwest Indian Ocean into the southeast Atlantic Ocean: a case study, *J. Geophys. Res., 99*, 14,053-14,070, 1994.

Byrne, D.A., A.L Gordon and W.F. Haxby. Agulhas eddies: A Synoptic view using Geosat ERM Data, *J. Phys. Oc, 25*, 902-917, 1995.

Desai, D.S., J.M. Wahr and Y. Chao, Accuracy assessment of recent tide models. *J. Geophys. Res., 102*, 25,173-25,194, 1997.

Eanes, R. and S. Bettadpur, The CSR 3.0 global ocean tide model: Diurnal and semi-diurnal ocean tides from TOPEX/POSEIDON altimetry, *CSR-TM*, *96-05*, Univ. of Tex. Cent. for Space Res., Austin, Texas, 1996.

Garzoli, S.L., A.L. Gordon, V. Kamenkovich, D. Pillsbury and C.M. Duncombe Rae, Variability and sources in the southeastern Atlantic circulation. *J. Mar. Res., 54*, 1039-1071, 1996.

Garzoli, S., M. Maccio, A. Martino and M. Colwell, BEST IES Data Report: 1992-1994. *LDEO-94-1*, Lamont-Doherty Earth Obs., Columbia Univ., Palisades, New York, 1994.

Goni, G.J. S.L. Garzoli, A.J. Roubicek, D.B. Olson and O.B. Brown, Agulhas ring dynamics from TOPEX/POSEIDON altimeter data, *J. Mar. Res., 55*, 861-883, 1997.

Gründlingh, M. L., Tracking eddies in the southeast Atlantic and southwest Indian oceans with TOPEX/POSEIDON, *J. Geophys. Res., 100*, 24,977-24,986, 1995.

Shum, C.K., P.L. Woodworth, O.B. Anderson, G.D. Egbert, O. Francis, C. King, S.M. Klosko, C. Le Provost, X. Li, J.-M. Molines, M.E. Parke, R.D. Ray, M.G. Schlax, D. Stammer, C.C. Tierney, P. Vincent and C.I. Wunsch, Accuracy assessment of recent ocean tide models, *J. Geophys. Res., 102*, 25,173-25,194, 1997.

Witter, D.L and A.L. Gordon. Interannual variability of South Atlantic circulation from four years of TOPEX/POSEIDON satellite altimeter observations. *J. Geophys. Res., 104*, 20,927-20,948, 1999.

Figure 3-1. Positions of the hydrographic stations occupied and moorings deployed during the BEST program in the southeastern South Atlantic ocean. Only those moorings which yielded data are figured. The moorings along 30°S were equipped with BP sensors. The groundtrack of the TOPEX/POSEIDON satellite has been overlaid in a thin dotted line.

Figure 3-2. Power spectral density of bottom pressure from BEST moorings. The semi-diurnal tides dominate the energetic spectrum.

Figure 3-3. Unfiltered bottom pressure records from the four PIES moorings recovered during the BEST program. The tidal signal has a peak-to-trough amplitude of $\sim$2 m in this area.

Figure 3-4. Amplitude and phase of barotropic tides at the BP sensors. The M2 tide contains most of the energy.

Figure 3-5. Lowpass filtered BP records, showing the 6th degree polynomial correction used to correct for low amplitude, long-term drift in the records, as suggested by Garzoli et al., [1996].

Figure 3-6. a,c,e,g (left hand side, top to bottom): BP records corrected for tides using CSR 3.0 (in black) compared with the same records corrected by a least squares fit at tidal frequencies (in gray). b,d,f,h (right hand side, top to bottom): The difference between CSR 3.0 and the least squares solution to the tides.

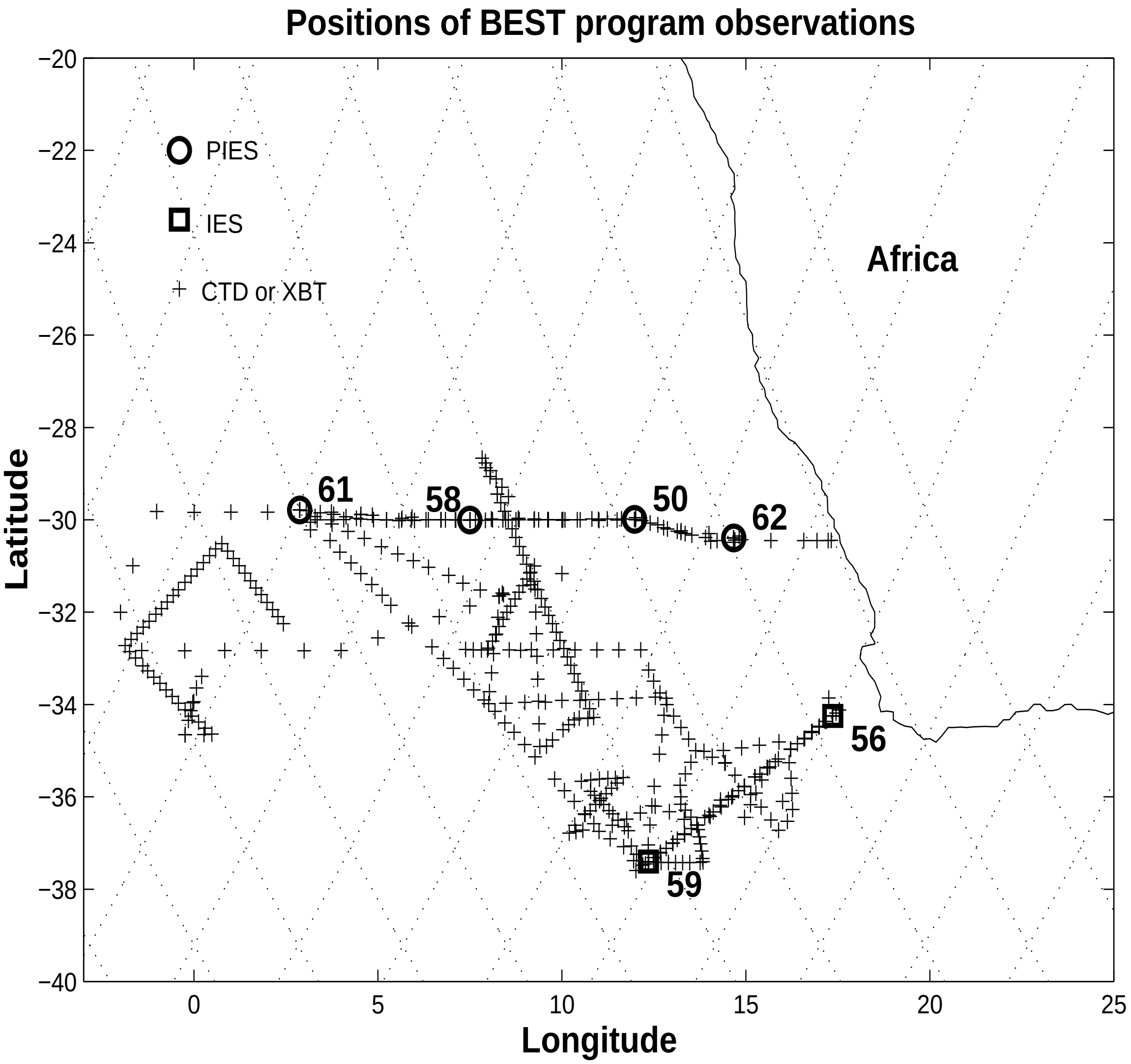
Positions of BEST program observations
PIES
IES
CTD or XBT
Africa
61
58
50
62
56
59
Latitude
Longitude
−20
−22
−24
−26
−28
−30
−32
−34
−36
−38
−40
0
5
10
15
20
25

Figure 3-1.

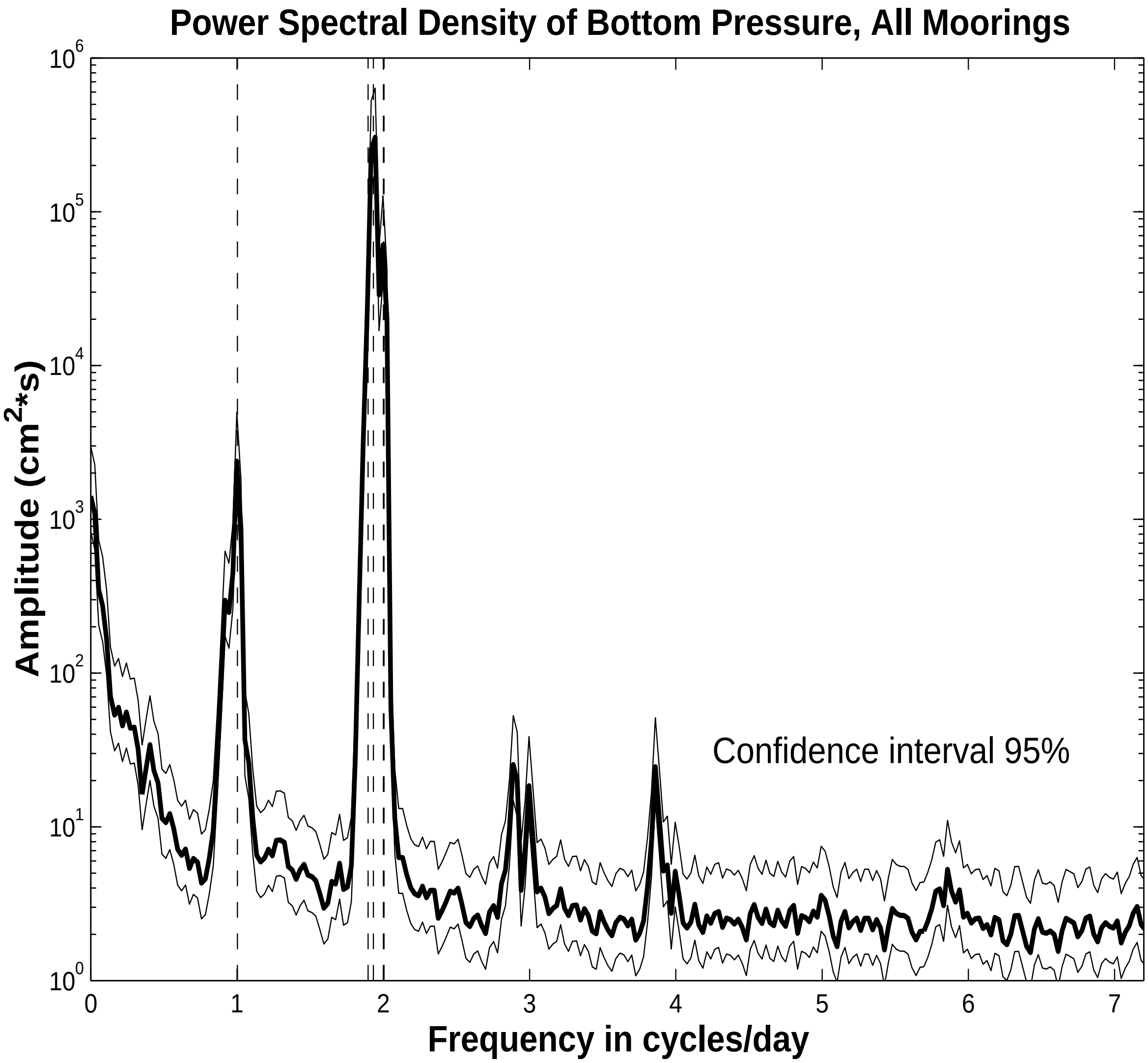
Power Spectral Density of Bottom Pressure, All Moorings
Amplitude (cm^2*s)
10^0
10^1
10^2
10^3
10^4
10^5
10^6
Confidence interval 95%
0
1
2
3
4
5
6
7
Frequency in cycles/day

Figure 3-2.

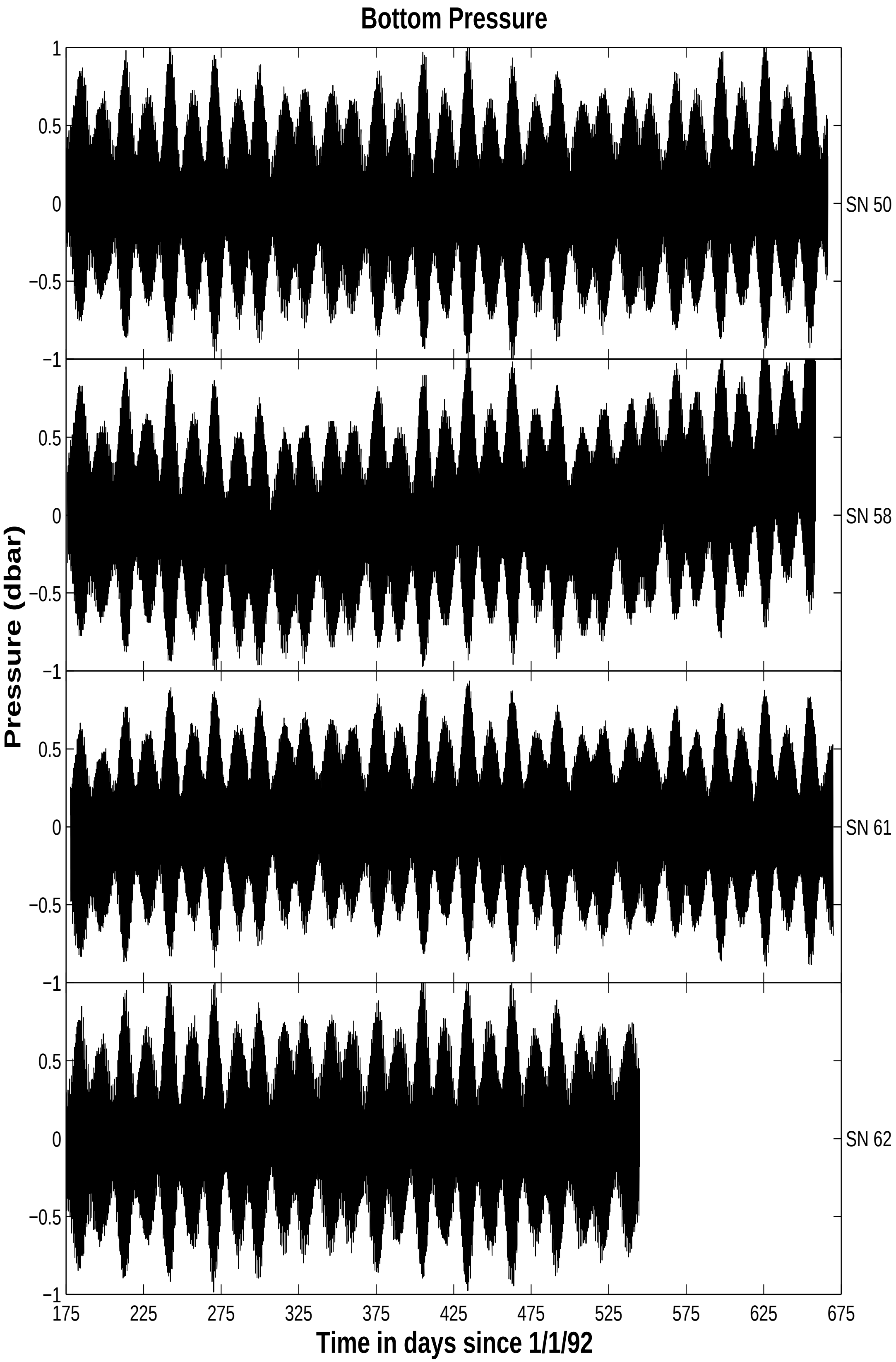
Bottom Pressure
Pressure (dbar)
1
0.5
0
−0.5
−1
SN 50
SN 58
SN 61
SN 62
175
225
275
325
375
425
475
525
575
625
675
Time in days since 1/1/92

Figure 3-3.

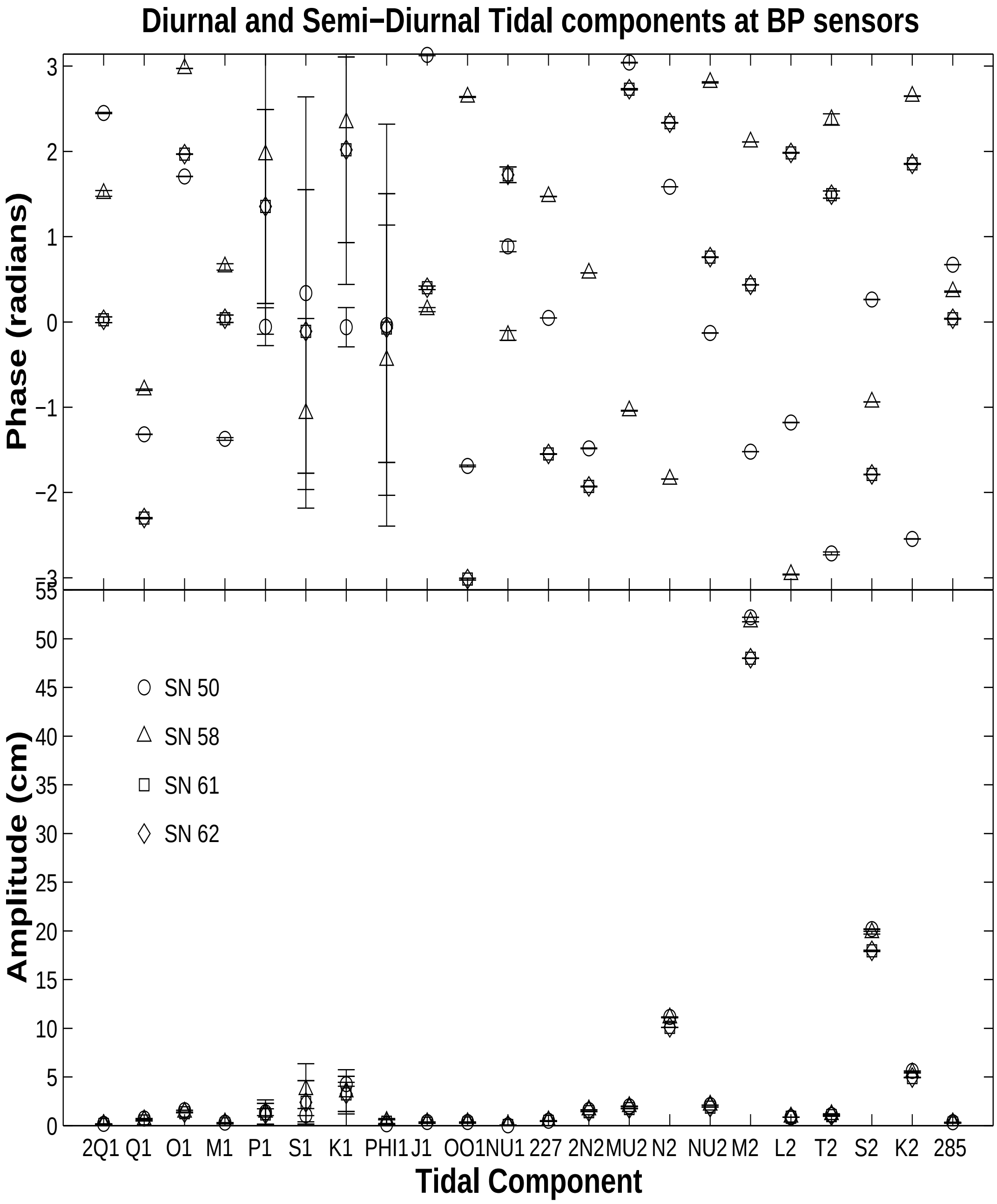
Diurnal and Semi−Diurnal Tidal components at BP sensors
Phase (radians)
3
2
1
0
−1
−2
−3
Amplitude (cm)
55
50
45
40
35
30
25
20
15
10
5
0
SN 50
SN 58
SN 61
SN 62
2Q1
Q1
O1
M1
P1
S1
K1
PHI1
J1
OO1
NU1
227
2N2
MU2
N2
NU2
M2
L2
T2
S2
K2
285
Tidal Component

Figure 3-4.

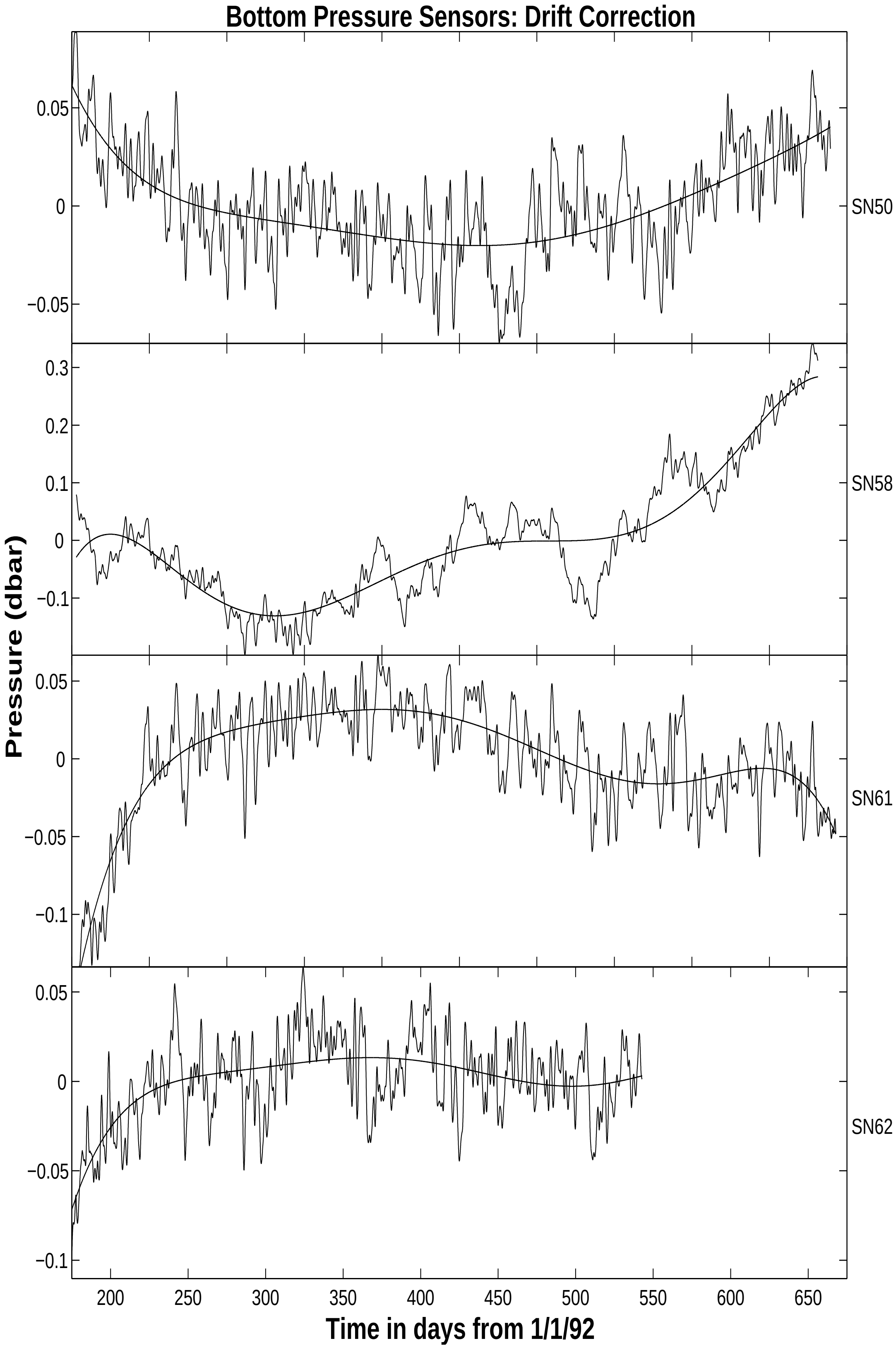
Bottom Pressure Sensors: Drift Correction
Pressure (dbar)
0.05
0
−0.05
SN50
0.3
0.2
0.1
0
−0.1
SN58
0.05
0
−0.05
−0.1
SN61
0.05
0
−0.05
−0.1
SN62
200
250
300
350
400
450
500
550
600
650
Time in days from 1/1/92

Figure 3-5.

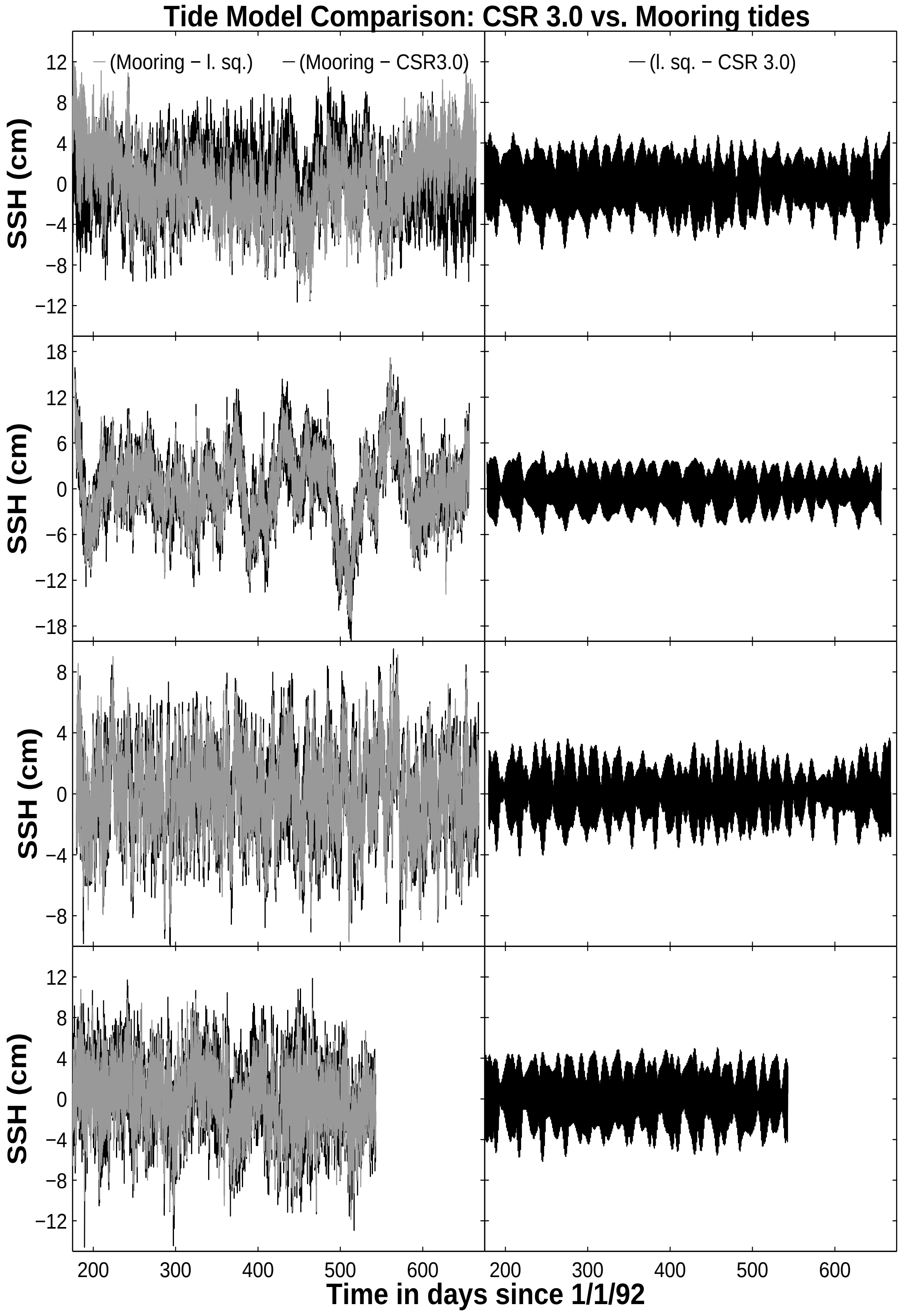
Tide Model Comparison: CSR 3.0 vs. Mooring tides
(Mooring − l. sq.)
(Mooring − CSR3.0)
(l. sq. − CSR 3.0)
SSH (cm)
12
8
4
0
−4
−8
−12
18
6
−6
−18
200
300
400
500
600
Time in days since 1/1/92

Figure 3-6.

Chapter 4

Eddies in the South Atlantic: Remote Monitoring of Inter-ocean Thermohaline Transport

Abstract

Enhanced Thermohaline Transport Analysis (ETTA) allows mass and thermohaline fluxes to be measured from time-series of anomaly sea surface height (SSH) and anomaly acoustic travel time ($\delta\tau$). In this technique, developed here, groups of water masses commonly observed in the same water column are parameterized as water column types, which are used to determine empirical mass, heat and salt transport coefficients. Water column type, in turn, is parameterized as a function of SSH and $\delta\tau$, both of which can be calculated from hydrography. Mass and thermohaline fluxes are then able to be estimated from paired time-series of $\delta\tau$ and SSH such as those that can be obtained from inverted echo sounder (IES) moorings and satellite altimetry, respectively. Interpreted using ETTA, $\delta\tau$ and SSH function as proxies for the vertically averaged temperature, salinity and density of the water column.

In a preliminary trial of the ETTA method three water column types are identified which dominate the hydrography of the southeastern South Atlantic, each with a very different thermohaline signature: "Agulhas water", warm water of the type found at the center of Agulhas eddies; "13 °C stad" water, Subantarctic water from the Indian Ocean with a deep isothermal layer near 13 °C, and "modified Atlantic" water, water from the South Atlantic subtropical gyre that has mixed to some extent with Agulhas water. Bulk (vertically averaged) heat, salt, and transport coefficients are calculated from the hydrography for each of the three water column types and the each type is parameterized as an empirical function of $\delta\tau$ and SSH.

Records from three Pressure/Inverted Echo Sounder (PIES) and two IES moorings deployed in 1992-1993 in the southeastern South Atlantic as part of the BEST (Benguela Sources and Transports) program supply time-series of $\delta\tau$. Combined with concurrent measurements of SSH from TOPEX/POSEIDON ($\mathrm{SSH}_{T/P}$) these paired records are used to obtain ETTA estimates of the heat, salt and mass fluxes between mooring pairs as functions of time. The Agulhas Current system is found to add O(14.5×10^{6}) $\mathrm{m^3s^{-1}}$, O($15\mathrm{x}10^{20}$) J (0.048 PW) and O($83\mathrm{x}10^{12}$) kg salt into the South Atlantic annually through the BEST array at 30°S (2°E - 17°E). The majority of that

transport is carried out by modified Atlantic water. At least 18% of the transport at this location is carried by Agulhas eddies.

4.1 Introduction

Previous studies have attempted to measure the strength of the Indian-Atlantic thermohaline exchange and to elucidate the controlling dynamics using a variety of methods: direct measurement (for a summary see Duncombe Rae [1991]), thermal infrared imagery from satellites combined with hydrography (e.g., Lutjeharms and van Balleygooyen [1988] and Lutjeharms and Cooper [1996]), altimetry [Feron et al, 1992], altimetry combined with hydrography [Gordon and Haxby, 1990, van Ballegooyen et al., 1994, Byrne et al., 1995], numerical models (e.g., Ou and de Ruijter [1986], Boudra and Chassignet [1988], Chassignet and Boudra [1988], Kamenkovich et al. [1996], Beismann et al. [1999]), and more recently, by using moored instruments [Garzoli and Gordon, 1996, Garzoli et al., 1996, DuncombeRae et al., 1996]. But until now, almost all efforts to measure inter-ocean fluxes (including the Agulhas) have been confined to hydrographic surveys, which convey water mass identity, or to mooring deployments and other remote sensing methods which can resolve ocean currents or their variable components, but which do not distinguish between water masses or must resort to assumptions about their identities. Success in measuring inter-ocean mass and thermohaline transports depends on the ability to determine at least velocity, temperature and salinity fields simultaneously. Enhanced Thermohaline Transport Analysis (ETTA) approaches this problem by allowing parameters that can be remotely sensed to serve as proxies for the quantities of interest. In ETTA, the baroclinic component of sea surface height (SSH) and acoustic travel time (τ) are used as proxies for the thermohaline properties of the water column. This information is generated from hydrographic data. When these same quantities are then measured remotely from a bottom-moored inverted echo sounder and a satellite altimeter the thermohaline composi tion of the water column lying between them can be determined by reference to the hydrographic parameterization.

To test the ETTA technique, high-quality hydrographic data from a series of three cruises in the southeastern South Atlantic and data from Pressure/Inverted Echo Sounder (IES and PIES) moorings are used; both were collected during 1992 - 1993 as part of the Benguela Sources and Transports (BEST) Project. These are combined with data from the TOPEX/POSEIDON altimeter, which provides a concurrent, independent measurement of sea surface height. These datasets are discussed in Section 4.2. In Section 4.3, water column type parameterizations are defined based on water mass identifications; their expression in acoustic travel time (τ) and the baroclinic component of SSH (η_{BC}), both calculated from the hydrography itself, are discussed. The computations and assumptions involved in obtaining mass and thermohaline fluxes from ETTA parameterizations are presented in Section 4.4. The feasibility of using ETTA to identify water column type in this region with is assessed in Section 4.5 by comparing τ derived from hydrography to sea surface height from the TOPEX/POSEIDON altimeter ($\mathrm{SSH}_{T/P}$). In Section 4.6, time-series of anomaly τ ($\delta\tau$) at moorings are compared with concurrent series of $\mathrm{SSH}_{T/P}$; the parameterization developed in Sections 4.3 and 4.5 is used to determine the water column types present at each mooring as a function of time. Mass and thermohaline fluxes of each water column type are then able to be estimated. The mooring and altimeter records and their uncertainties are discussed in Section 4.7, the measured ETTA fluxes in Section 4.8 and our conclusions presented in Section 4.9.

4.2 Data and Data Processing

Four principle data sets are used in this study: data from moored inverted echo sounders, from bottom pressure sensors (deployed on some of the same moorings), hydrographic data, and altimeter data. Along with the altimeter data a semi-empirical tidal model is used. Each data set and its processing is discussed below.

4.2.1 The BEST project: mooring and hydrographic data

The BEST project was designed to measure the sources and transports of the Benguela Current, the eastern arm of the South Atlantic subtropical gyre. The project included the deployment of six inverted echo sounder (IES) moorings, four of which were equipped with bottom pressure (BP) sensors (PIES). The moorings were deployed for ~18 months during which three hydrographic surveys of the area were conducted (Fig. 3-1). The PIES moorings, of primary interest to us, were located along 30°S. One of the IES sensors (SN50) flooded immediately on deployment; data from this mooring are not used here. Several more IES moorings (without BP sensors) were deployed south of the 30°S line and will be considered briefly.

The BEST hydrographic dataset consists of 133 conductivity-temperature-depth (CTD) casts and 316 expendable bathythermograph (XBT) casts. The hydrographic and mooring data are described by Belinne et al [1996] and Garzoli et al. [1994]. Each processed CTD cast consists of measurements of potential temperature (θ) and salinity (S) with pressure at a resolution of 1 dbar. Each processed XBT cast consists of measurements of temperature (T) with depth (z) at a resolution of 1 m. The first cruise, during which the moorings were deployed, took place before the TOPEX/POSEIDON satellite was launched. The second and third (during which the moorings were retrieved) occurred between repeat cycles 2 and 43 of the satellite.

In Section 4.3, we examine the casts again for their thermohaline (water mass) information; in Section 4.5, we use them to simulate both $\delta\tau$ and η_{BC} to help in the later interpretation of the time-series data. The simulated travel time anomalies are also compared directly with $\mathrm{SSH}_{T/P}$.

4.2.2 Inverted Echo Sounders

An inverted echo sounder (IES) is composed of a low-frequency sound source and a receiver. Deployed on the bottom of the ocean, an IES produces an acoustic signal which is eventually reflected off the air-water interface at the ocean's surface. The receiver, combined with an accurate clock, measures the time (τ) it takes for the signal to be reflected and to return:

$$\tau = 2\int_{-D}^{\eta} \frac{dz}{c(S,T,p)} \tag{4.1}$$

where:

$$dz = \frac{dp}{\rho(S,T,p)g} \tag{4.2}$$

(this is equivalent to He [1993] Equation (4)). Here D is the mean depth of the water column above the sounder; $z = 0$ is the mean sea surface height over the length of the mooring deployment and η is its time-varying component, and ρ, g and p are *in situ* density, gravitational acceleration and pressure, respectively. Over 99% of the value of τ is invariant, essentially a record of the depth at which the IES was deployed (D) and the mean speed of sound in the water above it, c. For each mooring the mean for the deployment period ($\overline{\tau}$) is calculated and removed. The remaining signal, $\delta\tau$, contains information about η and changes in $c(S,T,p)$. η can be further broken down into a baroclinic and a barotropic component:

$$\eta = \eta_{BC} + \eta_{BT} \tag{4.3}$$

With the addition of an assumption of a baroclinic "level of no motion" (LNM), also known as a reference level, $\delta\tau$ becomes a proxy for the variable part of the baroclinic component of η, η_{BC}. We use a LNM of 1000 dbar as suggested by Garzoli and Gordon [1996] in their analysis of these same mooring data.

For the purposes of this study, barotropic variability in sea surface elevation (η_{BT}) is assumed to be that part of η which is related to changes in bottom pressure, that is to say, changes (over time) in the pressure field that would in a frictionless world produce a horizontal velocity field with no shear in the vertical. Baroclinic SSH variability, η_{BC}, refers to the remainder. η_{BC} is here interpreted as the SSH signal from thermohaline variability above the LNM. Tidal amplitudes, expected to be the major component of η_{BT} in this region (see Chapter 3), contribute variability to η on the order of ten times the baroclinic signal and tidal corrections must therefore be made with care. This is done by lowpass filtering the PIES records since, as will be seen, the frequency of the signals of interest are far lower than the dominant tidal frequencies identified in Chapter 3.

As can be seen in Eq. 4.1, τ can easily be calculated from a hydrographic station. This is done to aid in interpretation of the PIES signals, as it provides information about the effects of water column structure on $\delta\tau$. The use of fixed pressure coordinates in the limits of the integration with an upper limit of 0 dbar automatically includes increases (decreases) in $\delta\tau$ due to increases (decreases) in η_{BC} – a signal on the order of 0.2 ms; it also adds some variability not present in $\delta\tau$ measured by a bottom-moored IES because the depth of the lower limit of integration may vary slightly. This variability is on the order of 0.02 ms.

A strong correlation exists between values of $\delta\tau$ and η_{BC} computed from hydrographic data, allowing a regionally dependent relation to be defined between the two quantities, or:

$$\eta_{BC} = \alpha\,\delta\tau \tag{4.4}$$

where α is an empirically determined constant. Techniques such as this one have been used in studies of the Brazil Current [Garzoli and Bianchi, 1987, Garzoli and Garraffo, 1989], of the equatorial Pacific [Katz et al., 1995], of the Gulf Stream [Watts and Olson, 1978, He, 1993], and of the eastern South Atlantic ocean [Garzoli and Gordon, 1996, Garzoli et al., 1996, DuncombeRae et al., 1996]. A reduced gravity model can of course be used to link dynamic height to the depth of the thermocline, typically quantified in this region by the depth of the 10°C isotherm, Z_{10}, [Olson and Evans, 1986, DuncombeRae et al., 1992, Byrne et al., 1995, DuncombeRae et al., 1996]. Using the 118 travel times computed from the CTD casts, $\delta\tau$ correlates to $r^2 = 98\%$ with the η_{BC}, also calculated from the hydrography. For these data, using a LNM of 1000 dbar, and with η expressed in mm, [Garzoli and Gordon, 1996] (Equation 2) found $\alpha = -26.7$. For a 1000 dbar reference level, we find $\alpha = -30.8 \pm 0.6$.

Excursions in $\delta\tau$ from the five IES-equipped moorings are on the order of -9.5 ms to +6 ms. With $\alpha = -30.8$, the changes in $\delta\tau$ are expected to correspond to changes in η_{BC} of 30 cm to -20 cm.

4.2.3 Bottom Pressure

Four of the BEST moorings were equipped with BP sensors and recorded pressure at one hour intervals for approximately 18 months [Garzoli et al., 1994]. A problem with SN62 late in its deployment leads us to discard the data collected after June 27, 1993. Because CSR 3.0 accounts for almost all of the variability in the BP records (see Section 3.4) the model is used to fill occasional data gaps in the pressure records before processing (33 missing records in PIES 62 and 5 in PIES 61).

Bottom pressure variability is converted to η_{BT} using information from CTD stations taken at and near the mooring locations and the hydrostatic equation. To correspond with the conversion of $\delta\tau$, bottom pressure was referenced to variability in the water column above 1000 dbar to sea surface height:

$$\eta_{BT} = dp/\overline{\rho}g \tag{4.5}$$

which, given the relative sensor accuracy (Section 3.2) results in an uncertainty of ±20 mm in η_{BT}.

4.2.4 TOPEX/POSEIDON data

The T/P data used in this study are the Merged Geophysical Data Records (MGDR) produced by V. Zlotnicki and A. Hyashi of NASA's Jet Propulsion Laboratory. These data have been interpolated to a uniform along-track spacing on a standard groundtrack. We apply the standard adjustments and corrections supplied with the data (sea state bias, ionospheric, wet and dry tropospheric, inverse barometer, TOPEX oscillator drift). The uncertainty in measurement after these corrections have been applied is estimated to be ±2.4 cm [Benada, 1997]. Final processing included removal of the mean SSH over the time period of IES/PIES mooring deployment and removal of the CSR 3.0 tide, proven in Chapter 3 to be a good estimator of the tide in this region. These SSH anomalies comprise our basic T/P dataset. Throughout this paper it is assumed that in the absence of errors, the variability in η from a PIES is identical to the variability in sea surface height mapped by a time-series of T/P measurements taken over the mooring location and of approximately the same duration as the mooring time-series: $\eta = \mathrm{SSH}_{T/P}$.

For use with $\delta\tau$ calculated from hydrography, the basic T/P dataset described above is first filtered with a 2-dimensional Loess filter (see [Chelton and Schlax, 1994]) with a time constant of 20 days and a distance radius of 25 km. This filter was used to obtain estimates of $\mathrm{SSH}_{T/P}$ interpolated to the times and locations of the hydrographic stations, which varied greatly in their temporal and geographic distance from TOPEX/POSEIDON overflight times and locations; while its use had some drawbacks, detailed below, the Loess filter performed better at this task than a number of other methods evaluated. The filter constants were chosen empirically to preserve meso-scale, (O(100) km), variability while providing $\mathrm{SST}_{T/P}$ estimates at as many hydrographic stations as possible. The use of this filter means that a minimum of 100 and a maximum of 212 measurements went into each estimate of $\mathrm{SSH}_{T/P}$ used in the hydrographic-altimetric comparison.

For comparison with the moorings, time-series of the nearest points on the T/P groundtrack were compiled, then cross-correlated with the mooring records subsampled at overflight times. Those along-track points exhibiting the highest correlations were then averaged. For this purpose averaging produced better results than Loess filtering, which was initially tried to obtain estimates of $\mathrm{SSH}_{T/P}$ more closely spaced in time but which was found to degrade the correlation between the altimeter record and the subsampled mooring. The averaging reduces the original ±2.4 cm uncertainty to ±1.0 cm (see Section 4.2.4).

As noted in Chapter 3, instantaneous differences between tides measured at the BEST mooring records and the CSR 3.0 tide averaged between 1.0 cm and 1.75 cm, reaching a maximum of 6.5 cm (see Chapter 3). While energy at tidal frequencies was effectively excluded from the mooring data with low-pass filtering (Fig. 4-1), this recourse is not available in processing the T/P data; instead, at the PIES mooring locations where BP information was available, a correction was generated using the difference between the BP tide record and the CSR 3.0 record. This correction was applied to the $\mathrm{SSH}_{T/P}$ time-series used in conjunction with the PIES moorings. The value of the correction is between -4.0 cm and 4.9 cm at SN58, -2.7 cm and 3.0 cm at SN61, and -3.8 and 5.3 cm at SN62. A sample correction is illustrated in Fig. 4-2. While the value of the correction is not large, in at least one case it was responsible for a change the interpretation of one of the meso-scale events in the mooring record. Thus interpretation of $\mathrm{SSH}_{T/P}$ time-series at the two IES moorings (SN56 and SN59), where no such correction is available, must be pursued with greater caution.

Errors and other factors that may affect the correlation between η and $\mathrm{SSH}_{T/P}$ are use of an incorrect LNM in converting the IES data, discrepancies between *in situ* tides and the tidal model (where no BP correction is available), errors in the standard adjustments and corrections to the raw altimeter data described above, and uncertainty introduced by limitations in the resolution of the IES and BP sensors. The sum total of these uncertainties and errors at each mooring location is discussed in Section 4.6.

4.3 Thermohaline variability of the southeastern South Atlantic

To be able to be parameterized, sources of the complex thermohaline variability of the southeastern South Atlantic must first be characterized. The subtropical South Atlantic water column which predominates in the Agulhas region may be described as follows [Valentine et al., 1993]: Antarctic Bottom Water (AABW, θ = -0.9 °C - 1.7 °C, S = 34.64 - 34.72), North Atlantic Deep Water (NADW, θ = 1.5 °C - 4.0 °C, S = 34.80 - 35.00), Antarctic Intermediate Water (AAIW, θ = 2.0 °C - 6.0 °C, S = 33.8 - 34.8), South Atlantic Central Water (SACW, θ = 6.0 °C - 16.0 °C, S = 34.5 - 35.5) and Atlantic Subtropical Surface Water (SSW, θ = 16.0 °C - 26.0 °C, $S > 35.5$). Fig. 4-3 displays a number of the BEST hydrocasts which were taken in

Atlantic water columns. The sources of observed variability in these reference water masses are examined level by level, starting with surface and central waters.

In the Benguela upwelling regime near the African coast, Atlantic SSW is not present and is replaced by warmed and upwelled SACW [Stander, 1994, Shannon, 1966], which begins at temperatures no colder than $\theta = 12$ °C ($S = 34.9$), and is warmed to no more than 23 °C [Lutjeharms and Valentine, 1987]. Filaments and eddies of upwelled water are advected further west and have been detected 700 km from the coast [Lutjeharms and Stockton, 1987]. This water then mixes into the South Atlantic [Lutjeharms and Stockton, 1987]. To the south, Atlantic SSW may be replaced by modified Subantarctic Surface Water (SASW), which is at its source considerably colder and less saline ($S < 34.0$). Filaments of SASW have been observed as far north as 33°S and can extend to more than 200 m below the surface [Shannon, 1989]. At a given density horizon, upwelled water will be relatively fresher and colder than the reference Atlantic [Lutjeharms and Valentine, 1987, DuncombeRae et al., 1992].

In the Agulhas region, Atlantic SSW and SACW are often replaced by South Indian SSW and South Indian Ocean Central Water (SIOCW), respectively [Bennett, 1988, Duncombe Rae, 1991]. The South Indian SSW and SIOCW are warmer and saltier than Atlantic SSW and SACW at equivalent density horizons (see Valentine et al. [1993], Table 1) and in passing through the Agulhas Current are often further enriched in salt due to evaporative cooling [Gordon and Haxby, 1990, Olson et al., 1992]. A pool of nearly isothermal South Indian SSW at 17 °C - 18 °C found within the Agulhas is known as South Indian Subtropical Mode Water (STMW), so-called because its temperature is constant over a large depth range [Gordon et al., 1987]. Evaporation, cooling and vertical mixing at the surface creates this mode water [Olson et al., 1992]. It is often but not always encountered at the center of Agulhas eddies (see Duncombe Rae [1991], Fig. 10 and Byrne et al. [1995], Fig. 10). One more water mass of note has been observed – a well-defined mode water of between 12 °C and 13 °C, ~35.35 psu found in extensive (> 400 m) layers. This water, found in anticyclonic rings smaller than typical Agulhas rings (see Section 4.7), was at first posited to be of Brazil Current origin [Smythe-Wright et al., 1996, DuncombeRae et al., 1996] and more recently proposed to be a species of Subantarctic Mode Water (SAMW) formed in the Indian Ocean near 60°E which has become entrained into the Agulhas Current [McDonagh and Heywood, 1999]. Because of its strong and distinct signature, the SAMW entering the southeastern South Atlantic via this route is distinguished from the relatively milder influence of SAMW seen in AAIW (described below), which has another source. The input of water to the South Atlantic from the Drake Passage input results in the presence of a relatively colder, less saline AAIW [McCartney, 1977] to the south and west of Africa [Shannon and Hunter, 1988]. Below the thermocline, the AAIW layer in the southeastern South Atlantic is freshened by the influence of this water. The fresher AAIW may enter the southeastern South Atlantic episodically, perhaps entrained by Agulhas eddies [Shannon, 1989]. In areas south and east of Africa, AAIW is markedly higher in salinity due its greater age and to the influence of Red Sea Water (RSW, $\theta = \sim 6.2$ °C $S = \sim 35.1$) in the $\sigma_\theta =$ 27.0 - 27.5 layer [Gründlingh, 1985, Gordon et al., 1987]. In addition, there is good evidence that higher salinity AAIW (S = 34.55) originating in the tropical eastern Atlantic flows down the African coast as far as 33°S [Shannon and Hunter, 1988]. The large range in θ - S found at every upper and intermediate density horizon in the BEST hydrography (Fig. 4-3) reflects the remarkably varied sources for them described here. As mentioned in Section 4.2.2, in concordance with Gordon et al. [1987], thermohaline variability is found to decrease sharply below $\sigma_\theta = 27.5$ so variations in the deep and bottom waters (NADW and AABW layers) will not be considered.

Using these water mass definitions, we select an Atlantic reference station from the BEST hydrography to provide a basis for comparisons made in the following discussion. This reference station is not intended to be representative of the mean $\theta - S$ profile in the dataset because the mean will have been influenced by the large number of intrusive water masses. Rather, the reference profile is defined by the absence of any exotic water masses and is somewhat colder and fresher than the mean of the dataset (Figs. 4-4, 4-5). Geographically, it is located relatively farther away from the Agulhas Retroflection than most of the station occupied (Fig. 4-6).

4.3.1 Agulhas eddies

As mentioned above, Agulhas eddies have at their core a lens of relatively warm SIOCW, which often but not always exhibits a mode (thermostad) at 16 °C - 17 °C. The cores of Agulhas eddies show a great deal of variation (Figs. 4-4, 4-5, 4-7, and DuncombeRae et al. [1996]) in accordance with both the initial thermohaline variability in their source region and also with the wide range of atmospheric conditions encountered in the Retroflection (i.e., cooling and evaporation) [van Ballegooyen et al., 1994] but are, in keeping with their origin, warmer at a given depth than Atlantic water. Particularly near the surface (0 m - 300 m) the Agulhas eddies surveyed during the BEST project carry a notable thermohaline ($\theta - S$) anomaly at their centers with a mean $\theta - S$ of 16.9 °C and 35.53 psu as opposed to the Atlantic stations with a mean $\theta - S$ of 15.3 °C and 35.31 psu (for a similar characterization see DuncombeRae et al. [1996]). On a density horizon, for example $\sigma_\theta = 26.0$, this amounts to a thermohaline anomaly of 1 °C and 0.27 psu relative to the Atlantic reference station. The eddies are on average saltier than the mean in the intermediate water layer, carrying traces of RSW (Fig. 4-5), with eddies near the Retroflection reaching salinities of up to 34.54 at the core of the AAIW (0.22 psu saltier than the reference station).

Its large volume [Duncombe Rae, 1991, van Ballegooyen et al., 1994, Byrne et al., 1995] means that *in toto* an Agulhas eddy carries a significant amount of heat and salt into the Atlantic (see Table 1A and Gordon and Haxby [1990]). Furthermore, in the BEST hydrography the surface layers of many Agulhas eddy stations do not fall on a mixing line with the rest of the casts, (Fig. 4-8), a result of evaporation at the surface [Walker and Mey, 1988, Olson et al., 1992]. However, at a few stations the surface layers are distinctly fresher than their surroundings rather than saltier – suggesting entrainment of SASW, which was posited by Shannon and Hunter [1988]. The *in situ* properties of the Agulhas filaments identified and described by Lutjeharms and Cooper [1996] carry similar if less pronounced anomalies being warmer and more saline than Atlantic SSW, with an average annual salt flux per filament of between 4.7x10^{11} kg and 13.8x10^{11} kg. It should be noted that while not overly sensitive with regard to reference *density* (see Appendix A), anomaly calculations are extremely sensitive to the choice of reference *profile*. A seemingly slight difference in the choice of profile can change the computed thermohaline anomaly by a factor of two or more, or even change the sign of the anomaly.

4.3.2 13 °C stad eddies

13 °C stad eddies are much less well-documented than the warmer Agulhas eddies having been first observed in January of 1993 [Smythe-Wright et al., 1996] and then again in June and November of that year [DuncombeRae et al., 1996]. The distinctive water mass in the 13 °C stad eddy, discovered in 1983 by Gordon et al. [1987] in the main part of the Agulhas Retroflection, was identified by them as "highly modified STMW". It is characterized by a well-ventilated thick isopycnal layer at about 13 °C and 35.35 psu, now thought to be SAMW. To distinguish it from other water than may contain a Subantarctic influence or remnant, the water column containing this type of SAMW is referred to "13 °C stad" (Fig. 4-4); regardless of its origin, its signature in θ-S space is quite distinct (see Fig. 4-5, Smythe-Wright et al. [1996], Fig. 3 and DuncombeRae et al. [1996], Fig. 10). Unlike DuncombeRae et al. [1996] we find significant anomalies in 13 °C stad eddies below the thermocline; the AAIW layer ($\sigma_\theta = 27.12 - 27.30$) is significantly colder/fresher than the Atlantic reference station, with a mean salinity (based on 6 casts taken at the cores of 13 °C stad eddies) of only 34.30 psu and a potential temperature of 4.4 °C – 0.05 psu fresher and 0.28 °C colder than the average southeastern South Atlantic intermediate water in the BEST surveys (see Figs. 4-6, 4-7). The positive thermohaline anomaly of the pycnostad is slightly deeper in the water column than the typical warm Agulhas water, and with respect to the subtropical Atlantic a source of salt, with a thermohaline anomaly of 0.7 °C and 0.21 psu at $\sigma_\theta = 26.2$. As with the Agulhas eddies, the surface layer of 13 °C stad eddies shows a distinct departure from the conservative mixing line (Fig. 4-8). McDonagh and Heywood [1999] calculate that a net surface heat flux in excess of 2500 W m^{-2} would be required to convert water of the type found in Agulhas eddies to that found in 13 °C stad eddies. This leads them to reject the possibility

that 13 °C stad eddies are simply modifications of typical Agulhas eddies.

Interestingly, some of the Agulhas eddies encountered in the BEST cruises showed remnant halo- and thermostads at around 400 dbar strongly reminiscent of the more pronounced one found in the 13 °C stad eddies (Fig. 4-4). This gives weight to McDonagh's and Heywood's, [1999] hypothesis that the 13 °C stad water comes through the Agulhas Retroflection on its way to the South Atlantic. Using a combination of ERS-1 along-track scanning radiometer (ATSR) and ERS-1 and T/P altimeter SSH anomaly data, McDonagh and Heywood [1999] trace the passage of one 13 °C stad eddy where it was sampled during WOCE cruise A-11 back to its origin in the Agulhas Retroflection. If this is indeed the pathway by which 13 °C stad water enters the South Atlantic one question that remains to be answered is how the potential vorticity barrier of the highly anticyclonic Agulhas Current is overcome enough to allow inclusion of this colder (relatively cyclonic) water mass. One other possibility, suggested by the origin of this eddy and the freshness of the AAIW is that these eddies are shed from the Agulhas Retroflection as demonstrated, and soon after undergo a southward excursion, replacing their more saline intermediate water with fresher AAIW from a more westerly source. Such an excursion would be consistent with the production of a 13 °C stad layer. To complete the picture, however, some of those eddies would then have to merge or become at least partially re-incorporated into the Agulhas Current to produce the "double mode" or "double stad" observed by Gordon et al. [1987] and seen in Fig. 4-4; while reported to have been observed elsewhere in the ocean [Cresswell, 1983] this merging has never been observed within the Agulhas system.

4.3.3 The effect of thermohaline variability on observed quantities

In this region, 97%-98% of the observed variability in $\delta\tau$ is due to changes in temperature in the water column; salinity plays a very minor role. The correlation between $\delta\tau$ and η_{BC} (Eq. 4.4), and further, the success of a simple reduced gravity model

($Z_{10} \propto \eta_{BC}$), therefore depend on the dominance of a single mode of variability in the thermal stratification – an assumption not necessarily valid in a region such as the Agulhas, where a number of water masses merge. Appendix B contains a detailed discussion of how different modes of variability in the stratification affect the relationship between $\delta\tau$ and η_{BC}.

In their study of Agulhas eddies using Geosat altimetry and hydrography from the Subtropical Convergence and Agulhas Retroflection Cruise (SCARC), van Ballegooyen et al. [1994] remark that "some stations deviated significantly from the linear fit" of dynamic height to Z_{10}, particularly those containing SASW. These stations were excluded in their regression. This practice unfortunately results in the exclusion of just those stations which are contributing to the thermohaline variability of the region while producing an artificially high regional correlation between thermocline depth and sea surface height. The exercise of this kind of discrimination in the regression of η_{BC} on $\delta\tau$ produces a similar result. Hence the complexity of the region is often masked by researchers' attempts to develop an accurate linear model which serves well for the predominant water column type; much of the information about water mass composition is contained in outliers which are discarded.

4.3.4 Water column types

Despite the high variability in individual water masses found in the southeastern South Atlantic, changes in the water column tend to happen in concert – for example, Agulhas eddies bring in surface, central and intermediate waters from the Indian Ocean (roughly 0 dbar - 1000 dbar). All of these tend to be warmer and saltier than their Atlantic counterparts at equivalent density horizons. The advection of filaments from the Subantarctic of the type observed by Shannon [1989] tends to bring colder fresher water – again at surface, thermocline and intermediate levels. One possible exception to this trend would be warm filaments from the Agulhas, some of which extend only through the top 50 m [Lutjeharms and Cooper, 1996]. However, their shallowness also implies that such filaments will in addition make only a small contribution to the Agulhas-Atlantic inter-ocean transport – O(5%) [Lutjeharms and

Cooper, 1996].

The tendency of surface, central and intermediate water masses to vary in concert justifies a generalization of the hydrographic complexity of the region into a set of water column "types" (although these are clearly only a subset the possible water columns that might be encountered in the region). Five basic types of water column occur in the BEST hydrography: subtropical Atlantic, Subantarctic, upwelled, Agulhas and 13 °C stad. Their spatial distribution in the cruise hydrography is mapped in Fig. 4-9. Of the five water column types we concentrate our attention on three: the predominant subtropical Atlantic (described at the beginning of this Section), Agulhas, and 13 °C stad (SAMW). These types were identified in θ-S space on the basis of their water mass signatures.

In areas such as this one, where a number of differently stratified water masses merge, $\delta\tau$ does not uniquely define η_{BC}. Rather, it defines a suite or range of possible sea surface heights; the actual value of η_{BC} will depend on the water mass configuration above the sounder (see Appendix B). With the exception of the few moments at which reference casts are being taken above the mooring – typically three or four times in a deployment of a year or more (e.g, Garzoli and Gordon [1996]) – this is unknown.

A closer look at the relationship of $\delta\tau$ to η_{BC} shows deviations from the simple linear regression are not unconnected to water column type (Fig. 4-10). The three distinct water column types outlined above occupy to some extent dissimilar ranges and exhibit different slopes in $\delta\tau - \eta$ space. One quick way to illustrate why this happens is to look again at the water column type characterizations in Fig. 4-9; in Fig. 4-11, the average near-surface temperature of each station (0 m - 300 m) is plotted against the depth of the 10° isotherm – clearly no simple linear model is going to account for this distribution. The existence of differently stratified water column types will cause an error of 5 cm - 15 cm in the value of η calculated from $\delta\tau$ (for a strong thermohaline anomaly), and which in the presence of another independent sensor not similarly affected will introduce a discrepancy between the two. While first detected in travel times and sea surface heights simulated from the BEST hydrography, this potentially informative mismatch is evident when the analysis is extended to include a second, independent sensor – the TOPEX/POSEIDON altimeter, as will be shown in Sections 4.5 and 4.6. Fig. 4-12 shows an idealized schematic of the phenomenon.

4.3.5 The modified Atlantic water column

It is worthwhile to revisit the stations categorized as being primarily composed of water from the Atlantic subtropical gyre. As noted above, even these stations exhibit a great deal of variability in their salinity and temperature (Fig. 4-3) but are generally warmer and saltier than the Atlantic reference station (Fig. 4-5); at densities less than $\sigma_\theta = 26.4$ (roughly, the top 300 m), the mean is 0.5 °C warmer and 0.10 saltier than the Atlantic reference station. In the middle of the thermocline ($26.5 < \sigma_\theta < 27.0$), the mean is 0.9 °C warmer and 0.14 saltier than the reference station while in the intermediate water ($27.0 < \sigma_\theta < 27.5$) the mean is 0.3 °C warmer. The warmer, saltier stations appear to have been modified by mixing with water of Agulhas origin (see Figs. 4-3 and 4-5). This result agrees with the findings of Gordon et al. [1992] and Garzoli and Gordon [1996]. Using Agulhas eddies B1-1 and B2-2 (Figs. 4-4, 4-5, 4-7), an "Agulhas source" thermohaline profile is defined. Using this profile and the Atlantic reference station the extent to which the stations mentioned above have been modified by mixing with Agulhas water can be determined. For simplicity, isopycnal mixing is assumed. The amount of mixing appears to be extensive, with approximately 62±4% of the water in each of the modified stations being from the Atlantic and the remaining 38±4% from the Agulhas (Fig. 4-13). We will hereafter refer to this water column type as "modified Atlantic" to reflect this result. Approximately 70% of the Atlantic stations show some extent of modification.

4.4 Methodology

The goal of ETTA is to use directly measurable parameters such as $\delta\tau$ and SSH as proxies for quantities of interest such as the mean temperature, salinity, or velocity of a water column. To accomplish this end, a number of assumptions must be applied and proxies established. The conversions of $\delta\tau$ to η_{BC} and of BP to η_{BT} have already been treated; these are straightforward and unambiguous. In this Section, the remaining calculations are outlined: using η_{BC} to obtain estimates of baroclinic transport, η_{BT} to obtain the barotropic transport, and going from these to thermohaline fluxes.

4.4.1 Baroclinic Transport

Mooring-derived time-series of η are converted to surface geostrophic velocity using Garzoli and Gordon [1996], Eq. 3:

$$V_g = (g/f)\Delta DH/\Delta x \tag{4.6}$$

where ΔDH (in dyn. meters) is the difference between η at two moorings, $\Delta DH = 9.81\eta/1\mathrm{x}10^4$ (with η in mm), Δx is the distance between the moorings, and f is the Coriolis parameter.

To obtain η at each mooring, ETTA uses an improved version of Eq. 4.4, allowing α to vary with water column type. The initial assumption of zero mean for $\delta\tau$ no longer holds since the mean travel time, $\overline{\tau}$ is calculated for the entire deployment period. The mean of estimates of $\delta\tau$ for an anomalous water mass may therefore differ significantly from zero. For this reason, an offset must be added to Eq. 4.4, or:

$$\eta_{BC} = \alpha\,\delta\tau + \beta \tag{4.7}$$

Next, an empirical constant of proportionality, k, is derived from the hydrographic data, relating surface geostrophic velocity to integrated transport between the surface and the LNM, or:

$$Tr_{BC}(Sv) = kV_g\Delta x\Delta z \tag{4.8}$$

where 1 Sv $\equiv 10^6$ m^3 s^{-1}, and Δz is the depth from surface to LNM.

4.4.2 Barotropic Transport

To obtain the barotropic transport, a version of Eq. 4.6 is used, this time with the sea surface heights obtained from BP sensors.

$$Tr_{BT}(Sv) = V_g \Delta x Z \tag{4.9}$$

where Z is the mean depth of each sensor pair.

4.4.3 Thermohaline anomaly transports

To measure the heat and salt fluxes (relative to the reference station) a similar set of equations is employed. The baroclinic transports of anomaly heat and salt can be expressed by:

$$Tr_{\Delta Q}(BC) = \Delta x \int_{\theta_Z}^{0} V_{gi}\rho_i C_p h_i [T_{\sigma\theta i} - T_{\sigma_{\theta i}}(ref)] d\theta \tag{4.10}$$

$$Tr_{\Delta\Sigma}(BC) = \Delta x \int_{\theta_Z}^{0} 0.001 V_{gi}\rho_i h_i [S_{\sigma_{\theta i}} - S_{\sigma_{\theta i}}(ref)] d\theta \tag{4.11}$$

where the subscript i denotes an isopycnal layer, h the thickness of that layer (in pressure coordinates), (ref) denotes the reference thermohaline profile, C_p is the heat capacity of seawater, T_{σ_θ} is potential temperature along an isopycnal surface, S_{σ_θ} the salinity along the same, and $Tr_{\Delta Q}$ and $Tr_{\Delta\Sigma}$ are the anomaly heat and salt fluxes, respectively. We would still like the equations to be in the form of Eq. 4.8, so that surface geostrophic velocities from the mooring records can be used. Rearranging the terms of Eq. 4.10 produces:

$$k_{\Delta Q_{BC}} = \frac{\int_{\theta_Z}^{0} V_{gi}\rho_i C_p h_i [T_{\sigma\theta i} - T_{\sigma_{\theta i}}(ref)] d\theta}{\Delta z V_g(0)} \tag{4.12}$$

and similarly:

$$k_{\Delta\Sigma_{BC}} = \frac{\int_{\theta_Z}^{0} 0.001 V_{gi}\rho_i h_i [S_{\sigma_{\theta i}} - S_{\sigma_{\theta i}}(ref)] d\theta}{\Delta z V_g(0)} \tag{4.13}$$

Thus:

$$Tr_{\Delta Q}(BC) = k_{\Delta Q_{BC}} \Delta z \Delta x V_g(0) \quad \text{and} \quad Tr_{\Delta\Sigma}(BC) = k_{\Delta\Sigma_{BC}} \Delta z \Delta x V_g(0) \tag{4.14}$$

where $k_{\Delta Q}$ and $k_{\Delta\Sigma}$ are, like k, empirical constants of proportionality determined from hydrographic data. Computations for the barotropic transports of anomalous heat and salt are similar. In the barotropic case,

$$Tr_{\Delta Q}(BT) = \Delta x V_{gBT} \int_{\theta_Z}^{0} \rho_i C_p h_i [T_{\sigma_{\theta i}} - T_{\sigma_{\theta i}}(ref)] d\theta \tag{4.15}$$

and

$$Tr_{\Delta\Sigma}(BT) = \Delta x V_{gBT} \int_{\theta_Z}^{0} 0.001 \rho_i h_i [S_{\sigma_{\theta i}} - S_{\sigma_{\theta i}}(ref)] d\theta \tag{4.16}$$

so that:

$$k_{\Delta Q_{BT}} = \frac{\int_{\theta_Z}^{0} \rho_i C_p h_i [T_{\sigma_{\theta i}} - T_{\sigma_{\theta i}}(ref)] d\theta}{Z} \tag{4.17}$$

and similarly:

$$k_{\Delta\Sigma_{BT}} = \frac{\int_{\theta_Z}^{0} 0.001 \rho_i h_i [S_{\sigma_{\theta i}} - S_{\sigma_{\theta i}}(ref)] d\theta}{Z} \tag{4.18}$$

giving us:

$$Tr_{\Delta Q}(BT) = k_{\Delta Q_{BT}} Z \Delta x V_{gBT} \quad \text{and} \quad Tr_{\Delta\Sigma}(BT) = k_{\Delta\Sigma_{BT}} Z \Delta x V_{gBT} \tag{4.19}$$

In ETTA, $k_{\Delta Q}$ and $k_{\Delta\Sigma}$ are calculated for each water column type. It should be noted that in addition to allowing $k_{\Delta\Sigma}$ and $k_{\Delta Q}$ to vary with water column type, it is important to allow the LNM to vary as well. The location where vertical shear in the geostrophic velocity disappears has been found to be a good approximation of the LNM [Defant, 1961]. Characteristic velocity profiles may vary significantly between water column types, meaning that comparable levels of shear occur at dissimilar depths. This tendency is at least partially countered by determining the appropriate LNM for anomalous water column types and using it.

Before the transport calculations can be applied something must be done to determine how much of the transport between a mooring pair is apportioned to each water column type. Concurrent values of $\mathrm{SSH}_{T/P}$ and η determine which water column is directly above each sensor but what is going on between them? Should the moorings be spaced closely enough together, at the length scales of the phenomena of interest, this problem is easily solved, as the mooring records themselves will indicate the extent of features passing through the array. Should moorings be deployed along a colinear altimeter groundtrack, the additional information able to be obtained from the along-track altimeter record will serve the same purpose. Failing either of these conditions, an additional assumption must be made as is the case with the BEST mooring array.

A nominal length scale (L) for meso-scale anomalies passing through the array is adopted, using sizes of eddies determined from the BEST hydrographic data by DuncombeRae et al. [1996] as a measure. Agulhas eddy features averaged 102 km in radius, while 13 °C stad eddies averaged only 29 km in radius. When an anomalous water column above one of the BEST PIES moorings is detected in the SSH-$\delta\tau$ fields, that anomaly is traced forward and backward in the mooring time-series. From the beginning of its detection until the end, a rectangular portion of the cross-sectional area between the moorings is labeled with the anomalous water mass (e.g., Agulhas) and the total transport measured between the mooring pair is divided proportionally (Fig. 4-14).

For each sensor pair, then, a set of transports (mass, anomaly heat, anomaly salt) is calculated (one for each water column type) and if length scaling is being used these are merged in a scaled manner using $L/\Delta x$ and the appropriate LNMs.

4.5 Feasibility Test: SSH$_{T/P}$ and $\delta\tau$ from hydrography

The purpose of this comparison is to inform us about the possible results of a direct comparison of SSH$_{T/P}$ and η from the PIES moorings at times when no information about water mass identity is available. In the hydrography, only those stations occupied at depths $>$ 1000 dbar which fell within 20 km of a T/P groundtrack were used. 123 stations fit these criteria; of those, 109 were occupied after the beginning of cycle 2 of the T/P overflights. Unfortunately, out of the 109, only 26 were CTD casts while the rest were XBT casts (Fig. 4-15). This poses a problem, because $\delta\tau$ and η can only be calculated for stations where the salinity (density) is known. Therefore the relation mentioned in Section 4.2.2 is used, a linear conversion of 10°C isotherm depths to $\delta\tau$. To preserve as much of the expressed thermohaline variability as possible, a linear regression of each water column type is calculated independently. The basic equation is:

$$\delta\tau = \kappa Z_{10} + \mu \tag{4.20}$$

It should be noted that as with η, the correlation is negative – a deepening (increase) of Z_{10} leads to a decrease in travel time anomaly, as c increases in warm water. For 13 °C stad water, $\kappa = -0.028 \pm 0.003$, $\mu = 13.2 \pm 1.8$; for Agulhas water $\kappa = -0.037 \pm 0.002$, $\mu = 16.3 \pm 1.0$ and for Atlantic water (together with subantarctic and upwelled, which exhibit the same slope) $\kappa = -0.033 \pm 0.001$ and $\mu = 15.1 \pm 0.5$, with Z_{10} in meters and $\delta\tau$ in milliseconds. Estimating $\delta\tau$ in this way adds some uncertainty; the rms error of the conversion is 0.6 ms (based on the 118 CTD stations originally used to compute $\delta\tau$), with a maximum in individual errors of $\sim$2.0 ms.

This series of $\delta\tau$ values calculated from hydrography and the set of Loess-filtered SSH$_{T/P}$ used with it are primarily spatial in character and not temporal as will be the case for our target datasets. Because of the difficulty in properly referencing SSH$_{T/P}$ for comparison with a series of points scattered over 2x10^6 km^2 and 30 days and the lack of any information about η_{BT} (the signal of which will be present in the T/P record but absent from the CTD and XBT data) more noise can be expected in the simulation than in a comparison of a PIES time-series with $\mathrm{SSH}_{T/P}$ derived at a single location. The results of this comparison are visible in Fig. 4-16. The Loess interpolation of $\mathrm{SSH}_{T/P}$ has also added uncertainty to the relationship – the rms difference between the Loess-filtered value of SSH and a non-filtered version is 34 mm for a line of 27 BEST-2 XBT stations that were taken directly along a T/P groundtrack (Fig. 4-17). Despite the additional scatter, the ranges of $\mathrm{SSH}_{T/P}$ for Agulhas and 13 °C stad water differ so greatly that the same patterns discovered in Fig. 4-10 are clearly apparent. The dynamic ranges are also similar; an absence of values for $\delta\tau > 4$ can be explained by the fact that none of the stations included in the comparison were at the southern (relatively cold) part of our study region. Strongly anomalous Agulhas water falls at the far end of the ranges (low $\delta\tau$, high $\mathrm{SSH}_{T/P}$), while strong 13 °C stad water clearly follows a different slope, far from the values predicted by the initial, fixed value of α.

Interestingly, some of the stations identified as being of Agulhas origin cluster near the 13 °C stad water in Fig. 4-16. These stations are characterized as having 10°C isotherm depths between 515 m - 560 m. All are < 11 km from a T/P groundtrack. One such station, number 54 from the BEST-2 cruise, is near the observed center of a large eddy, BEST2-3 [DuncombeRae et al., 1996]. The center of the BEST2-3 was located ~56 km to the west (at station 53), but is too far from a T/P groundtrack for a reliable estimate of $\mathrm{SSH}_{T/P}$ to be made. Based on hydrographic information about $\delta\tau$ and η alone, this eddy appears in no way unusual, that is to say the baroclinic component of SSH is predicted quite well from Eq. 4.4. But $k_{\Delta\Sigma_{BT}}$ and $k_{\Delta Q_{BT}}$ (which can also be interpreted as the vertically-averaged temperature and salinity anomalies) for this station are 1.0 J m^{-3} and 0.06 kg (salt) m^{-3}, which fall right in the range where the 13 °C stad and Agulhas eddies mingle and become indistinguishable. This means that an ETTA estimate of the thermohaline anomaly transport based on $\mathrm{SSH}_{T/P}$ and $\delta\tau$ will still be accurate.

Most of the Agulhas stations clustered where the three water column types are indistinguishable in Fig. 4-16 exhibit a warm isopycnal surface layer at around 19°C and between 35.65 - 35.71 psu. In $\theta - S$ space, they show the distinct mark of saline enrichment near 16°C that is the hallmark of Agulhas eddies [Gordon and Haxby, 1990]. But several stations show both the warm Agulhas signal and a deeper remnant mixed layer at ~13 °C - 14 °C. This type of feature was also noticed by McDonagh and Heywood [1999]. Perhaps the best examples of this are BEST-2 stations 13 and 35, the centers of eddies B2-0 and B2-2, respectively (for locations, see DuncombeRae et al. [1996], Fig. 3). In $\theta - S$ space, these stations show a distinct signature similar to but weaker than that of the 13 °C stad eddies in addition to a warm STMW layer which corresponds to the more classic conception of an Agulhas eddy (Fig. 4-18). However in $\delta\tau$-η space, these stations fall into the Agulhas population. Their locations are unfortunately quite far ($>$ 90 km) from a T/P groundtrack so no accurate value of SSH$_{T/P}$ is available for either one. The prevalence of this type of double stad the BEST-2 cruise data provide further evidence that the source of the 13 °C stad water is indeed within the Agulhas. Otherwise a local and fairly ubiquitous source is required.

This comparison indicates that the parameterization of thermohaline properties by η and $\delta\tau$ should produce accurate thermohaline anomaly transports. Weaker 13 °C stad and Agulhas anomalies, indistinguishable in the proxy data from modified Atlantic water, contain excess heat and salt in amounts comparable to those in the modified Atlantic water column type.

4.6 Mooring signals vs. SSH$_{T/P}$

In the processed records, η_{BC} is dominated by long (50 - 100 day) events with amplitudes on the order of 10 - 30 cm (3 - 10 ms) – scales characteristic of the meso-scale eddies in this region [Byrne et al., 1995]. Table 1 lists the meso-scale events recorded by the IES sensors and is based on DuncombeRae et al. [1996], Table 5; differences between that table and this one have been underlined. Strong eddy events are typically two to four standard deviations away from the mean for the sensor (Fig. 4-19).

For comparison with $\text{SSH}_{T/P}$, the IES records were low-pass filtered with a 96-point Cosine-Lanczos filter (quarter-power point, 48 hours) and the BP records with a 39-pt Hamming filter. Both types of records (BP and IES) were transformed to sea surface height and in the case of the PIES moorings, combined into a single estimate of η (Fig. 4-20). The paired mooring and T/P time-series are pictured in Fig. 4-21; individual events in the mooring records are identified and discussed below:

Table 1. Meso-scale events in the mooring record

Start Date	days from 1992/01/01	Date at Max.	days from 1992/01/01	Duration (days)	$\delta\tau$ (ms)	ETTA ID W.C. Type
IES SN56						
1992/11/25	330	1992/12/25	360	60	-9.0	Agul.
1993/04/30	486	1993/05/27	513	45	-7.9	13 °C
IES SN58						
1992/10/06	280	1993/01/08	373	110	-3.7	Agul.
1993/04/05	461	1993/05/03	488	50	-7.0	Agul.
1993/05/23	510	1993/07/14	560	80	-3.4	?
IES SN59						
1992/10/22	296	1992/11/03	308	40	-9.8	13 °C
1992/12/05	340	1992/12/25	360	45	-5.9	Agul.
1993/01/25	391	1993/02/12	409	40	-7.5	?
1993/04/27	481	1993/05/08	495	30	-11.1	Agul.
1993/05/28	514	1993/06/14	530	40	-15.1	Agul.
1993/08/08	586	1993/08/22	600	33	-9.0	Agul.
1993/09/12	621	1993/09/23	632	15	-6.3	?
1993/10/01	640	1993/10/16	655	30	-7.5	?
IES SN61						
1992/10/04	278	1992/10/24	298	60	-3.3	?
1992/12/23	358	1993/02/04	401	100	-4.1	Agul.
IES SN62						
1992/12/08	343	1993/02/10	407	88	-1.4	Agul.
1993/03/25	448	1993/04/12	467	42	-1.4	?

At the height of each anomaly listed in Table 1, paired estimates of η (from IES or PIES) and $\mathrm{SSH}_{T/P}$ were extracted. These events were then compared with the values of η_{BC} and $\mathrm{SSH}_{T/P}$ generated from the BEST hydrography and the Loess-filtered T/P series (Fig. 4-22) and on the basis of that comparison, labeled with a probable water column identity. In the following discussion of these records, a common time scale of days from 1992/01/01 is used.

IES SN56 was deployed at a nominal depth of 1926 m on the continental slope only 2.55 km from a T/P groundtrack. While no Agulhas eddies have been tracked this far northeast with altimetry (e.g., Gordon and Haxby [1990], Byrne et al. [1995], and Witter and Gordon [1999]), DuncombeRae et al. [1992] document the flooding of the continental shelf with warmer water as a stalled Agulhas eddy stripped the upwelled water away. It is therefore not surprising that SN56 recorded two strong anomalies centered on days 360 and 513 (Fig. 4-19a, Table 1). The sensor values of the first event indicates that it is Agulhas water (Fig. 4-22). A difference of 14 cm between $\mathrm{SSH}_{T/P}$ and η_{BC} at the climax of the second event indicates the passage of 13 °C stad water over this sensor, presumably a meso-scale eddy (Figs. 4-21a, 4-22). This identification, combined with the location of this mooring, lend additional support to the conclusions of McDonagh and Heywood [1999] that 13 °C stad water enters the South Atlantic via the Agulhas Retroflection. None of the features recorded at mooring SN56 were observed *in situ* although the strongest perturbation in the mooring record occurred during the BEST-2 cruise. This underscores the limitations of ship-based sampling with regard to meso-scale features. This mooring was not equipped with a BP sensor, but if the results of the tide analysis at SN62, deployed at a similar depth further north, are indicative, the CSR3.0 tidal correction can expected to be within 7 cm of the real tidal amplitude. Collectively, rms uncertainties at this location are estimated to reach a total of ± 6.3 cm in η and ± 3.4 cm in $\mathrm{SSH}_{T/P}$.

PIES SN58 is one of the moorings most likely to generate a good record of eddy crossings due to its placement with respect to previously observed eddies. In the center of the Cape Basin, it is located in a spot where the CSR 3.0 tide model (correction to $\mathrm{SSH}_{T/P}$) is likely to be extremely accurate. In addition, the presence of the BP sensor allowed a correction to CSR 3.0 based on the *in situ* tide record to be calculated and applied, as described in Section 4.2. Unfortunately this location also happens to be 76 km west of the nearest T/P groundtrack. Still, a good resemblance is obtained between the PIES and T/P records (Fig. 4-21b). The addition of an eight day offset to the mooring record was used, which increases the agreement between the times of major events recorded by the two sensors. Presumably this lag is indicative of the characteristic propagation speeds of the major meso-scale events recorded at the mooring.

At SN58, three meso-scale events are recorded between cycles 2 and 42 of the T/P mission. The first event, centered at day 373, appears to be a weak Agulhas anomaly (Fig. 4-22). During the second event, which reaches its maximum on day 488, the sensors record a difference of 4 cm and clearly indicate the Agulhas water column type. This appears to be the passage of Agulhas eddy B2-0 overhead. This eddy was also observed in the T/P altimeter record by Witter and Gordon [1999], (Witter, pers. comm.), who were able to follow it for approximately 860 days. In the third event, centered at day 560, the sensors show a discrepancy of ~11 cm. The water column type of this event cannot be determined with certainty from the remotely sensed parameters (see Fig. 4-22), but it is probably either eddy B2-2 or B2-3. The identities of these two eddies, encountered quite close together during the BEST-2 cruise, seems to be confused in the altimeter record as well, appearing as a merged feature in Witter's and Gordon's, [1999] record (Witter, pers. comm.). Uncertainties at the deployment site of SN58 (including sensor resolution limits, possible error due to mis-calculation of the correct LNM, and errors in CSR 3.0) are ±4.7 cm in η and ± 1.0 cm in $\mathrm{SSH}_{T/P}$. Note that the error $\mathrm{SSH}_{T/P}$ has been reduced by 2.0 cm by application of the correction to CSR 3.0. The magnitude of these uncertainties is displayed graphically in Fig. 4-22.

IES SN59 was deployed ~17 km west of T/P groundtrack 133 at a nominal depth of 5002 m (Fig. 3-1). Of all the mooring locations this is the one that can be expected to show the strongest meso-scale variability based on prior observations [van Ballegooyen et al., 1994, Byrne et al., 1995, Witter and Gordon, 1999]. No fewer than eight meso-scale events were observed during the 493-day deployment (see Fig. 4-21c, Table 1). Unfortunately the mooring lacked a BP sensor and so only η_{BC} can be obtained from the sounder. Of the eight events, three (reaching maxima at days 409, 632 and 655, respectively) are not able to be cleanly categorized. Of the remaining five meso-scale features, the first one (peaking on day 308) exhibits an 18 cm difference between sea surface height measured by the T/P altimeter and by the IES, with the IES-derived height being the greater. This places it clearly in the 13 °C stad range (Fig. 4-22), regardless of the possible value of η_{BT}. The remaining four features (days 360, 495, 530 and 600) appear to contain Agulhas water. SN59 was deployed well to the south and east of any eddies identified by either the BEST hydrographic cruises [DuncombeRae et al., 1996] or by Witter and Gordon [1999] using the T/P altimeter, so no corroboration is possible. Lack of a BP sensor is anticipated to add approximately ±4.0 cm (rms) to the uncertainty in η at this location. Collected uncertainties are ±8.5 cm in η and ±3.0 cm in $\mathrm{SSH}_{T/P}$ at this site.

PIES SN61 was deployed at a T/P groundtrack cross-over point, but in an area of steeply sloping topography (the Walvis ridge), where the tidal model cannot perform as well as in a basin and topographic Rossby waves may also be expected to confuse the signal. In addition, PIES SN61 was located on the west (lee) side of the ridge, shielded from the Agulhas Retroflection; as noted by DuncombeRae et al. [1996], the meso-scale signal is not expected to be as strong as in the sensors to the east of the ridge and indeed is not (Figs. 4-19b, 4-21d). Two meso-scale events can be identified, one centered on day 298 and the other on day 401. The first event cannot be unequivocally identified from its parameterization by $\delta\tau$ and $\mathrm{SSH}_{T/P}$. Nor has it a strong enough anomaly in $\delta\tau$ to be able to be categorized as something other than Atlantic water on that basis alone. The second event in this records appears to be Agulhas water (Fig. 4-22). Witter and Gordon [1999] did not observe any of the (albeit weak) anomalies recorded in SN61, although significantly, some strong anomalies in the Witter and Gordon [1999] T/P altimeter record were observed to cross this location well after the mooring had been recovered (Witter, pers. comm), thus indicating that the Walvis ridge does not completely shield the location from the passage of eddies. A BP-based correction was applied to $\mathrm{SSH}_{T/P}$ that reduced uncertainty by 1.3 cm rms. Uncertainty in η is estimated at ±4.7 cm and in $\mathrm{SSH}_{T/P}$ at ±1.0 cm at this mooring location.

Similar to SN59, SN62 was deployed within high SSH variability of the Agulhas Retroflection and of the continental slope, thus no previous record of altimeter-tracked eddies exists for this location, nor did it appear that any of the eddies identified during the BEST cruises were situated where they were likely to pass over the echo sounder. However, two anomalous events were recorded and are displayed in Fig. 4-22. The first, centered on day 407 in the record, appears to be Agulhas water. The water column type of the second, weaker anomaly (centered on day 467) is not able to be determined. PIES SN62 was located at a nominal depth of only 980 m, on the continental slope. This depth (~1000 m) is generally considered to be at the limit for which accurate $\mathrm{SSH}_{T/P}$ measurements can be obtained because of distortion of the tidal frequencies (e.g., Witter and Gordon [1999]). For this reason, even though a correction based on BP information was applied, the time-series of $\mathrm{SSH}_{T/P}$ is considered to be less accurate. The noise level in $\mathrm{SSH}_{T/P}$ is approximately double what it is at the other PIES sites (±2.0 cm). Uncertainty in η is estimated at ±4.7 cm at this location.

As a result of this analysis two of the seventeen meso-scale anomalies in Table 1 are able to be identified as 13 °C stad eddies, and nine as Agulhas eddies (Fig. 4-22). Six were of ambiguous origin. It should be noted that eddies on the near side of the Walvis ridge often carry a strong barotropic signal [Kamenkovich et al., 1996, Clement and Gordon, 1995]. More scatter in the charted relationship is therefore expected for IES moorings SN56 and SN59, the positions of these moorings relative to T/P groundtracks and topography aside.

4.7 Application of the ETTA Method

4.7.1 Baroclinic Transports

Using paired estimates of anomaly SSH from TOPEX/POSEIDON and η from IES-PIES moorings, pronounced thermohaline anomalies are able to be identified most of the time at five moorings in the southeastern South Atlantic, producing a time-series of water column type definitions at each of the moorings. Now the baroclinic transport of each water column type can be calculated from Eq. 4.8 once surface geostrophic velocity has been determined with Eq. 4.6. For the baroclinic transport, [Garzoli and Gordon, 1996] find $k = 0.4$ for the BEST project data and we use this value.

However, an examination of typical geostrophic velocity profiles of the three water column types under consideration (Fig. 4-23) reveals significantly greater shear (2 to 4 times larger) in the 13 °C stad and Agulhas water columns below 1000 dbar than in the modified Atlantic water column. Not until 1400 dbar does the shear in the anomalous water columns drop to a level comparable to that of the Atlantic water column at 1000 dbar. The regional hydrography also indicates a lot of variability in intermediate water masses. These factors lead us to believe that a reference level of 1400 dbar is appropriate for all the calculations relating to Agulhas and 13 °C stad water columns. This result agrees with the conclusions of Gordon et al. [1987] and McDonagh et al. [1999] who found evidence that the Agulhas introduces intermediate water masses as well as surface and central waters to the region (i.e., water at levels of $\sigma_\theta \leq 27.5$). Therefore a LNM of 1400 dbar is used for Agulhas and 13 °C stad water columns while the LNM of 1000 dbar is retained for modified Atlantic water. This affects the calculation of α (Eq. 4.7). For the BEST hydrography, $\alpha = -35 \pm 1$, $\beta = 12 \pm 3$ for modified Atlantic water to 1000 dbar , $\alpha = -34 \pm 1, \beta = 12 \pm 6$ for Agulhas water to 1400 dbar and $\alpha = -19 \pm 2, \beta = 43 \pm 9$ for 13 °C stad water to 1400 dbar.

Because of the very large spacing between the BEST moorings (263 km - 1453 km) compared to the length scales of the Agulhas and 13 °C stad eddies, nominal length scales (L) are assumed for any meso-scale anomalies detected, using the sizes of eddies determined from the BEST hydrographic data by DuncombeRae et al. [1996] as a measure; Agulhas eddy features averaged 102 km in radius, while 13 °C stad eddies averaged only 29 km in radius. With α, L and the LNM determined, all of the parameters necessary to complete the transport equations are available (Eqs. 4.8 and 4.9, Fig. 4-14).

The initial mean transport through each mooring pair is set to the values given by Garzoli and Gordon [1996] who improved the skill of their calculation by adjusting the estimates of V_g from mooring pairs to values obtained at the mooring locations during the hydrographic cruises. We add one additional step, which is to invoke conservation of mass (volume) to set the time-mean accumulation of mass inside the array volume to zero. Thus one measure of the accuracy of the baroclinic transports is the fluctuation of the transport through the array volume over time; this error ranges between -3 Sv to +4 Sv, with a rms value of 1.2 Sv (Fig. 4-24). Fig. 4-25 shows the time-series of transports between mooring pairs for both the fixed (type-insensitive) and variable (water column type-sensitive) calculations. The directional sense of the transports is illustrated in Fig. 4-26 and statistics for each set of mooring pairs are given in Table 2 (all values rounded to the nearest 1 Sv):

Table 2. ETTA Baroclinic Transports

	Mooring Pairs			The 30°S line	
	59-56	56-62	61-59	61-58	58-62
TOTAL Baroclinic Transport					
mean	5	3	6	4	10
std. dev.	7	4	8	6	5
min.	-16	-7	-13	-10	-3
max.	20	11	29	20	22
Atlantic and modified Atlantic water					
mean	4	3	6	4	9
std. dev.	6	3	7	5	4
min.	-11	-5	-13	-10	-2
max.	20	11	26	14	22
Agulhas eddies					
mean	0	0	1	1	1
std. dev.	2	1	1	2	1
min.	-4	-3	-1	-3	-1
max.	7	3	3	6	5
13 °C stad eddies					
mean	0	0	0	0	0
std. dev.	0	0	0	0	0
min.	-1	0	0	0	0
max.	1	1	0	0	0

The instantaneous baroclinic transport reaches a peak of 29 Sv between moorings SN61 and SN59, which is where it is expected based on the geometry of the region and previously observed paths of eddies and the Benguela current. Transport of the dominant water mass, modified Atlantic water (Fig. 4-27) is found to be for the most part unaffected by corrections to α, which is as it should be. The instantaneous value of the Agulhas water transport reaches at least 3 Sv in each mooring pair considered, but is the largest between moorings SN56 and SN59, reaching almost 7 Sv (Fig. 4-28). Mooring pair SN58 - SN61 is a close second with a maximum Agulhas water transport of 6 Sv. If instead a LNM of 1000 dbar is used for Agulhas water these transports drop to 5 Sv and 4 Sv respectively, suggesting that a significant amount of Agulhas water between 1000 dbar and 1400 dbar is being moved around in the region.

The transport of 13 °C stad water is only observed through the southernmost moorings (SN56 and SN59), possibly indicating a different preferred pathway for these eddies as they propagate into the southeastern south Atlantic. The transport of 13 °C stad water is dominated by a single event; the extremely strong anticyclonic feature that passed over SN56 around day 513 (Fig. 4-29). Its effect on SN56 was an estimated change in transport of more than 4 Sv. As noted above, this mooring was placed < 3 km from the T/P groundtrack, so this event is not likely to be undersampled in the altimeter record compared with its strength in the mooring record. Despite that, a large and consistent discrepancy is apparent between $\mathrm{SSH}_{T/P}$ and η during the duration of this event (Figs. 4-21, 4-22). A similarly strong event earlier in the mooring record had a $\mathrm{SSH}_{T/P}$ amplitude 5 cm higher. Oddly, although the RRS *Discovery* conducting the BEST-2 survey at the time, and soon after the peak of the event (4-6 days) was within 400 km of the mooring location, no eddy was found closer than that – a large, strong Agulhas eddy (B2-4) was present to the SW, but the required translation speeds of 77 km day^{-1} seem to rule out this eddy as the source of the anomaly. By the time the ship reached the mooring, the thermocline had shallowed to just 336 m, the relative dynamic height was negative, and the next measurement of $\mathrm{SSH}_{T/P}$ was also negative. Perhaps a strongly barotropic intrusion from the Agulhas is responsible for these observations; as SN56 was one of the two moorings without BP sensors a strongly barotropic feature could have introduced or exacerbated the difference between the altimeter and the mooring record. Clement and Gordon [1995] have shown that as much as 50% of the total flow in Agulhas eddies is barotropic.

The mass transport of both Agulhas and 13 °C stad water types calculated here is only that from individual and distinct events; it must be remembered that modified

Atlantic water will carry a great deal of additional heat and salt from the Indian Ocean. The work of Gordon et al. [1992] suggests that as well as the mixing we have posited, leakage from the Agulhas into the South Atlantic subtropical gyre occurs regularly. Based on their measurements of chlorofluoromethane-11 and -12 these researchers estimate that 60%-65% of the thermocline water (9 °C - 14 °C) in this region is of Agulhas origin. Garzoli and Gordon [1996] using these same mooring data, estimated that roughly 25% of the water passing through the mooring array at 30°S came from the Indian Ocean. We find the time-averaged baroclinic transport through 30°S is 14.5 Sv, with at least 2 Sv (14%) of that being from distinct Agulhas anomalies. The Agulhas component in modified Atlantic water results in an additional flux of O(3) Sv from the Agulhas Retroflection into the South Atlantic through the array at 30°S, for a total of 5 Sv (36%).

Garzoli et al. [1996] re-analyzed these mooring data using additional information from a suite of deep current meter moorings that were deployed among the IES-PIES array. To reference the baroclinic LNM directly to the deep (barotropic) current measurements, the LNM was moved to 2600 m. Hence we calculated transports using this level as well for comparison. Using this LNM, the time-averaged baroclinic transport through the mooring line at 30°S is 35 Sv, with a total of 12 Sv (36%) being from the Agulhas water via eddies or a mixed water column. The large increase (from 5 Sv to 12 Sv) is offset by the fact that the deep waters ($\sigma_\theta > 27.5$, where $\sigma_\theta = 27.5$ is around 1200 dbar - 1400 dbar) carry only very weak thermohaline anomalies (see Fig. 4-7).

4.7.2 Barotropic Transports

Barotropic transport is only able to be calculated for the 30°S mooring line (SN61 - SN58 and SN58 - SN62), where the PIES moorings were deployed. Barotropic transport variability along 30°S is profiled in Fig. 4-30. For the barotropic transports, anomalous water columns are assumed to extend only to 1400 dbar, as discussed in the previous section. The remainder of the water column below this depth is presumed to be Atlantic at all times. The same anomaly event records used in the baroclinic analysis are employed, the transport divided into water column types, and the results pictured in Fig. 4-31. The transport calculations made here are referenced to the time-mean barotropic transport for this array, 21 Sv to the south, which was determined by Garzoli et al. [1996] using current meter moorings as a reference. Of that, 1 Sv (5%) is Agulhas water and none is 13 °C stad water.

4.7.3 Mass, Heat and Salt Fluxes at 30°S

Barotropic and baroclinic transports are combined to get a measure of the absolute, or total transport. The results will simply be the sum of the transports presented in Sections 4.7.1 and 4.7.2. Of more interest is the total thermohaline anomaly transport across the mooring line at 30°S. A great deal of the literature on the circulation of the South Atlantic concerns estimates of the amount of heat and salt the South Atlantic provides to the thermohaline "conveyor belt", preconditioning the North Atlantic for the formation of NADW [Gordon, 1986]. The South Atlantic thermocline gains heat and salt from the Indian Ocean via the Agulhas Current as part of the warm water route. However, until now the only possibilities for estimating the amount of heat and salt provided by this leg of the warm water route have been deductions from point estimates of the heat and salt contained in eddies and other distinct intrusive events (e.g., van Ballegooyen et al. [1994], Lutjeharms and Cooper [1996] and McDonagh et al. [1999]), which do not supply adequate geographic coverage, and inverse calculations (e.g., Rintoul [1991]), which neglect the time-dependent behavior of the system. The BEST PIES mooring array provides us with the opportunity to monitor at least part of this exchange over a significant period of time. To measure the heat and salt imports through the 30°S line, the equations developed in Section 4.4.3 are employed.

As noted by Garzoli et al. [1996] thermohaline anomalies are probably correlated with transport strength, so the ETTA method is not ideal; it assumes that within each water column type, anomaly strength is fixed regardless of transport strength. The use of continuous parameterizations of k, $k_{\Delta Q}$ and $k_{\Delta \Sigma}$ with SSH and $\delta\tau$ similar to the parameterizations developed by Meinen and Watts [2000] and Watts et al.

[2000] would be an improvement but is outside the scope of this work.

$k_{\Delta Q}$ and $k_{\Delta\Sigma}$ are calculated for each of the three water column types analyzed here. Their typical velocity profiles are pictured in Fig. 4-23. Typical thermohaline anomalies for Agulhas and 13 °C stad water have already been illustrated in Figs. 4-4 and 4-7. Values of $k_{\Delta Q_{BT}}$ (Eq. 4.17) for modified Atlantic, Agulhas and 13 °C stad water are $0.66\pm0.06\times10^6$ J m^{-3}, $1.57\pm0.11\times10^6$ J m^{-3}, and $1.20\pm0.27\times10^6$ J m^{-3}. respectively, while values of $k_{\Delta\Sigma_{BT}}$ (Eq. 4.18) are $3.1\pm0.3\times10^{-2}$ kg (salt) m^{-3}, $8.2\pm0.6\times10^{-2}$ kg (salt) m^{-3} and $8.1\pm2.7\times10^{-2}$ kg (salt) m^{-3}. Baroclinic transport coefficients are not all that different, with values of $k_{\Delta Q_{BC}}$ (Eq. 4.12) for modified Atlantic, Agulhas and 13 °C stad water at $0.78\pm0.05\times10^6$ J m^{-3}, $1.31\pm0.09\times10^6$ J m^{-3}, and $0.94\pm0.20\times10^6$ J m^{-3}. respectively; values of $k_{\Delta\Sigma_{BC}}$ (Eq. 4.13) are $4.3\pm0.3\times10^{-2}$ kg (salt) m^{-3}, $7.5\pm0.5\times10^{-2}$ kg (salt) m^{-3} and $5.7\pm1.0\times10^{-2}$ kg (salt) m^{-3}. Again, 70% of the Atlantic water column carries positive heat and salinity anomalies because ~38% of it has actually been replaced by water from the Agulhas. The error in values of $k_{\Delta Q}$ and $k_{\Delta\Sigma}$ for 13 °C stad water are large (~20%) because of the small number of samples (8) available with which to compute the coefficients. In the modified Atlantic and Agulhas water columns, which are of most interest because these are the only ones observed to be transported through the 30°S mooring line, the errors in the mean values of the thermohaline transport coefficients are 6% - 9%.

For the thermohaline flux calculations the velocities obtained in Sections 4.7.1 and 4.7.2 are used with 2600 dbar as the LNM, following Garzoli et al. [1996]. All of the transport below 1400 dbar is considered to be Atlantic or modified Atlantic water. Table 3 lists statistics of the annual average fluxes of mass, heat and salt (rounded to the nearest whole number):

Table 3. ETTA Total Transports at 30°S

SN	61-58	58-62	61-58	58-62	61-58	58-62
TOTAL Transport **(BC+BT)** (Sv)			**TOTAL Heat** (10^{20} J)		**TOTAL Salt** (10^{12} kg)	
mean	1	13	4	14	21	78
std. dev.	30	29	9	12	47	64
min.	-86	-68	-20	-14	-106	-78
max.	79	99	25	49	141	266
modified Atlantic water						
mean	0	10	2	10	14	58
std. dev.	27	27	6	7	30	40
min.	-80	-68	-14	-10	-69	-54
max.	70	99	16	35	87	185
Agulhas eddies						
mean	1	2	1	3	7	20
std. dev.	4	4	3	4	17	24
min.	-12	-9	-7	-5	-37	-24
max.	12	13	10	14	54	82

4.8 Discussion

As a result of the calculations presented above it is apparent that Indian Ocean is indeed acting as source of heat and salt on the annual time scale, with the greatest proportion of these being transported by modified Atlantic water and the remainder by periodic influxes which are tied to discrete intrusions (for the most part, presumably meso-scale eddies). Based on the averages over the mooring deployment period, geostrophic mass, heat and salt transports across the mooring line at 30°S are 14 Sv, 18x10^{20} J (0.057 PW) and 99x10^{12} kg salt per annum. These figures are on the order of 10 - 20 times the values estimated for individual Agulhas eddies which were measured at various distances from their source (see a summary in McDonagh et al.

[1999], Table 2). At 14 Sv, the volume transport is very close to the 13 Sv found by Garzoli et al.'s, [1996] prior analysis of this mooring array. The Agulhas water column, carried in Agulhas eddies, accounts for 3.2 Sv (23%) of the transport and about 27% of the excess heat and salt. No 13 °C stad water is present at all. We estimate, given the position of the mooring line with respect to eddy activity, that the flow measured here is only a fraction of the total Agulhas-South Atlantic exchange – on the order of one third or less as the location of the 30°S mooring line lies inshore of most of the Agulhas eddy corridor (see Fig. 4-32).

The stability of the calculations presented above can be tested by varying the values of $k_{\Delta\Sigma}$ and $k_{\Delta Q}$ by the amounts given in their respective uncertainties. In these cases, the heat flux through 30°S is within $\pm 1 \times 10^{20}$ J of its value in Table 3 and the salt flux is within $\pm 7 \times 10^{12}$ kg. The effect of the meso-scale eddies in the thermohaline balance can be estimated by assuming that all of the Agulhas eddy transport is replaced by modified Atlantic water. In this case, the heat and salt fluxes drop to O($15\text{x}10^{20}$) J and O($84\text{x}10^{12}$) kg.

The average heat and salt fluxes between moorings SN58 - SN62 reported here may be larger than are characteristic of the location on longer time scales; because of the loss of the BP data in mooring SN62 after day 543, only 260 days of data were available for analysis of the combined baroclinic + barotropic flow between these moorings. In the full record of SN58, the Agulhas water column is present only 38% of the time. But in the first 260 days, that figure jumps to 54%. Hence it is possible that average annual heat and salt fluxes due to Agulhas eddies reported between this mooring pair are O(20%) higher than a longer measurement would indicate. A 20% reduction in Agulhas water reduces the heat and salt fluxes to O($15\text{x}10^{20}$) J and O($83\text{x}10^{12}$) kg salt per annum.

Errors in transport calculations may also effect the thermohaline transport. No integrated, long-term estimate of the uncertainty is available for the BP sensors (as it is for the IESs) but the instrumental accuracy results in a possible error in the instantaneous barotropic transport of $\sim$ 6 - 12 Sv between either of the two the 30°S mooring pairs. However, this type of error is unlikely to be correlated with any of the transports or sustained in a way that would affect the average annual fluxes very much. As mentioned in Section 4.7.1, the rms error in the baroclinic mass transport was estimated at 1.2 Sv and the magnitude of the error is definitely correlated with the presence of thermohaline anomalies passing through the sensor array and will therefore magnify the uncertainty in thermohaline fluxes; propagating it increases uncertainties in the heat and salt transports to O(3×10^{20}) J and O(14×10^{12}) kg salt.

It should also be remembered that the proportion of heat, salt and mass fluxes assigned to the anomalous (Agulhas and 13 °C stad) water column types would be different if the three unidentified features passing the 30°S array (see Table 1) were assigned a water column type. Most probably these features are Agulhas eddies; adding the fluxes due to these undetermined events to the Agulhas portions might raise the amounts transported by Agulhas eddies up to 29% of the mass and 31% of the heat and salt.

Total ETTA heat and salt transports compare favorably with the results of van Ballegooyen et al. [1994] who estimated the annual thermohaline fluxes due to Agulhas eddies at 14x10^{20} J (0.045 PW) and 78x10^{12} kg. The amounts of heat and salt per eddy in van Ballegooyen's et al.'s, [1994] measurements are expected to be larger than those here because theirs were made much closer to the Agulhas Retroflection (see Appendix A). If, in addition to serving as a source for modified Atlantic water, Agulhas eddies are a mechanism for accomplishing the mixing seen to have occurred, this mixing should occur very close to the source of the eddies, where they are the strongest; this implies the *proportion* of heat and salt in the modified Atlantic water column would increase very quickly with distance from the Retroflection. By combining the results presented here with those of van Ballegooyen et al. [1994] we conclude that if measured close to the Agulhas Retroflection, approximately one third to one half of the Agulhas-South Atlantic thermohaline transport would be contained in discrete meso-scale eddies with the remainder in modified Atlantic water; the inter-ocean transports (baroclinic + barotropic) would be O(28 - 42) Sv, O(32 - 50x10^{20}) J (O(0.10 - 0.16) PW) and O(166 - 244x10^{12}) kg salt.

As noted by McDonagh et al. [1999] there may be a return flow elsewhere which is not accounted for in this calculation so the heat and salt transports are not "absolute" but only relative to what may be going on elsewhere. However, using the reasonable assumption that any return flow is going to be colder and fresher, these fluxes can be taken as minimum estimates of the inter-ocean thermohaline transfer.

One shortcoming of the ETTA method as implemented in this work is the use of a fixed value for k ($k = 0.4$ for LNM = 1000 dbar, $k = 0.3$ for LNM = 2600 dbar). From Fig. 4-24 it is apparent that the larger errors in the transport are still strongly correlated with the passage of anomalous water masses through the mooring array. Obviously when such events do occur, the entire vertical structure of the water column changes and thus the k should be allowed to vary as well. During the determination of $k_{\Delta\Sigma}$ and $k_{\Delta Q}$ it was found that for 13 °C stad water, k averaged quite a bit higher than 0.3 or 0.4 – values of 0.6 - 0.9 were more common. Agulhas waters, true to form, were extremely variable, with k ranging from 0.35 to 0.47. Because of the predominance of modified Atlantic water in the time-series and our expectation that k is the most accurate for this water column type, changes in k are not expected to vary the overall fluxes estimates by a great deal.

A smoothly varying parameterization of k, or better yet, a smoothly varying identification of water column composition would be an improvement over the small number of estimated parameters used here. The work of Meinen and Watts [2000] and Watts et al. [2000] suggests that this might be feasible and the possibility is examined in detail in the next Chapter.

Despite the large number of simplifications and assumptions used in this implementation of the ETTA technique, ETTA provided unambiguous identification of eleven (out of seventeen) anomalously stratified meso-scale features and estimates of inter-ocean heat and salt fluxes through 30°S (2°E - 17°E) that appear to be within 16% of the actual values. It seems that the dominance of modified Atlantic water in the heat and salt transports is not subject to question and is in part an indication of how much mixing has already taken place by the time water from the Agulhas Retroflection has reached 30°S. Had all the BEST moorings been placed directly along the altimeter groundtrack in deep water close to the Retroflection and had all of them been equipped with BP sensors it is likely that the Agulhas and 13 °C stad transports would be seen to increase. These improvements await a future experiment. The calculations presented here should be regarded as first-order estimates and a proof-of-concept implementation upon which to base future work.

4.9 Conclusions

In Enhanced Thermohaline Transport Analysis (ETTA), mass and thermohaline fluxes are estimated from time-series of anomaly sea surface height (SSH) and anomaly acoustic travel time ($\delta\tau$). ETTA parameterizes groups of water masses commonly observed in the same water column into water column "types", which are then used to determine empirical mass, heat and salt transport coefficients. Water column type, in turn, is parameterized as an empirical function of SSH and $\delta\tau$ using information from hydrography. The time-varying thermohaline circulation can then be monitored using time-series of $\delta\tau$ and SSH which can be obtained from inverted echo sounder (IES or PIES) moorings and satellite altimetry. A portion of the Indian - South Atlantic Ocean thermohaline exchange is analyzed by applying ETTA to five IES and PIES moorings deployed in 1992 - 1993 as part of the BEST (Benguela Sources and Transports) program.

The hydrography of the southeastern South Atlantic is found to be dominated by three water column types, each of which has a very different thermohaline signature: Atlantic water, a local or background water column typical of the south Atlantic subtropical gyre; "Agulhas water", relatively warm and salty water of the type found at the center of Agulhas eddies; "13 °C stad" water, a water column characterized by the presence of subantarctic mode water (SAMW) from the Indian Ocean which has a thick ($>$ 400 m) isothermal layer near 13 °C. When examined more closely, it is found that approximately 70% of hydrographic stations which are basically Atlantic water have mixed to some extent with Agulhas water; the average amount of replacement due to this mixing is 38%, indicating that overall 26% of the water from the South Atlantic subtropical gyre has been replaced with water from the Agulhas Retroflection.

Bulk (vertically averaged) heat, salt, and transport coefficients are calculated from hydrography for each of the three water column types and the each type is parameterized as a unique (empirical) function of $\delta\tau$ and SSH.

Differences in the thermohaline stratification and mode of thermohaline variability of these water column types determine a unique relationship between $\delta\tau$ and SSH for each one. This concept (explained in detail in Appendix B) is demonstrated by simulating both signals from hydrography and then tested using $\delta\tau$ calculated from the hydrography and sea surface height measured by TOPEX/POSEIDON ($\mathrm{SSH}_{T/P}$). Despite the noise created by the presence of a barotropic component of SSH in the T/P record and by the necessity of interpolating of $\mathrm{SSH}_{T/P}$ to the station locations and times, the method is found to be practicable. Since Agulhas and 13 °C stad waters are relatively warm, the absolute value of $\delta\tau$ helps indicate the presence of these waters, as the acoustic travel times are smaller than those of Atlantic waters.

Seventeen pronounced meso-scale anomalies are observed in the paired IES - T/P records of which eleven are able to be identified – nine as Agulhas and two as 13 °C stad water. Modified Atlantic water, infused with heat and salt from the Indian Ocean, makes up the bulk of the baroclinic transport, accounting for between 70% and 85% of the 14.5 Sv measured at 30°S. 13 °C stad water is only observed at the southernmost two moorings, possibly indicating a different preferred pathway for this water.

For the PIES moorings, information from BP sensors is added to obtain estimates of total (barotropic + baroclinic) transport. The time-mean total transport northward through 30°S is 13.6±1.2Sv, with 12.6 Sv passing between moorings SN58 - SN62. These values agree very well with those obtained by Garzoli and Gordon [1996] who used *in situ* current measurements to reference their calculation.

At the 30°S mooring line, water from the Indian Ocean contained in Agulhas eddies (parameterized as the Agulhas water column type) provided a minimum of O($4\mathrm{x}10^{20}$) J and O($23\mathrm{x}10^{12}$) kg salt annually to the South Atlantic during the course of the mooring deployment and a maximum of O(5×10^{20}) J and O(30×10^{12}) kg salt. The lower numbers are considered more realistic because of the predominance of Agulhas water during the short life of SN62. The Indian ocean component of a mixed Atlantic-Indian water column (modified Atlantic water) provided an additional 10 - 12 x10^{20} J and 60 - 72x10^{12} kg salt for an estimate of $15 \pm 3 \times 10^{20}$ J excess heat and $83 \pm 14 \times 10^{12}$ kg excess salt entering the South Atlantic from the Indian Ocean at this location. These results, combined with those of van Ballegooyen et al. [1994] suggest that the total inter-ocean heat and salt fluxes coming through the Agulhas Retroflection will be two to three times the amounts measured here and that one third to one half of the total fluxes, if measured close to the Agulhas Retroflection, would be contained in Agulhas eddies.

The use of parameterized water column types (and hence parameterized transport profiles and parameterized values of k, $k_{\Delta Q}$ and $k_{\Delta \Sigma}$), while an improvement over previous treatments of IES and PIES data, is a generalization and a shortcoming of this implementation of the idea. The "Gravest Empirical Mode" method developed by Meinen and Watts [2000] and Watts et al. [2000] suggests it might be feasible to extending ETTA to use continuous empirical parameterizations of salinity and temperature based on SSH, $\delta\tau$, and pressure. This possibility will be examined in Chapter 5.

Critical features of an experimental PIES array designed specifically for ETTA include co-locating the mooring array directly along an altimeter groundtrack and in deep water, to minimize uncertainties in the $\delta\tau$ - SSH parameterizations, with the moorings close enough to the source of the inter-ocean exchange (in this case, the Agulhas Retroflection) that mixing has little chance to occur, and with the moorings close enough to each other that features of interest cannot slip undetected through the array (in this case O(80) km). Placement of a suite of PIES moorings directly along an altimeter groundtrack would also allow use of the altimetry to monitor events along the array, meaning that measured and not assumed spatial scales of anomaly events could be used in the transport calculations. With such improvements, more accurate and precise water mass and thermohaline transports could be obtained from

ETTA, even in its current implementation.

Ten to twelve PIES moorings deployed along T/P groundtrack 235 would cover the area in which Agulhas and 13 °C stad eddies have been observed by both *in situ* instruments such as ship-based observations and the BEST moored array, and almost the entire span of westward-bound eddies tracked with altimetry by Gordon and Haxby [1990], Byrne et al. [1995] and Witter and Gordon [1999] (Fig. 4-32). With such an array and the improvements to ETTA mentioned above, accurate monitoring of inter-ocean mass and thermohaline transports could become a reality.

Acknowledgments. I would like to thank my advisor Arnold Gordon for his continued support of and enthusiasm for my work. Victor Zlotnicki hosted me at JPL and gave me the opportunity to learn the basics of T/P altimetry; any shortcomings in my treatment of those data are my own fault entirely. Thanks are due Silvia Garzoli for clear and concise explanations of her prior analyses of the mooring data. Donna Witter proffered timely advice and criticism at several points, provided me with her T/P-derived eddy tracks, and reviewed this manuscript. This work was supported in part by a National Aeronautics and Space Administration (NASA) Global Change Fellowship.

Appendix A: Salinity and Temperature anomaly computations

The total temperature and salinity anomalies (ΔQ and $\Delta\Sigma$, following DuncombeRae et al. [1996]) brought into the Atlantic by the eddies surveyed during BEST were evaluated using the following scheme (after Joyce et al. [1981] and van Ballegooyen et al. [1994]):

$$\Delta Q = \int_0^{2\pi} \int_0^R \rho_i C_p h_i [T_{\sigma_{\theta i}}(r) - T_{\sigma_{\theta i}}(ref)] r dr d\theta \qquad (4.21)$$

$$\Delta\Sigma = \int_0^{2\pi} \int_0^R 0.001 \rho_i h_i [S_{\sigma_{\theta i}}(r) - S_{\sigma_{\theta i}}(ref)] r dr d\theta \qquad (4.22)$$

The total anomalies are listed in Table 1A. (from Tables 1 and 2, DuncombeRae et al. [1996]); for comparison, we have also included the four eddies evaluated by van Ballegooyen et al. [1994], (cf Table 2). Distance is computed from the Retroflection, assumed to be located at 40°S, 20°E (cf Lutjeharms and van Balleygooyen [1988]):

Table 1A

Eddy	$\Delta Q, 10^{20}$J	$\Delta\Sigma, 10^{12}$kg	Distance (km)
B1-1	0.19	1.21	502
B3-1	0.60	3.88	901
B2-2	0.57	3.80	1536
A6	1.06	4.59	343
A4	2.36	13.10	511
A5	0.73	4.35	520
A3	1.50	8.74	963

Because of the dominance of surface and thermocline waters within the trapped eddy volume (see McCartney and Woodgate-Jones [1991], van Ballegooyen et al. [1994], Byrne et al. [1995]) and the greater heterogeneity of these waters compared with intermediate water, the anomaly calculations are not terribly sensitive to reference level as long as it is kept below the thermocline (example, $\sigma_\theta = 27.2 - 27.5$). They are however, very sensitive to the choice of reference profile.

The heat content of an Agulhas eddy can be expected to depend on the eddy's size, and to decline with increasing age (distance) from its origin due to large losses to the atmosphere [Lutjeharms and Gordon, 1987, DuncombeRae et al., 1989, Olson et al., 1992]. The salinity anomaly can also be expected to decrease with decrease in trapping radius [Flierl, 1981, McCartney and Woodgate-Jones, 1991] as the eddy spins down. The actual interocean transports of heat and salt are presumably closer to the values found in eddies found closer to the Retroflection, but on the other hand, is all that water truly transported into the South Atlantic subtropical gyre? Perhaps the eddies lying further from the source region and closer to the gyre are actually more accurate indicators of the effective interocean transport carried out by Agulhas eddies. This kind of uncertainty underscores the difficulty in obtaining accurate estimates of interocean thermohaline transports by measurements of individual eddies encountered in a variety of locations.

Appendix B: Acoustic Travel Time and Sea Surface Height

Because SSH and acoustic travel time have heretofore been considered quantities that should empirically correlate to some degree, it is worthwhile to consider conditions under which they may not. In the following, five simulations of the relationship between anomaly acoustic travel time ($\delta\tau$) and the baroclinic expression of anomaly SSH (η_{BC}) are compared. The thickness and mean temperature (θ) and salinity (S) of each isopycnal layer are held constant over the first three simulations. The depth and value of each isopycnal is pictured in Fig. 4-33a. Figs. 4-34a, b and c show the three families of θ, S curves that comprise these simulations. Each simulation expresses variability in the water column in a slightly different way; they were chosen because they represent simple models of observed thermohaline variability. In the first three simulations, the constant depths and values of the isopycnals mean that any changes in η_{BC} are due changes in the compressibility of seawater with θ and S. In the following two, the temperature and salinity of the water column do not change, but the thickness of the isopycnal layers does. In all five simulations, the total amount of mass in the water column remains constant.

Simulation 1: Deep, intermediate, central and surface temperatures and salinities vary in concert, increasing and decreasing together throughout the whole water column. The mean change between beginning and ending profiles is about 0.9 °C and 0.17 psu (Fig. 4-34a). This type of variability produces ranges η_{BC} and $\delta\tau$ that are the largest of the first three simulations (Fig. 4-35b).

Simulation 2: Temperatures and salinities again vary in concert along each isopycnal. However in this simulation, an increase in deep and intermediate temperatures and salinities is accompanied by a decrease in central and surface values. The point at which there is negligible variability is approximately 34.5 psu and 6.5 °C, at $\sigma_\theta = 27.07$ (Fig. 4-34b). Variability in the upper layer partially compensates for that in the lower, so the changes in mean temperature and salinity in the water column remain small: 0.1 °C and -0.03 psu – limiting the range of $\delta\tau$ and η_{BC} to less than 2 ms and 30 mm (Fig. 4-35b).

Simulation 3: Temperatures and salinities at densities less than $\sigma_\theta = 27.1$ ($<$ 700m) are identical to those in the first simulation. As σ_θ increases from 27.1 to 27.2, variability within the simulation decreases; there is no variability in either θ or S at $\sigma_\theta > 27.2$, producing homogeneous intermediate and deep waters (Fig. 4-34c). This produces mean changes in θ and S of 0.5 °C and 0.12 psu and consequently a range in η_{BC} and $\delta\tau$ smaller than in the first simulation but larger than the second (Fig. 4-35b). The entire thermohaline range of each of the first three simulations is parameterized as a function of $\delta\tau$ and pressure (p) in Figs. 4-34d,e,f,g,h, and i.

Simulation 4: In this simulation, the $\theta - S$ profile is held constant to the coldest and freshest profile in Simulation 1 while the $\sigma_\theta = 26.75$ isopycnal is depressed from 400 dbar to 575 dbar. This creates an increasingly thick layer of water at 9.6 °C, 34.67 psu; the thickness of the deep water ($\sigma_\theta > 27.75$) is progressively decreased to compensate so that the depth of the 28.0 isopycnal is unperturbed. Changes in the isopycnal depths are pictured in Fig. 4-33b. This simulation produces a range in η_{BC} quite a bit larger than in any of the first three, since extra mass at the surface is required to balance the the changes in the water column; in Simulation 4 η_{BC} reaches $\pm$75 mm (pictured in Fig. 4-35a).

Simulation 5: This final simulation is very similar to the previous one. θ and S are again held constant. In this case, however, it is the $\sigma_\theta = 25.75$ isopycnal which is depressed, creating an increasingly thick layer of water at 16.9 °C, 35.28 psu. Again the thickness of the deep water layer is decreased to compensate. This simulation produces the largest range of all in both $\delta\tau$ and η_{BC}, -8ms - 3 ms, and $\pm$ 270 mm; values which are realistic for the Agulhas Retroflection region. While it might be thought that the solution in for this simulation would be similar in some way to Simulation 4 this is not the case. First of all the range of the solution is larger because the thick layer of 16.9 °C water produces more variability in both η_{BC} and $\delta\tau$. Nor are the slopes of the solutions to Simulations 4 and 5 the same; nonlinearities in the equations for density and acoustic velocity with p produce slightly dissimilar slopes in the solutions (Fig. 4-35a).

Any type of thermohaline variability, even the simplest, such as a uniform increase in temperature at all depths, will produce a unique line in η_{BC}-$\delta\tau$ space. However, all possible uniform increases (decreases) in one parameter (S, θ, or p) of a θ-S-p curve will fall along a single line in η_{BC}-$\delta\tau$ space. Furthermore, while it is the case that within each of the first three simulations S and θ are both changing at once along isopycnal surfaces, this is *still* not sufficient to produce anything other than a single curve for each; what *does* cause the curves Fig. 4-35 to differentiate is the fact that the structure of the thermohaline variability is different in each simulation.

In each of the five simulations, the coordinated thermohaline variability determines a unique surface of integrated acoustic travel time and relative sea level (the surface expression of which is η_{BC}) defined at each p-S-θ point. The solution for the first simulation is illustrated in Fig. 4-36a, while several simulations together are pictured in Fig. 4-36b. The expression of each solution at surface pressure is the information displayed in Figs. 4-35a and b. In contrast to these surfaces, random variability in θ-S-p produces not a smooth surface, but a relatively uncorrelated locus of points.

Observations indicate that the deep ocean, far from shore, tends to exhibit coordinated variability not unlike the types simulated here (e.g., Levitus and Boyer [1994], Levitus et al [1994]). The pattern of this variability is a reflection of the effects of regional forcing on the initial thermohaline structure. The types of variability presented in these simulations are simplifications of what might be found in different regions of the world ocean; at inter-ocean connections such as the Agulhas Retroflection, the different regional modes of variability will co-exist, which may produce solutions like those in Fig. 4-35.

Bibliography

van Ballegooyen, R.C., M.L. Gründlingh and J.R.E. Lutjeharms, Eddy fluxes of heat and salt from the southwest Indian Ocean into the southeast Atlantic Ocean: a case study, *J. Geophys. Res., 99*, 14,053-14,070, 1994.

Benada, J.R., Physical Oceanography Distributed Active Archive Center Merged GDR (TOPEX/POSEIDON), Generation B, User's Handbook, Version 2.0., Physical Oceanography Distributed Active Archive Center Publication Number D-11007, http://podaac.jpl.nasa.gov/cdrom/mgdr-b/Document/HTML/usr_toc.htm, 1997.

Beismann, J.-O., R. H. Käse, and J.R.E. Lutjeharms. On the influence of submarine ridges on translation and stability of Agulhas rings. *J. Geophys. Res., 104*, 7897-7906, 1999.

Belinne, J., P. Mele and B. Huber. CTD and Hydrographic data from the BEST 2 cruise, 1993, Lamont-Doherty Data Report 96-1, 1996.

Bennett, S.L., Where three oceans meet: the Agulhas retroflection region, Ph. D. thesis, 367 pp., Massachusetts Institute of Technology/Woods Hole Oceanographic Institute Joint Program, 1988.

Boudra, D.B. and E.P. Chassignet, Dynamics of Agulhas retroflection and ring formation in a numerical model. I. The vorticity balance, *J. Phys. Oc., 18*, 280-303, 1988.

Byrne, D.A., A.L Gordon and W.F. Haxby. Agulhas eddies: A Synoptic view using Geosat ERM Data, *J. Phys. Oc, 25*, 902-917, 1995.

Clement, A.C. and A.L. Gordon, The absolute velocity field of Agulhas eddies and the Benguela Current. *J. Geophys. Res., 100*, 22,591-22,601, 1995.

Chassignet, E.P. and D.B. Boudra, Dynamics of Agulhas retroflection and ring formation in a numerical model. II. Energetics and ring formation, *J. Phys. Oc., 18*, 304-319, 1988.

Chelton,D.B. and M.G. Schlax, The resolution capability of an irregularly sampled data set: with application to GEOSAT altimeter data, *J. Atmos. Oceanic Technol. 11*, 534-550, 1994.

Cresswell, G.R., Physical evolution of Tasman Sea Eddy J, *Austral. J. Mar. and Fresh. Res., 34*, 495-513, 1983.

Defant, A., Physical Oceanography, v. 1, 729 p., MacMillan, New York, 1961.

Duncombe Rae, C. M., Agulhas Retroflection Rings in the South Atlantic Ocean: An Overview, *S. Afr. J. mar. Sci., 11*, 327-344, 1991.

Duncombe Rae, C.M., S.L. Garzoli and A.L. Gordon, The eddy field of the southeast Atlantic ocean: a statistical census from the Benguela Sources and Transports Project, *J. Geophys. Res., 101*, 11,949-11,964, 1996.

Duncombe Rae, C.M., F.A. Shillington, J.J. Agenbag, J. Taunton-Clark and M.L. Gründlingh, An Agulhas ring in the South Atlantic Ocean and its interaction with the Benguela upwelling frontal system *Deep-Sea Res., 39*, 2009-2027, 1992.

Duncombe Rae, C.M., L.V. Shannon and F.A. Shillington. An Agulhas ring in the South Atlantic Ocean, *S. Afr. J. Mar Sci., 85*, 747-748, 1989.

Feron, R.C., W.P.M. de Ruijter and D. Oskam, Ring shedding in the Agulhas Current system, *J. Geophys. Res., 97*, 9467-9477, 1992.

Flierl, G.R., Particle motions in large-amplitude wave fields, *Geophys. Astrophys. Fluid Dyn., 18*, 39-74, 1981.

Garzoli, S. and A. Bianchi, Time-space variability of the local dynamics of the Brazil-Malvinas Confluence as revealed by inverted echo sounders. *J. Geophys. Res., 92*, 1914-1922, 1987.

Garzoli, S. and Z. Garraffo, Transports, frontal motions and eddies at the Brazil-Malvinas Confluence, *Deep-Sea Res., 36*, Part A, 681-703, 1989.

Garzoli, S., M. Maccio, A. Martino and M. Colwell, BEST IES Data Report: 1992-1994. *LDEO-94-1*, Lamont-Doherty Earth Obs., Columbia Univ., Palisades, New York, 1994.

Garzoli, S.L. and A.L. Gordon, Origins and variability of the Benguela Current, *J. Geophys. Res., 101*, 897-906, 1996.

Garzoli, S.L., A.L. Gordon, V. Kamenkovich, D. Pillsbury and C.M. Duncombe Rae, Variability and sources in the southeastern Atlantic circulation. *J. Mar. Res., 54*, 1039-1071, 1996.

Goni, G.J. S.L. Garzoli, A.J. Roubicek, D.B. Olson and O.B. Brown, Agulhas ring dynamics from TOPEX/POSEIDON altimeter data, *J. Mar. Res., 55*, 861-883, 1997.

Gordon, A.L., Interocean exchange of thermocline water, *J. Geophys. Res.*, 91, 5037-5046, 1986.

Gordon, A.L., Indian-Atlantic transfer of thermocline water at the Agulhas Retroflection, *Science, 227*, 1030-1033, 1985.

Gordon, A.L. and W.F. Haxby, Agulhas eddies invade the South Atlantic: evidence from Geosat Altimeter and shipboard Conductivity-Temperature-Depth survey, *J. Geophys. Res., 95*, 3117-3125, 1990.

Gordon, A.L., J.R.E. Lutjeharms and M.L. Gründlingh, Stratification and circulation at the Agulhas Retroflection, Deep-Sea Res., 34, 565-599, 1987.

Gordon, A.L., R.F. Weiss, W.M. Smethie and M.J. Warner, Thermocline and intermediate water communication between the South Atlantic and Indian Oceans, *J. Geophys. Res., 97*, 7223-7240, 1992.

Gründlingh, M.L., The occurrence of Red Sea Water in the southwestern Indian Ocean, *J. Phys. Oc., 14*, 207-212, 1985.

He, Y., Determining the baroclinic geostrophic velocity structure with inverted echosounders, M. Sc., thesis. 135 pp., Univ. of R.I., Narragansett, Rhode Island, 1993.

Joyce, T. M., S. L. Patterson and R. C. Millard, Jr., Anatomy of a cyclonic ring in the Drake Passage. *Deep-Sea Res 28A*, 1265-1287, 1981.

Kamenkovich, V.M., Y.P Leonov, D.A. Nechaev, D.A. Byrne and A.L. Gordon, On the influence of bottom topography on the Agulhas eddy, *J. Phys. Oc., 26*, 892-912, 1996.

Katz, E.J., A. Busalacchi, M. Bushnell, F. Gonzalez, L. Gourdeau, M. McPhaden and J. Picaut, A comparison of coincidental times series of the ocean surface height by satellite altimeter, mooring and inverted echo sounder, *J. Geophys. Res., 100*, 25101-25108, 1995.

Levitus, S., R. Burgett and T.P. Boyer, World Ocean Atlas 1994, Volume 3: Salinity. NOAA Atlas NESDIS 3. U.S. Department of Commerce, Washington, D.C. 99 pp., 1994.

Levitus, S. and T.P. Boyer, World Ocean Atlas 1994, Volume 4: Temperature. NOAA Atlas NESDIS 4. U.S. Department of Commerce, Washington, D.C. 117 pp., 1994.

Lutjeharms, J.R.E. and J. Cooper, Interbasin leakage through Agulhas Current filaments, . *Deep-Sea Res, 43*, Part I, 213-238, 1996.

Lutjeharms, J.R.E and R.C. van Ballegooyen, The Retroflection of the Agulhas Current, *J. Phys. Oc., 18*, 1570-1583, 1988.

Lutjeharms, J.R.E. and A.L. Gordon, Shedding of an Agulhas ring observed at sea, . *Nature, 325*, 138-140, 1987.

Lutjeharms, J.R.E., and P.L. Stockton, Kinematics of the upwelling front off southern Africa, *S. Afr. J. Mar. Sci., 5*, 35-49, 1987.

Lutjeharms, J.R.E. and H.R. Valentine, Eddies at the subtropical convergence south of Africa. *J. Phys. Oc., 18*, 761-774, 1988.

Lutjeharms, J.R.E. and H.R. Valentine, Water types and volumetric considerations of the south-east Atlantic upwelling regime. *S. Afr. J. Mar. Sci., 5*, 63-71, 1987.

McCartney, M.S., Subantarctic Mode Water, in *A Voyage of Discovery, George Deacon 70th Anniversary Volume.* Edited by M. Angel, Pergamon, New York, 103-119, 1977.

McCartney, M. S. and M. E. Woodgate-Jones, A deep-reaching anticyclonic eddy in the subtropical gyre of the eastern South Atlantic, *Deep-Sea Research, 38*, S411-S443, 1991.

McDonagh, E.L. and K.J. Heywood, The origin of an Anomalous Ring in the Southeast Atlantic. *J. Phys. Oc., 29*, 2050-2064, 1999.

McDonagh, E.L. K.J. Heywood, and M.P. Meredith, On the structure, paths, and fluxes associated with Agulhas rings. *J Geophys. Res., 104*, 21,007-21,020, 1999.

Meinen, C. S. and D. R. Watts, Vertical structure and transport on a transect across the North Atlantic Current near 42°N, *J. Geophys. Res.*, submitted, 2000.

Olson, D.B. and R.H. Evans. Rings of the Agulhas Current. *Deep-Sea Res., 33*, 27-42, 1986.

Olson, D.B. R. Fine and A.L. Gordon, Convective modification of water masses in the Agulhas, *Deep-Sea Res., 39*, suppl. 1, S163-S181, 1992.

Ou, H.W. and W.P.M. de Ruijter, Separation of an inertial boundary current from a curved coastline, *J. Phys. Oc., 16*, 280-289, 1986.

Rintoul, S.R., South Atlantic interbasin exchange, *J. Geophys. Res., 96*, 2675-2692, 1991.

Shannon, L.V., Hydrology off the south and west coasts of South Africa, *Invest. Rep. Div. Sea Fish. S. Afr, 58*, 22 pp., 1966.

Shannon, L.V., J.J. Agenbag, N.D. Walker and J.R.E. Lutjeharms, A major perturbation in the Agulhas retroflection area in 1986. *Deep-Sea Res., 37*, 493-512, 1990.

Shannon, L.V. and D. Hunter, Notes on Antarctic Intermediate Water around southern Africa, *S. Afr. J. Mar. Sci., 6*, 107-117, 1988.

Shannon, L.V., J.R.E. Lutjeharms and J.J. Agenbag, Episodic input of Subantarctic water into the Benguela region, *S. Afr. J. Sci., 85*, 317-322, 1989.

Smythe-Wright, D., A.L. Gordon, P. Chapman and M.S. Jones, CFC-113 shows a Brazil eddy cross the South Atlantic to the Agulhas Retroflection area. *J. Geophys. Res., 101*, 885-895, 1996.

Stander, G.H., The Benguela Current off South West Africa, *Invest. Rep. mar. Res. Lab. S.W. Afr., 12*, 43pp, 1964.

Stramma, L., Geostrophic transport of the South Equatorial Current in the Atlantic, *J. Mar. Res., 49*, 281-294, 1991.

Stramma, L. and R.G. Peterson, The South Atlantic Current, *J. Phys. Oc., 20*, 846-859, 1990.

Stramma, L. and R.G. Peterson, Geostrophic transport in the Benguela Current region, *J. Phys. Oc., 19*, 1440-1448, 1989.

Valentine, H.R., J.R.E. Lutjeharms and G.B. Brundrit, The water masses and volumetry of the southern Agulhas Current region, *Deep-Sea Res., 40*, 1285-1305, 1993.

Walker, N.D. and R.D. Mey, Ocean/Atmosphere heat fluxes within the Agulhas Retroflection region, *J. Geophys. Res., 93*, 15,473-15,483, 1988.

Watts, D.R., and D.B. Olson, Gulf stream ring coalescence with the Gulf Stream off Cape Hatteras, *Science, 202*, 971-972, 1978.

Watts, D.R, C. Sun and S. Rintoul, Gravest Empirical Modes determined from hydrographic observations in the Subantarctic Front, *J. Geophys. Res.*, submitted, 2000.

Witter, D.L and A.L. Gordon. Interannual variability of South Atlantic circulation from four years of TOPEX/POSEIDON satellite altimeter observations. *J. Geophys. Res., 104*, 20,927-20,948, 1999.

Zlotnicki, V. L.-L. Fu and W. Patzert, Seasonal variability in global sea level observed with Geosat altimetry, *J. Geophys. Res., 94*, 17,959-17,970, 1989.

Figure 4-1. The difference between the *in situ* record of bottom pressure and CSR 3.0 (in black) compared with the lowpass-filtered version of bottom pressure (in white) at the locations of the BEST PIES moorings. Aside from a few spikes, agreement between the two is strong (see Chapter 3 for quantification). The higher-frequency tidal variability of the continental slope, not modeled in CSR3.0, is visible in the record of PIES 62.

Figure 4-2. Sample tide model correction applied to $\mathrm{SSH}_{T/P}$ based on the difference between the CSR 3.0 model tide and the tide derived from *in situ* measurements.

Figure 4-3. θ-S diagram of the BEST hydrography. In the background (in black) is the full BEST hydrography. In the foreground (in gray) is the subset of the BEST hydrographic stations selected for their lack of intrusive water masses, the Atlantic water column. The great variability of of surface, central (thermocline) and intermediate water properties column in the southeastern south Atlantic is striking.

Figure 4-4. Profiles of potential temperature (on the left) and salinity (on the right) with depth taken at the centers of two Agulhas and one 13 °C stad eddy, showing the extreme mode water of the 13 °C stad water compared with the more typical and warmer Agulhas STMW. A remnant halostad at $\sim$400 m in the Agulhas eddies suggests that the 13 °C stad water reaches the southeastern south Atlantic by being injected into the Agulhas Current. The large differences in the STMW seen here indicates the atmospheric forcing in the Agulhas region is both intense and highly localized.

Figure 4-5. $\theta - S$ diagram of the eddies pictured in Fig. 4-4. Extremely fresh AAIW in the 13°C stad eddy indicates that this intermediate water has a source different from that of the Agulhas eddies; Agulhas eddy B1-1, surveyed close to the Retroflection, shows a remnant of highly saline RSW (see text) in its intermediate water layer, while Agulhas eddy B2-2, 900 km further away, has an AAIW layer that is not differentiable from that of the 'background', Atlantic water. The water in 13 °C stad eddy B3-1 appears to have undergone much more intense evaporation and/or cooling than that of the Agulhas eddies.

Figure 4-6. Locations of the hydrographic stations used in Figs. 4-4, 4-5, and 4-7. The choice of reference station is critical to obtaining accurate estimates of thermohaline anomalies. It must be far from the sources of thermohaline variability or at least isolated from them, yet close enough to be recognizable as the 'host' water column type.

Figure 4-7. Thermohaline anomalies on potential density surfaces. Profiles of thermohaline anomalies for the stations pictured in Figs. 4-4 and 4-5 plotted on density-neutral surfaces. The differences in the depths of the maximum anomalies in the Agulhas eddies (B1-1 and B2-2) and the 13 °C stad eddy (B3-1) and in the composition of their intermediate water is immediately noticeable.

Figure 4-8. Average near-surface temperature and salinity for all stations occupied during the BEST program. The evaporation that has taken place in the surface of the stations containing significant amounts of 13°C stad water is readily apparent. Many of the Agulhas stations also show evidence of having undergone cooling and evaporation; interestingly, others are anomalously fresh, probably containing SASW.

Figure 4-9. Water column categorizations of the BEST hydrographic stations. Groundtracks of the TOPEX/POSEIDON satellite are overprinted in dotted black lines. Bathymetry, contoured at 1000 m intervals, shows the location of the continental shelf and the Walvis ridge. The scattering of water column types (associations of water masses) with different source regions and properties shows the positions of several eddies encountered during these cruises and also illustrates the complex hydrography of the region.

Figure 4-10. Estimated values of $\delta\tau$ and η_{BC} calculated from the BEST hydrography. Typically in the development of such a linear regression (used to convert $\delta\tau$ to surface dynamic height) outlying points are discarded. From this figure it is clear that the points which would have been discarded (with values $> 1\sigma$ from the regression) are not simply outliers but rather a collection of stations which lie along a completely different slope in $\delta\tau - \eta$ space.

Figure 4-11. The mean temperature of the upper 300 m is plotted against the depth of the 10° isotherm. The non-linearity of the distribution shows why a linear model of the stratification fails at times in this region.

Figure 4-12. A schematic of two possible scenarios occurring at a satellite-sensed sea surface maximum in the southeastern south Atlantic ocean. Anticyclonic eddies with different thermohaline anomalies underlie the altimeter. At the center of each eddy, an inverted echo sounder return will be 3 - 4 ms different, leading to a $\sim$10 cm difference in the sea surface heights estimated from the mooring alone. The satellite, meanwhile, may report an intermediate value.

Figure 4-13. Amount of mixing that has occurred in the modified Atlantic water column. Approximately 70% of the Atlantic stations showed this type of modification. The isopycnal mixing between the Atlantic reference station and an Agulhas source needed to produce each of 49 modified Atlantic stations was calculated at 18 isopycnal depths. Separate salinity and temperature equations provided independent estimates of the source fractions for each type of water. The error of the mean at each level is included.

Figure 4-14 A schematic of the transport model used in our calculations. When an anomalous water column above one of the PIES moorings is detected in the SSH-$\delta\tau$ fields, that anomaly is traced forward and backward in the mooring time-series. From the beginning of its detection until the end, a rectangular portion of the cross-sectional area between the moorings is labeled with the anomalous water mass (e.g., Agulhas) and the total transport measured between the mooring pair is divided proportionally. The depth of the anomaly is assumed to extend up to 1400 dbar – any water column below that is considered to remain Atlantic – and the width is assumed to be one of the eddy length scales determined from the BEST hydrography (see Section 4.4.1).

Figure 4-15. Locations of hydrographic stations used in the comparison of $\delta\tau$ with $\text{SSH}_{T/P}$ (in black), plotted over the entire set available (in gray). 26 CTD and 83 XBT stations fit the selection criteria (see Section 4.5).

Figure 4-16. Hydrographic estimates of $\delta\tau$ (from the stations in Fig. 4-15) with $\text{SSH}_{T/P}$. CTD stations are indicated by the heavier symbols, XBT measurements by the lighter ones. At the the CTD stations, η_{BC} was calculated directly from the station data; at the XBT stations, it was estimated using thermocline depth (Z_{10}). Because of the spatial and temporal mismatches in the data, and the addition of the barotropic component in $\text{SSH}_{T/P}$ there is much more scatter visible than in Fig. 4-10. The slope of the $\text{SSH}_{T/P}$-$\delta\tau$ relation has also been plotted for each water column type; these were calculated using CTD data alone.

Figure 4-17. Along-track profiles of $\text{SSH}_{T/P}$ across Eddy B2-3 showing the reduction in feature resolution and maximum amplitude that Loess filtering produces.

Figure 4-18. Thermohaline properties at the center of Agulhas eddies B2-0 (in red) and B2-2 (in blue) and for comparison, the center of 13 °C stad eddy B3-1 (in black), which was located over 370 km away to the SSE. A remnant 13°C stad (at around 35.18 psu, lower arrow) is visible in the Agulhas eddies, in addition to the warmer STMW more typically characteristic of them (upper arrow).

Figure 4-19. Time series from four of the IES moorings. These records have been detided, but not yet lowpass filtered for comparison with SSH from the T/P altimeter.

At its maximum extent, each meso-scale event identified in Table 1 is marked by a vertical line. TOPEX/POSEIDON cycle number is indicated on the upper axis, and time in days on the lower.

Figure 4-20. Bottom pressure and inverted echo sounder measurements from PIES moorings are combined to yield estimates of total (baroclinic + barotropic) sea surface height.

Figure 4-21, a,b,c,d, and e. Data from IES and PIES records has been lowpass filtered, converted to estimates of η, and subsampled at coincident TOPEX/POSEIDON (T/P) overflight times. A BP-based tide model correction has been applied to the $\text{SSH}_{T/P}$ series over the PIES moorings. Thick lines indicate the subsampled mooring and T/P records used in the ETTA parameterization (blue for T/P, black for the mooring component); thin lines indicate the lowpass filtered mooring records. Distances between the moorings and the T/P groundtrack vary widely, from < 2 km to > 75 km. An 8-day lag has been added to the data from SN58 to offset the differences introduced by this distance ($\sim$76 km).

Figure 4-22a,b. a) (top) Each data point in black was created by taking paired estimates of $\delta\tau$ (from mooring data) and $\text{SSH}_{T/P}$ at the maximum extent of the meso-scale events listed in Table 1 and is labeled with sensor number and date from the table. Labels in boldface type indicate PIES data, and those in plain type, IES data. The identities of most of the anomalous meso-scale events (11 of 17) have been able to determined. These data are plotted over the data from Fig. 4-16 to show the relative distributions of the datasets. The relative position, combined with the error estimate for each data point was used to identify the water column type of the event. b) (bottom) The same mooring-altimeter data pairs shown in part a). Error bars indicate cumulative uncertainty from sources such as the CSR 3.0 tide model, correlated variability in $\delta\tau$ below the chosen LNM, and uncertainty introduced by lack of a BP sensor (SN56 and SN59). Sources of error and their magnitudes are discussed in detail in the text.

Figure 4-23 Typical (baroclinic) geostrophic velocity profiles of the water column types found in the study region. The much larger shear in the Agulhas and 13 °C stad water columns at 1000 dbar led to an increase in the LNM used for these water column types. The strong velocity peak of the 13 °C stad water at approximately 300 dbar was also noted by McDonagh and Heywood, [1999] in their 13 °C stad eddy, Ring 1.

Figure 4-24. A measure of the change in mass in the fixed volume formed by the IES mooring array, indicative of the error level in the transport calculations. The times when eddies are present in the array are the times at which the magnitude of the error is largest; the lack of BP sensors in the southern array, changes in the vertical structure of geostrophic velocity, and fluctuations in the real LNM are likely causes.

Figure 4-25. Geostrophic transport in the upper 1000 dbar calculated using both fixed (thin line) and variable (thick line) values for α, the empirical constant of proportionality used to convert $\delta\tau$ to η.

Figure 4-26. Map of the paired mooring transects for which geostrophic transport is calculated. The heavy arrows indicate the direction in which the transport is taken to be positive.

Figure 4-27. Transport of Atlantic water (thick line) measured using ETTA, versus total transport (thin line). The transport of Atlantic water is significantly reduced during times when anomalous meso-scale features are passing through the mooring array.

Figure 4-28. Transport of Agulhas water (water containing STMW from the Indian Ocean) through the mooring array. This calculation uses an assumed spatial scale factor, L, for the Agulhas water based on observed length scales of Agulhas eddies. Here L is 102 km, while Δx, the distance between moorings, is anywhere from 497 km to 1218 km.

Figure 4-29. Transport of 13 °C stad water through the mooring array. 13 °C water was only detected at SN56 and SN59, the southernmost moorings. This calculation uses an assumed spatial scale factor, L, for the 13 °C stad water based on observed length scales of 13 °C stad eddies. Here L is 29 km, while Δx, the distance between moorings, is anywhere from 497 km to 1218 km.

Figure 4-30 Barotropic transport through the mooring array at 30°S. Large excursions in the BP signal at SN58 account for the nearly opposing transports which to a large extent cancel each other.

Figure 4-31 Barotropic transports of different water column types through the moored array at 30°S. The same spatial scaling factor described in Figs. 4-28 and 4-29 was used.

Figure 4-32. The southeastern south Atlantic. Bathymetry is contoured at 1000 m intervals. Proposed mooring locations (~75 km apart) are plotted in black squares, over the groundtracks of the TOPEX/POSEIDON and JASON satellite altimeters (black lines) and the Agulhas eddy "corridor" (light gray shading). For reference, the locations of the BEST moorings (1992 - 1993) have been included (dark gray circles).

Figure 4-33. Depths of the isopycnal levels at which the simulations are defined. Although for completeness, θ and S were defined down to ~3200 dbar, the reference level used in the simulations was 2000 dbar as the allowable variability below that was negligible. a) (top) Crosses indicate the depths of the isopycnals in the first three simulations. b) (bottom) Lines shows the depths of the same isopycnals for representative members of the fourth simulation.

Figure 4-34a, b, c, d, e, f, g, h, i. a), b) and c) (top row) Representative profiles, 5 of 50, of temperature (θ) and salinity (S) for Simulations 1, 2, and 3. a) (top left) In the smoothly varying case, both θ and S change along isopycnals, stepping evenly from an initial colder/fresher condition to a final warmer/saltier one. b) (top center) In the compensated case decreases (increases) in in the temperature and salinity of intermediate and deep waters are partially offset by increases (decreases) in those of surface and central waters. c) (top right) In this case, S and θ are held constant below $\sigma_\theta = 27.2$ ($\sim$ 1200 dbar) but in intermediate, central and surface waters increase smoothly from initial to final conditions. In the middle (d,e,f) and bottom (g,h,i) rows, the full set of S and θ profiles for each simulation is contoured. For contouring, profiles were arranged in order of decreasing $\delta\tau$ (on average warmer from left to right).

Figure 4-35a, b. η_{BC} and $\delta\tau$ for the simulations. The mean values of $\delta\tau$ and η_{BC} from Simulation 1 have been removed from each, to mimic the fact that in the ocean, one mode of variability will typically dominate, largely determining the mean. While the values for each simulation follow a tightly defined curve, those curves exhibit different slopes and positions. The fact that the center of the η_{BC}-$\delta\tau$ solutions fall for the first three simulations fall very close to one another indicates that the mean temperatures and salinities for these three are roughly the same, around 34.7 psu and 6.3 °C. Simulations 4 and 5, with a significantly different thermohaline mean, are centered in different locations. a) (top) Axes set to show the full range of η_{BC} and $\delta\tau$ for all simulations. b) (bottom) Close-up of the boxed-in area in a).

Figure 4-36. a) (top) The solution space defined by the integration of $\delta\tau$ and relative sea level (which at pressure = 0 is η_{BC}) over pressure for the first simulation. The solution at pressure = 0 (η_{BC} vs. $\delta\tau$) is highlighted. Away from the reader, as pressure approaches the reference level of 2000 dbar, the solution surfaces collapses to a point. b) (bottom) As a), with the solutions for the second and third simulations added. The viewpoint has been rotated clockwise eighty degrees from a), to better show the intersection of all three surfaces. Each solution is uniquely determined by one of the simulations pictured in Fig. 4-34. Toward the reader, the solutions flare out, defining distinct surfaces. the information portrayed in Fig. 4-35. is simply the intersections of these surfaces in the 0 dbar plane.

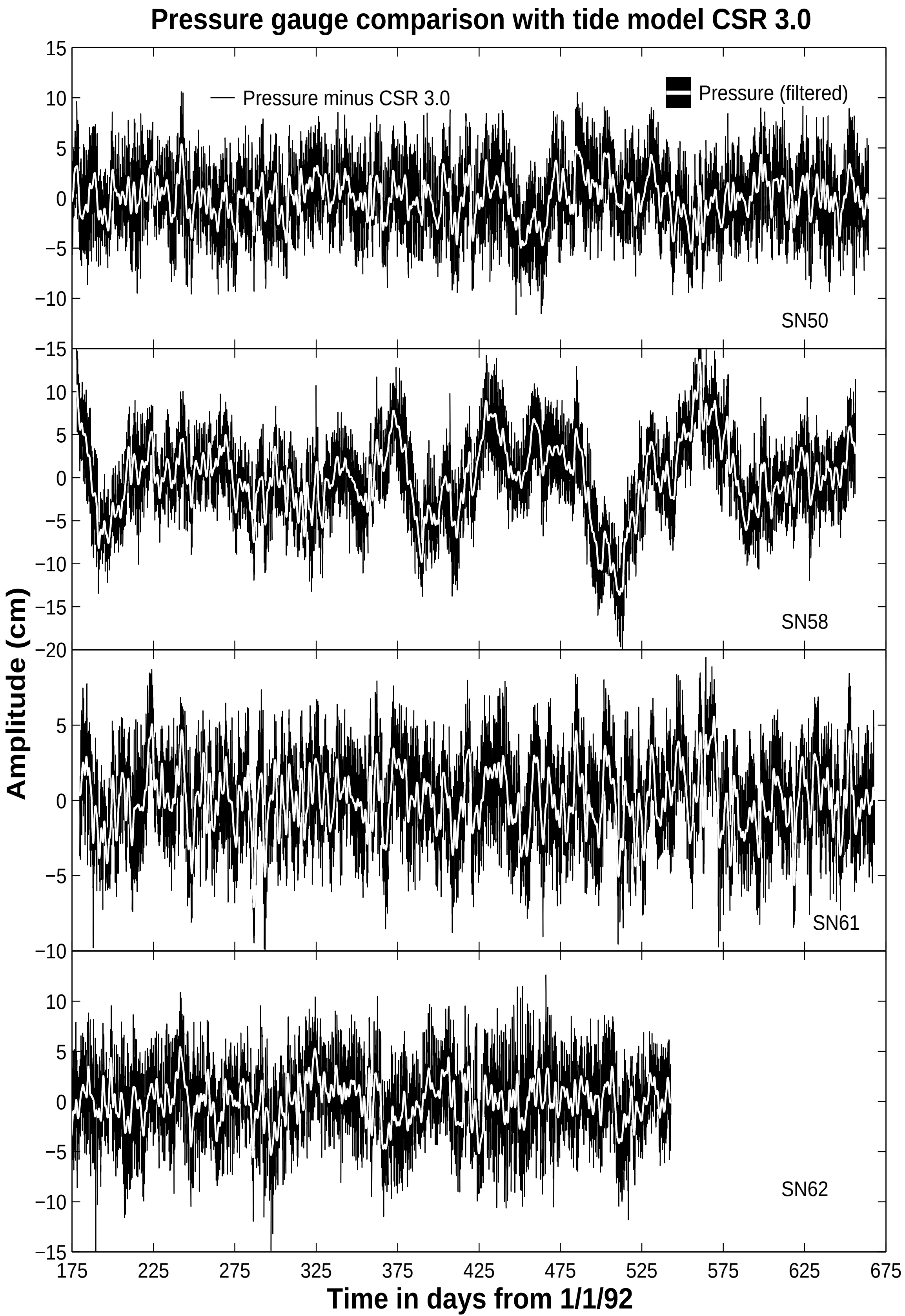
Pressure gauge comparison with tide model CSR 3.0
Pressure minus CSR 3.0
Pressure (filtered)
SN50
SN58
SN61
SN62
Amplitude (cm)
Time in days from 1/1/92
15
10
5
0
−5
−10
−15
−20
175
225
275
325
375
425
475
525
575
625
675

Figure 4-1.

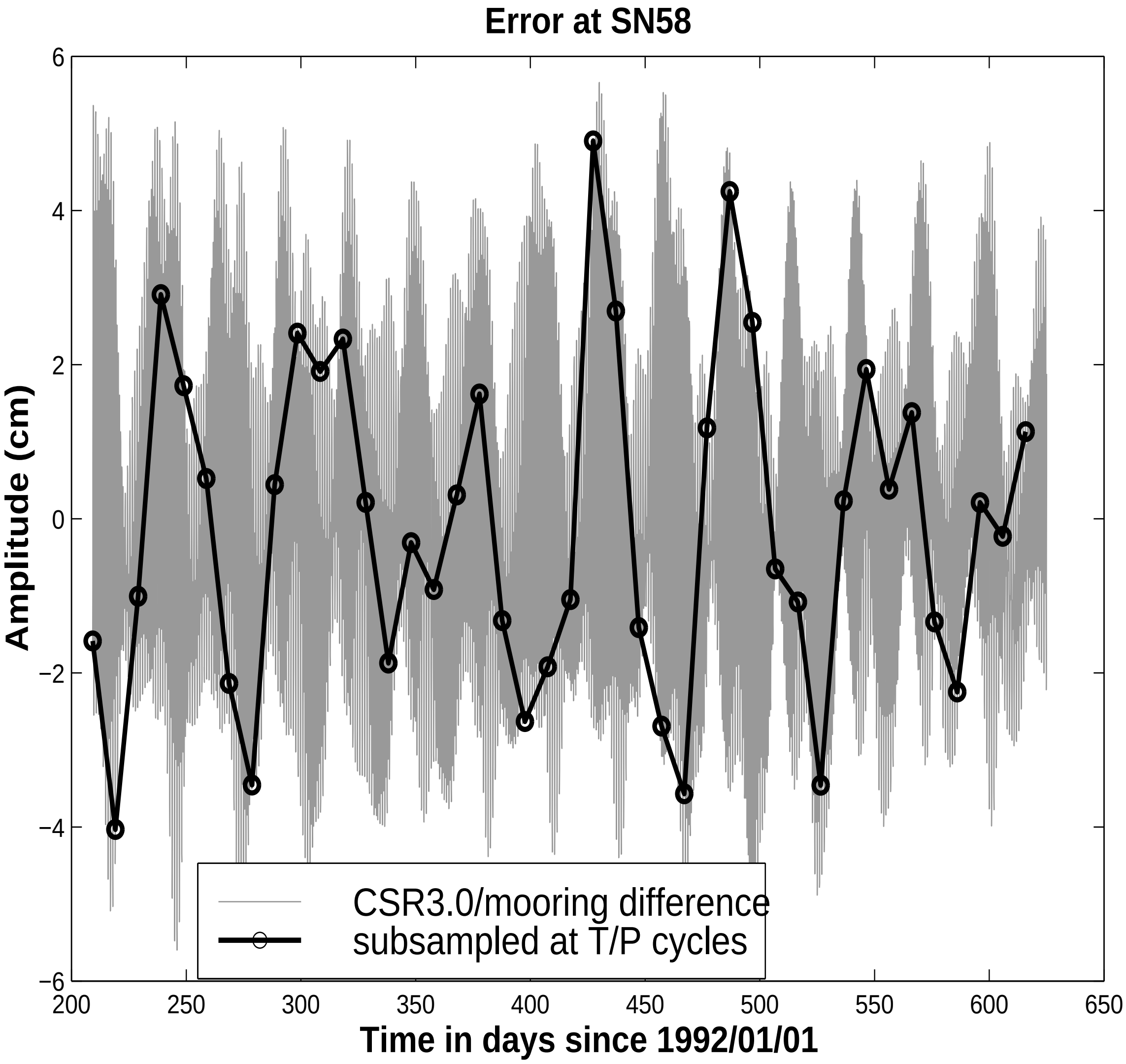
Error at SN58
Amplitude (cm)
6
4
2
0
−2
−4
−6
200
250
300
350
400
450
500
550
600
650
Time in days since 1992/01/01
CSR3.0/mooring difference
subsampled at T/P cycles

Figure 4-2.

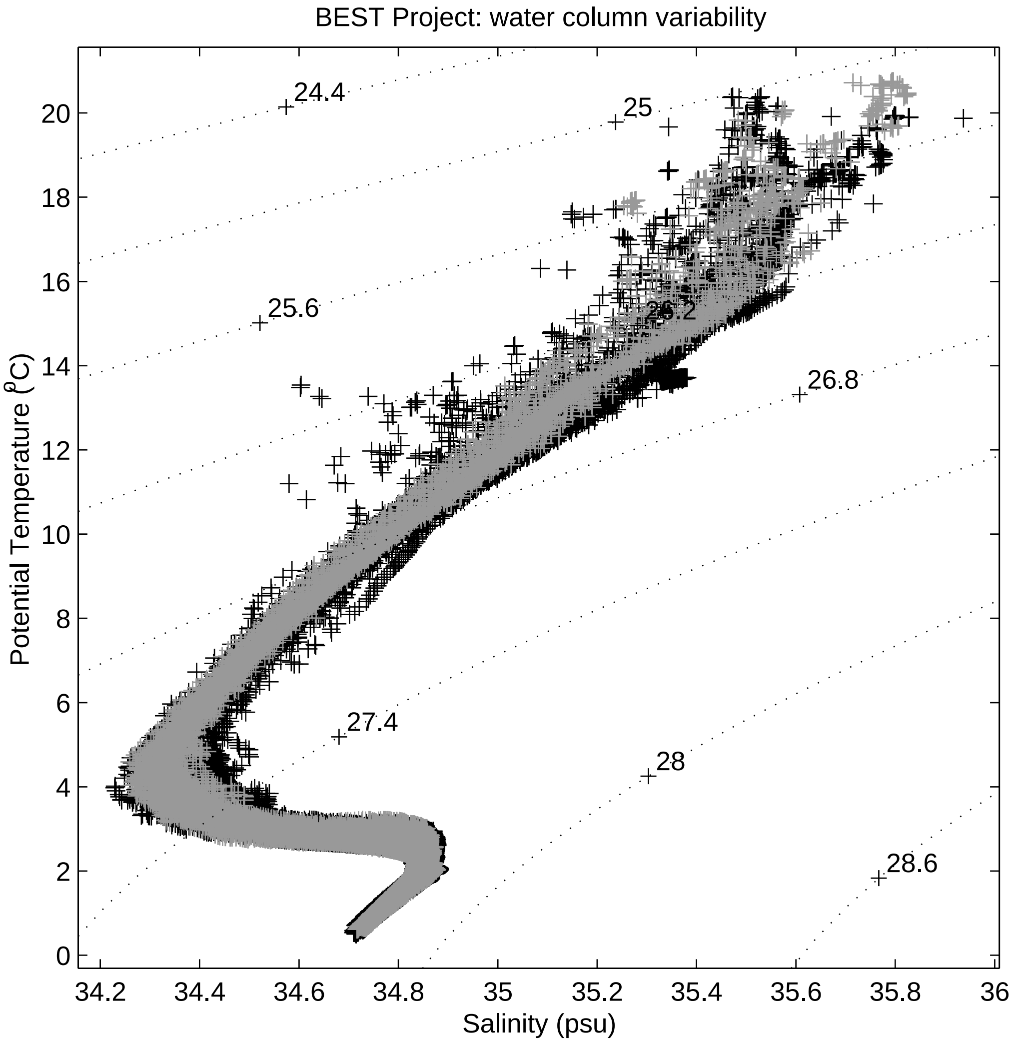
BEST Project: water column variability
Potential Temperature (°C)
Salinity (psu)
0
2
4
6
8
10
12
14
16
18
20
34.2
34.4
34.6
34.8
35
35.2
35.4
35.6
35.8
36
24.4
25
25.6
26.2
26.8
27.4
28
28.6

Figure 4-3.

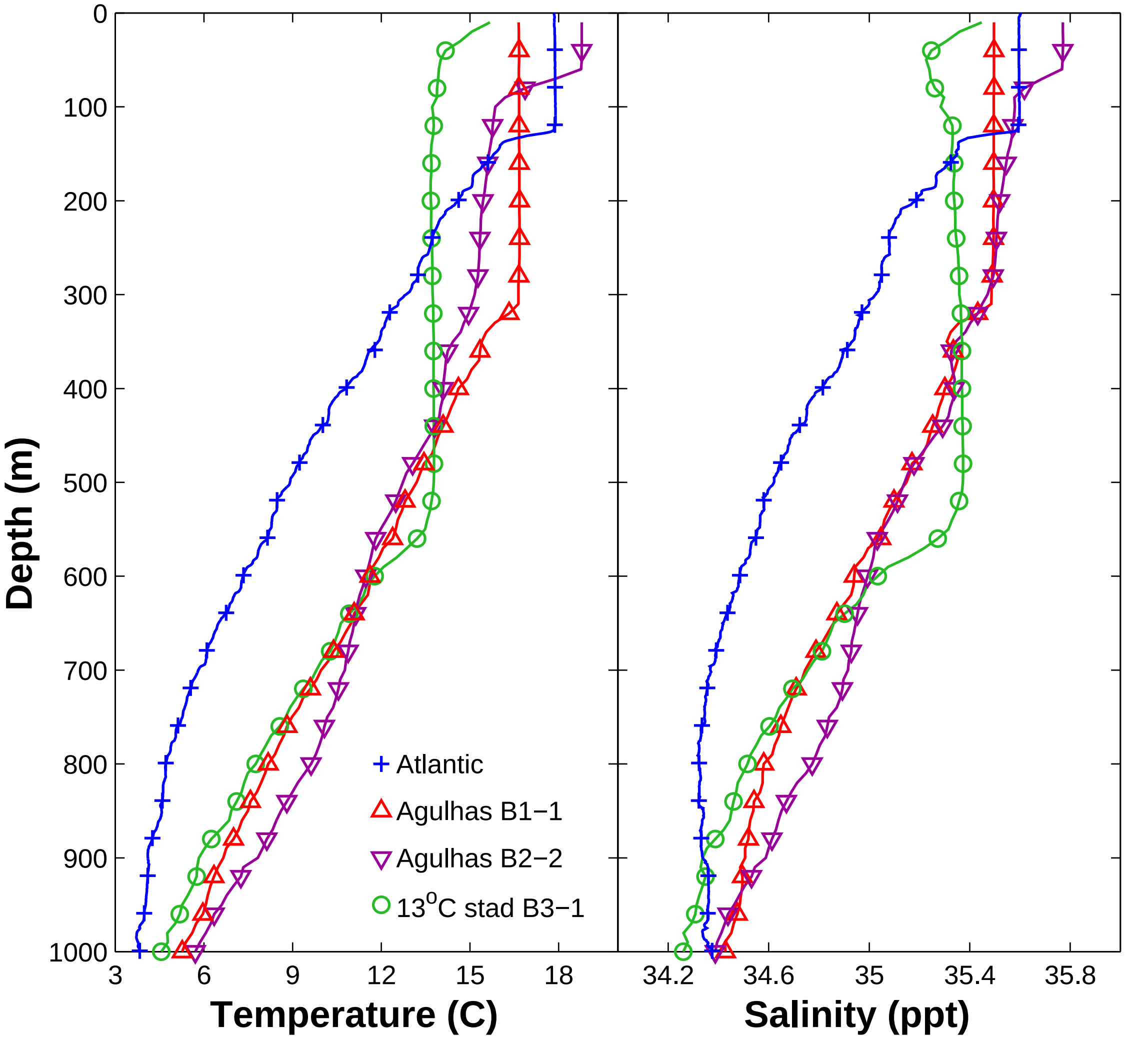
Depth (m)
0
100
200
300
400
500
600
700
800
900
1000
3
6
9
12
15
18
Temperature (C)
34.2
34.6
35
35.4
35.8
Salinity (ppt)
+ Atlantic
△ Agulhas B1−1
▽ Agulhas B2−2
○ 13°C stad B3−1

Figure 4-4.

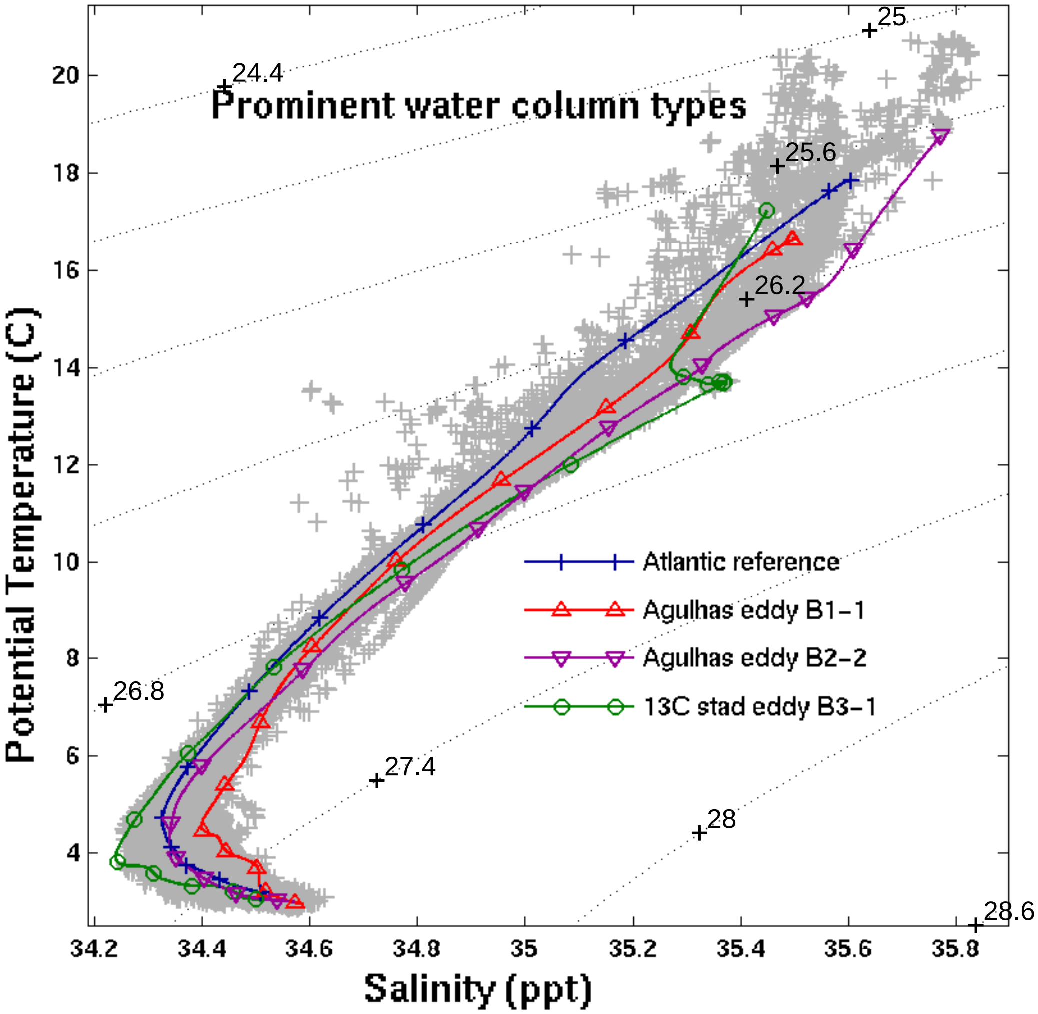
Prominent water column types
Potential Temperature (C)
Salinity (ppt)
20
18
16
14
12
10
8
6
4
34.2
34.4
34.6
34.8
35
35.2
35.4
35.6
35.8
24.4
25
25.6
26.2
26.8
27.4
28
28.6
Atlantic reference
Agulhas eddy B1−1
Agulhas eddy B2−2
13C stad eddy B3−1

Figure 4-5.

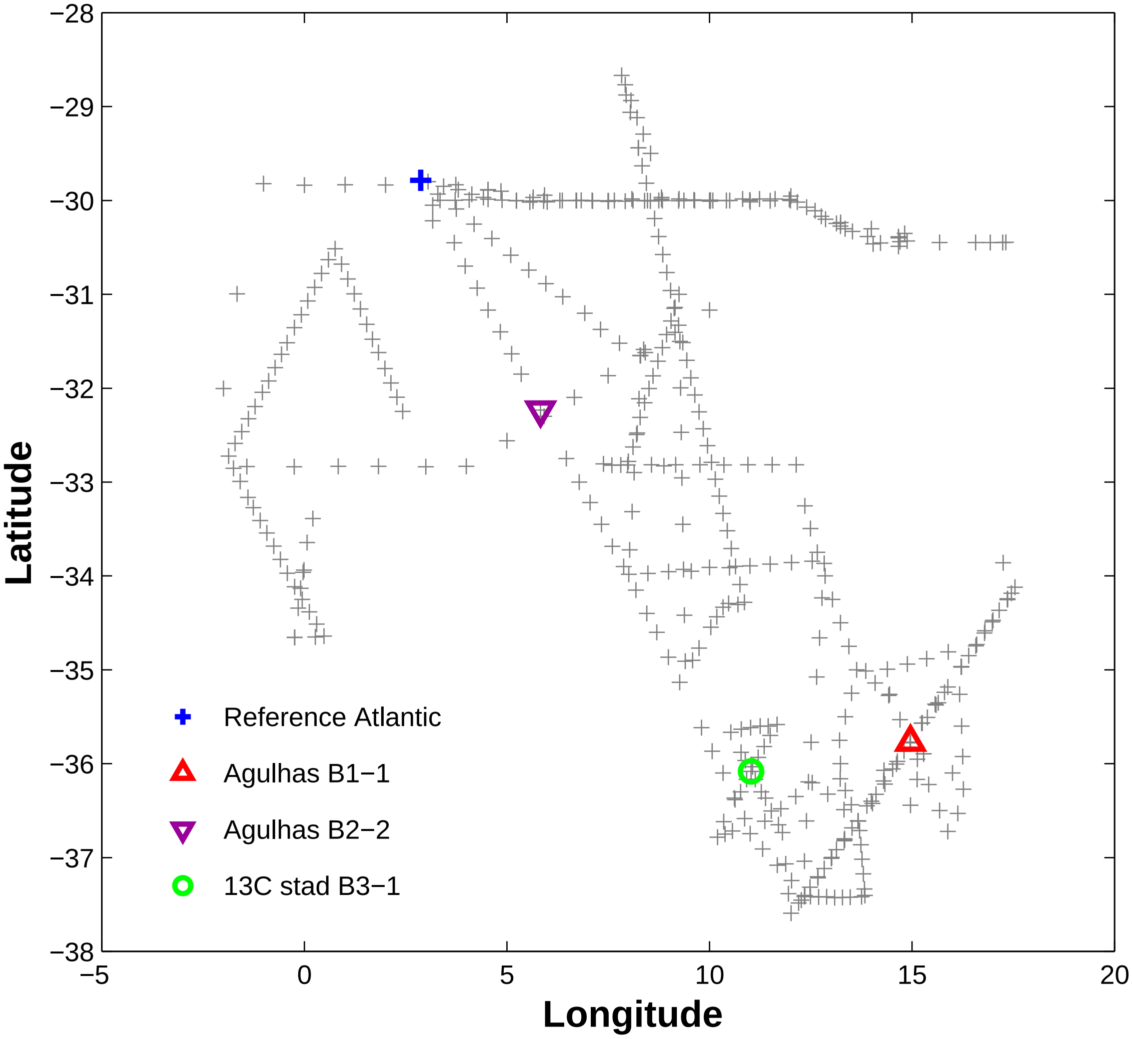
Latitude
Longitude
−28
−29
−30
−31
−32
−33
−34
−35
−36
−37
−38
−5
0
5
10
15
20
Reference Atlantic
Agulhas B1−1
Agulhas B2−2
13C stad B3−1

Figure 4-6.

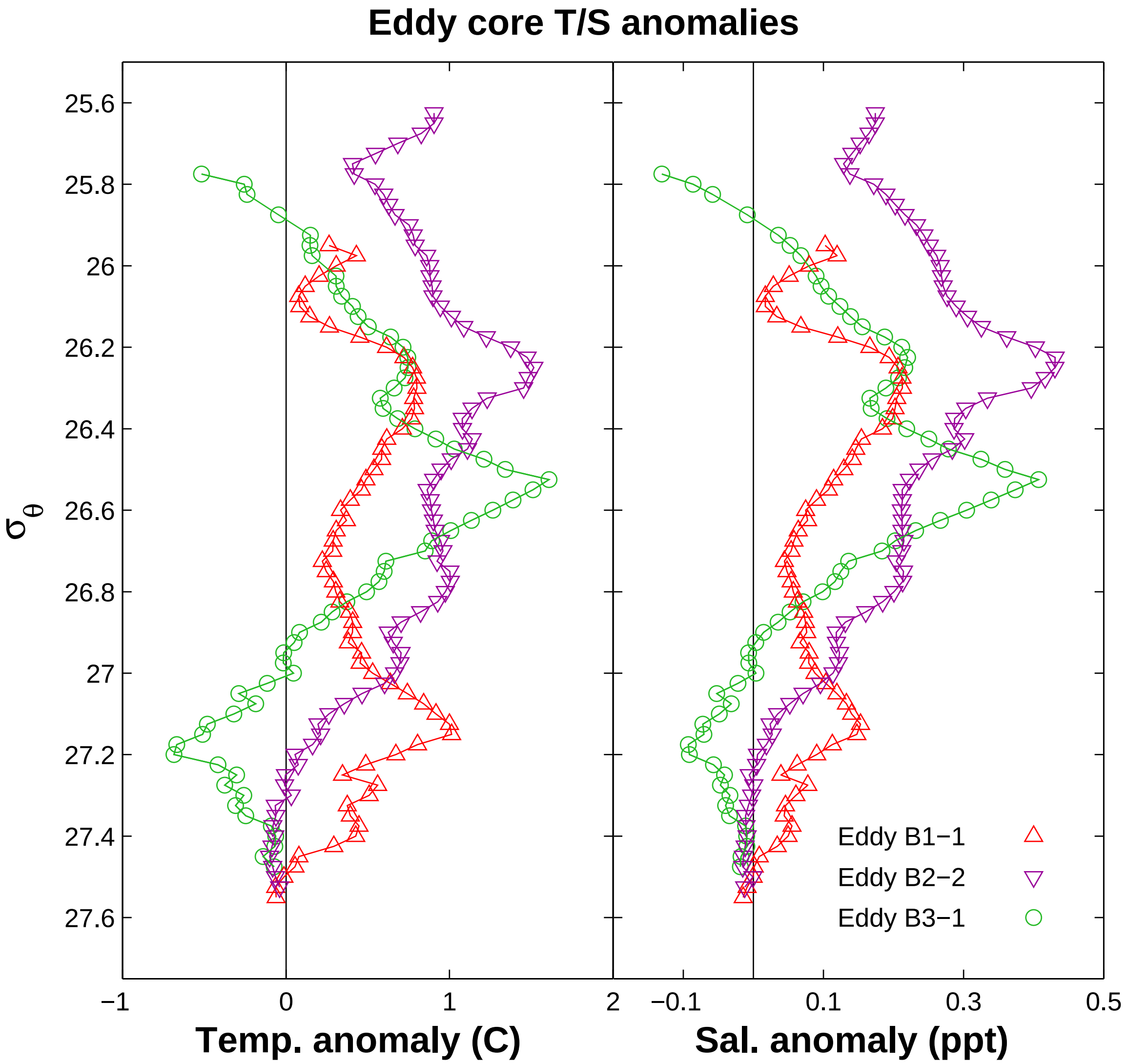
Eddy core T/S anomalies
σθ
25.6
25.8
26
26.2
26.4
26.6
26.8
27
27.2
27.4
27.6
−1
0
1
2
−0.1
0.1
0.3
0.5
Temp. anomaly (C)
Sal. anomaly (ppt)
Eddy B1−1 △
Eddy B2−2 ▽
Eddy B3−1 ○

Figure 4-7.

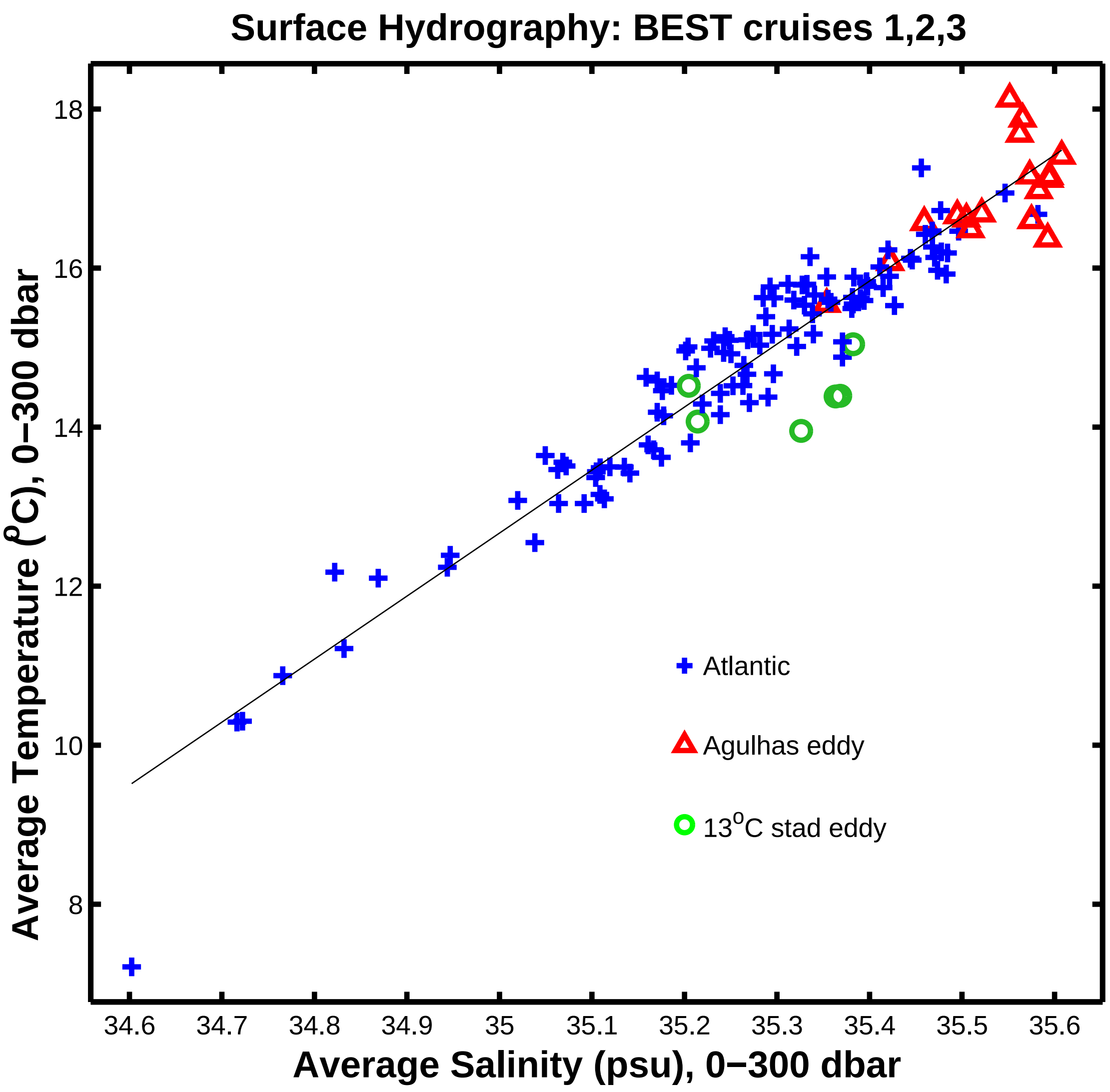
Surface Hydrography: BEST cruises 1,2,3
Average Temperature (°C), 0−300 dbar
Average Salinity (psu), 0−300 dbar
18
16
14
12
10
8
34.6
34.7
34.8
34.9
35
35.1
35.2
35.3
35.4
35.5
35.6
Atlantic
Agulhas eddy
13°C stad eddy

Figure 4-8.

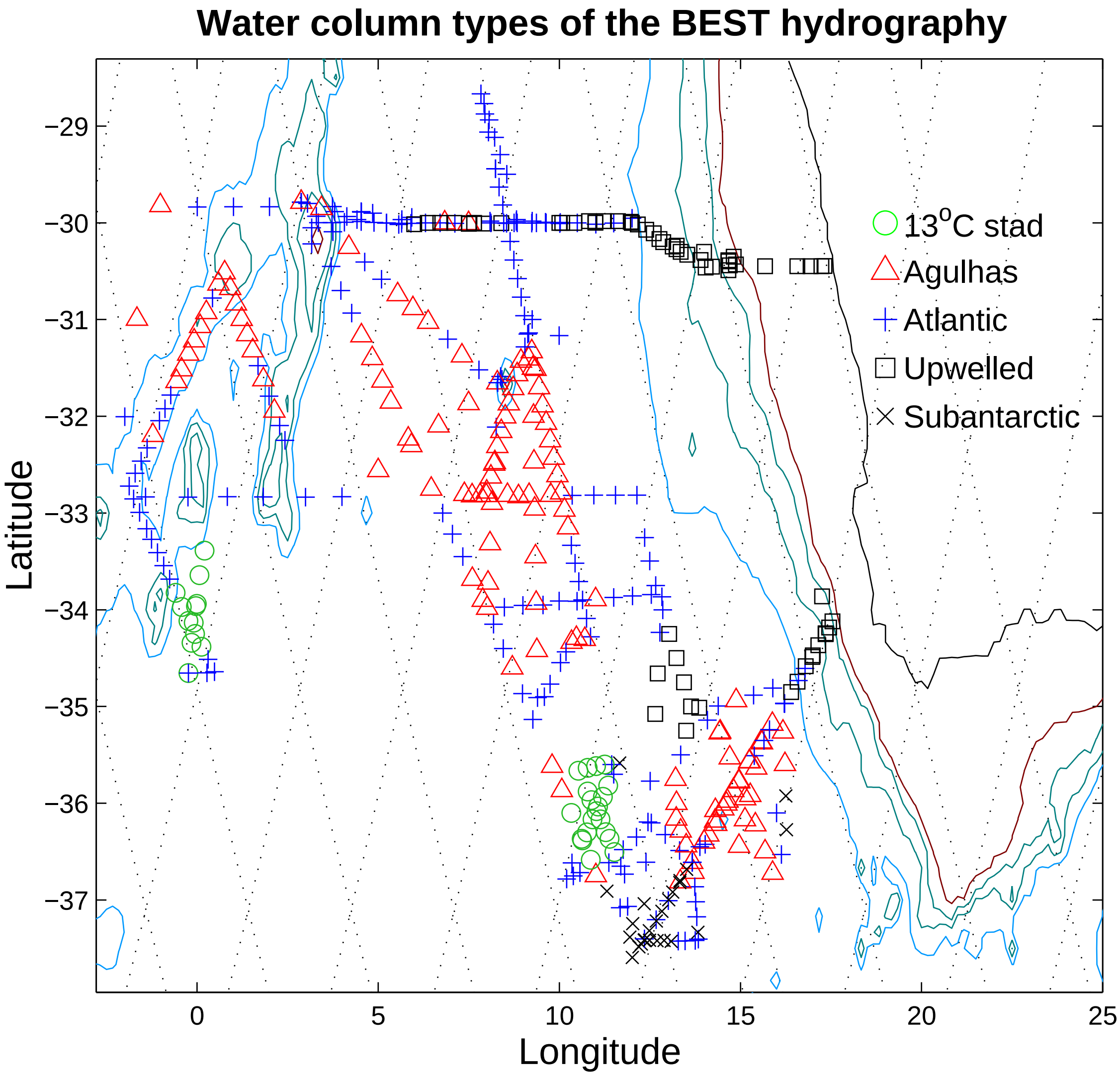
Water column types of the BEST hydrography
13°C stad
Agulhas
Atlantic
Upwelled
Subantarctic
Latitude
−29
−30
−31
−32
−33
−34
−35
−36
−37
Longitude
0
5
10
15
20
25

Figure 4-9.

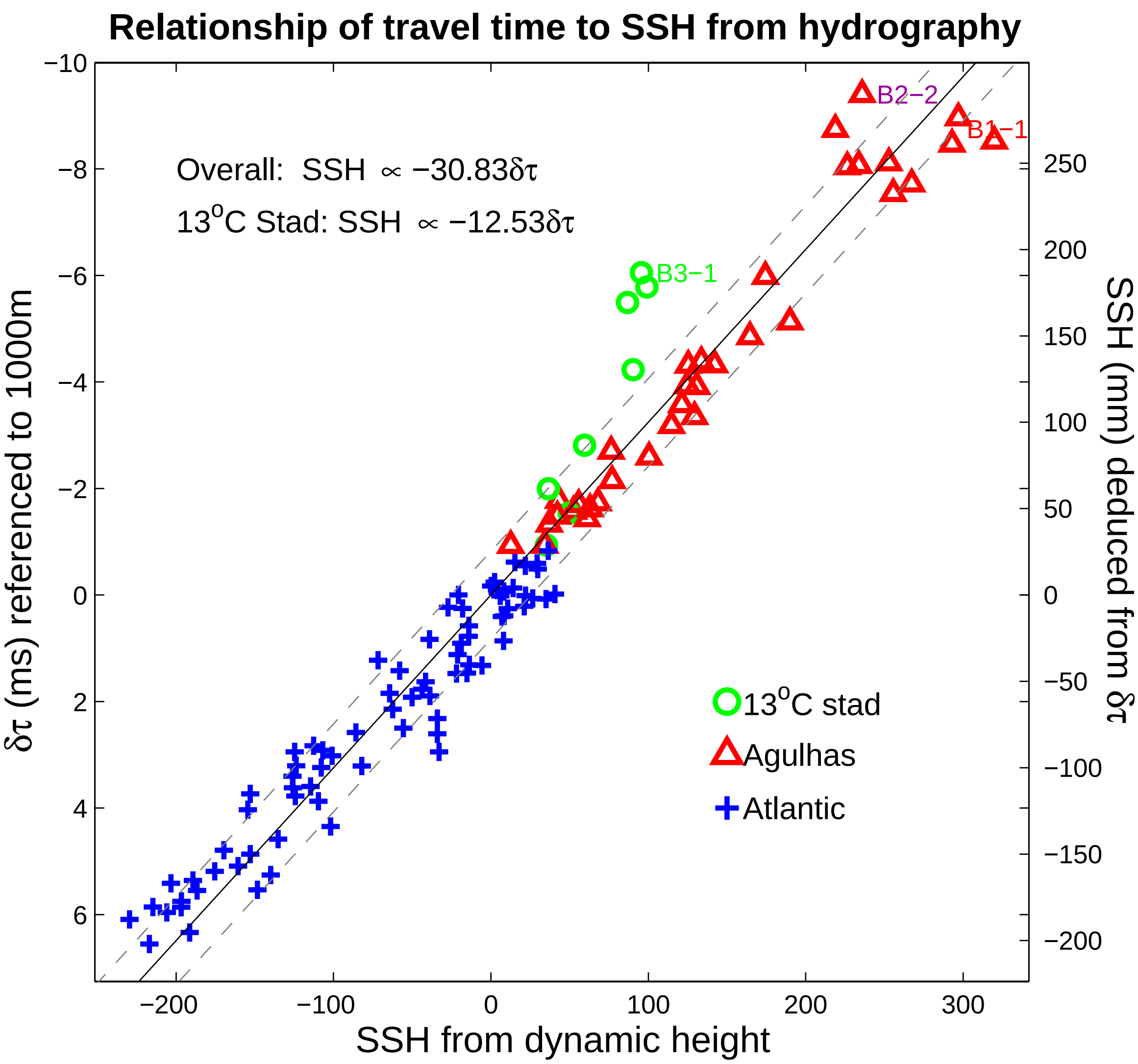
Relationship of travel time to SSH from hydrography
Overall: SSH ∝ −30.83δτ
13°C Stad: SSH ∝ −12.53δτ
B2−2
B1−1
B3−1
13°C stad
Agulhas
Atlantic
δτ (ms) referenced to 1000m
SSH (mm) deduced from δτ
SSH from dynamic height
−10
−8
−6
−4
−2
0
2
4
6
250
200
150
100
50
0
−50
−100
−150
−200
−200
−100
0
100
200
300

Figure 4-10.

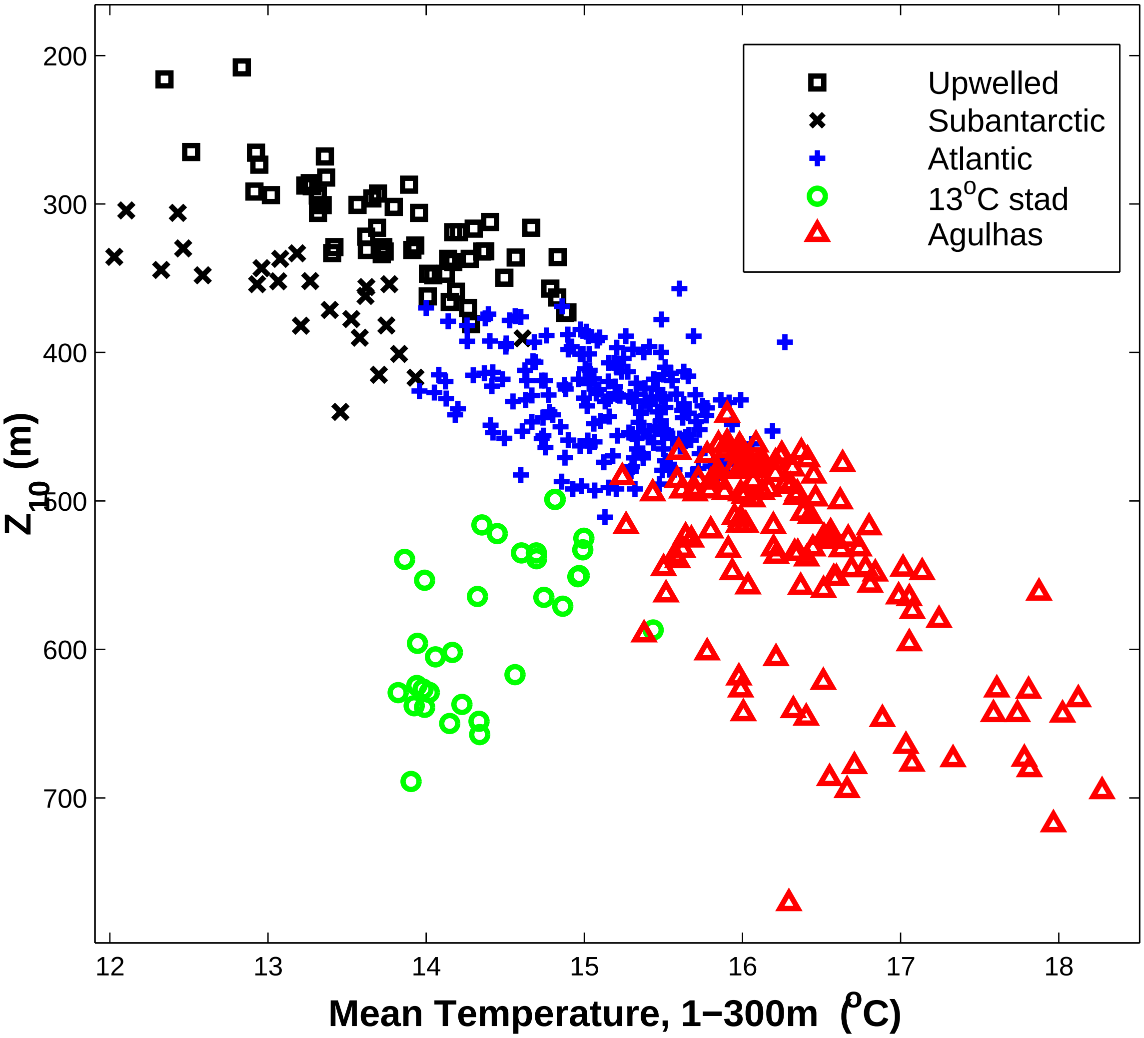
Upwelled
Subantarctic
Atlantic
13^oC stad
Agulhas
200
300
400
500
600
700
Z_{10} (m)
12
13
14
15
16
17
18
Mean Temperature, 1−300m (^oC)

Figure 4-11.

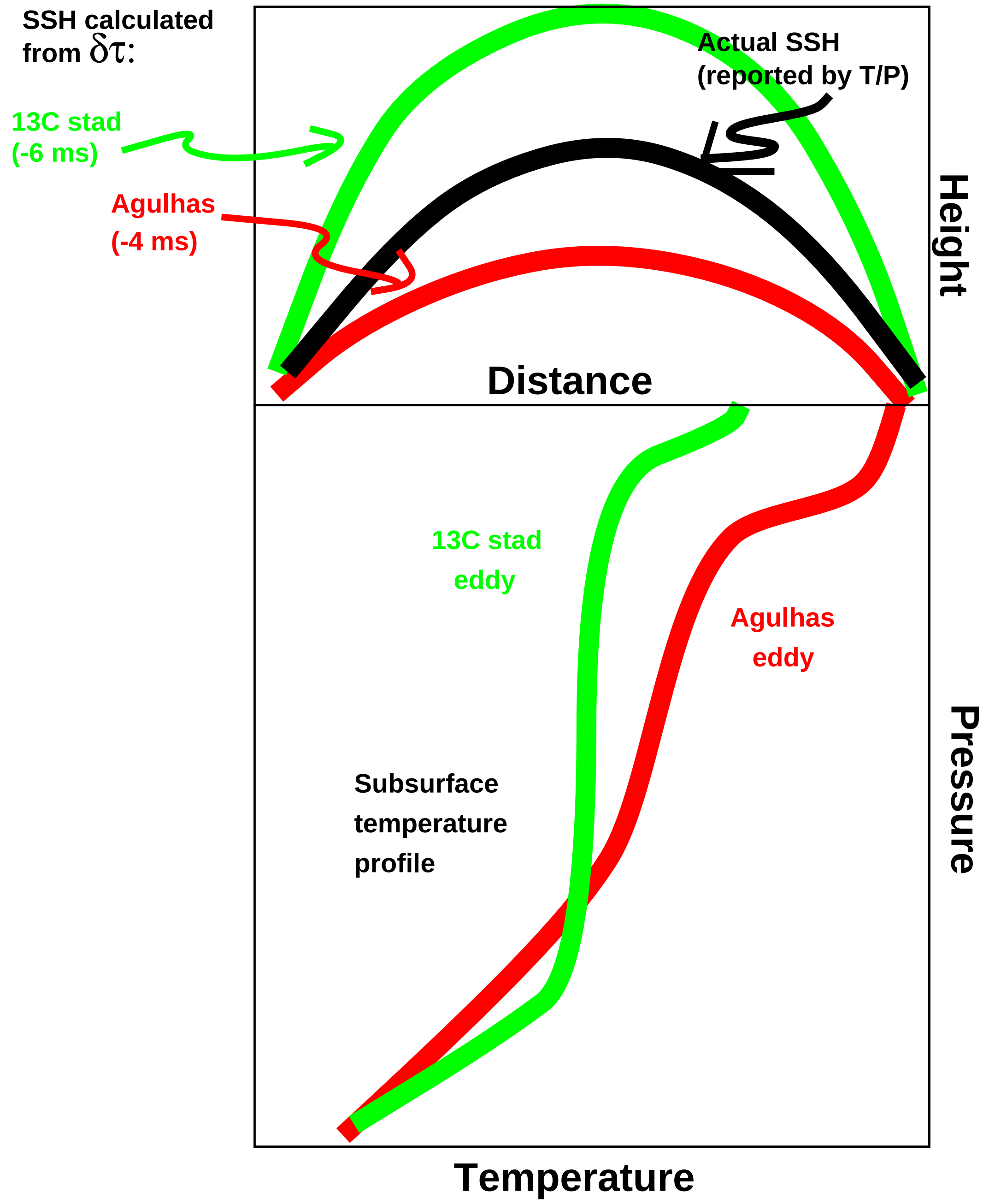
SSH calculated
from δτ:
13C stad
(-6 ms)
Agulhas
(-4 ms)
Actual SSH
(reported by T/P)
Height
Distance
13C stad
eddy
Agulhas
eddy
Subsurface
temperature
profile
Pressure
Temperature

Figure 4-12.

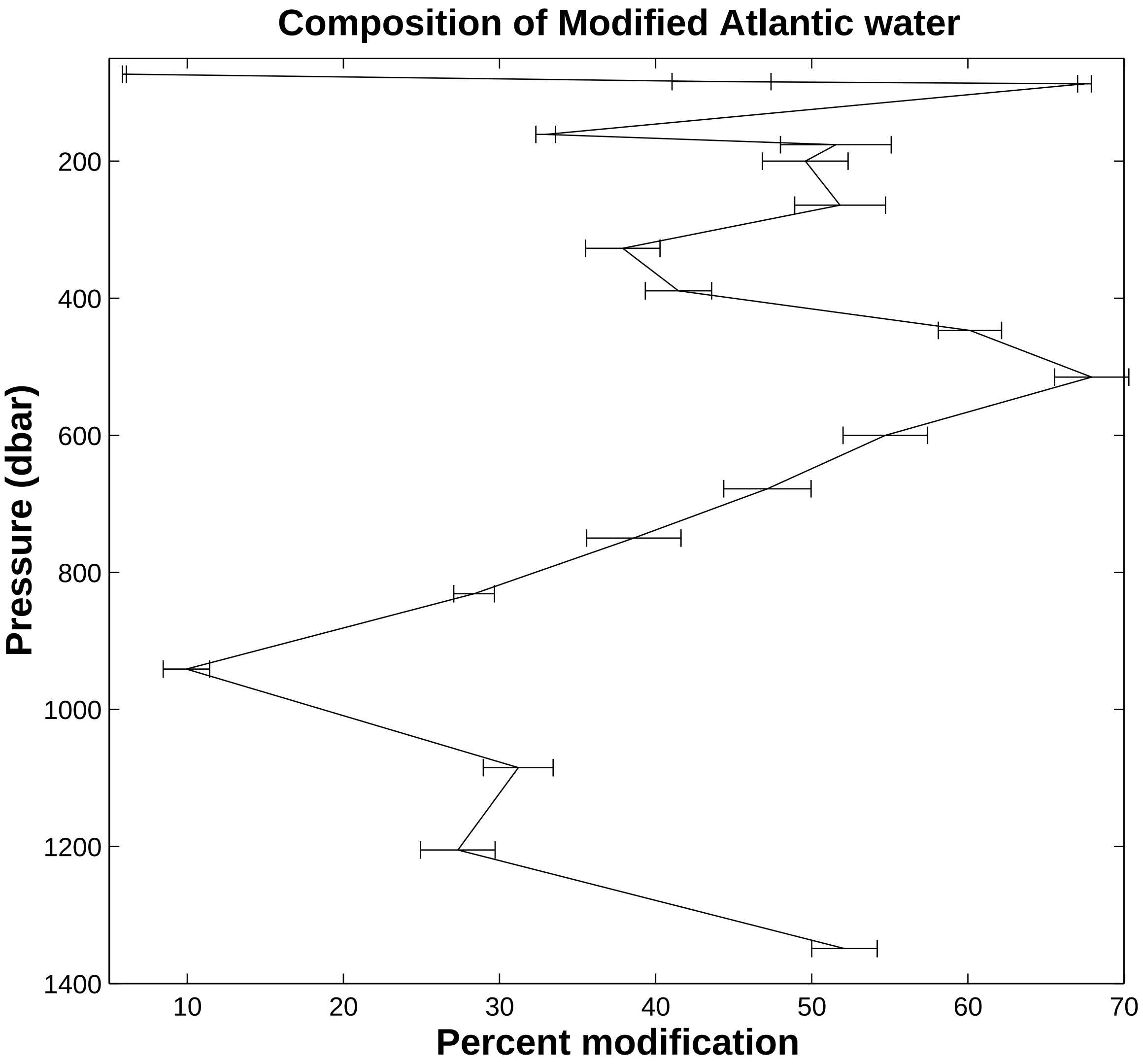
Composition of Modified Atlantic water
Pressure (dbar)
200
400
600
800
1000
1200
1400
10
20
30
40
50
60
70
Percent modification

Figure 4-13.

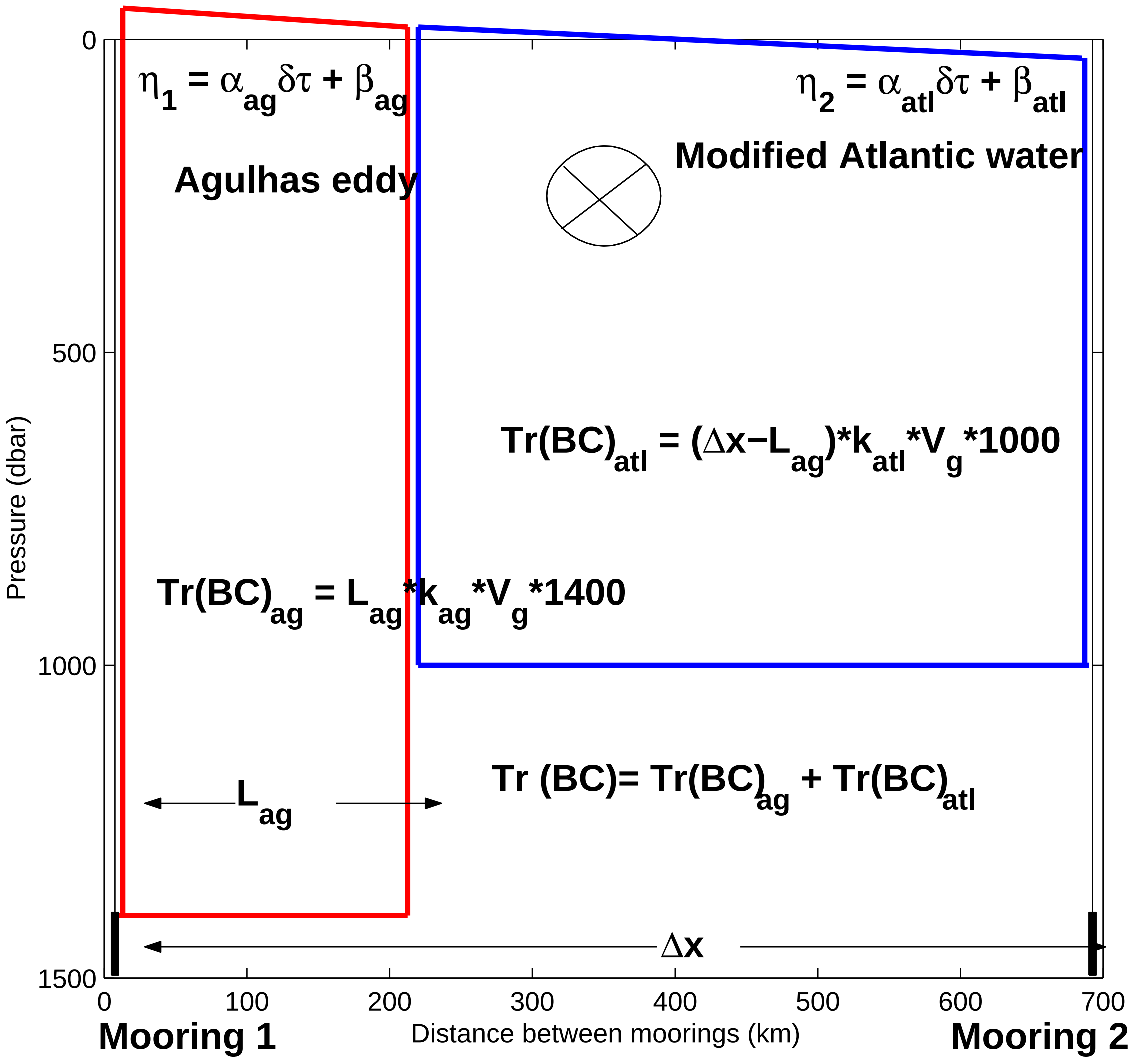
$\eta_1 = \alpha_{ag}\delta\tau + \beta_{ag}$
$\eta_2 = \alpha_{atl}\delta\tau + \beta_{atl}$
Agulhas eddy
Modified Atlantic water
$Tr(BC)_{atl} = (\Delta x - L_{ag}) * k_{atl} * V_g * 1000$
$Tr(BC)_{ag} = L_{ag} * k_{ag} * V_g * 1400$
L_{ag}
$Tr\ (BC) = Tr(BC)_{ag} + Tr(BC)_{atl}$
Δx
Pressure (dbar)
0
500
1000
1500
0
100
200
300
400
500
600
700
Distance between moorings (km)
Mooring 1
Mooring 2

Figure 4-14.

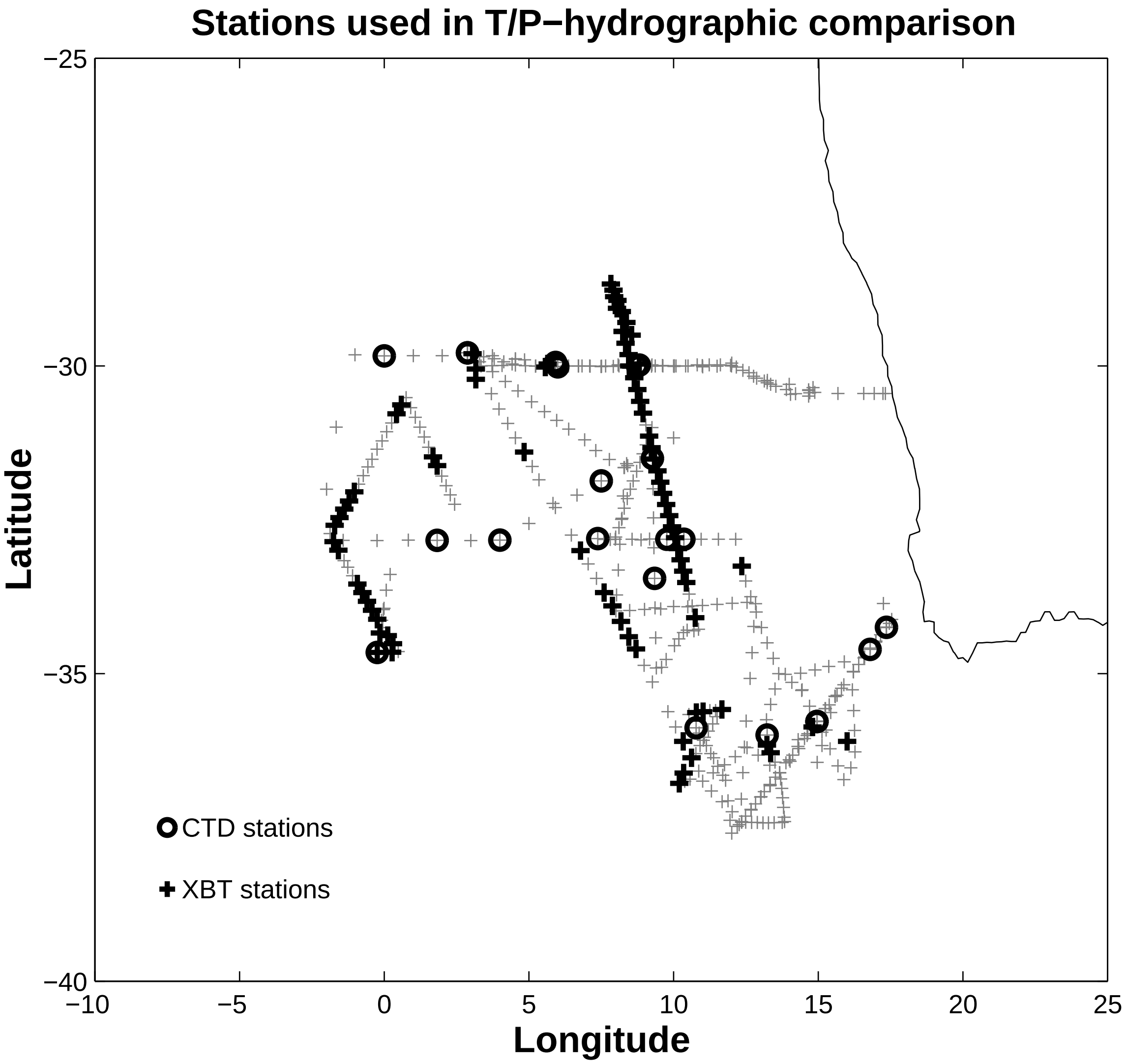
Stations used in T/P−hydrographic comparison
Latitude
Longitude
−25
−30
−35
−40
−10
−5
0
5
10
15
20
25
CTD stations
XBT stations

Figure 4-15.

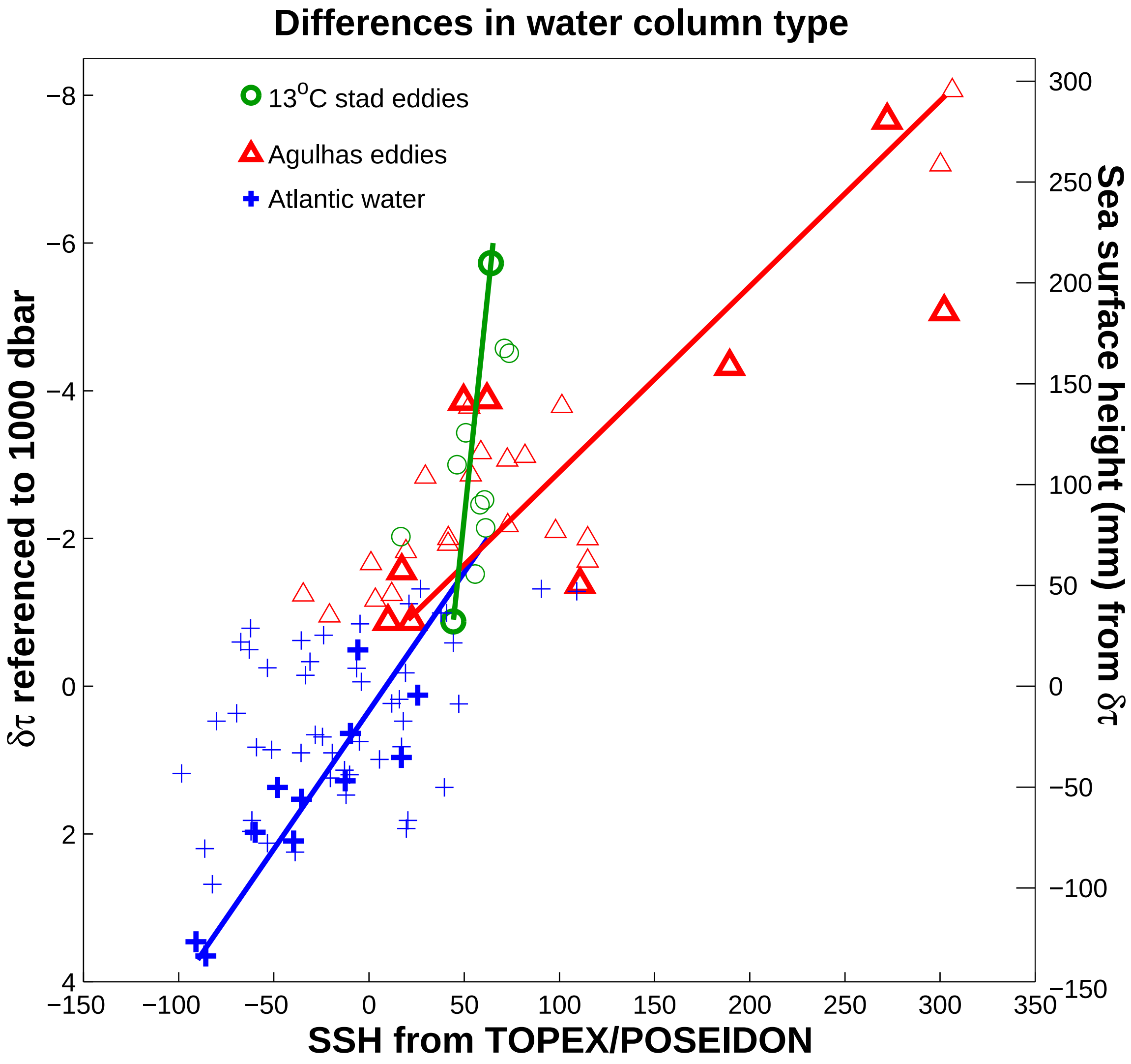
Differences in water column type
13⁰C stad eddies
Agulhas eddies
Atlantic water
δτ referenced to 1000 dbar
−8
−6
−4
−2
0
2
4
Sea surface height (mm) from δτ
300
250
200
150
100
50
0
−50
−100
−150
SSH from TOPEX/POSEIDON
−150
−100
−50
0
50
100
150
200
250
300
350

Figure 4-16.

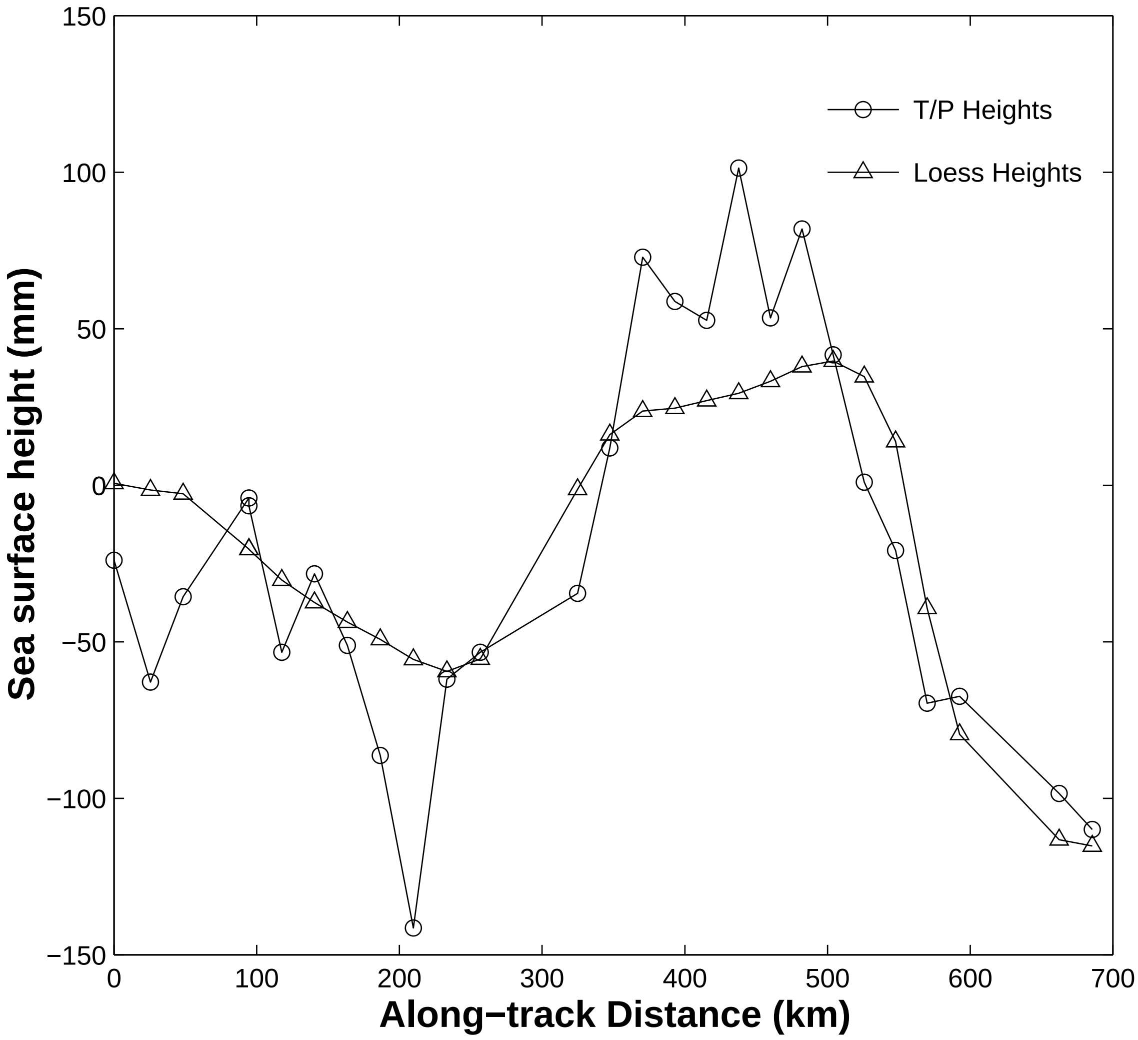
Sea surface height (mm)
150
100
50
0
−50
−100
−150
0
100
200
300
400
500
600
700
Along−track Distance (km)
T/P Heights
Loess Heights

Figure 4-17.

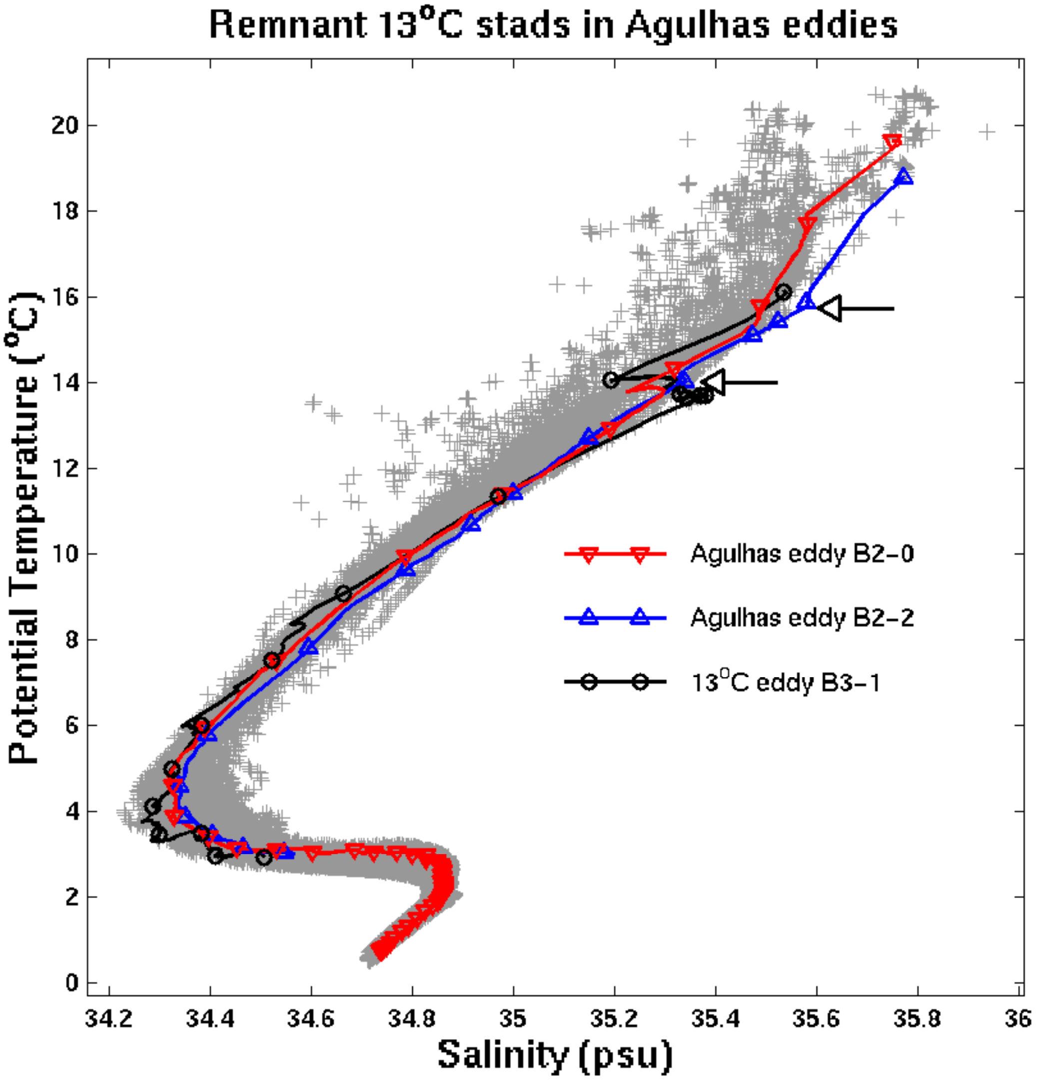
Remnant 13°C stads in Agulhas eddies
Potential Temperature (°C)
Salinity (psu)
0
2
4
6
8
10
12
14
16
18
20
34.2
34.4
34.6
34.8
35
35.2
35.4
35.6
35.8
36
Agulhas eddy B2-0
Agulhas eddy B2-2
13°C eddy B3-1

Figure 4-18.

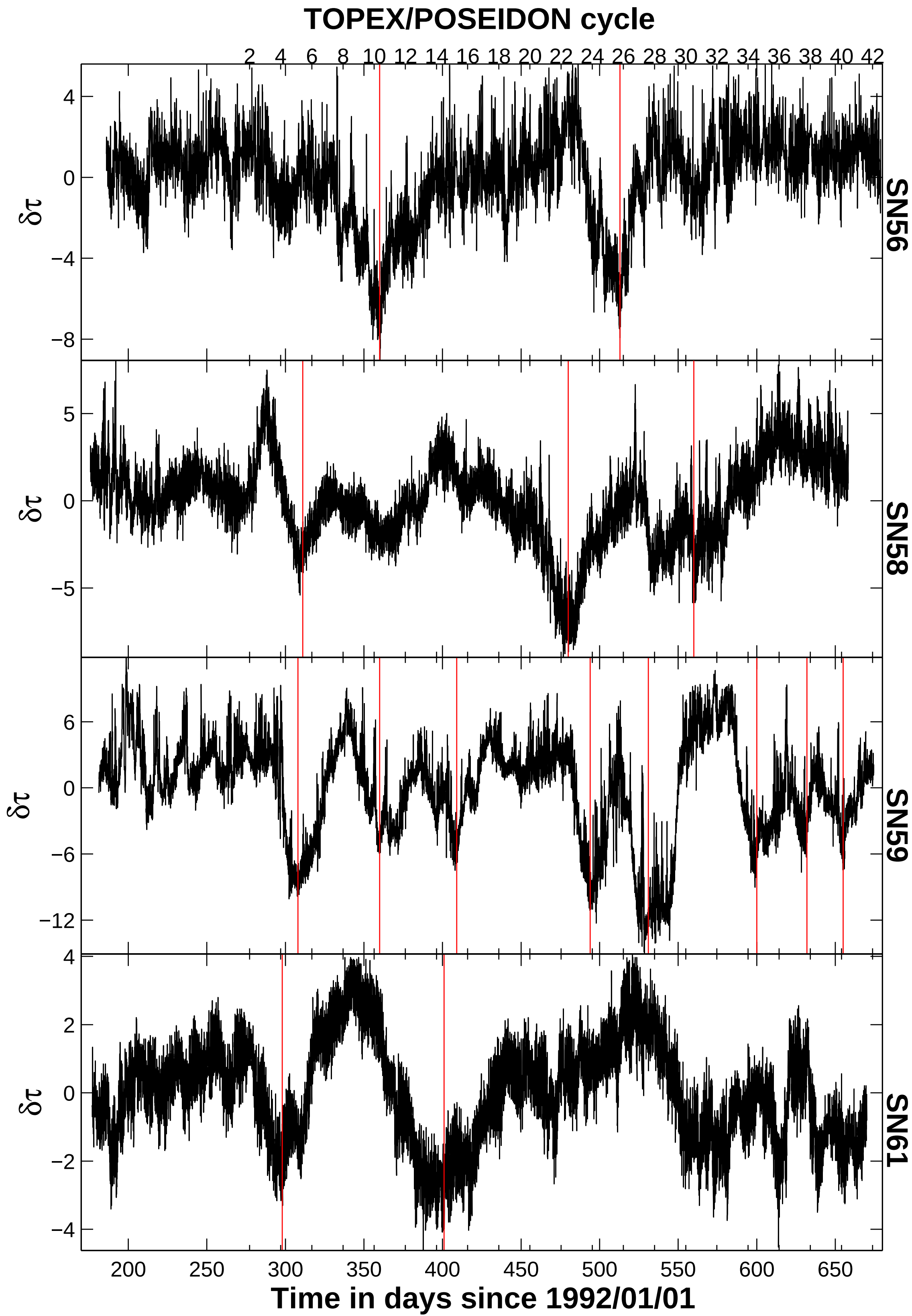
TOPEX/POSEIDON cycle
2
4
6
8
10
12
14
16
18
20
22
24
26
28
30
32
34
36
38
40
42
δτ
4
0
−4
−8
SN56
δτ
5
0
−5
SN58
δτ
6
0
−6
−12
SN59
δτ
4
2
0
−2
−4
SN61
200
250
300
350
400
450
500
550
600
650
Time in days since 1992/01/01

Figure 4-19.

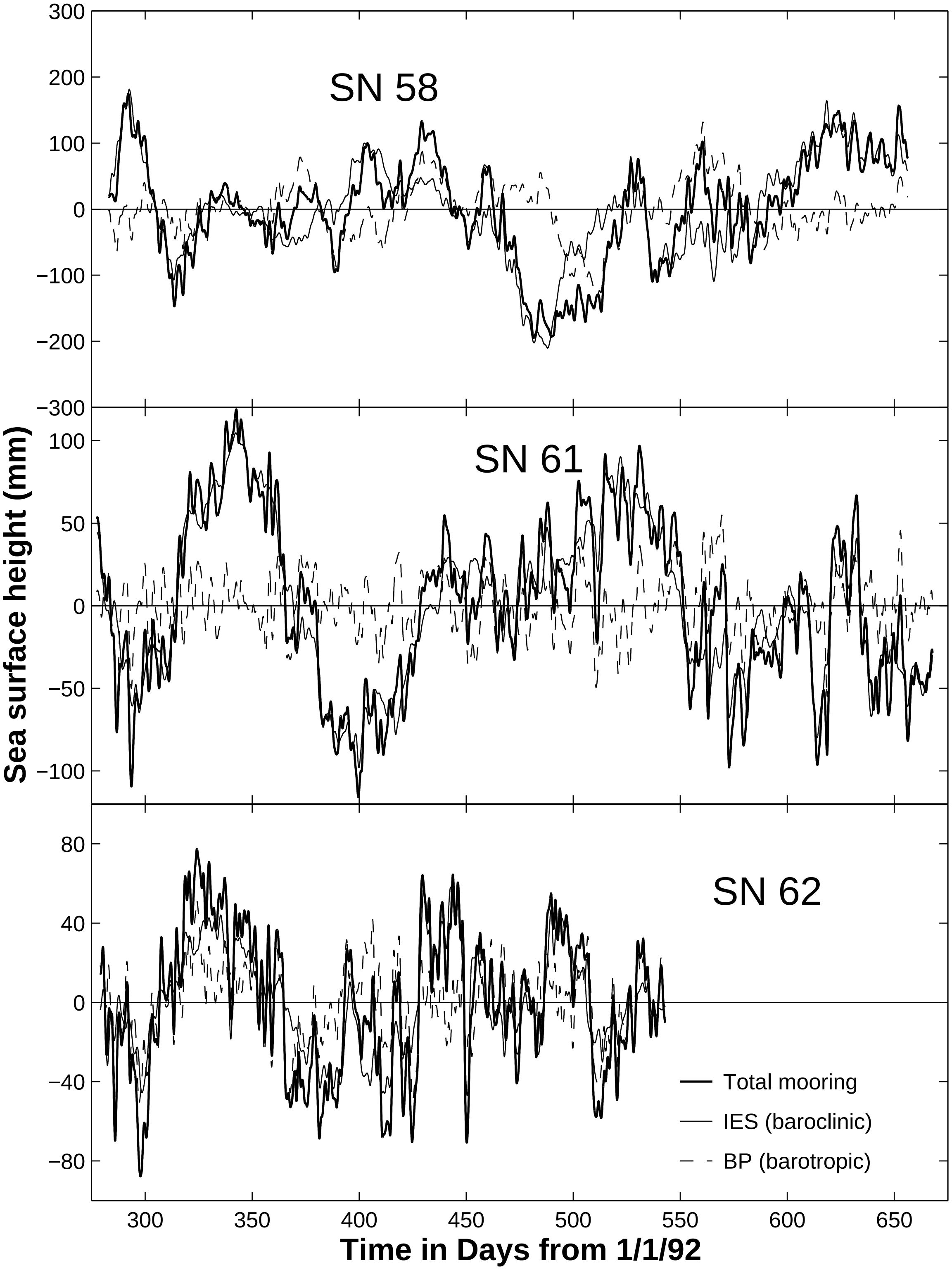
SN 58
SN 61
SN 62
300
200
100
0
−100
−200
−300
100
50
0
−50
−100
80
40
0
−40
−80
300
350
400
450
500
550
600
650
Sea surface height (mm)
Time in Days from 1/1/92
Total mooring
IES (baroclinic)
BP (barotropic)

Figure 4-20.

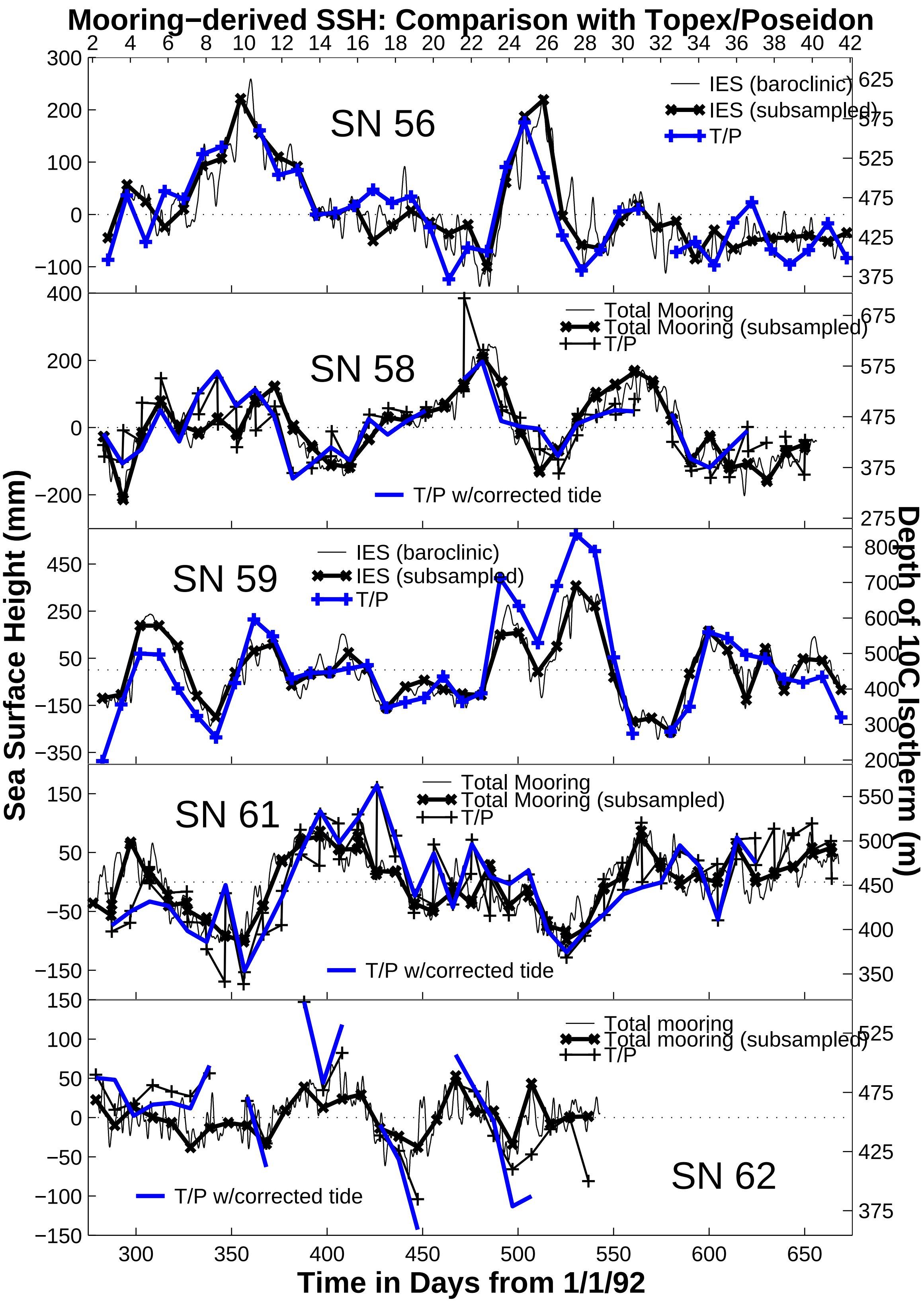
Mooring−derived SSH: Comparison with Topex/Poseidon
2 4 6 8 10 12 14 16 18 20 22 24 26 28 30 32 34 36 38 40 42
SN 56
IES (baroclinic)
IES (subsampled)
T/P
300 200 100 0 −100
625 575 525 475 425 375
SN 58
Total Mooring
Total Mooring (subsampled)
T/P
T/P w/corrected tide
400 200 0 −200
675 575 475 375 275
SN 59
IES (baroclinic)
IES (subsampled)
T/P
450 250 50 −150 −350
800 700 600 500 400 300 200
SN 61
Total Mooring
Total Mooring (subsampled)
T/P
T/P w/corrected tide
150 50 −50 −150
550 500 450 400 350
SN 62
Total mooring
Total mooring (subsampled)
T/P
T/P w/corrected tide
150 100 50 0 −50 −100 −150
525 475 425 375
300 350 400 450 500 550 600 650
Sea Surface Height (mm)
Depth of 10C Isotherm (m)
Time in Days from 1/1/92

Figure 4-21.

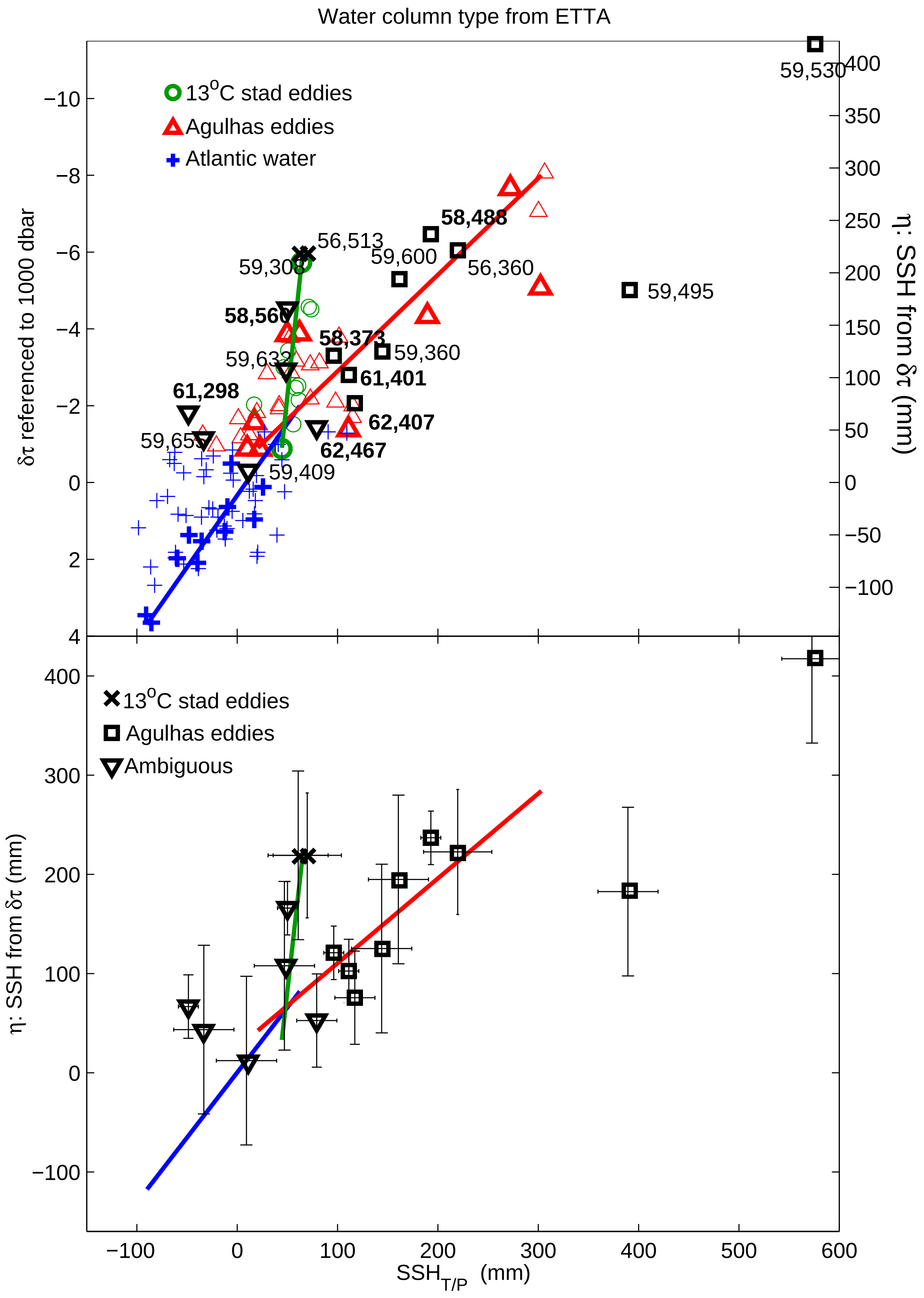
Water column type from ETTA
13°C stad eddies
Agulhas eddies
Atlantic water
δτ referenced to 1000 dbar
η: SSH from δτ (mm)
−10
−8
−6
−4
−2
0
2
4
400
350
300
250
200
150
100
50
0
−50
−100
59,530
58,488
56,513
59,600
59,308
56,360
59,495
58,560
58,373
59,360
59,632
61,401
61,298
62,407
59,653
62,467
59,409
13°C stad eddies
Agulhas eddies
Ambiguous
η: SSH from δτ (mm)
400
300
200
100
0
−100
−100
0
100
200
300
400
500
600
SSH$_{T/P}$ (mm)

Figure 4-22.

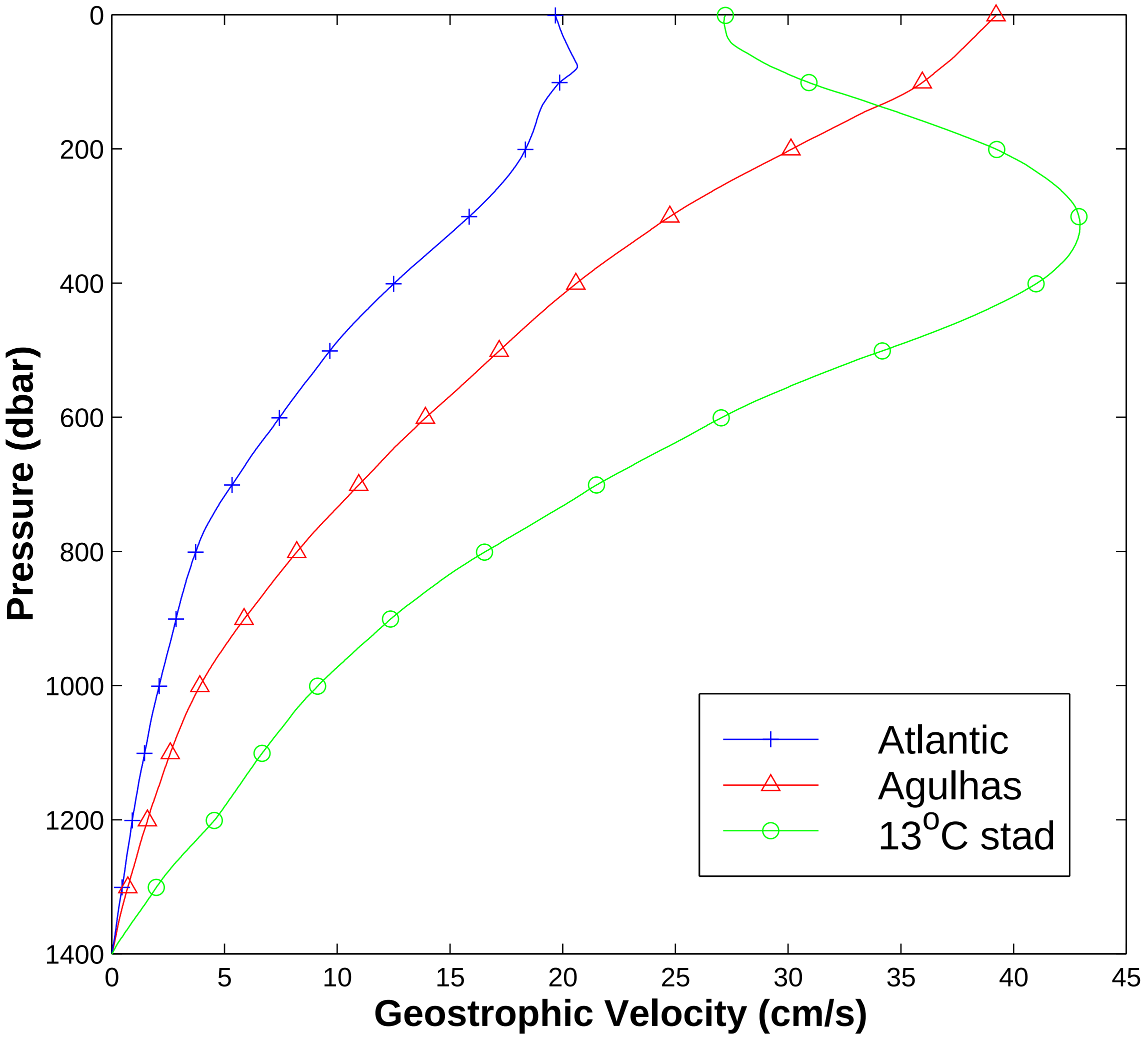
Pressure (dbar)
0
200
400
600
800
1000
1200
1400
0
5
10
15
20
25
30
35
40
45
Geostrophic Velocity (cm/s)
Atlantic
Agulhas
13^{o}C stad

Figure 4-23.

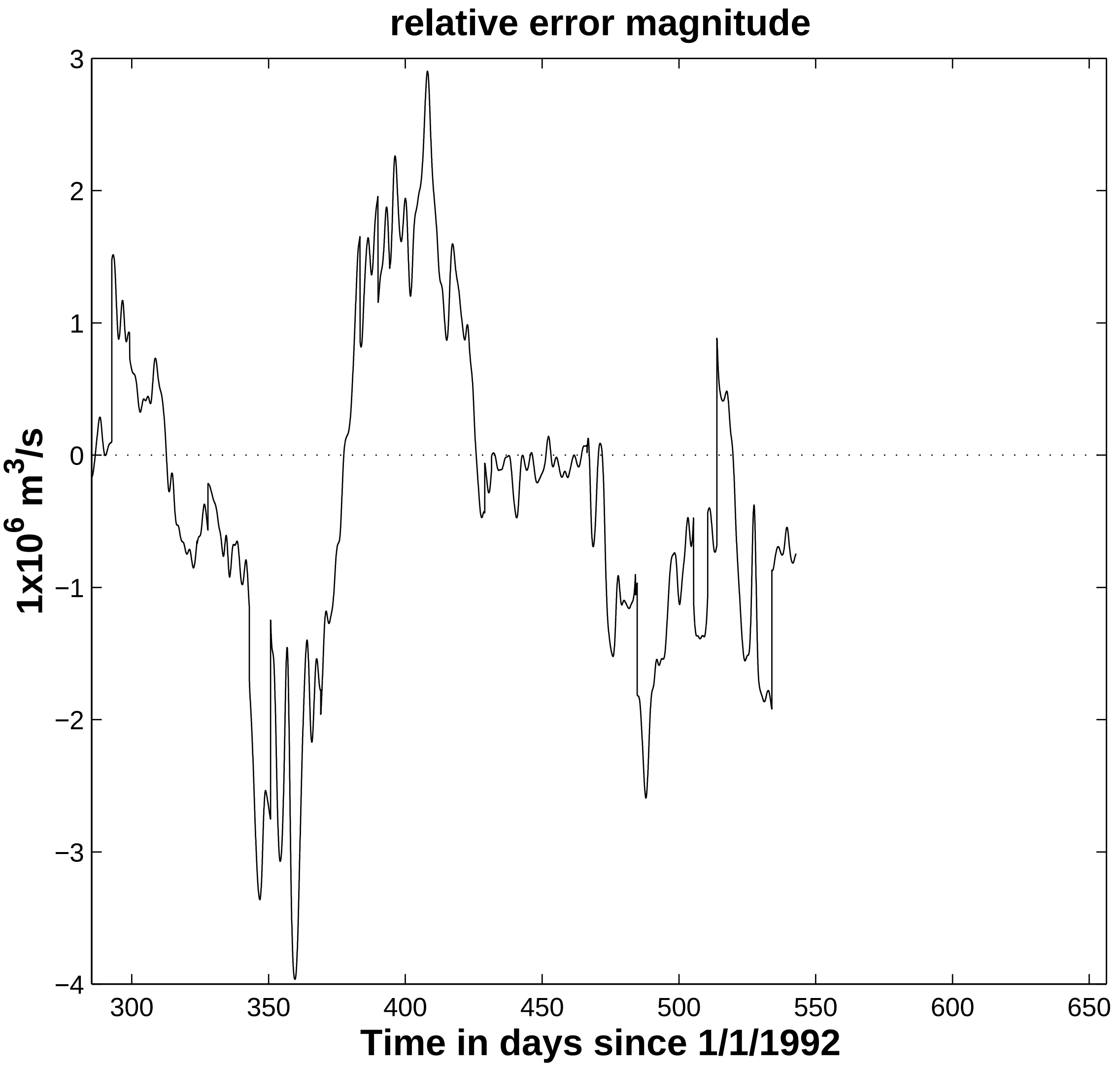
relative error magnitude
1x10⁶ m³/s
3
2
1
0
−1
−2
−3
−4
300
350
400
450
500
550
600
650
Time in days since 1/1/1992

Figure 4-24.

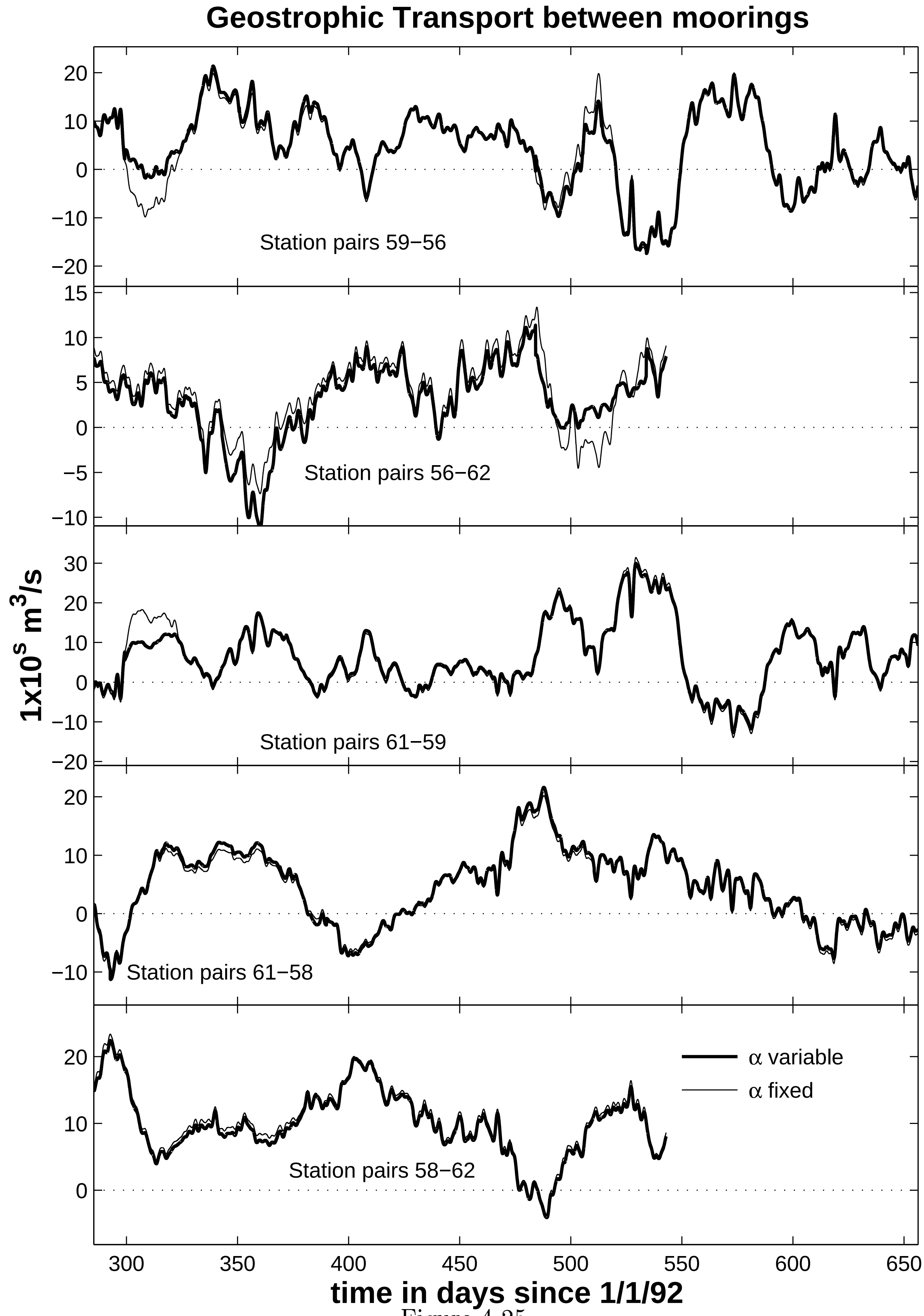
Geostrophic Transport between moorings
Station pairs 59−56
Station pairs 56−62
Station pairs 61−59
Station pairs 61−58
Station pairs 58−62
α variable
α fixed
1x10^5 m^3/s
time in days since 1/1/92
300
350
400
450
500
550
600
650
20
10
0
−10
−20
15
5
−5
30

Figure 4-25.

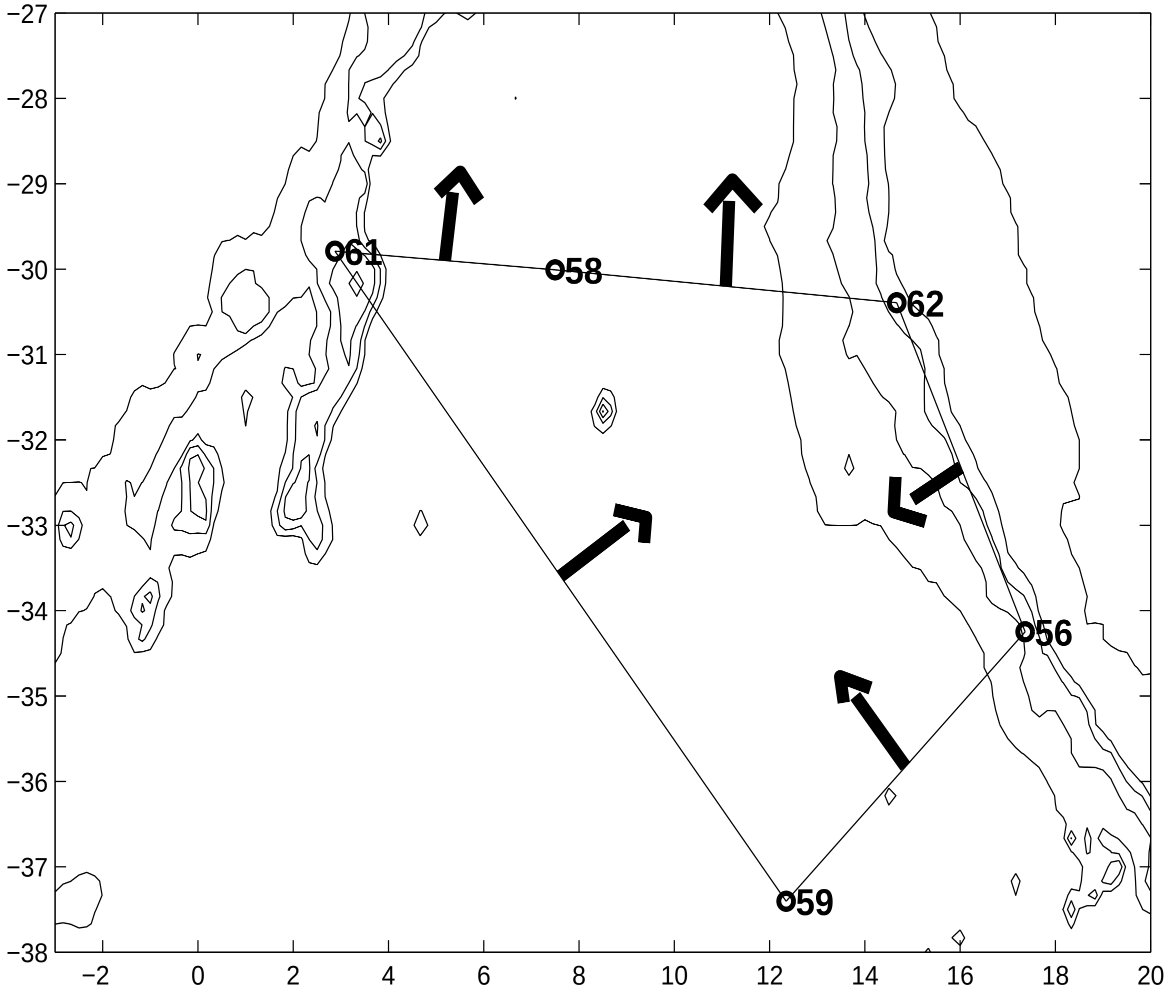
61
58
62
56
59
−27
−28
−29
−30
−31
−32
−33
−34
−35
−36
−37
−38
−2
0
2
4
6
8
10
12
14
16
18
20

Figure 4-26.

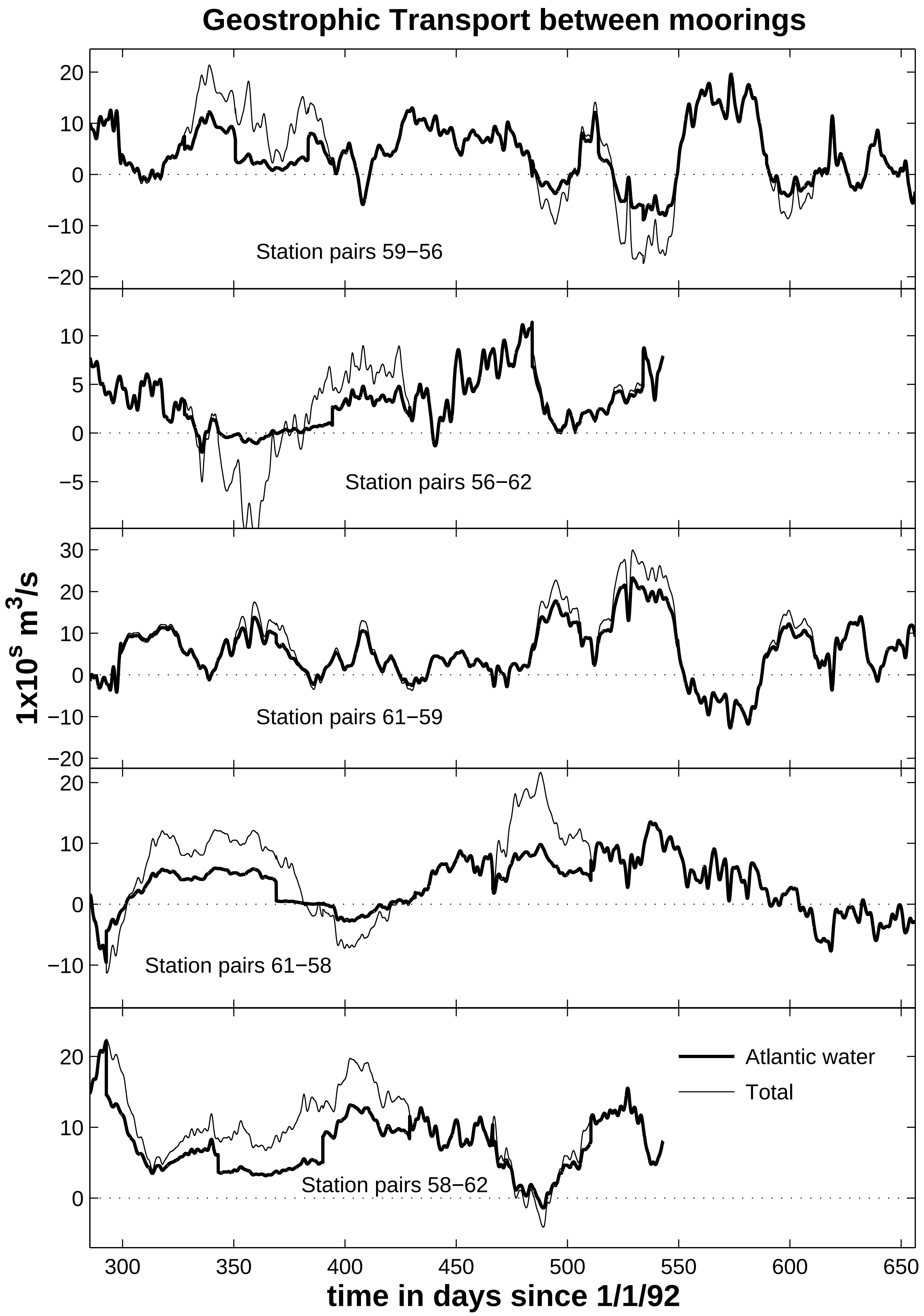
Geostrophic Transport between moorings
1x10^5 m^3/s
20
10
0
−10
−20
Station pairs 59−56
10
5
0
−5
Station pairs 56−62
30
20
10
0
−10
−20
Station pairs 61−59
20
10
0
−10
Station pairs 61−58
20
10
0
Station pairs 58−62
Atlantic water
Total
300
350
400
450
500
550
600
650
time in days since 1/1/92

Figure 4-27.

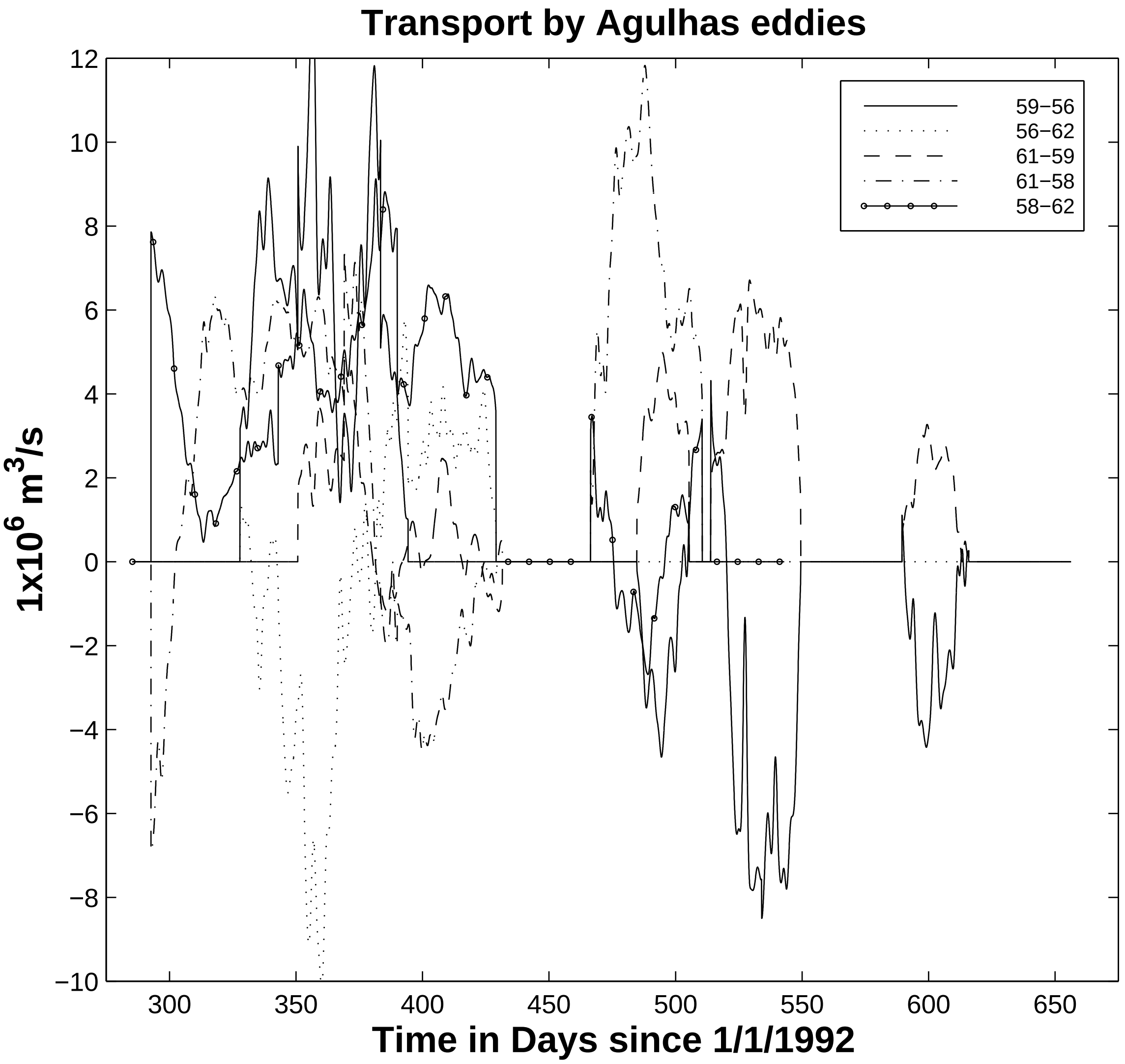
Transport by Agulhas eddies
1x10^6 m^3/s
Time in Days since 1/1/1992
12
10
8
6
4
2
0
−2
−4
−6
−8
−10
300
350
400
450
500
550
600
650
59−56
56−62
61−59
61−58
58−62

Figure 4-28.

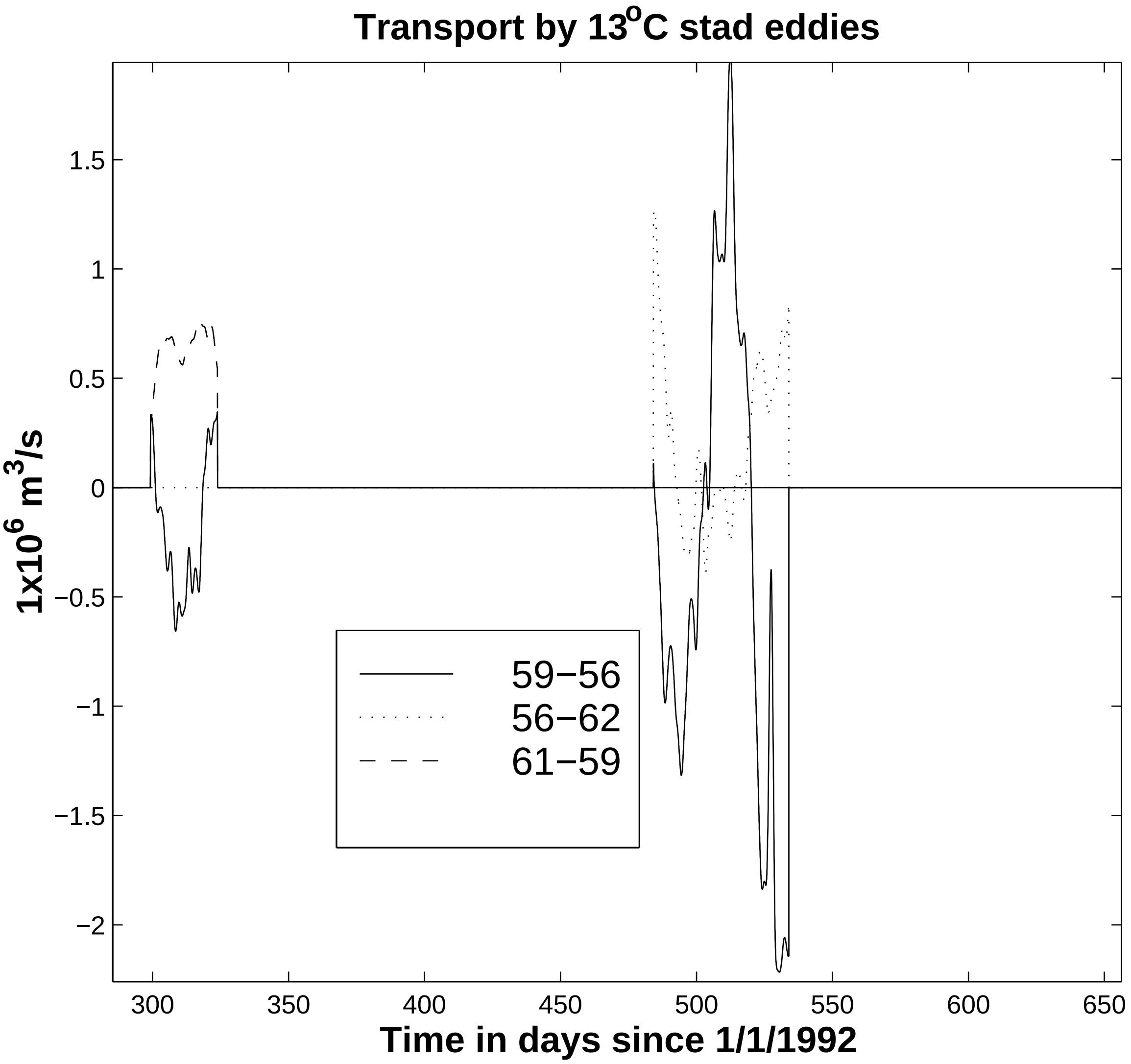
Transport by 13^{o}C stad eddies
1x10^6 m^3/s
Time in days since 1/1/1992
1.5
1
0.5
0
−0.5
−1
−1.5
−2
300
350
400
450
500
550
600
650
59−56
56−62
61−59

Figure 4-29.

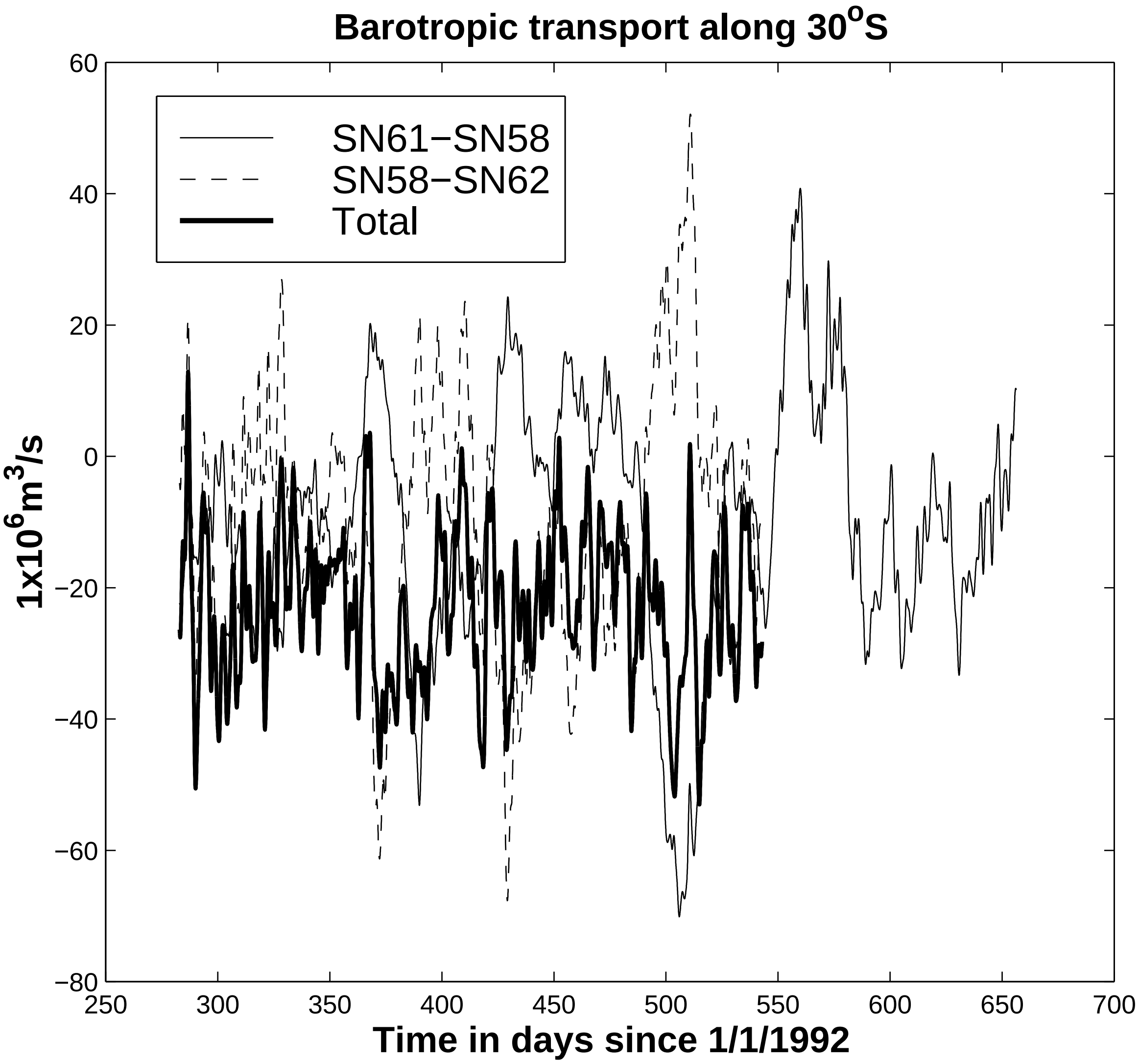
Barotropic transport along 30^{o}S
SN61−SN58
SN58−SN62
Total
1x10^{6}m^3/s
60
40
20
0
−20
−40
−60
−80
250
300
350
400
450
500
550
600
650
700
Time in days since 1/1/1992

Figure 4-30.

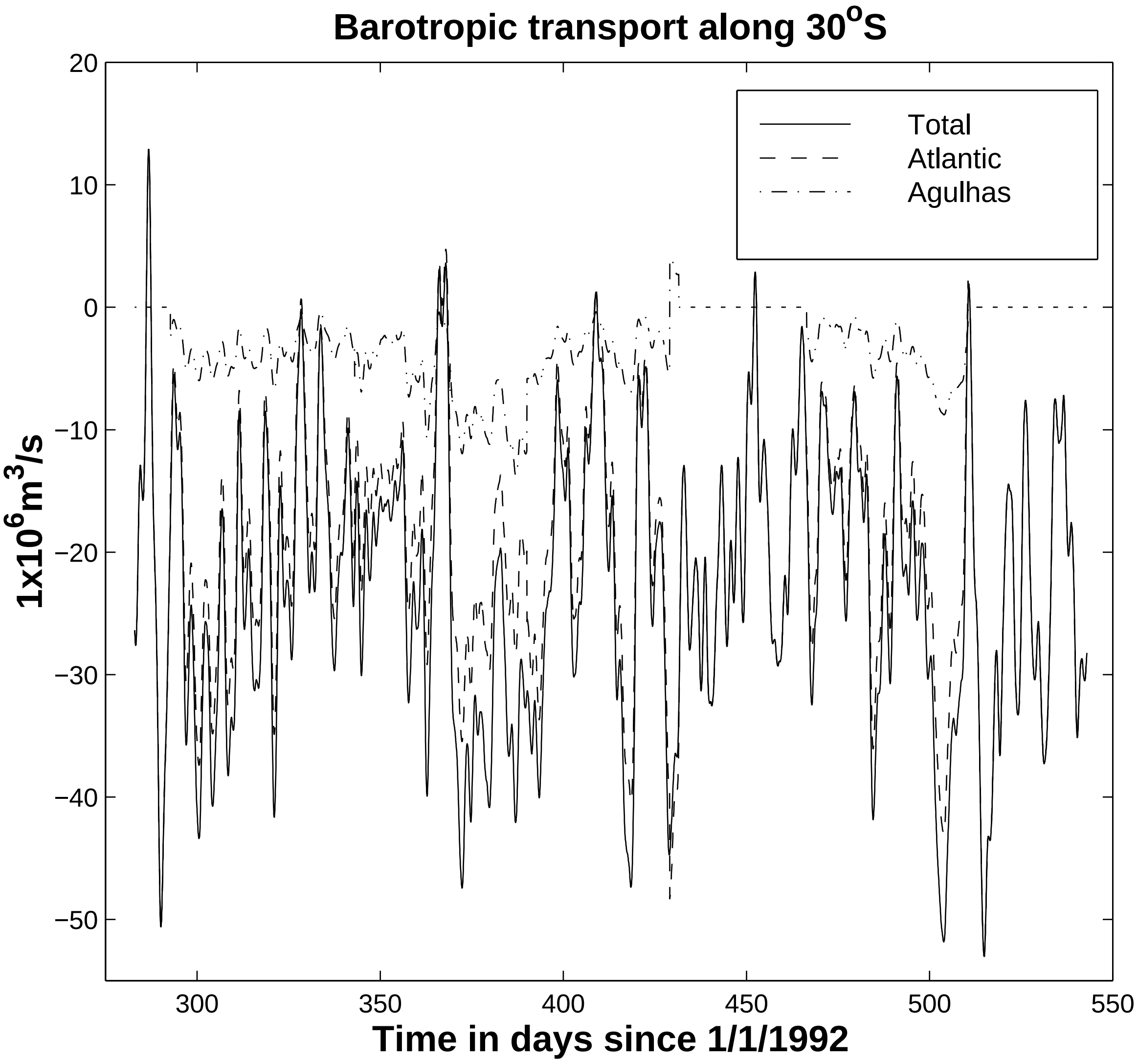
Barotropic transport along 30^{o}S
20
10
0
−10
−20
−30
−40
−50
1x10^{6}m^3/s
300
350
400
450
500
550
Time in days since 1/1/1992
Total
Atlantic
Agulhas

Figure 4-31.

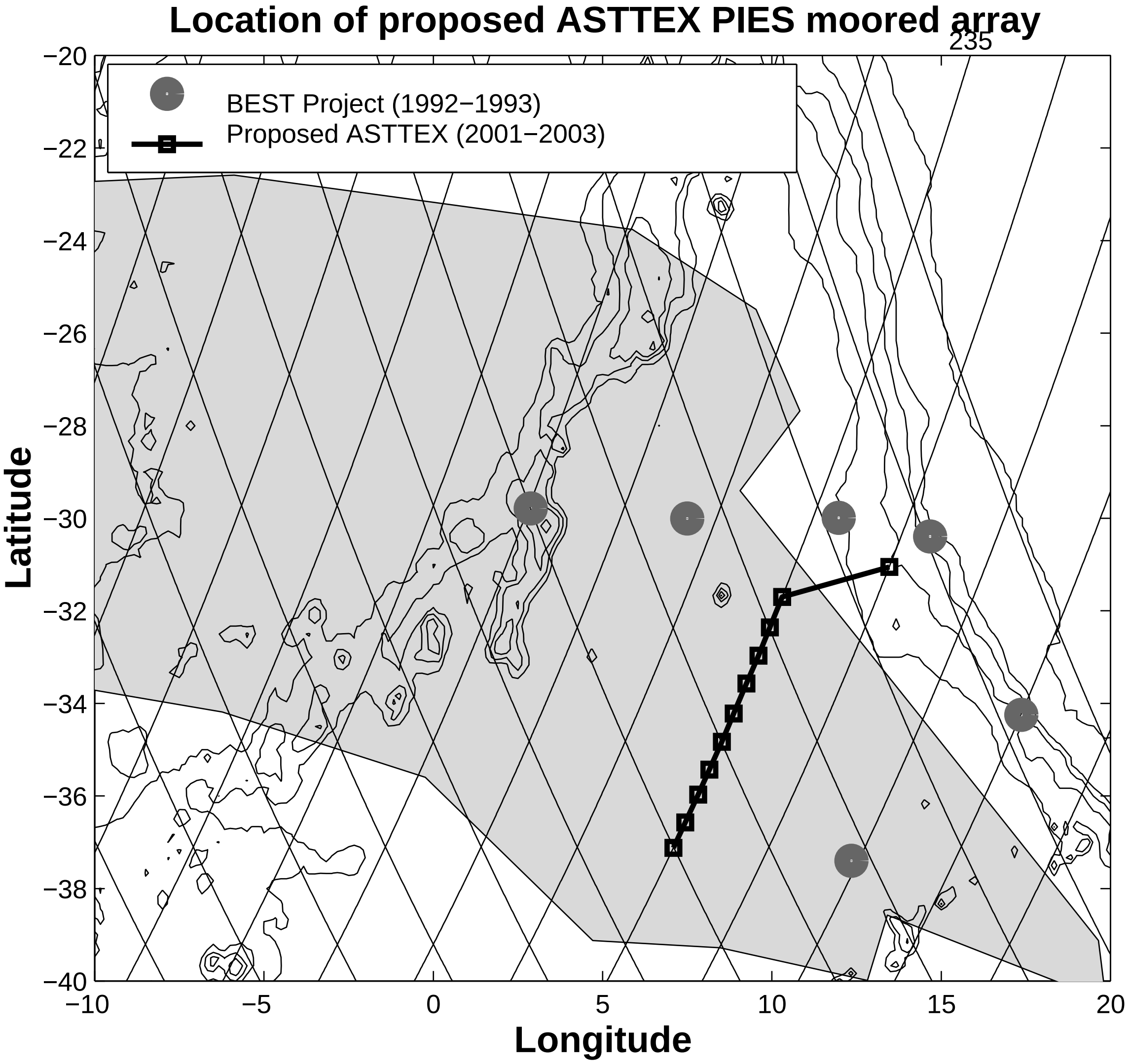
Location of proposed ASTTEX PIES moored array
235
BEST Project (1992−1993)
Proposed ASTTEX (2001−2003)
Latitude
Longitude
−20
−22
−24
−26
−28
−30
−32
−34
−36
−38
−40
−10
−5
0
5
10
15
20

Figure 4-32.

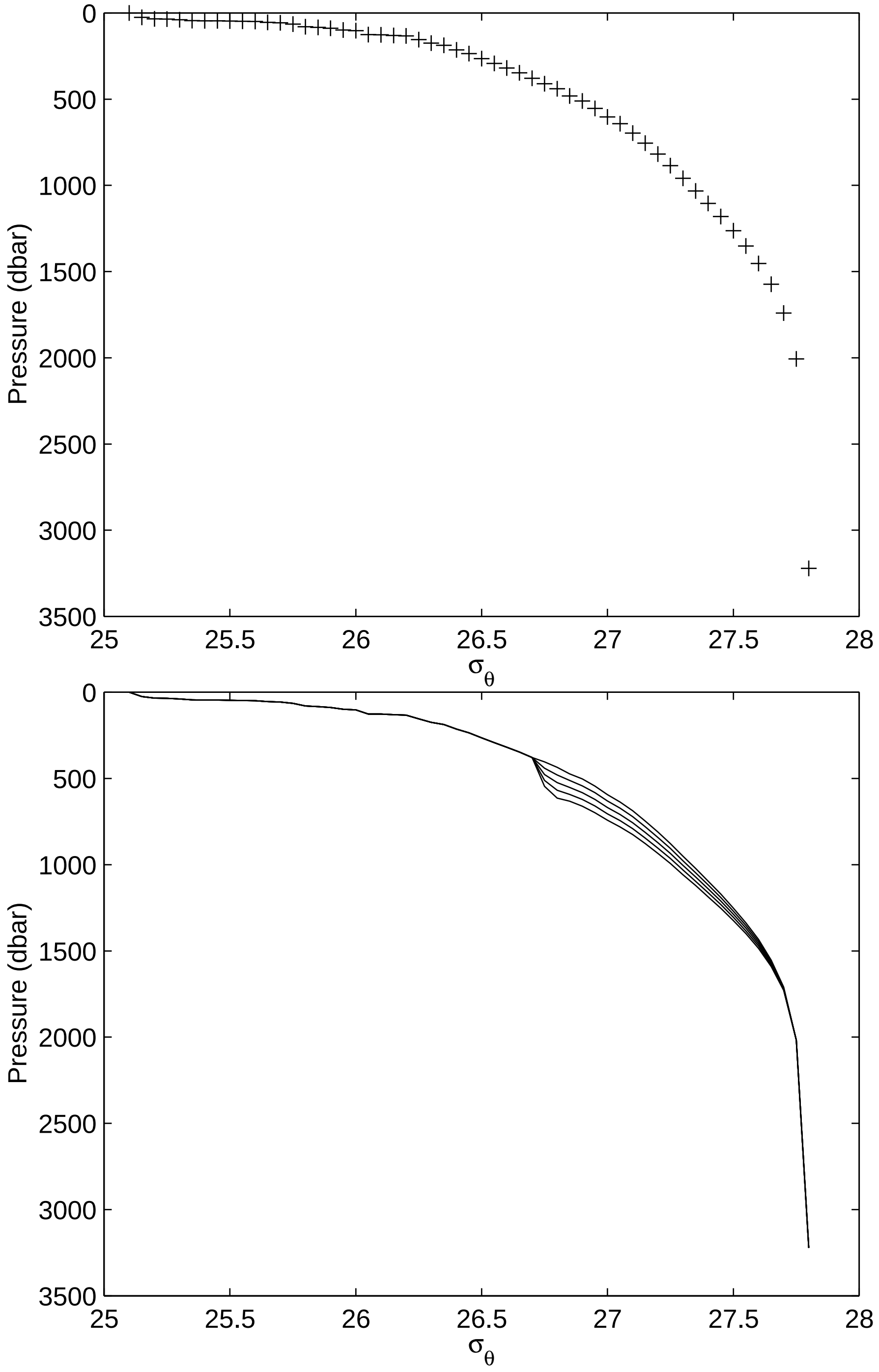
0
500
1000
1500
2000
2500
3000
3500
Pressure (dbar)
25
25.5
26
26.5
27
27.5
28
σ_θ
0
500
1000
1500
2000
2500
3000
3500
Pressure (dbar)
25
25.5
26
26.5
27
27.5
28
σ_θ

Figure 4-33.

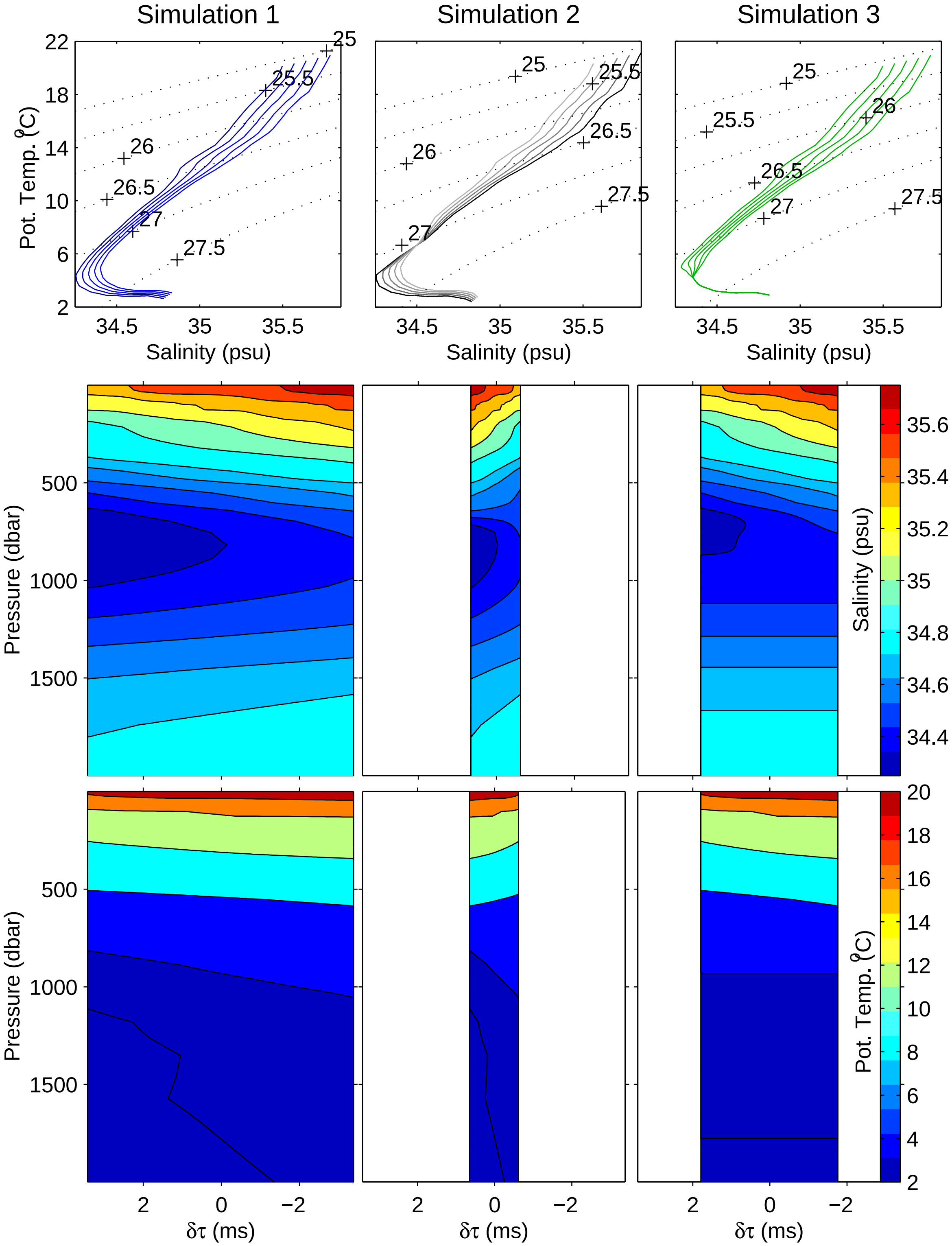
Simulation 1
Simulation 2
Simulation 3
Pot. Temp. (°C)
Salinity (psu)
22
18
14
10
6
2
34.5
35
35.5
25
25.5
26
26.5
27
27.5
Pressure (dbar)
500
1000
1500
35.6
35.4
35.2
35
34.8
34.6
34.4
Salinity (psu)
20
18
16
14
12
10
8
6
4
2
Pot. Temp. (°C)
2
0
−2
δτ (ms)

Figure 4-34.

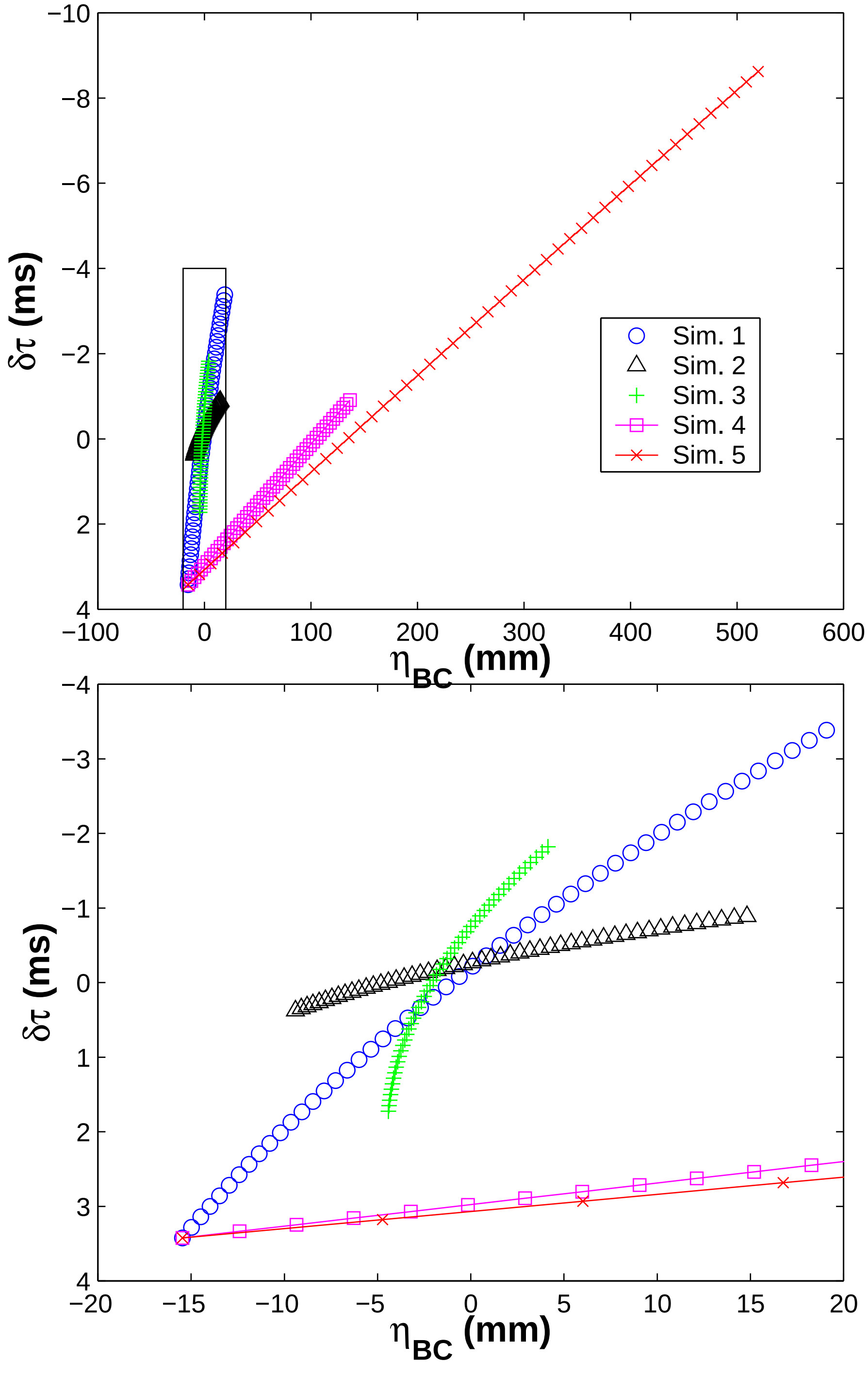
−10
−8
−6
−4
−2
0
2
4
δτ (ms)
−100
0
100
200
300
400
500
600
η_{BC} (mm)
Sim. 1
Sim. 2
Sim. 3
Sim. 4
Sim. 5
−4
−3
−2
−1
0
1
2
3
4
δτ (ms)
−20
−15
−10
−5
0
5
10
15
20
η_{BC} (mm)

Figure 4-35.

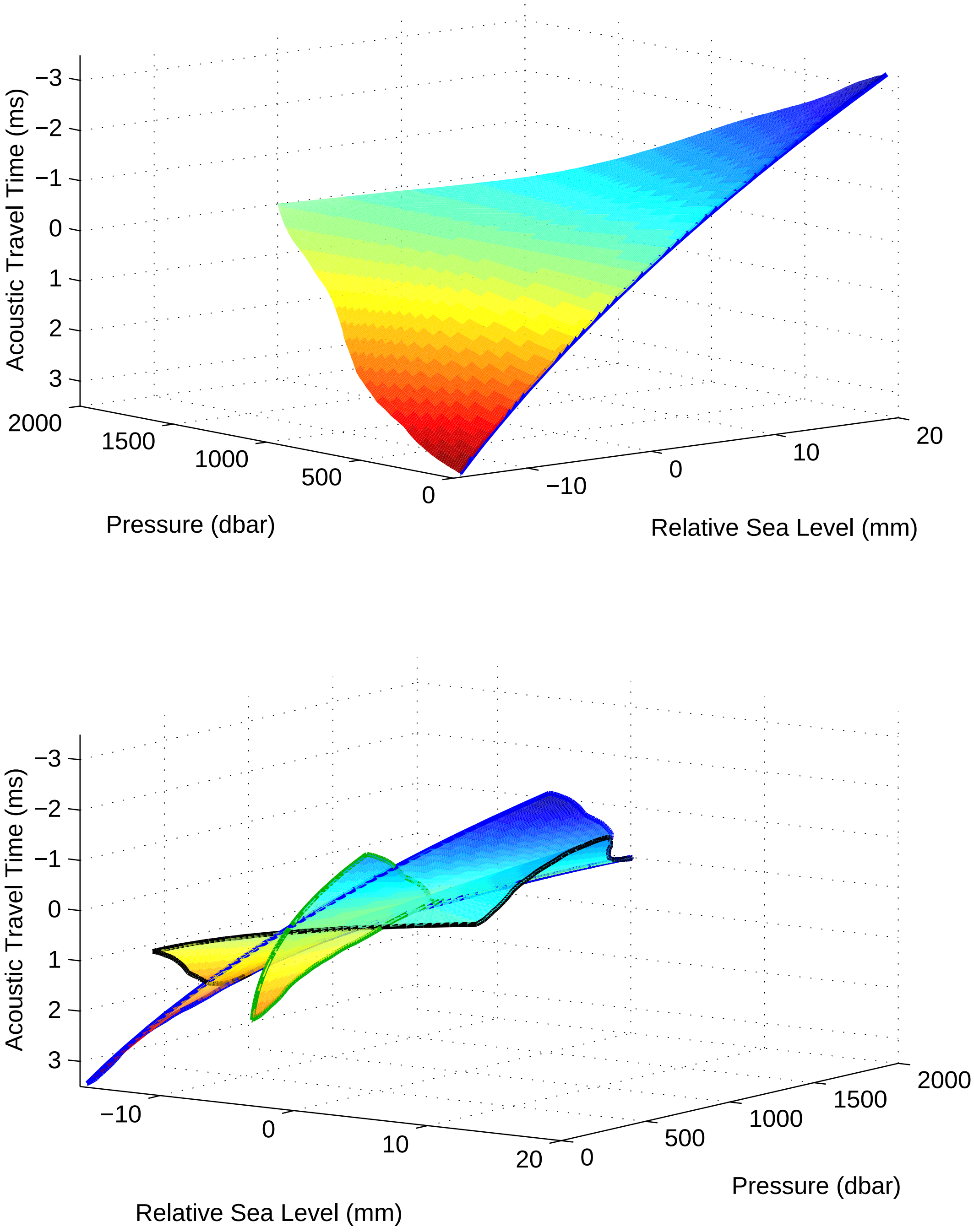
Acoustic Travel Time (ms)
−3
−2
−1
0
1
2
3
2000
1500
1000
500
0
Pressure (dbar)
−10
0
10
20
Relative Sea Level (mm)
Acoustic Travel Time (ms)
−3
−2
−1
0
1
2
3
−10
0
10
20
Relative Sea Level (mm)
0
500
1000
1500
2000
Pressure (dbar)

Figure 4-36.

Chapter 5

Future Work: GEM-ETTA in the Caribbean

Abstract

The Caribbean is a region of significant inter-ocean exchange; through its northern channels comes water from the North Atlantic and through its southern, water from the South Atlantic. The combined throughflow of North and South Atlantic water passes through the Yucatan Channel to eventually enter the Gulf Stream. The thermohaline properties of the Caribbean source waters are quite varied, creating a potential for the use of Enhanced Thermohaline Transport Analysis (ETTA) to distinguish North and South Atlantic contributions to the Caribbean throughflow. That potential is examined here. First ETTA is expanded by combining it with the Gravest Empirical Mode, a method which creates vertically resolved parameterizations of salinity and temperature based on acoustic travel time. In the combined (GEM-ETTA) method, this parameterization is extended into a third dimension, to include sea surface height. GEM-ETTA is found to be able to distinguish proportions of source water in the Caribbean to within ±12% throughout most of the water column.

5.1 Introduction

In this chapter, the potential of Enhanced Thermohaline Transport Analysis to distinguish between the sources of water for the Caribbean is examined. In addition the ETTA method is extended to parameterize the thermohaline variability of the water column in a smoothly varying way. This is done by combining ETTA with the "Gravest Empirical Mode" (GEM) initially developed by Watts et al. [2000] and Meinen and Watts [2000]. The three-dimensional representations of thermohaline variability in the water column are created from 585 casts obtained from NOAA's National Oceanographic Data Center (NODC). Salinity (S) and temperature (θ) are parameterized as functions of η_{BC}, $\delta\tau$ and pressure.

In this analysis, the parameterized GEM-ETTA fields are compared with the original data and then utilized in the analysis of simulated pressure-inverted echo sounder (PIES) mooring and altimeter data. The potential utility of the GEM-ETTA method for several purpose is assessed: the accuracy of the representation of individual profiles, the potential resolution in proportional estimates of source waters, the construction of proxy sections between mooring pairs, and the construction of time-series of water column composition at a single mooring.

5.2 The Data

The basic data set used in this analysis is a suite of 585 $\theta - S$ profiles obtained from the NODC's Oceanographic Profile Data Base. These are examined for their water mass properties and used to generate a set of acoustic travel time anomalies ($\delta\tau$) and baroclinic sea surface heights (η_{BC}). An arbitrary reference level of 1000 dbar was used for these calculations.

In the Caribbean region, thermohaline variability along isopycnals is large (Fig. 5-1a), creating correspondingly large ranges of η_{BC} and $\delta\tau$ (74 cm and 23 ms, respectively). As can been seen in Figs. 5-1a and 5-2, there is a strong correspondence between the shape of the $\theta - S$ profile and relationship of η_{BC} and $\delta\tau$. Waters of mixed source occupy a distinct intermediate area in η_{BC}-$\delta\tau$ space (Fig. 5-2) such that the ranges occupied by the source waters do not even overlap. The southern Caribbean has uniformly low values of η_{BC} and high $\delta\tau$; some of the highest acoustic travel times found in the region are associated with the South Atlantic source waters just outside of the Caribbean. The nearby North Atlantic has relatively high sea surface heights and much lower acoustic travel time anomalies. In between the two lie the Caribbean waters themselves, the thermohaline mixing mirrored by the central values of η_{BC} and $\delta\tau$. This distribution augers well for the use of η_{BC} and $\delta\tau$ as proxy-interpreters of the proportional contributions of source waters to the observed water column.

5.3 Thermohaline variability in the Caribbean region

The Caribbean (Fig. 5-3) is a region of significant inter-ocean exchange; through its northern channels comes water from the North Atlantic and through its southern, water from the South Atlantic [Wüst, 1963]. These mix energetically and then enter the North Atlantic via the Yucatan Channel, forming a source for the Florida Current [Molinari, 1976]. Bathymetric sills at depths between 800 m and 1815 m restrict the intermediate water and deep water flow into the Caribbean; thus all deep and most bottom waters are prevented from entering. As shown by Macready et al. [1999] Upper North Atlantic Deep Water (NADW) can enter at only one location, the Jungfern-Grappler sill complex. Most of the observed flow is in the upper 200 dbar [Johns et al., 1999]. Below the thermocline, the South Atlantic source for the Caribbean is fresher than that coming from the North, with a much more distinct Antarctic Intermediate Water (AAIW) salinity minimum (almost entirely lacking in the North Atlantic profiles) and somewhat less saline NADW (Figs. 5-1a and 5-3, in dark green). In the thermocline as well, the South Atlantic source water is fresher than the North at any given isotherm. Above the thermocline, the situation is reversed; the South Atlantic water has a distinct subsurface salinity maximum between 100 - 200 dbar, a mark of its passage through the equatorial region (see Sverdrup et al. [1942]). The North Atlantic water is relatively isohaline in the upper 200 dbar (Figs. 5-1a and 5-3, in red). In the central Caribbean, the North and South Atlantic waters mix (Figs. 5-1a and 5-3, in light green and purple). How the ratio of source waters varies as a function of time and space is an important question that has yet to be answered definitively.

5.4 The GEM-ETTA Method

The GEM uses fields of temperature and salinity, parameterized as functions of pressure and acoustic travel time (τ) to reproduce the observed baroclinic variability.

The GEM can be thought of as the logical extension of the common parameterization of ocean variability into the first dynamical mode, the GEM representing both the vertical structure of the ocean and its potential lateral or temporal variability, thus avoiding the limitations of projecting all variability onto a single vertical mode. It has been applied with success in areas as complex as the Subantarctic Front (SAF) south of Australia [Watts et al., 2000], and the entire Antarctic Circumpolar Current (ACC) [Sun, 2000]. In the GEM, as in ETTA, historical hydrographic data form the basis of the analysis. Two dimensional look-up tables are created where τ becomes a proxy for the vertical thermohaline structure.

The GEM-ETTA method is created by added yet a third dimension to the GEM, where both τ and η_{BC} are used to parameterize the vertical thermohaline structure. This improves the GEM by allowing it to be used in areas where η_{BC} and $\delta\tau$ are not well correlated – in other words, in areas where inter-ocean thermohaline exchange occurs. The combination of methods improves ETTA by allowing the thermohaline transports to be calculated by treating salinity and temperature as smooth functions of $\delta\tau$ and η_{BC}, rather than the "step functions" which were created by switching between different water column types in the initial implementation.

To create the GEM-ETTA parameterizations, all of the hydrographic profiles were sorted according to their values of η_{BC} and $\delta\tau$, binned at 2 cm, 2 ms, 1 dbar intervals (Fig. 5-4a) and gridded (a two-dimensional linear interpolation on pressure surfaces). The gridded fields at each pressure (p) level are smoothed and interpolated to 1 cm, 1 ms, 1 dbar intervals by fitting with fourth-degree polynomial along lines of constant $\delta\tau$, then a cubic spline along lines of constant η_{BC}. This procedure creates 3-dimensional look-up tables which are smoothed fields of parameterized S and θ at a 1 cm, 1 ms, 1 dbar resolution, (e.g., Fig. 5-4b). Wherever a bin contains more than one profile, the reduction in observed variability caused by using the GEM-ETTA field as a proxy for *in situ* θ and S at that point is well-determined. Obviously the density of available historic hydrography has a significant effect on the accuracy of the GEM-ETTA fields.

5.5 Results

While some of the variability in *in situ* temperature and salinity is reduced as a result of the GEM-ETTA parameterizations, the results are strikingly realistic. In Fig. 5-1b, parameterized GEM-ETTA salinity and temperature are plotted for each of the original hydrographic stations. What is immediately apparent is not how much variability has been lost, but how much of the information about the original structure of the water column has been retained.

The standard errors in the GEM-ETTA representation of each cast are 0.32 ppt and 1.4 °C at the surface, 0.08 ppt and 0.6 °C at 200 dbar, 0.05 ppt and 0.3 °C at 400 dbar, and 0.04 ppt and 0.3 °C at 800 dbar.

In the raw data, the difference between source waters at those levels is 1.00 ppt and 1.1 °C, 0.65 ppt and 5.5 °C, 1.42 ppt and 8.1 °C, and 1.06 ppt and 7.4 °C, respectively. Thus the errors inherent in using the parameterizations of S and θ are O(10 - 30) times less than the variability found in the source waters below 100m. The creation of seasonal GEM-ETTA fields, not attempted here, is expected to significantly reduce the error in the GEM-ETTA temperature and salinity fields in the upper 100 - 200 m of the water column. Assuming the altimeter and PIES records are exactly accurate, the current (non-seasonal) GEM-ETTA parameterization would allow the proportions of different source waters to be distinguished to within $\sim \pm 23\%$ between 0 - 200 dbar, to within $\sim \pm 5\%$ between 200 - 900 dbar and to within $\sim \pm 7\%$ between 900 - 1000 dbar.

In practice, the GEM-ETTA parameterization is applied to measurements of $\delta\tau$ from a PIES sensor and measurements of total sea surface height (SSH) from an altimeter. Bottom pressure (BP) measurements provide both a tide record, for use in correcting the altimetry, and an accurate measure of the sub-tidal barotropic component of SSH (η_{BT}, uncertainty at ±2 cm). The difference between the altimetric estimate of SSH and η_{BT} is the baroclinic component of SSH, η_{BC}. Assuming levels of collected error and uncertainty in processed PIES and altimeter records of 1 ms and 3 cm (the latter assuming collected processing errors at 1 cm rms), respectively, this would still allow proportions of different sources to be distinguished to within ±12% through most of the water column.

The creation of seasonal GEM-ETTA fields, not attempted here, is expected to significantly enhance agreement in the upper 100 - 200 m of the water column. Additional data density would improve agreement at the edges of the parameterized fields, and with some small adjustments to the parameterization technique, the ratio of dataset variability to GEM-ETTA uncertainties could likely be improved still further. Another possibility yet to be explored would be the GEM-ETTA parameterization of other quantities of interest, such as the dissolved oxygen field. It remains to be seen if sufficient data are available to construct such fields.

5.6 Using GEM-ETTA

Vertical sections through the the GEM-ETTA temperature and salinity fields at the locations indicated in Fig. 5-4 are shown in Fig. 5-5. These have been plotted as functions of $\delta\tau$. Each of the sections in Fig. 5-5 could be the GEM-ETTA parameterization or "proxy-representation" of the waters lying between a pair of PIES moorings, with the instantaneous values of $\delta\tau$ at each mooring plus a satellite altimeter/bottom-pressure estimate of η_{BC} determining one of the endpoints in the slice (Fig. 5-4b). Sections like these can be used to calculate the transport of individual water masses through a moored array. The appropriate horizontal and vertical scales of the water masses are implicit in the proxy data, precluding the need for assumed scaling factors of any kind.

Note that the low-salinity AAIW core, (Fig. 5-5a at 800 dbar and 13.5 ms), is almost absent in Fig. 5-5c but where present extends to more negative values of $\delta\tau$ (warmer water columns). In addition, in Fig. 5-5a AAIW is associated with very low sea surface height, whereas along the sections in Fig. 5-5c and d, it is associated with relatively high sea surface height. The fact that temperature and salinity can vary considerably over a single value of $\delta\tau$ in this region is proof of the necessity of using the GEM-ETTA parameterization (as opposed to just the GEM) to encompass the complexity of the thermohaline variability in this region. This phenomenon is expected be observed wherever inter-ocean exchange occurs (see Chapter 4, Appendix B).

GEM-ETTA time-series sections at individual mooring locations can also be generated. Mooring and altimeter records were simulated with a red spectrum, random walk through observed values of η_{BC} and $\delta\tau$. These series were then subsampled at the TOPEX/POSEIDON repeat interval to create the kind of dataset that might be used with GEM-ETTA. The subsamples were used as look-up indices into the parameterized GEM-ETTA fields. In Fig. 5-6, semi-periodic intrusions of AAIW into the water column (arriving in concert with fresher deep water, as would occur with a strong influx of South Atlantic water) are the most noticeable feature of the resultant time-series sections.

5.7 Conclusions

Preliminary GEM-ETTA fields for the Caribbean Sea and vicinity show sea surface height and acoustic travel time are likely to be successful as proxies for the discrimination of North Atlantic and South Atlantic fluxes into the Caribbean. The standard error in GEM-ETTA parameterizations is O(10 - 30) times less than the difference between source waters at depths between 0 - 1000 dbar, surface temperature excepted. When compared with the original *in situ* data, parameterized fields reproduce the major features observed in the water column. When estimates of instrumental error in the measured proxies ($\delta\tau$ and η_{BC}) are taken into account, mixes in the source waters should be able to be distinguished to within ±12% throughout most of the water column.

Future refinements might include the incorporation of additional data from the Caribbean, the determination of an appropriate baroclinic reference level for the region, and the calculation of seasonal GEM-ETTA fields for the upper few hundred meters.

Acknowledgments. Randy Watts and Che Sun shared their expertise on the Gravest Empirical Mode and Randy in particular provided enthusiastic support for the idea of its synthesis with ETTA. Paul Marchese provided some of the Caribbean data used herein and very timely advice on some of the early work in that region.

Bibliography

Johns, E., W. D. Wilson and R.L. Molinari, Direct observations of velocity and transport in the passages between the intra-American Sea and the Atlantic Ocean. *J. Geophys. Res., 104*, 25,805-25,820, 1999.

Macready, P., W. E. Johns, C. G. Rooth, D. M. Fratantoni and R. A. Watlington, Overflow into the deep Caribbean: Effects of plume variability, *J. Geophys. Res., 104*, 25,913-25,935, 1999.

Meinen, C. S. and D. R. Watts, Vertical structure and transport on a transect across the North Atlantic Current near 42°N, *J. Geophys. Res.*, submitted, 2000.

Molinari, R.L., The Formation of the Yucatan Current Based on Observations of Summer 1971, *J. Phys. Oc, 5*, 596-602, 1976.

Sun, C. and D. R. Watts, A Study of Heat Flux Carried by the Mean ACC Flow, presented at the American Geophysical Union Ocean Sciences meeting, January 2000.

Sverdrup, H. U., M. W. Johnson and R. H. Fleming, The Oceans: Their Physics, Chemistry and General Biology, Prentice-Hall, New York, 1942.

Watts, D.R, C. Sun and S. Rintoul, Gravest Empirical Modes determined from hydrographic observations in the Subantarctic Front, *J. Geophys. Res.*, submitted, 2000.

Wüst, G., On the stratification and the circulation in the cold water sphere of the Antillean-Caribbean basins, *Deep-Sea Res., 10*, 165-187, 1963.

Figure 5-1a, b. a) (top) Hydrography of the Caribbean region. Water from the North Atlantic, with little or no AAIW and relatively saline NADW, is plotted in red x's. In dark green squares are three stations characteristic of the South Atlantic source waters for the Caribbean, with a strong AAIW layer and relatively fresh NADW. Purple crosses mark profiles of mixed origin which are relatively salty, and light green circles mark those which are relatively fresh. b) (bottom) GEM-ETTA parameterizations of the same profiles based on $\delta\tau$ and η_{BC}.

Figure 5-2. Distribution of η_{BC} and $\delta\tau$ calculated for the 585 hydrographic profiles plotted in Figs. 5-1 and 5-3. The color key is identical to the one in those figures. The strong effect of thermohaline composition on these parameters is visible, fanning the observed values out into three distinct groups; Caribbean data form the central group (in purple and light green) lying between North Atlantic (red) and South Atlantic (dark green).

Figure 5-3. Station map of the hydrographic data used in this study; station colors and symbols are identical to those in Figs. 5-1 and 5-2. The coast, 1000 m and 2000 m isobaths have been contoured.

Figure 5-4a, b. a) (top) The observed distribution of salinity at 200 dbar, as a function of η_{BC} and $\delta\tau$. Salinity values at this level have been binned at 2 cm, 2 ms intervals preparatory to gridding them. b) (bottom) The resultant GEM-ETTA parameterization of salinity at 200 dbar. (both) Black lines indicate the locations of transects pictured in Fig. 5-5.

Figure 5-5a, b, c, d. a) (top left). Salinity section through the GEM-ETTA field. Black dots indicate the locations of hydrographic data available for the determination of the field in the vicinity of this transect (here subsampled at 50 dbar for clarity). b) (top right) Temperature section taken at the same location as in a). Note that sea surface height decreases by 68 cm from left to right along this section. c) (bottom left) Vertical section of salinity from GEM-ETTA parameterization as in a), except that sea surface height increases by 9 cm from left to right along the section. d) (bottom right) Temperature section from the same location as in c).

Figure 5-6a, b. Vertical GEM-ETTA sections created by a constrained red-spectrum, random walk in η_{BC}, $\delta\tau$ space. These sections simulate the information that could be obtained from a single PIES mooring deployed on or near an altimeter groundtrack. The temporal spacing of the sampling is based on the TOPEX/POSEIDON (JASON) exact repeat interval. a) (top) Salinity b) (bottom) Temperature.

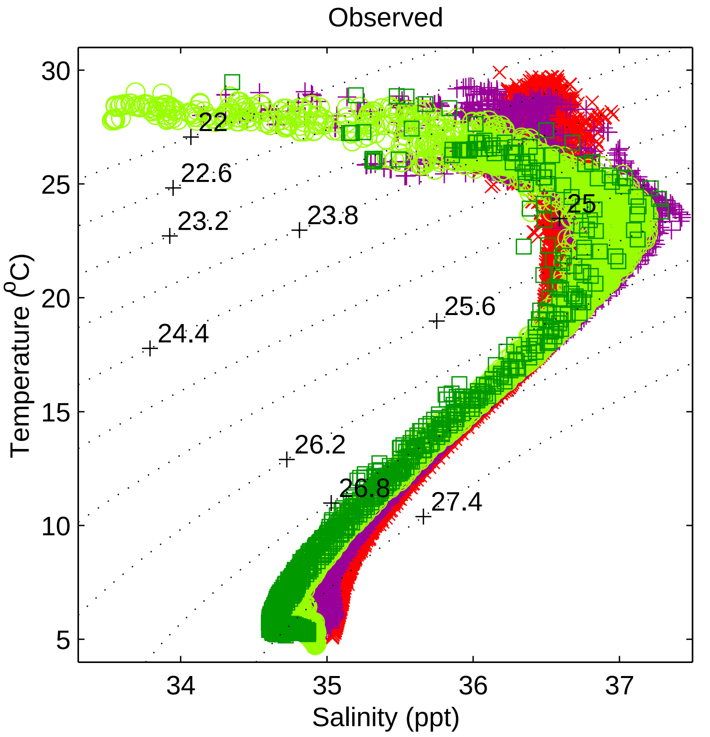
Observed
Temperature (°C)
Salinity (ppt)
30
25
20
15
10
5
34
35
36
37
22
22.6
23.2
23.8
24.4
25
25.6
26.2
26.8
27.4

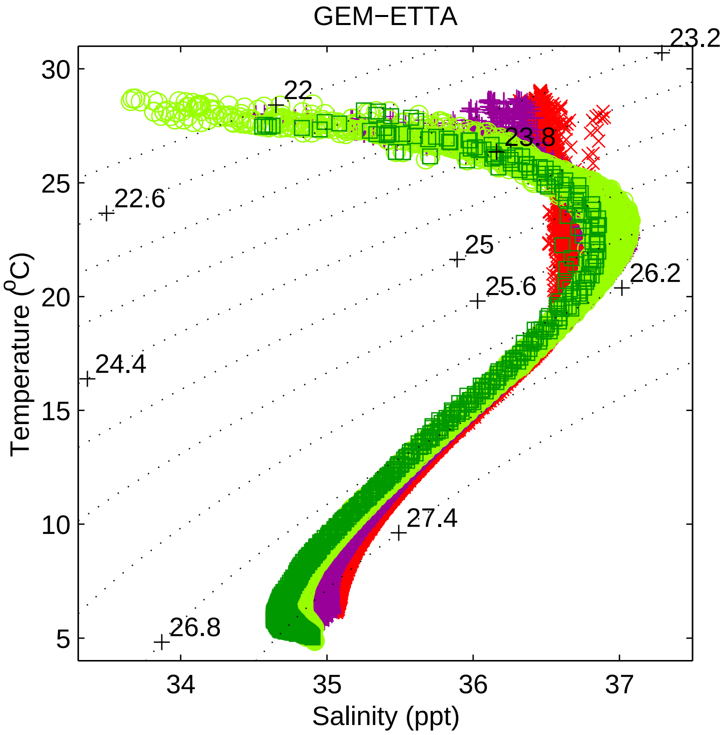
GEM−ETTA
Temperature (°C)
Salinity (ppt)
30
25
20
15
10
5
34
35
36
37
22
22.6
23.2
23.8
24.4
25
25.6
26.2
26.8
27.4

Figure 5-1.

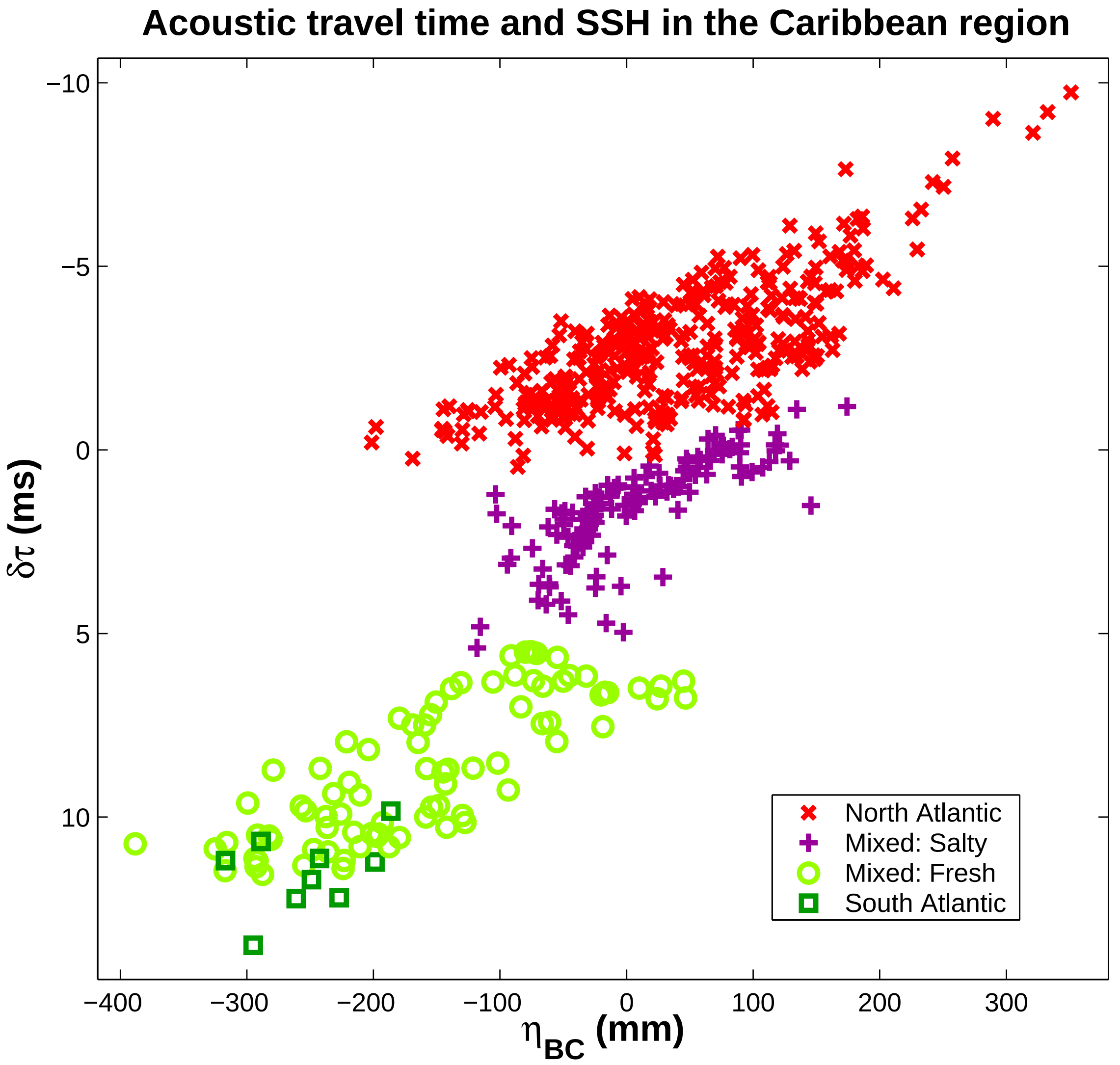
Acoustic travel time and SSH in the Caribbean region
δτ (ms)
−10
−5
0
5
10
−400
−300
−200
−100
0
100
200
300
η_{BC} (mm)
North Atlantic
Mixed: Salty
Mixed: Fresh
South Atlantic

Figure 5-2.

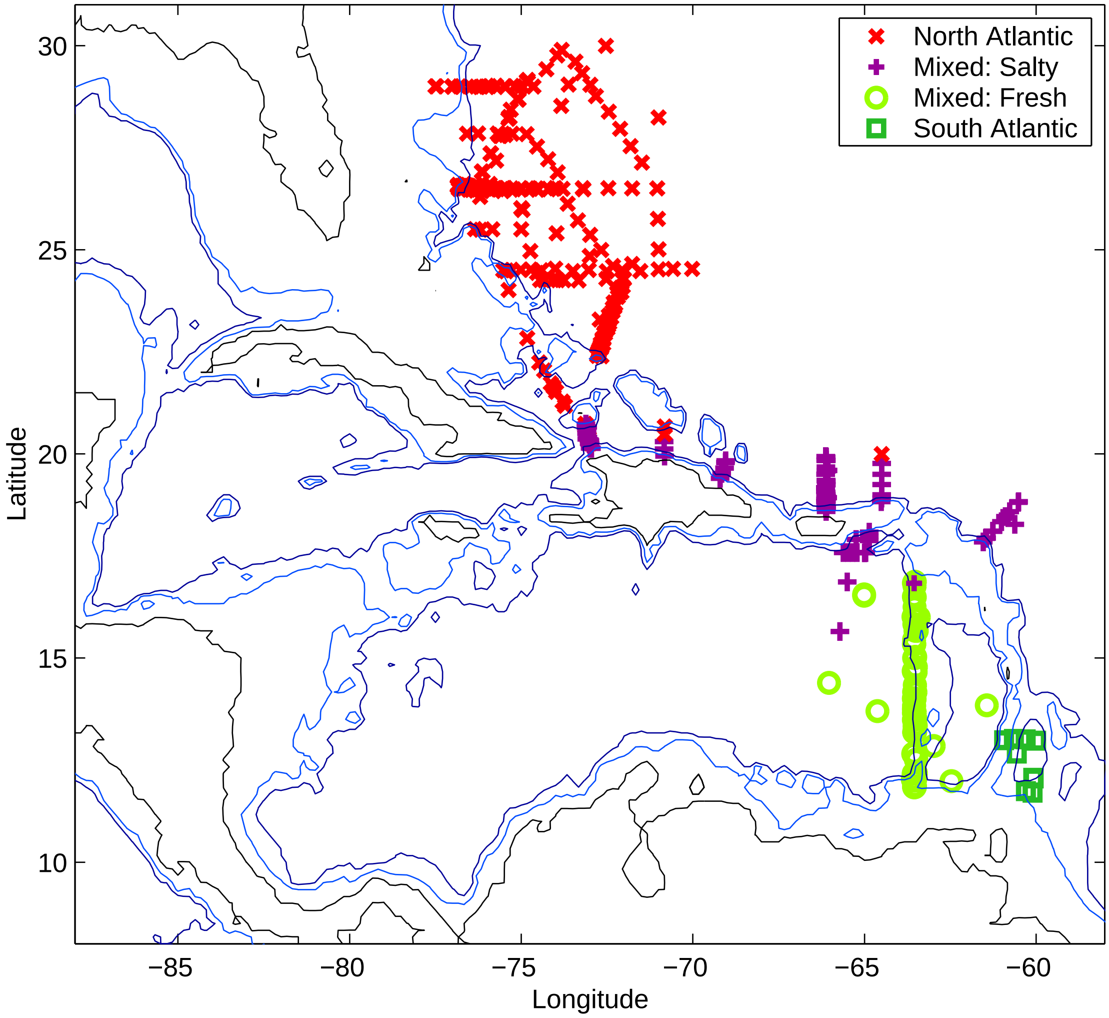
North Atlantic
Mixed: Salty
Mixed: Fresh
South Atlantic
Latitude
Longitude
30
25
20
15
10
−85
−80
−75
−70
−65
−60

Figure 5-3.

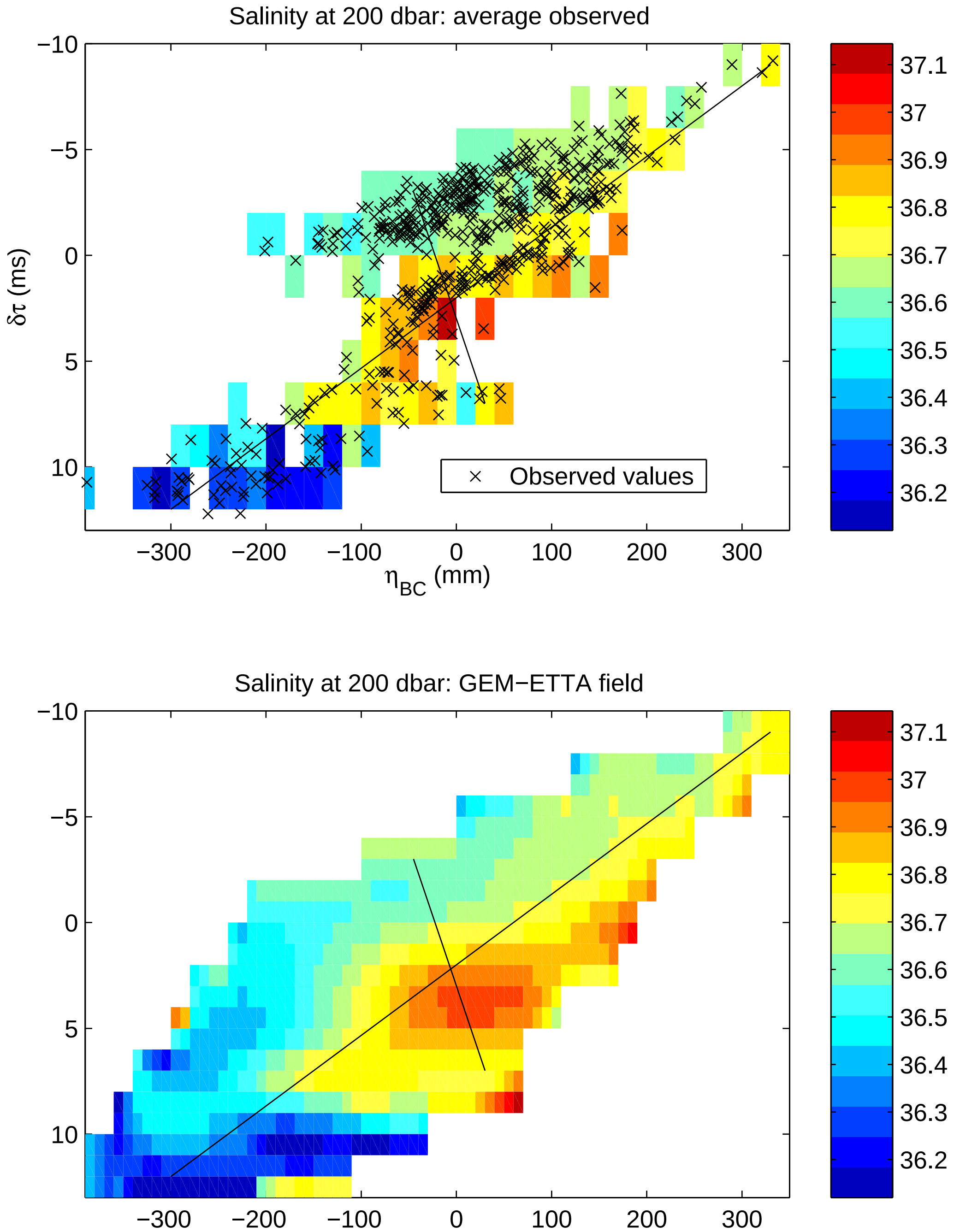
Salinity at 200 dbar: average observed
−10
−5
0
5
10
δτ (ms)
−300
−200
−100
0
100
200
300
η_{BC} (mm)
Observed values
37.1
37
36.9
36.8
36.7
36.6
36.5
36.4
36.3
36.2
Salinity at 200 dbar: GEM−ETTA field
−10
−5
0
5
10
−300
−200
−100
0
100
200
300
37.1
37
36.9
36.8
36.7
36.6
36.5
36.4
36.3
36.2

Figure 5-4.

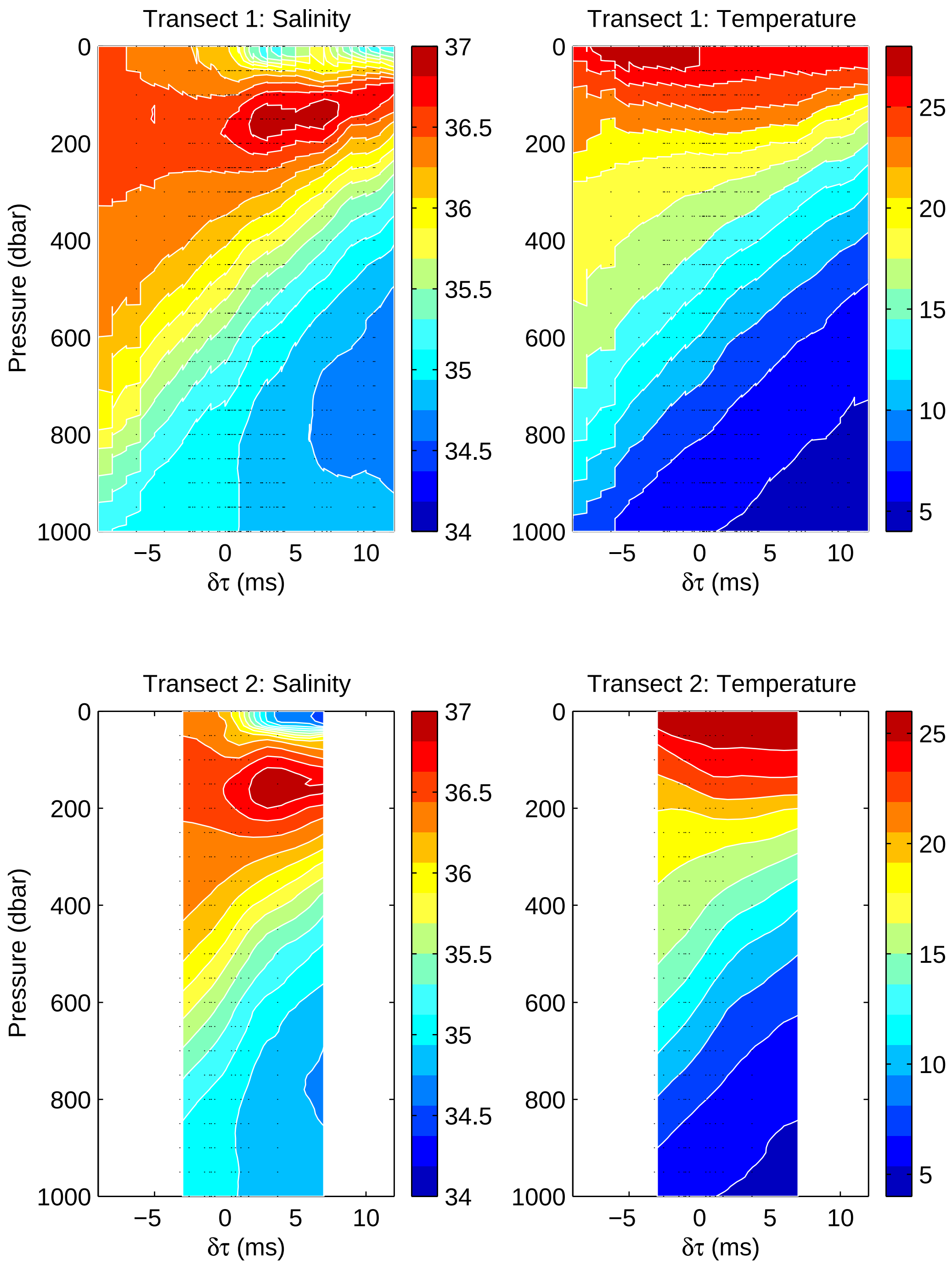
Transect 1: Salinity
Transect 1: Temperature
Transect 2: Salinity
Transect 2: Temperature
Pressure (dbar)
0
200
400
600
800
1000
−5
0
5
10
δτ (ms)
37
36.5
36
35.5
35
34.5
34
25
20
15
10
5

Figure 5-5.

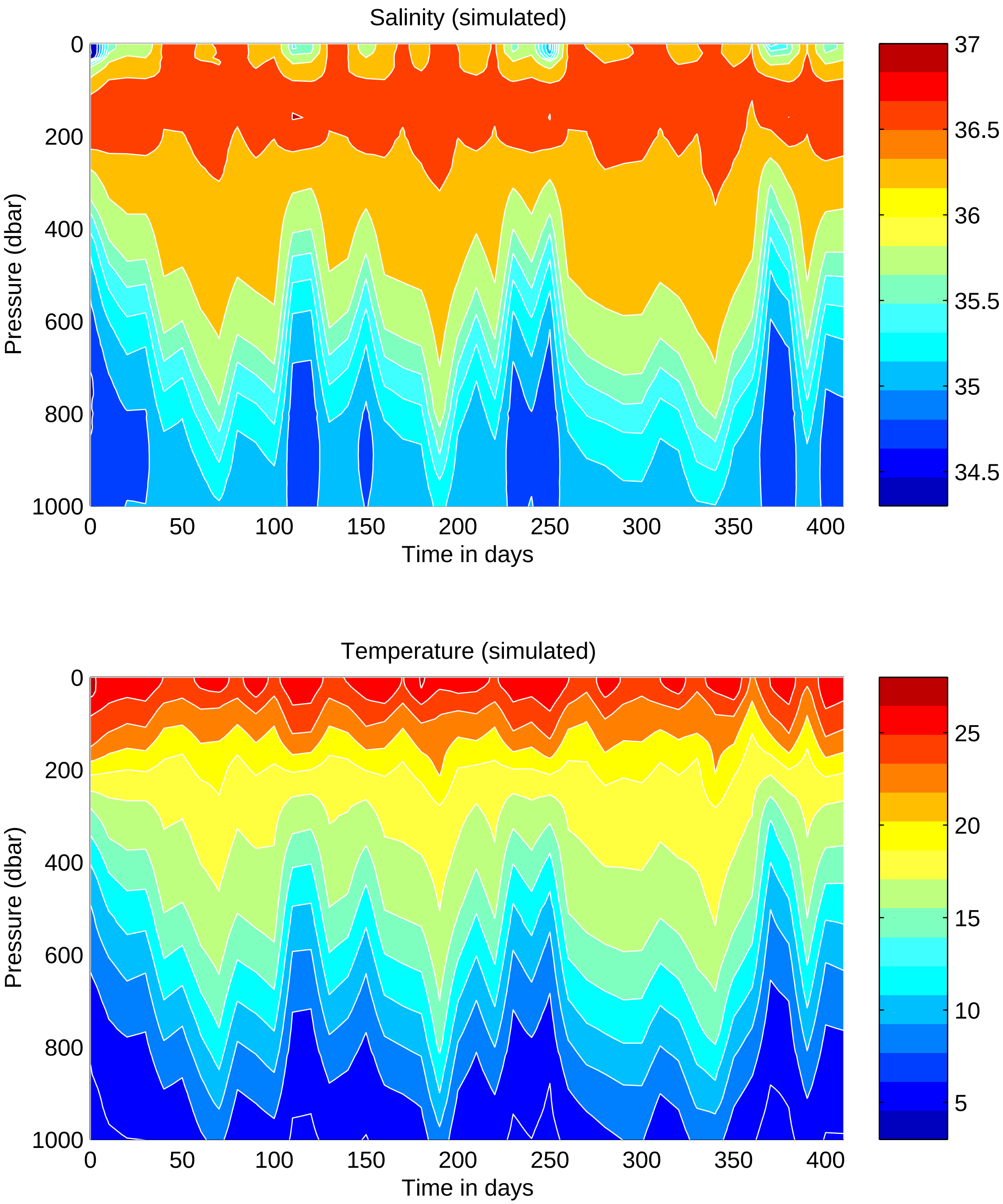
Salinity (simulated)
Pressure (dbar)
0
200
400
600
800
1000
0
50
100
150
200
250
300
350
400
Time in days
37
36.5
36
35.5
35
34.5
Temperature (simulated)
Pressure (dbar)
0
200
400
600
800
1000
0
50
100
150
200
250
300
350
400
Time in days
25
20
15
10
5

Figure 5-6.